Vasco Fernandes

Palladium alloy model systems for understanding the surface properties of Pd-based membranes and catalysts

Thesis for the degree of Philosophiae Doctor

Trondheim, January 2014

NTNU – Trondheim
Norwegian University of
Science and Technology

Para a minha família
Til min familie
To my family

Abstract

Palladium has high solubility, permeability and selectivity for hydrogen, thus being a suitable membrane material for hydrogen separation. In addition, palladium is a versatile catalyst with applications in industrial processes such as CO removal in car exhaust or total oxidation of hydrocarbons. In this thesis, surface science techniques such as X-ray photoelectron spectroscopy, scanning tunneling microscopy, and low energy electron diffraction, as well as theoretical tools including solid state kinetic analysis and density functional theory, have been utilized for atomic level investigations of Pd(100) and PdAg(100) surfaces as model systems for Pd-based membranes and catalysts.

Clean Pd(100) and PdAg(100) have distinct surface signatures. While for Pd(100) the contribution from the surface region in the Pd $3d_{5/2}$ core level is observed at lower binding energy relative to the bulk Pd component, for $Pd_{75}Ag_{25}$(100) the surface contribution is observed at higher binding energies relative to the bulk $Pd_{75}Ag_{25}$ component, which is found to be a signature of Pd embedded in Ag. The composition of the clean $Pd_{75}Ag_{25}$(100) surface shows enrichment of Ag at the top most layers. On both surfaces a $(\sqrt{5} \times \sqrt{5})$R27° surface oxide structure can be formed. The oxidation of the $Pd_{75}Ag_{25}$(100) surface by molecular oxygen results in a $(\sqrt{5} \times \sqrt{5})$R27° surface oxide structure similar to the one reported for Pd(100). The interface layer between the surface oxide and the bulk $Pd_{75}Ag_{25}$ was found to be rich in Ag. The calculated core level shifts for the oxidized surface are in good agreement with the experimental observations.

The reduction of the $(\sqrt{5} \times \sqrt{5})$R27° surface oxide structure on the Pd(100) and $Pd_{75}Ag_{25}$(100) surfaces by CO was found to proceed faster with increasing temperature. Kinetic analysis indicates that the reduction process is phase boundary controlled for Pd(100) in the temperature range from 30°C to 120°C. On $Pd_{75}Ag_{25}$(100) the surface oxide reduction is significantly slower compared to Pd(100). A phase boundary controlled surface oxide reduction is observed at temperatures of 120°C and above, while at and below 70°C the reduction is found to be diffusion limited. Density functional theory calculations show that the presence of silver in the outermost surface layer significantly increases the CO diffusion barriers on the reduced areas, supporting a diffusion limited reduction process for $Pd_{75}Ag_{25}$(100) at lower temperatures. Compared to the CO case, reduction by H_2 is significantly more complex. The reduction of the $(\sqrt{5} \times \sqrt{5})$R27° surface oxide on Pd(100) and $Pd_{75}Ag_{25}$(100) using H_2 show a complex non monotonic temperature dependent behavior. For Pd(100) the surface oxide reduction is rather independent of temperature, while for $Pd_{75}Ag_{25}$(100) is slowest at 30°C, increases at intermediate temperatures, and decreases at 170°C. The dependence in tempera-

ture of the reduction rates for $Pd_{75}Ag_{25}(100)$ correlates with the amount of surface Pd atoms. As with CO, reduction proceeds slower on $Pd_{75}Ag_{25}(100)$ compared to Pd(100).

In situ high-pressure x-ray photoelectron spectroscopy of the catalytic CO oxidation over Pd(100) at different partial pressures of O_2 and CO form both O-covered Pd(100) and a $(\sqrt{5} \times \sqrt{5})R27°$ surface oxide as stable, highly active phases. It was concluded that at near stoichiometric O_2/CO pressure ratios a total pressure of 1.3 mbar is at the edge of the "pressure gap", above which formation of oxide phases on Pd(100) should be observed. In comparison no oxide phase is observed on $Pd_{75}Ag_{25}(100)$ at similar pressure. The catalytic CO and H_2 oxidation on Pd(100) and $Pd_{75}Ag_{25}(100)$ surfaces under oxygen rich conditions at near-realistic pressures show that below a critical temperature of about 185°C and 200°C for Pd(100) and $Pd_{75}Ag_{25}(100)$, respectively, the oxidation activity is low, showing no significant CO_2 and H_2O production due to CO poisoning of the surface. Above the critical temperature the reaction enters a high activity regime, which is accompanied by formation of a $(\sqrt{5} \times \sqrt{5})R27°$ surface oxide on Pd(100) and a chemisorbed oxygen phase on $Pd_{75}Ag_{25}(100)$. Additionally, for $Pd_{75}Ag_{25}(100)$, above the critical temperature 200°C, further increasing the temperature leads to decay in CO_2 production, while H_2O formation is not affected. The presence of silver in the outermost surface layer significantly affects the surface chemistry during these reactions and thereby the reaction mechanism.

Acknowledgements

List of papers

I. Surface composition of clean and oxidized $Pd_{75}Ag_{25}(100)$ from photoelectron spectroscopy and density functional theory calculations.
L.E. Walle, H. Grönbeck, V.R. Fernandes, S. Blomberg, M.H. Farstad, K. Schulte, J. Gustafson, J.N. Andersen, E. Lundgren, A. Borg
Surface Science **606**, 1777-1782 (2012).

II. Reduction behavior of oxidized Pd(100) and $Pd_{75}Ag_{25}(100)$ surfaces using CO.
V.R. Fernandes, J. Gustafson, I.-H. Svenum, M.H. Farstad, L.E. Walle, S. Blomberg, E. Lundgren, A. Borg.
Surface Science **621**, 31-39 (2014).

III. H_2 reduction of surface oxides on Pd-based membrane model systems - the case of Pd(100) and $Pd_{75}Ag_{25}(100)$
V.R. Fernandes, J. Gustafson, M.H. Farstad, L.E. Walle, S. Blomberg, E. Lundgren, H.J. Venvik, A. Borg.
In manuscript.

IV. *In Situ* X-Ray Photoelectron Spectroscopy of Model Catalysts: At the Edge of the Gap.
S. Blomberg, M.J. Hoffmann, J. Gustafson, N.M. Martin, V.R. Fernandes, A. Borg, Z. Liu, R. Chang, S. Matera, K. Reuter, and E. Lundgren
Phys. Rev. Lett. **110**, 117601 (2013).

V. Near-Ambient Pressure CO and H_2 Oxidation over Pd(100) and $Pd_{75}Ag_{25}(100)$ Surfaces.
V.R. Fernandes, M.H. Farstad, J. Knudsen, J. Gustafson, S. Blomberg, E. Lundgren, H.J. Venvik, A. Borg
In manuscript.

Comments on my contribution to the included papers

The experimental and theoretical work presented in this thesis involved collaboration with several people both at the Department of Physics and Department of Chemical Engineering at the Norwegian University of Science and Technology, as well as at other universities, namely, Division of Synchrotron Radiation Research at the Lund University in Lund, Sweden, and Competence Centre for Catalysis and the Department of Applied Physics, Chalmers University of Technology in Gothenburg, Sweden.

In Papers II, III, and V I participated in the experiments, performed the data analysis and had the main responsibility in the manuscript. In Paper I, I performed the scanning tunneling microscopy measurements and respective data analysis and participated in the following discussion of results. In Paper IV I participated in the experimental work. The density functional theory calculations in Paper II were performed by Ingeborg-Helene Svenum at the Department of Chemical Engineering at NTNU. In papers in papers II and III, I performed the kinetic analysis.

Papers not included in this thesis

- Generation and oxidation of aerosol deposited PdAg nanoparticles
  S. Blomberg, J. Gustafson, N.M. Martin, M.E. Messing, K. Deppert, Z. Liu, R. Chang, V.R. Fernandes, A. Borg, H. Grönbeck, E. Lundgren
  Surf. Sci. **616**, 186-191 (2013).

- A high pressure XPS study of CO oxidation over Rh(100)
  J. Gustafson, S. Blomberg, N.M. Martin, V.R. Fernandes, A. Borg, Z. Liu, R. Chang, E. Lundgren
  J. Phys.: Condens. Matter 26(5), 055003 (2014).

Contents

II Papers   73

Paper I Surface composition of clean and oxidized Pd$_{75}$Ag$_{25}$(100) from photoelectron spectroscopy and density functional theory calculations.

Paper II Reduction behavior of oxidized Pd(100) and Pd$_{75}$Ag$_{25}$(100) surfaces using CO.

Paper III H$_2$ reduction of surface oxides on Pd-based membrane model systems - the case of Pd(100) and Pd$_{75}$Ag$_{25}$(100).

Paper IV *In Situ* X-Ray Photoelectron Spectroscopy of Model Catalysts: At the Edge of the Gap.

Paper V Near-Ambient Pressure CO and H$_2$ Oxidation over Pd(100) and Pd$_{75}$Ag$_{25}$(100) Surfaces.

Part I

Introduction

Chapter 1

Introduction

In 1817 Sir Humphrey Davy in a lecture to the Royal Society concerning the combustion of gaseous mixtures in safe-lamps noted the following [1]:

"*I had intended to expose fine wires to oxygene and olefiant gas, and to oxygene and hydrogene during their slow combination under different circumstances, when I was accidentally led to the knowledge of the fact, and, at the same time, to the discovery of a new and curious series of phenomena. ... the oxygene and coal gas in contact with the hot wire combined without flame, and yet produced heat enough to preserve the wire ignited, and to keep up their own combustion. ... The same phenomena were produced with mixtures of olefiant gas and air. Carbonic oxide, prussic gas and hydrogene, and in the last case with a rapid production of water.*"

In essence Sir H. Davy observed that a mixture of hydrogen and oxygen in the presence of platinum interacted chemically at room temperature to form water. In 1836 the Swedish chemist Jöns Berzelius recognized a more general property in several works after Sir H. Davy's observations, introducing the term catalysis [2].

Catalysis can be defined as a modification of a chemical reaction rate by addition of a catalyst in combination with the reactants, which reduces the activation energy barrier between the reactants and the products, without being consumed. In case more than one reaction occurs in the system, a catalyst may selectively enhance only one reaction pathway. If the catalyst and the reactants are in a single phase of matter (e.g., the catalyst is part of a gaseous mixture with the reactants), the process is referred to as homogeneous catalysis. Conversely, if the catalyst is in a different state of matter relative to the reactants (e.g., solid catalyst and the

reactants are gases) it is referred to as heterogeneous catalysis, which represents approximately 80% of all catalytic processes [3].

Almost 200 years have passed since Sir H. Davy observed catalytic water production on platinum and today more than 90% of the chemical manufacturing processes in use throughout the world utilize catalysts [4]. For example, most of the agricultural fertilizers, pharmaceuticals, and fuels are processed by means of catalysis. Among the many areas where catalysis is used, one of crucial importance is energy. Society faces important challenges concerning the environmental impacts from the use of fossil fuels and depletion of existing reserves of raw materials. Catalysis plays a key role in the development of innovative processes for production of clean fuels and reduction of greenhouse gases emissions such as CO_2, as well as vehicle emissions control in automotive catalysis.

Hydrogen is regarded as the ideal clean fuel and may potentially be produced from renewable sources. Burning hydrogen does not produce undesirable gases such as CO and CO_2 that fossil fuel burning generates. Moreover, hydrogen can be used to produce electricity using fuel cells, for example, proton exchange membrane fuel cells, which are attractive candidates to replace current battery technologies in electric transport systems and hand held devices. Fuel cells are electrochemical devices that convert the chemical energy from a fuel, usually hydrogen, into electricity through a chemical reaction with oxygen, generating water as a result. The use of hydrogen as fuel, however, is not without challenges. The main issues that limit widespread use of hydrogen for domestic and transportation purposes are hydrogen storage technologies which are not yet fully developed and the low energy density of H_2 compared to the carbon based fuels in use today. Nevertheless, an increase in hydrogen use, and perhaps the transition to the "hydrogen society" is foreseeable in the future, particularly in face of the pressures associated with fossil fuels.

Regardless of the future use or not of hydrogen as main fuel, it is today one of the most produced gases in the world for industrial purposes. Applications of hydrogen in industry include, for example, processing of fossil fuels and hydrogenations in the petroleum and chemical process industry, coolant for power station alternators and generators, rocket fuel, or as a general fuel [5, 6]. Currently, the leading process to obtain hydrogen is the separation of this gas from a primary source [5]. The most relevant industrial sources of hydrogen are steam reforming of hydrocarbon fuels, mainly natural gas, and partial oxidation of coal or hydrocarbons. Natural gas will likely continue to be in the short to medium term future, the primary source of hydrogen. This resource is abundant in the earth's crust, and contrary to oil, natural gas supplies are expanding. The main process to separate

hydrogen from a mixture of gases, such as natural gas, is pressure swing adsorption (PSA). This technology is based on a physical binding of gas molecules to adsorbent material. The force acting between the gas molecules and the adsorbent material depends on the gas component, type of adsorbent material, partial pressure of the gas component and operating temperature.

An alternative, and very promising, separation technology for hydrogen separation, particularly from natural gas, is membranes. Different types of membranes can be used for hydrogen separation, for example, dense metal membranes, dense metal alloy membranes, ceramic, polymeric membranes, or composite membranes. The notion of dense in this context implies that there are no intentional interconnected pores in the membrane other than atomic interstices and atomic vacancies [5]. The term composite refers to a membrane with two or more distinct layers.

Membrane reactors for hydrogen production have advantages compared to conventional reactors such as integration of reaction and separation into a single process, reduced operating temperatures and pressures, production of high purity hydrogen and ability to retain carbon dioxide (CO_2) and other species in the retentate stream [5–7]. Overall, the possibility of achieving lower deployment and operation costs is attractive and of major importance to allow the production of large hydrogen quantities for general use. The disadvantages of membrane reactors include [6, 7] the cost of palladium, the low pressure hydrogen gas produced requires compression, and permeance inhibiting or poisonous effects of species like carbon monoxide or sulfur on the membrane.

Palladium is extensively used as a membrane material due to its excellent ability to split molecular hydrogen and high solubility, permeability and selectivity for hydrogen [8–12]. This is not, however, without certain limitations, which will be discussed below. Nevertheless, the superior characteristic of Pd compared to alternative metals such as Zr or V for the task of hydrogen separation and the discovery of methods to improve upon the limitations, make palladium the preferred metal for dense metallic hydrogen separation membranes. Possible applications of palladium based membranes include, for example, small scale on site hydrogen generation (laboratory, military, and industrial use), hydrogen separation from hydrocarbons, hydrogenation and dehydrogenation reactions, or fuel cells. In addition, palladium is a metal which exhibits similar properties to platinum for oxidation catalysis, being applied, for example, in automotive catalysis as an oxidation catalyst for carbon monoxide and unburned hydrocarbons [13–16].

1.1 Palladium Based Membranes and Catalysis

It is known for more than one century that hydrogen permeates through palladium. The first patent for a hydrogen purification system using palladium was issued in 1916 [17]. Patents for systems based on palladium alloys were first issued in the 1960's. The interest in palladium as a membrane material comes from its relatively high hydrogen permeability compared to other pure metals, very high selectivity for hydrogen, reasonable mechanical characteristics and highly catalytic surface. On the down side, the high cost and the chemical stability inhibit the widespread application in large scale processes.

Palladium based membranes are able to separate hydrogen selectively because of the high solubility of this gas in the Pd crystal lattice. Hydrogen transport through a layer of palladium involves different steps [5, 6]: adsorption of molecular hydrogen, dissociation of the adsorbed molecular hydrogen into atomic hydrogen, transport of the hydrogen atoms through the bulk of the metal via hopping through defects and/or interstitial sites of the metal lattice, recombination of atomic hydrogen to molecular hydrogen, and desorption of the molecular hydrogen. The driving force is the difference of partial pressures on both sides of the membrane.

Palladium is also an oxidation catalyst. In the presence of oxygen, palladium catalyzes the oxidation of species such as CO and hydrocarbons to CO_2 and water. For this reason Pd is applied in automotive catalytic converters for emissions control, converting the toxic byproducts resulting of the fuel combustion process in internal combustion engines to less toxic substances.

1.1.1 The $\alpha - \beta$ Phase Transition

In the presence of hydrogen, Palladium shows a transition from α-phase, poor in hydrogen, to the β-phase, rich in hydrogen, at temperatures below 298°C and pressures below 2MPa, which depends on the hydrogen concentration in the metal. These phases are referred to as palladium hydrides. Above 298°C only the α phase can exist while both phases may coexist below this temperature as hydrogen atoms increasingly occupy the interstitials of the Pd lattice [11]. Figure 1.1 shows the pressure-concentration relation for the hydrogen-palladium system, showing the existence of the phases α and β.

One of the problems associated with using a pure palladium membrane is the hydrogen embrittlement caused by the phase transition between the α and β phase
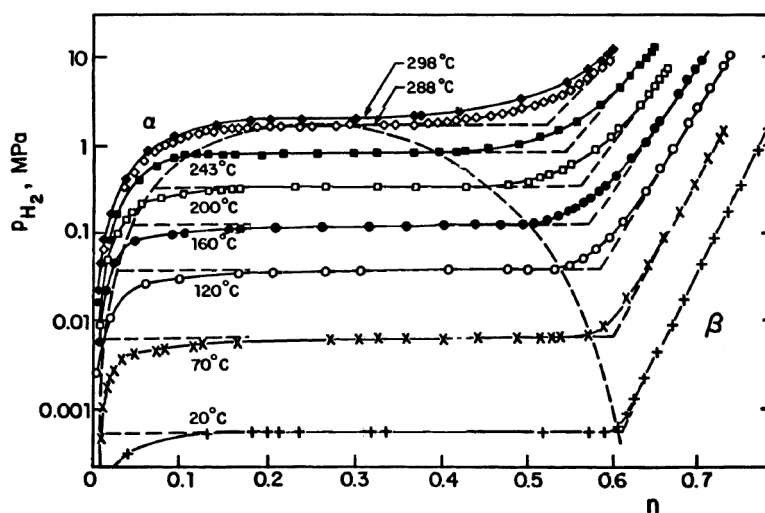
Figure 1.1: Absorption isotherms for the palladium-hydrogen system. The hydrogen vapor pressure is shown as function of the atomic ratio n = H/Pd. Reproduced from [5].

of palladium hydride. Although the lattice of palladium retains the face centered cubic structure while it expands during hydride formation, this process is accompanied by distortion of the metal lattice and the production of dislocations due to the coexistence of two unequal face-centered cubic (fcc) phases with different lattice constant, 3.89Å in the α phase and up to 4.10 Å in the β phase. The lattice constant in the β phase is larger than that of the α phase, leading to lattice strain, and, consequently, after a few cycles to lattice dislocations, causing the palladium structure to become disordered [11]. Exposing palladium to hydrogen bellow this temperature should be avoided to prevent warping and cracking. It should be noticed however that loading palladium with hydrogen at temperatures above 298°C also causes changes in the lattice parameter, but these changes are gradual and do not involve phase transitions.

1.1.2 Palladium Alloys

To tune the catalyst properties and improve upon the previously referred limitations, palladium alloys are used instead. Pd-based alloys membranes often display improved membrane performance and chemical robustness, increased mechanical strength, and reduced effect of the hydride phase change, while maintaining the high selectivity for hydrogen. Furthermore, alloying with cheaper metals reduces the amount of palladium, and therefore the cost.

Alloys of palladium lower the critical temperature for the $\alpha \rightarrow \beta$ phase transition by narrowing the α/β-Pd hydride miscibility gap (pressure plateau in the pressure-composition phase diagram) that pure palladium has below 298°C. Furthermore, the difference between the sizes of the α- and β-Pd lattice constants is smaller in alloys so less distortion occurs with successive hydrogen absorption-desorption cycles [11].

Palladium has been alloyed with elements such us boron, cerium, copper, iron, nickel, gold, silver, yttrium and others. Although all the metals alloyed with palladium alter the performance and mechanical resistance of membranes, cerium, copper, gold, silver, and yttrium are those that alloyed with palladium can exhibit higher permeability values than pure Pd membranes [5]. The observed change in permeability of the alloy is attributed to either increasing solubility and/or diffusivity, thus increasing the permeability

Alloying palladium, especially with silver, reduces the critical temperature for hydrogen embrittlement and increases the hydrogen permeability. Alloying (of palladium) with silver results in smaller lattice mismatch between the two hydride phases compared to pure palladium because the hydrogen solubility in the α and β phases is increased and decreased, respectively. For PdAg$_{23}$ and PdPt$_{19}$ wt.% the critical temperature for formation of the β phase is around room temperature. For example, PdAg$_{25}$ absorbs hydrogen more quickly and is up to 1.5 times as permeable as pure palladium [11]. The maximum hydrogen permeability is obtained for a silver content of approximately 23 % [18].

In addition, palladium alloys have higher tensile strength and hardness. This helps to eliminate membrane rupture, cracking, or failure associated with thermal cycling. Alloys are sometimes more resistant to poisoning by contaminants such as sulfur and carbon.

1.1.3   Surface Catalysis and Degradation Mechanisms

As previously described, the transport of hydrogen through palladium requires adsorption, dissociation and later recombination and desorption of molecular hydrogen. Reductions in any of these steps can cause decline in performance. For successful implementation, a membrane is required to retain both its mechanical and chemical integrity in the presence of gas phase constituents such as CO and H_2S.

Common poisons of palladium catalyst include CO, and elemental C, S, Cl, among

others. If the membranes are used in steam, oxides from diffusing species may form on the surface, blocking adsorption of molecular hydrogen. Oxide forming elements of concern include, for example, Fe, Si, Ca, and Mg. [5]. Palladium and PdAg are very susceptible to poisoning by sulfur and catalytic deactivation by adsorbed S [5]. Under some operating conditions, a few parts per billion by volume of H_2S is sufficient to form bulk Pd_4S. At low temperatures ($< 250°C$), CO can adsorb on Pd to form a monolayer on the metal surface, blocking the adsorption of hydrogen and poisoning the surface. At elevated temperatures ($> 300°C$), CO rapidly desorbs, allowing hydrogen to adsorb and dissociate. Elemental carbon can accumulate on the surface and block the adsorption of hydrogen. Although it is apparent that all major gasification constituents decrease the hydrogen flux through Pd-based membranes, the consensus is that CO has the largest effect.

1.2 Model Systems

Real membranes are complex system. It is generally quite challenging, if not difficult, to investigate, characterize, and understand properties of catalysts at atomic and molecular level under realistic operating conditions. For this reason, simplified models, "model systems", are usually studied first. Studies are carried out in a controlled environment, under ultra-high vacuum (UHV) conditions, using pure single crystals with clean and well defined surfaces.

In a model system the physical and chemical phenomena that occur at the catalyst surface are studied using surface science techniques such as photoemission spectroscopy or scanning tunneling microscopy. These methods are sensitive to the atomic level allowing the study of catalytic processes at the level of elementary reaction steps or probing reaction sites. In combination with modern *ab-initio* theoretical methods, surface science studies aim at understanding the nature of catalytic processes and to rationalize the design of new catalysts. Moreover, *in-situ* investigations of complex systems under reaction conditions have nowadays become feasible. Considerable effort has been put in the development of techniques to bridge the so called pressure gap, complementing the surface science investigations in UHV with experiments at near-realistic operating conditions.

Although the model systems are far from the "real-life catalysts", some of the fundamental properties are revealed. Investigation of crystal surfaces as model systems for Pd-based membranes is essential for detailed understanding of the catalyst under operating conditions. In this thesis, the (100) surface of pure Pd and $Pd_{75}Ag_{25}$ single crystals were used as model system for understanding the

surface properties of Pd-based membranes and catalysts.

1.3   Motivation

As previously discussed, palladium based membranes are important in technologies for natural gas conversion to fuels and chemicals in general and hydrogen production and use in particular. In this context, investigation of palladium model systems for atomic level studies of membrane surfaces and catalysis is therefore essential in the development of this technology.

Heat treatment of Pd/Ag alloy membranes in air has been reported to enhance the hydrogen permeation [19–22]. Recently, it was discovered within a collaboration between NTNU and SINTEF that the inhibition of hydrogen permeation through PdAg membranes by carbon monoxide could be significantly reduced by heat treatment of the membrane in air [23]. The process of heat treating the membranes in air is accompanied by the formation of surface oxides [24]. Moreover, several studies have found oxidation and subsequent reduction to increase permeation of membranes [19, 20, 24–26].

Analysis by modeling and surface spectroscopy indicated that changes in CO an H_2 adsorption, i.e., the binding energies, took place and that surface segregation phenomena could be involved. The experimental evidence was however insufficient to provide detailed insight. Full understanding of the thermal treatment and silver effects, as well as the interaction of CO and hydrogen with the oxide and its reduction behavior is still lacking.

Segregation effects in the alloy are likely to influence the performance of the system. In PdAg alloys, several studies have found that silver segregates to the surface under UHV conditions [27–35]. The situation may change in the presence of adsorbates interacting with the alloy surface, resulting in adsorbate-induced segregation due to differences in chemisorption energies [36, 37] of the interacting molecules. Reversed segregation of Ag, i.e., segregation of Pd atoms to the surface, in PdAg alloys has been found as a result of adsorption of oxygen [29,38,39], hydrogen [34, 39–42], and CO [39].

In addition, it has been reported that oxidation of CO to CO_2 over transition metal surfaces is often more efficient on oxidized surfaces than on the corresponding metallic surface [43–57]. For Pd(100) both experimental studies [45] and theoretical simulations [58, 59] indicate that the surface oxide could be responsible for a

higher reactivity compared to the bare metallic surface, which is interesting in its own right.

In this context, the studies presented in this thesis focus on investigating surface oxide formation on Pd-based model systems, namely Pd(100) and $Pd_{75}Ag_{25}(100)$, evaluating the reduction of this oxide structure towards H_2 and CO on both these surfaces, and understanding the influence of the alloying element Ag on this behavior. Finally, the most active phase in the catalytic oxidation of CO and H_2 in an oxygen rich environment was compared for these two surfaces.

Chapter 2

The Material System

2.1 Palladium

Palladium is a $4d$ transition metal, atomic number 46, which crystallizes in the face-centered cubic (fcc) structure. The lattice constant of Pd is $a = 3.89$ Å at temperature 298 K [60, 61]. Figure 2.1(left) displays the unit cell of a Pd crystal. The (100) surface of a Pd crystal was utilized for the studies in this thesis. Figure 2.1(right) displays a model of a Pd crystal with the (100) plane highlighted in pink color. The interatomic distance between two Pd atoms in this plane is $a/\sqrt{2} = 2.75$Å.
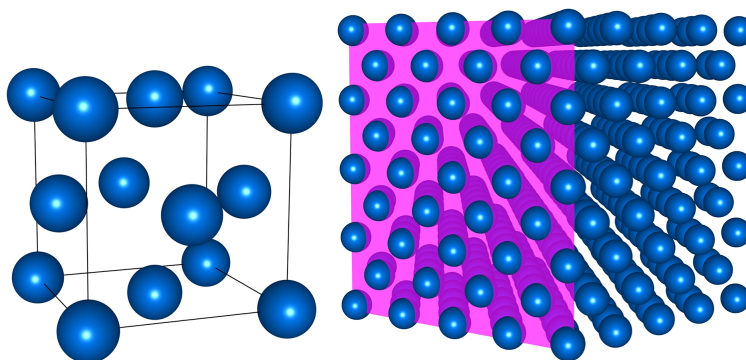
Figure 2.1: Pd unit cell (left) crystal with the (100) plane highlighted (right).

Oxidation of the Pd(100) surface is a complex process, involving several stages before bulk oxide formation. Exposing the Pd(100) surface to oxygen in ultra-high vacuum (UHV) results in the formation of up to four different oxygen induced

structures at coverages below 1 monolayer (ML), namely p(2×2) at 0.25 ML, c(2×2) at 0.5 ML, p(5×5) at 0.75 ML, and ($\sqrt{5} \times \sqrt{5}$)R27° (henceforth denoted $\sqrt{5}$) at 0.8ML [62,63]. The latter of these structures has been subjected to detailed investigations over the years [64–67]. At pressure above 1 Torr and temperature of 300°C, bulk PdO is formed [68,69].

As mentioned in the Motivation section, surface oxides are the focus in this thesis. The $\sqrt{5}$ surface oxide structure consists of a single, strained, PdO(101) layer on top of the underlying Pd(100) substrate. Figure 2.2(left) displays the PdO unit cell the with the (101) plane highlighted. Figures 2.2(center) and (right) show a model of the $\sqrt{5}$ surface oxide seen from two different angles.

● O   ● Pd   ● 2-fold Pd   ● 4-fold Pd   ● Interface Pd
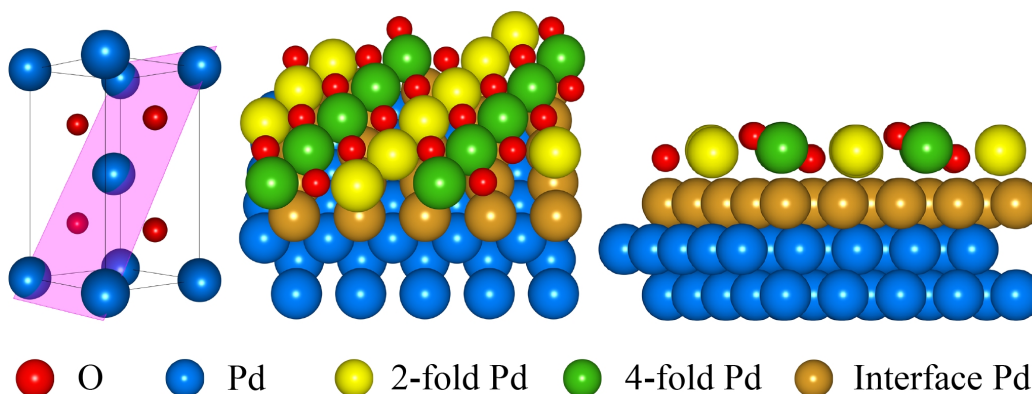
Figure 2.2: The PdO(101) model of the Pd(100)-($\sqrt{5} \times \sqrt{5}$)R27°-O surface oxide. (left): Crystal structure of a tetragonal PdO unit cell. The (101) plane of PdO is identified. Palladium and oxygen atoms are depicted in blue and red colors, respectively. (center) and (right): Perspective and side view of the ($\sqrt{5} \times \sqrt{5}$)R27° surface oxide on a Pd(100) substrate. This structure consist of a strained PdO(101) overlayer. The two-fold and four-fold oxygen coordinated Pd atoms are depicted in yellow and blue, respectively. Interface Pd atoms between the surface oxide and bulk substrate are colored brown.

The Pd atoms in the $\sqrt{5}$ surface oxide can be divided in two groups, two-fold oxygen coordinated Pd atoms in yellow, and four-fold oxygen coordinated Pd atoms in green. The four-fold Pd atoms are located slightly above the two-fold atoms. As seen in the Figure 2.2(right), and in accordance with the PdO(101) structure, the oxygen atoms reside in two positions in the surface oxide, close to the metallic surface of the substrate, 0.4 Å below the Pd atoms, and in the outermost layer, 0.6 Å above the Pd atoms. The $\sqrt{5}$ structure has eight domains resulting from mirror planes and 90° rotations of the unit $\sqrt{5}$ unit cell.

2.2 Palladium-Silver Alloys

As stated in the introduction, for commercial membranes PdAg alloys are used instead of pure Pd, due to the improved stability, with 23 wt.% of silver yielding the highest hydrogen permeation. In this thesis a palladium alloy crystal with composition of 25 wt.% silver was used as membranes model system. Silver has atomic number 47 and, as palladium, is a $4d$ transition metal with fcc crystal structure. Ag and Pd are miscible and can form alloys of the type Pd_xAg_{1-x}, which are, in general, disordered.

As a result of absorption of hydrogen the lattice constant of Pd increases and the bond strength between Pd atoms is reduced due to hydrogen filling antibonding states in the $4d$ band [70–72]. Analogously to the hydrogen atom, the alloying element silver has an electron-donating role relative to Pd, and thus both compete for the filling of the 4d band of palladium [73]. Alloying Pd with Ag leads to lower hydrogen concentration required to fill the $4d$ band and subsequently $5s$ band, and thus formation of hydride phases. The result is a substantial decrease in critical pressure and temperature for the $\alpha \rightarrow \beta$ transition in PdAg alloys.

The lattice constant of silver is 4.08 Å, a value slightly larger than that of Pd, 3.89 Å [60]. Therefore, the lattice parameter of a PdAg alloy is expected to have a similar value. A simple calculation using Vegard's rule [74, 75] for a Pd_3Ag structure results in $a = (3.89 \times 3 + 4.08)/4 = 3.94$ Å. Calculations performed using density functional theory in the context of the work in this thesis yielded values of 3.97 Å [76] and 4.01 Å [77].

Segregation studies under UHV of bulk PdAg alloys revealed a significant Ag enrichment on the surface [27–35, 78], reflecting the significantly lower surface energy of Ag compared to Pd [30, 32, 79–84], and the fact that the slightly larger Ag atoms induce less strain at the surface than in the subsurface region.

Chapter 3

Experimental and Theoretical Methods

This thesis focuses on the study of model systems using several, complementary, techniques. Each technique reveals only part of the picture for a given system. To completely understand the properties of the system it is necessary to combine different experimental techniques, as well as theoretical calculations. The present chapter is devoted to a brief presentation of the experimental techniques and theoretical methods used in this thesis. The intention is to provide the reader with a general, yet not exhaustive, description of the fundamental concepts involving each technique and the application in the context of this thesis.

3.1   Vacuum and sample preparation

3.1.1   Vacuum

Most of the experimental techniques used in this thesis need to operate under ultra-high vacuum (UHV) conditions. Also, the study of model systems by surface science methods requires clean, well defined and contaminant free surfaces. Once a clean surface is obtained UHV conditions are necessary in order for the surface to remain clean. At atmospheric pressure a clean crystal surface would instantly be covered by contaminants from the air, while a pressure of 10^{-6} mbar (=9.87×10^{-9} atm), and assuming that each molecule impinging on the surface sticks, it would require 3 seconds to cover the surface with 1 ML [85]. To keep the surface

clean for sufficiently long periods of time, up to a few hours, experiments were performed at base pressures of the order of 10^{-10} mbar.

Pressures in this range are achieved using specialized stainless steel vacuum chambers and a combination of different pumps. Regarding the latter, the most commonly used are turbo molecular pumps assisted by rotary pump, ion pumps, and titanium sublimation pumps. In addition, the vacuum system comprised of chamber and pumps, requires baking each time it is exposed to air. This procedure consists of heating the system to temperatures above 100°C, usually for a period of approximately 24 hours, ensuring the desorption of molecules from the stainless steel chamber walls.

3.1.2 Sample preparation

The samples, (100) oriented single crystals of Pd and $Pd_{75}Ag_{25}$, were cleaned by cycles of ion sputtering, oxygen treatment, and annealing. Ion sputtering consists of bombarding the sample surface with high energy Ar^+-ions, typically in the range 0.5-2 keV, removing impurities, atoms or molecules, as well as atoms from the crystal, therefore cleaning the surface. Oxygen treatment consists of heating the sample in an oxygen atmosphere in order to remove carbon impurities. Annealing consists of heating the sample to an adequate temperature for a given period of time, removing oxygen or other weakly bound species and smoothing the surface by reordering of the atoms. The annealing parameters, time and temperature, depend on the sample material. In this thesis, Pd(100) was annealed to 705°C and $Pd_{75}Ag_{25}$(100) to 625°C. Sample cleanness can be judged by surface sensitive techniques such as low energy electron diffraction and photoelectron spectroscopy, which will be discussed in the subsequent chapters. The above described procedure resulted in clean and well defined surfaces.

Several of the experiments in this thesis involve the oxidation of Pd(100) and $Pd_{75}Ag_{25}$(100) surfaces and/or exposure to gases such as O_2, H_2, and CO. The controlled introduction of gases in the vacuum chamber was performed using a leak valve. Oxidation of the samples was performed by exposing the surfaces to molecular oxygen at 320°C, using pressures 5×10^{-6} mbar for Pd(100) and about 5×10^{-4} mbar for $Pd_{75}Ag_{25}$(100).

3.2   The electron mean free path

Photoemission spectroscopy and low energy electron diffraction are experimental techniques used in this thesis which rely on the detection of electrons emitted from the sample. An electron traveling through a solid will have a certain inelastic mean free path, a characteristic length that it can travel without suffering an energy loss [85, 86].

An electron passing through a solid can lose energy via inelastic scattering processes such as phonon excitations, plasmon excitations, interband transitions, or ionization of core-levels. The net effect of these processes is that the inelastic mean free path of an electron in a solid is strongly dependent on its kinetic energy. Its dependence on kinetic energy is displayed in Figure 3.1. The theoretically calculated curve follows the method of Penn [87–89].
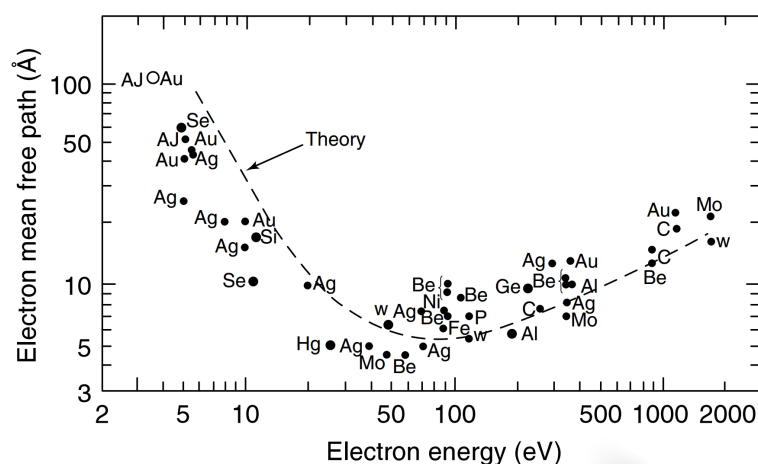
Figure 3.1: Electron inelastic mean free path as function of kinetic energy. The theory line follows Penn's method [87–89]. Reproduced from [86].

At very low kinetic energies the electron does not have enough energy to excite the processes listed above, therefore its mean free path is long. At high kinetic energies the electron spends less time passing through a given thickness of solid and thus is less likely to suffer an energy loss. Hence its mean free path in the solid is again quite long. However between these two regions the mean free path passes through a minimum. Electrons with kinetic energies in the $\sim 40 - 150$ eV range interact strongly with matter, resulting in a short mean free path. At the minimum of the "universal curve" the mean free path is ~ 1 nm. Even for quite high electron energies (1-2 keV) the mean free path is still only a few nm.

3.3 X-ray Photoelectron Spectroscopy

Photoelectron spectroscopy is a widely used technique to investigate the chemical composition and properties of surfaces, providing both qualitative and quantitative information. This experimental technique is based on the photoelectric effect, where a surface hit by photons emits electrons. The effect was discovered by Heinrich Hertz in 1887 [90] and later explained by Albert Einstein in 1905 [91], who was awarded the Nobel Prize in Physics in 1921 for this contribution. The process of using photons (light) to remove electrons from a material is called photoemission, and the emitted electrons are called photoelectrons.

The technique of electron spectroscopy for chemical analysis (ESCA), as it was denominated at the time, was developed in the mid-1960's by Kai Siegbahn and co-workers at the University of Uppsala, Sweden [92]. Kai Siegbahn was awarded the Nobel Prize in Physics in 1981. When the energy of the incident radiation falls within the X-ray region of the electromagnetic spectrum this technique is often called X-ray Photoelectron Spectroscopy. As this is the case in this work, the term XPS will be used henceforth.

3.3.1 Principles of X-ray Photoelectron Spectroscopy

Figure 3.2(a) illustrates the main features and the energies involved in the photoemission process. When a sample is irradiated by light, the energy is conserved, such that

$$E_i + h\nu = E_f + E_{kin}, \tag{3.1}$$

where $h\nu$ is the photon energy, E_{kin} is the kinetic energy of the ejected electron, and E_i and E_f are the initial and final state energies of the system, respectively. The energy difference between the initial and final state of the system is the ionization potential. For the photoemission process to occur, i.e., for an electron to be ejected from the solid, the energy of the incoming photon must be such that the photoelectron has sufficient energy to overcome its binding energy E_B and the work function of the sample Φ_S. Replacing the ionization potential, the kinetic energy is expressed as

$$E_{kin} = h\nu - (E_B + \Phi_s). \tag{3.2}$$

The kinetic energy distribution of the emitted photoelectrons is measured, in order to obtain accurate binding energies of the emitted electrons.

In XPS experiments the electron analyzer and the sample are electrically grounded, hence their Fermi levels will align. The sample and the electron analyzer may

have different work functions as shown in Figure 3.2(a). The binding energy of the photoelectron is referenced to the Fermi level, i.e., the zero of the binding energy scale is at the Fermi level. Hence, it is the spectrometer and not the sample work function that must be accurately known.

The spectrometer is generally calibrated using standard samples prior to the photoemission experiments and its work function determined. Therefore, the electron binding energy can be calculated using the measured kinetic energy of the photoelectrons as

$$E_B = h\nu - E_{kin} - \Phi_A. \tag{3.3}$$

The kinetic energy of the photoelectrons is measured by an electron analyzer. A depiction of typical XPS setup with a hemispherical type electron analyzer is displayed in Figure 3.2(b). Monochromatic photons of selected energy impinge on the surface producing photoelectrons. The emitted photoelectrons are collected, energy selected, and focused by electrostatic lenses into the electron analyzer entrance slit of the hemisphere. Only electrons with the right kinetic energy, the so-called pass energy, are transmitted through the electron analyzer to the detector. The electron analyzer is a concentric hemispherical analyzer (CHA), which is made of two concentric hemispheres with different applied voltages in each hemisphere, such that there is an electric field between the two hemispheres. Electrons traveling faster than the designated energy will impinge on the outer hemisphere, while if they are traveling slower, they will hit the inner hemisphere. The experimental measurements in this work were performed using a detector consisting of micro-channel plates connected to a phosphor screen. The CHA disperses the incoming electrons according to kinetic energy and momentum in a narrow energy range (although momentum information is not of concern in this work). Electrons accelerated onto the phosphor screen give off a light flash which is counted by a charge-coupled device (CCD) camera. The photoemission intensity spectrum is obtained by measuring the photoelectron yield (counts per energy interval) as a function of the kinetic energy of the electrons that reach the analyzer. The whole setup is evacuated to UHV, typically with pressure in the order of $\sim 10^{-10}$ mbar.
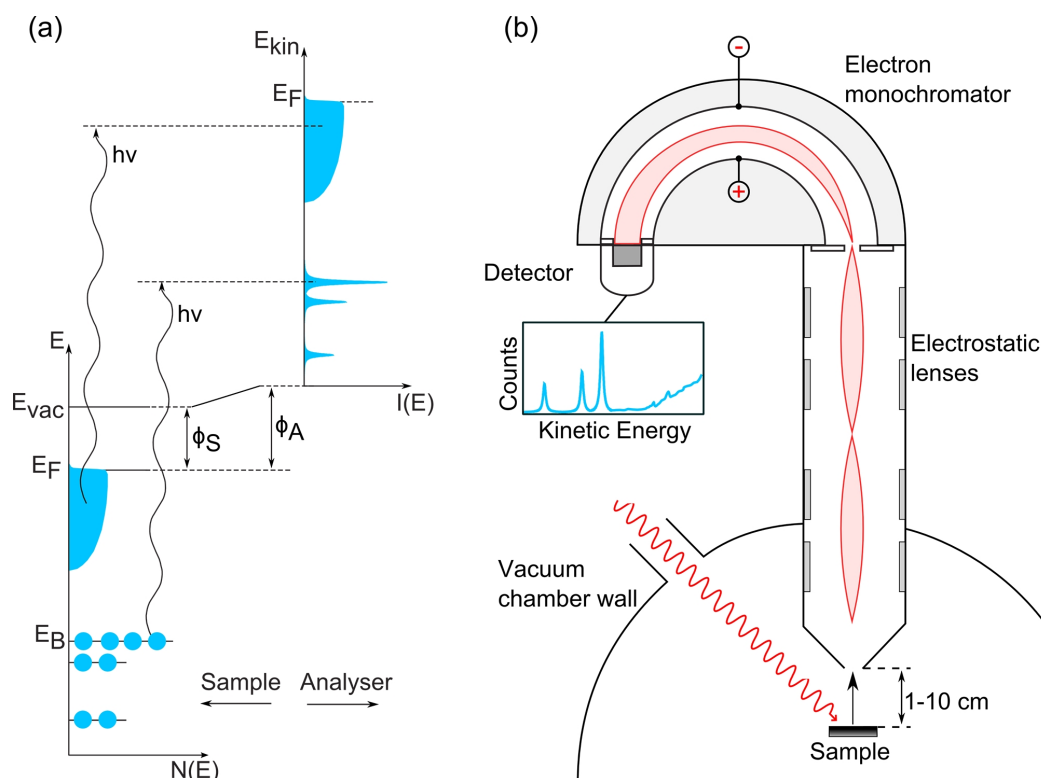
Figure 3.2: (a) Schematic illustration of the photoemission process. Electrons with binding energy E_B can be excited above the vacuum level E_{vac} by incoming photons with energy $h\nu > E_B + \Phi_S$. For the photoelectron to be detected, and its kinetic energy measured, it must overcome the work function of the electron analyzer, Φ_A. The photoemission intensity spectrum, $I(E)$, is related to the density of occupied electronic states, $N(E)$. The figure has been adapted from [93]. (b) Sketch of a XPS measurement system using a hemispherical electron analyzer with a lens system. The photoelectrons are focused into the hemisphere by electrostatic lenses. Energy-selected electrons are transmitted through the electron analyzer to the detector. XPS is usually performed in UHV to avoid inelastic losses of electrons due to collisions with gas molecules.

3.3.2   Core levels and core level shifts

Every element has a unique electronic structure, the core electrons have binding
energies characteristic of their particular element. Furthermore, the binding ener-
gies are dependent on the chemical environment in which a given atom is located.
The investigation of the surface chemistry becomes possible due to the chemical
shift of core level, depending, for example, on the oxidation state of the respective
element or its environment in the sample.

Rigorously, the binding energy of an electron is the difference between the total
energy of the final ionized state of the emitting atom/ion (with $n-1$ electrons and
a free photoelectron) and its initial state (with n electrons) [94].

$$E_B = E_{final}(n-1) - E_{initial}(n) \tag{3.4}$$

Total energies are not easy to calculate and approximations must be used to obtain
them. Therefore, binding energy is often discussed in terms of the most significant
quantities determining them. In a simplified picture, these are the orbital energy
of the state to be ionized, the response of the electrons in the system due to the
core hole relaxation, the chemical environment of the atom, and the electric field
resulting from interaction with the other atoms in the crystal. Thus the experimen-
tally measured binding energy, $E_{\mathrm{B}}^{\mathrm{exp}}$, can be approximated as combination terms
referring to the mentioned effects [94–96]:

$$E_{\mathrm{B}}^{\mathrm{exp}} = E_{\mathrm{B}} + \Delta E_{\mathrm{CS}} + \Delta E_{\mathrm{M}} + \Delta E_{\mathrm{R}} \tag{3.5}$$

where E_{B} represents the binding energy of the element, ΔE_{CS} the shift of the
core level energy due to ionization and chemical interaction with the environment,
ΔE_{M} the Madelung potential (field in ionic compounds), and ΔE_{R} the relaxation
energy. The term E_{B}, according to Koopman's approximation, which assumes that
the photoemission process does not produce any change in the remaining orbitals,
is the negative of the orbital energy (Hartree-Fock energy) [97, 98]. Spin-orbit
coupling resulting from the magnetic interaction between an electron's spin and
its orbital angular momentum is an initial state effect included in this term. The
chemical shift ΔE_{CS}, is determined by the effective charge of the respective atom
and by the influence of the adjacent atoms resulting, for example, from change of
the valency due to a modified valence electron distribution as a result of chemical
interaction [99]. The Madelung term represents the contribution of an additional
electrical potential due to the interaction of the excited atom with the rest of the
crystal [99–103]. The relaxation effects term, ΔE_{R}, represents in essence final
state effects. It includes the reaction of the system's electrons to the ionization
of the target atom (many-body effects) [98, 104] . With the creation of a core

hole the valence electron states are polarized by the core hole potential and screen it, thus inducing an electron density shift of the neighboring atoms towards the ionized atom, resulting in an unbalanced nuclear charge. The increase in positive charge pulls the electron levels of the probe atom to higher binding energies and the valence electronic charge can react, depending on its polarizability, to the formed local potential well. The effect of charge transfer from valence electrons is reflected in the XPS spectrum as a spectral asymmetry and satellite peaks [94,105–109]. A slow relaxation of the electrons in outer shells can result in an insufficient screening of the core hole and, thus, yields a higher measured binding energy. The shake-up and shake-off processes describe the transfer of energy of the final state configuration (due to insufficient screening of the core level electron that underwent photoemission) to excite electrons from valence levels either to bound states (shake up) or to free states (shake-off). The effect is seen as a seemingly increased binding energy.

Core Level Shifts

Changes of the local charge and potential of an atom lead to shifts in the core level binding energy position. Investigation of such shifts can give information of the local chemical environment and bonding of atoms.

Atoms in the topmost surface layer may have a different environment compared to the bulk crystal, leading to a binding energy shift. The atoms in the second and even deeper layers may also have surroundings that differ from the bulk, and shifts may arise. These are commonly referred to as surface core level shifts (SCLS). A surface contribution can be distinguished from a bulk contribution by changing the energy of the incident photons, effectively changing the surface sensitivity. Open surfaces, in general, have larger SCLS compared to close packed surfaces, where surface geometry and local charge properties more closely resemble the bulk properties.

As an example of core level shifts resulting from the different environment of the outermost surface atoms, Figure 3.3(a) and (b) display the SCLS on Pd(100) and $Pd_{75}Ag_{25}(100)$ measured in the Pd $3d_{5/2}$ core level spectra, respectively. Starting with the Pd(100) surface, the bulk component is located at a binding energy of 334.9 eV, and the component arising from the surface contribution is shifted -0.4 eV towards lower binding energy relative do the bulk peak [76].

For the $Pd_{75}Ag_{25}(100)$ surface the bulk $Pd_{75}Ag_{25}$ peak is located at a binding energy of 334.8 eV, while the surface contribution is shifted +0.4 eV towards higher
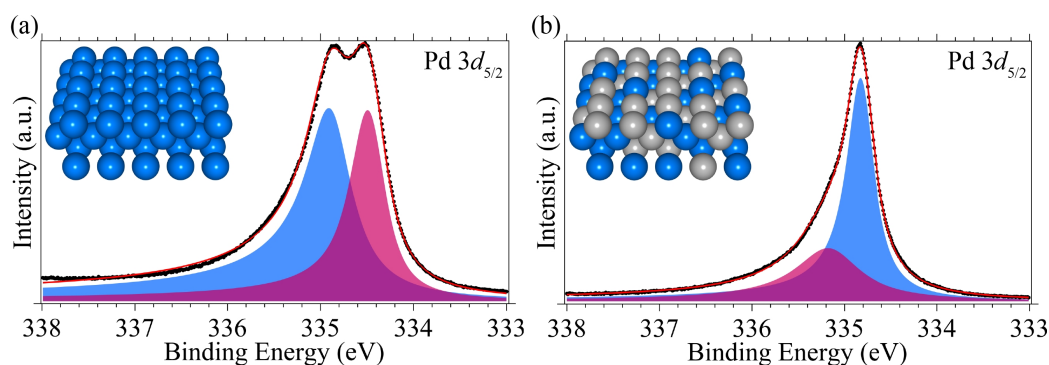
Figure 3.3: Surface core level shifts for (a) Pd(100) and (b) $Pd_{75}Ag_{25}(100)$, measured in the Pd $3d_{5/2}$ core level spectra.

binding energy relative to the bulk component. This positive shift, in contrast to the negative shift for Pd(100), in binding energy originates from Pd atoms embedded in the surface region of a silver terminated $Pd_{75}Ag_{25}(100)$ surface [76].

The presence of adsorbates on a surface effectively changes the environment of the surface atoms. Even though the core level electrons are not directly involved in the bonding they are affected by the surrounding environment, including adsorbate molecules. Bonding of adsorbates to surface atoms often induces core level shifts, normally referred to as adsorbate CLS. These CLS can be used to distinguish between different adsorbed species on a surface. As an example, Figure 3.4(a) and (b) display the Pd $3d_{5/2}$ core level signature resulting from adsorbed CO on Pd(100) and $Pd_{75}Ag_{25}(100)$ surfaces, respectively, at a sample temperature of 70°C. The CLS resulting from adsorbed CO is +0.5 eV and +0.7 eV towards higher binding energy relative to the bulk component for Pd(100) and $Pd_{75}Ag_{25}(100)$, respectively.

Oxidation of surfaces results in significant chemical changes compared to the bulk crystal. In the case of the $\sqrt{5}$ surface oxide on Pd(100), a full layer of oxide corresponds to 0.8ML oxygen coverage. Figure 3.5(a) and (b) display the Pd $3d_{5/2}$ core level spectra of the $\sqrt{5}$ surface oxide on Pd(100) and $Pd_{75}Ag_{25}(100)$, respectively.

For the $\sqrt{5}$ surface oxide on Pd(100), the spectrum consists of the bulk Pd component and three oxide induced contributions. The oxide induced contributions, located at +0.4 eV and at +1.3 eV relative to the bulk component, are attributed to two-fold and four-fold oxygen coordinated palladium atoms, respectively. The third oxide induced contribution, located at -0.3 eV relative to the Pd bulk peak, is attributed to a layer of interface Pd atoms between the surface oxide and the bulk
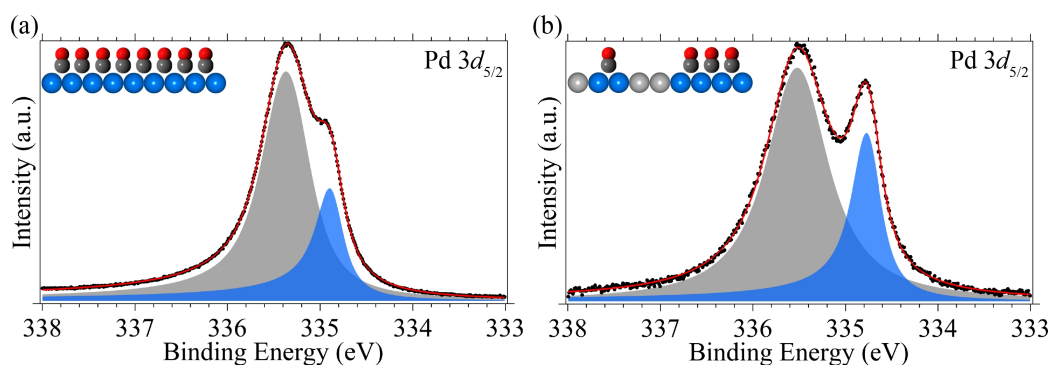
Figure 3.4: Core level shifts due to adsorbed CO on the (a) Pd(100) and (b) $Pd_{75}Ag_{25}(100)$ surfaces at 70°C, measured in the Pd $3d_{5/2}$ core level spectra.

Pd crystal [66].

For the case of $Pd_{75}Ag_{25}(100)$, the spectrum contains two oxide induced contributions shifted by +0.5 eV and +1.4 eV relative to the bulk $Pd_{75}Ag_{25}$ component, attributed to the two-fold and four-fold oxygen coordinated Pd atoms, respectively. The absence of interface component at lower binding energy, observed in the case of Pd(100), has been attributed to the presence of a silver rich interface layer between the surface oxide and bulk $Pd_{75}Ag_{25}$ [76].
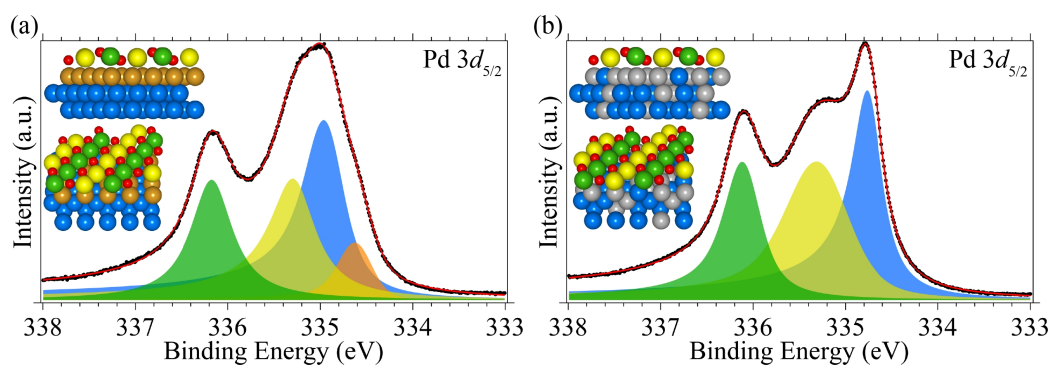

Figure 3.5: Core level spectra of the $(\sqrt{5} \times \sqrt{5})R27°$ surface oxide on the (a) Pd(100) and (b) $Pd_{75}Ag_{25}(100)$ surfaces, measured in the Pd $3d_{5/2}$ core level spectra.

3.3.3   High Pressure XPS

Processes in environmental chemistry, industrial catalysis, and industrial applications of membranes take place under non-UHV conditions. High pressure XPS (HPXPS), or alternatively near-ambient pressure XPS, provides the possibility to reduce the "pressure gap" [110,111] between UHV studies and realistic operating conditions, and thus allow for correlating the catalytic activity with the electronic structure of the catalyst surface under near realistic reaction conditions. Currently XPS measurements at gas pressures up to a few mbar can be performed. This is still far from the bar range at which a membranes can operate but, nevertheless, a significant leap forward compared to UHV.

The challenge of performing XPS measurements at near ambient pressures resides primarily in the very short mean free path of the photoelectron, limiting many surface sensitive techniques to UHV conditions. As an example, the elastic mean free path of an electron with energy of 400 eV through an oxygen gas environment at 1 mbar pressure is approximately 4 mm. This is a very short distance and essentially means that the number of electrons collected in the analyzer in a normal XPS system would be negligible. For this reason the sample needs to be placed at a very short distance from the analyzer nozzle. Adequate instrumentation has been under development since the 1960's [112–122]. A review on HPXPS is presented elsewhere [123].

Figure 3.6 depicts the two HPXPS instruments used in this work. Figure 3.6(a) shows a schematic diagram of the HPXPS system at the Molecular Science beam line 9.3.2 at the ALS [119, 120]. The sample is located a short distance from the (small aperture) nozzle of the analyzer. The distance between the nozzle and the sample surface is approximately equal to the diameter of the nozzle. Differential pumping is necessary in order to keep the detector under UHV conditions. This system creates a rapidly decreasing pressure gradient of several orders of magnitude (mbar range to UHV). The collection efficiency is improved by using electrostatic lenses in the differential pumping stage, which refocus the photoelectrons onto the apertures between the stages. In this system the entire vacuum chamber is filled with gas.

Figure 3.6(b) displays a schematic drawing of the HPXPS system at beamline I511 at the MAX IV laboratory [121]. This system uses a high pressure cell inside the vacuum chamber. In this case, gas pressure in the millibar range is confined to the inside of the cell, while the chamber remains in high vacuum. Photons reach the sample trough a small x-ray window in the cell, composed of silicon nitride, Si_3N_4. Because the volume of the cell is small, pumping of gas is fast, allowing a
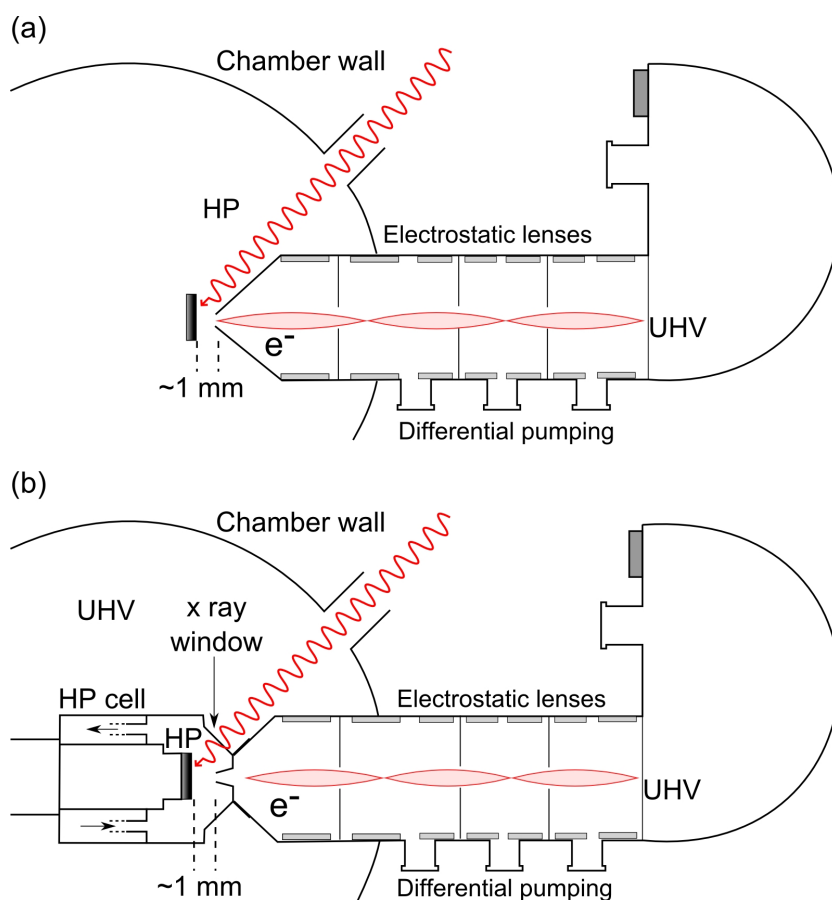
Figure 3.6: Schematic drawing of the two HPXPS systems used in this work. (a) Molecular Science beamline 9.3.2 at the ALS, Berkeley, CA, USA [119, 120]. (b) Beamline I511 on the MAX II ring at the MAX IV laboratory, Lund, Sweden [121].

relatively fast switch between different reactant gases. Additionally, small quantities of reaction products are easier to detect by the use of mass spectrometry.

HPXPS experiments are usually performed at synchrotron facilities to take advantage of a more focused X-ray spot on the sample and high photon intensity of a synchrotron compared to lab sources, which significantly reduces the data acquisition time.

One of the distinct features of high pressure XPS compared to a UHV system is the ability to observe gas phase components during an experiment. As an example, Figure 3.7 shows the simultaneous oxidation of H_2 and CO over the Pd(100) surface at total gas pressure of ≈ 1 mbar and temperature 262°C. The experiment

was performed using a partial pressure ratio O_2:CO:H_2 of 10:1:1. The supplied gas flows were 2.5, 0.25, and 0.25 cm^3/min and for O_2, CO, and H_2, respectively. The fitted O 1s spectrum, Figure 3.7(a) , shows two peaks at 528.7 eV and 529.4 eV, a signature of the $\sqrt{5}$ surface oxide, depicted in Figure 3.7(b), and in good agreement with previous observations [66]. The Pd 3$p_{3/2}$ peak is located at 531.8 eV.

(a)   (b)
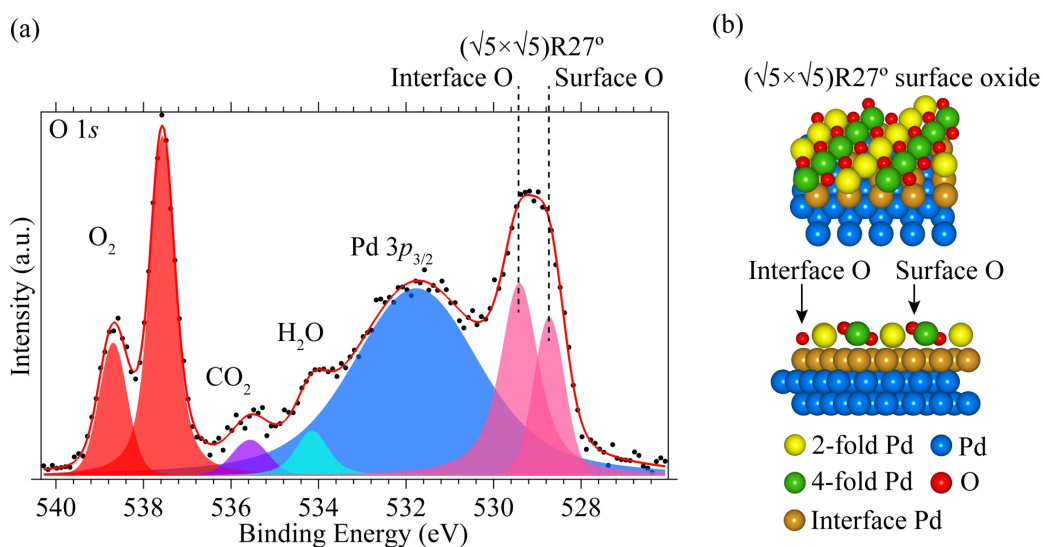
Figure 3.7: CO and H_2 oxidation over the Pd(100) surface at pressure $\approx$ 1 mbar, temperature 262°C, and partial pressure ratio O_2:CO:H_2 of 10:1:1. (a) O 1s core level region. (b) Model of the $(\sqrt{5} \times \sqrt{5})$R27° surface oxide.

In addition to peaks related to the sample, gas phase peaks due to H_2O and CO_2 are observed at 534.1 eV and 535.6 eV, respectively. The oxygen gas phase peaks are located at 537.6 eV and 538.7 eV. The two gas phase peaks for O_2 are due final state effects resulting from core polarization [94].

3.3.4   Core level analysis, line shapes and fitting procedure

To extract detailed information about the atoms in different chemical environments, for example in the crystal surface, the photoemission spectra have to be decomposed into individual contributions by a fitting procedure. This decomposition consists of finding the binding energy and line shapes of each spectral component. The line shapes of photoemission spectra depend on factors such as core hole life time, electron-hole pair excitations, and instrumental broadening. The

line shapes are commonly described by a convolution of Lorentzian and Gaussian functions and an asymmetry factor.

Lorentzian contribution – lifetime broadening

Excitation of a core electron gives a transition of the system to a state of finite lifetime, different from the ground state. From the Heisenberg uncertainty principle, a state that has a finite lifetime must be regarded as having an imprecise energy [124]. Therefore, the final state in the photoemission process does not have a well defined energy, giving rise to lifetime broadening of the spectral lines. The decay of the excited state depends exponentially on time, resulting in the following relation between intensity and lifetime

$$I(t) = I(0)e^{-2\gamma t}, \tag{3.6}$$

where $t = 0$ is the time of excitation. The Fourier transform of equation 3.6 with respect to energy, yields the intensity distribution as a function of energy, i.e., the Lorentzian contribution of the spectral line shape:

$$I_L(E) = I_0 \frac{\gamma^2}{(E - E_0)^2 + \gamma^2}, \tag{3.7}$$

where I_0 is the peak intensity at $E = E_0$ and 2γ is the Lorentzian full width at half maximum (FWHM) [125].

Asymmetry – electron-hole pair excitations

During the photoemission process additional electrons in the sample may be excited, leading to a partial energy loss for the photoelectron. A potential (coupling) is created between the localized hole left by the photoemission process and the remaining (conduction) electrons. Intrinsic energy losses through the excitation of electron-hole pairs, which are created simultaneously with the core hole, results in an asymmetric line shape [105–108]. In addition to creating an asymmetric line shape the (conduction) electron-hole interaction can also give rise to satellite peaks. The electron-hole pair creation permits excitation of electrons near E_F to empty states just above it, giving rise to a shake-up process. There is also the possibility of ejecting a second electron in this relaxation process, called a shake-off satellite [106–108].

Mahan proposed in 1967 that the conduction electron scattering amplitude for interband absorption or emission at the Fermi level, E_F, is a singularity [126].

Subsequently, Nozières and De Dominicis demonstrated that such a singularity could arise from the competition between the scattering resonance and deep level broadening [127]. Doniach and Šunjić [105] and later Gadzuk and Šunjić [106] showed that, when applied to photoelectron emission in metals, an XPS spectral asymmetry, extending to higher binding energies, was expected. The asymmetry line shape α is expressed as

$$I_\alpha(E) \propto \frac{1}{(E - E_0)^{(1-\alpha)/2}} \tag{3.8}$$

When $E = E_0$, $I_\alpha(E)$ becomes infinite, which does not have physical meaning. This was addressed by combining the effect of finite lifetime with electron-hole production, resulting in the Doniach-Šunjić line shape [105]

$$I_{DS}(E) = I_0 \frac{\Gamma(1-\alpha)\cos\left[\frac{\pi\alpha}{2} + (1-\alpha)\tan^{-1}\left(\frac{E-E_0}{\gamma}\right)\right]}{[(E-E_0)^2 + \gamma^2]^{(1-\alpha)/2}}, \tag{3.9}$$

where α is the asymmetry parameter, Γ is the gamma function and 2γ is the FWHM. For $\alpha = 0$ equation 3.9 reduces to a Lorentzian, while for $(E - E_0)/\gamma \gg 1$ the form of equation 3.8 is obtained. Experimental observations of this phenomenon in metals are presented and discussed, for example, in [107, 128].

Gaussian contribution – phonon and experimental broadening

Other factors that affect the line shape is the creation of phonons and the limited experimental resolution of the electron analyzer. These effects are often assumed to give rise to Gaussian broadening, which can be described by [94]

$$I_G(E) = I_0 e^{-\ln 2 \frac{(E-E_0)^2}{\sigma^2/4}}, \tag{3.10}$$

where σ is the Gaussian FWHM. Small unresolved chemical shifts due to inequivalent atomic sites may further broaden the peak, and can be accounted by a broader Gaussian contribution. Unresolved vibrational contributions in the core level spectra may lead to asymmetric broadening, and can be accounted for by an increased asymmetry factor α together with an increased Gaussian broadening [94].

Background Contribution

The core level peaks in photoemission spectra are superimposed on a background due to inelastically scattered electrons. The background can be fitted by dif-

ferent models, of which the most common are a linear function, Shirley background [129], and Tougaard background [130]. A linear function often suffices to model the background intensity, provided the slope is small. A discussion and comparison of background subtraction procedures is presented elsewhere [131]. A linear background was used for all core level spectra presented in this work.

Fitting procedure

The final line shape for each spectral component can be found by convoluting the Doniach-Šujić function with the Gaussian contribution, given by

$$I(E) = \int_{-\infty}^{\infty} I_{DS}(E')I_G(E - E')dE'. \qquad (3.11)$$

A core level line shape is described by the following parameters given in equations 3.9 and 3.10: intensity (I_0), binding energy (E_0), Lorentzian FWHM (2γ), asymmetry factor (α) and Gaussian FWHM (σ). In a spectrum consisting of several components, the total line shape is the sum of the individual components. The parameters are automatically varied by an iterative mathematical optimization program in order to obtain a total line shape as close as possible to the measured spectra.

A fitting procedure was implemented in a combination of MATLAB$^{\circledR}$ and C++ programing languages. The optimization of the parameters was performed using a non-linear least squares Levenberg-Marquardt type algorithm. The numerical integral convolution was performed using a 61-point Gauss-Kronrod quadrature. The use of least squares for XPS fitting is discussed elsewhere [132].

3.3.5 Surface Sensitivity

In the photoemission process, some of the photoelectrons produced travel out from the surface without losing energy while others lose energy via inelastic collisions. With the appropriate choice of experimental parameters, such that the photoelectrons detected originate only from the uppermost layers of sample, photoemission can be used to probe just the first few monolayers at the surface of a solid. This surface sensitivity arises from the strong interaction of electrons with matter.

As discussed in Section 3.2, electrons with kinetic energies in the $\sim 40 - 150$ eV range have very short mean free paths, ~ 1 nm. This is a significant result regarding the use of photoelectron spectroscopy as a surface sensitive probe. It implies

that even though the penetration depth of the incident X-rays is typically of the order of microns, the electrons that escape from the solid, due to their mean free path, will only have originated from the top few layers. The information on the sample electronic states, obtained from elastic, i.e., unscattered photoelectrons, is only obtained for electrons that have been generated at or near the uppermost surface layers of the sample.

Synchrotron radiation provides the possibility to tune the photon energy and adjust it to yield ultrahigh surface sensitivity or to obtain information from the same probing depth. Because of the surface sensitivity of XPS, where the escape depths range between 0.3 and 3 nm, only the topmost 1-10 atomic layers of the sample surface are analyzed. Surface sensitivity can also be achieved by experimental geometry. By rotating the spectrometer (or sample) so that the electrons are collected at a glancing angle, the electrons have to traverse a longer distance in the solid. The larger the angle the greater the path length for the electrons to exit the sample. The effective probing depth in this case is reduced, resulting in higher surface sensitivity of the photoemission measurement.

3.3.6   Synchrotron Radiation

Incident photons of suitable energy for photoemission emission experiments lie in the UV and X-ray region of the electromagnetic spectrum. Light in this energy range can be obtained from a number of sources such as He-lamps, Al/Mg anodes, and synchrotron radiation facilities. The conventional laboratory sources are primarily Al Kα (1486.6 eV) and Mg Kα (1253.6) eV. Synchrotron radiation sources can produce X-rays in a wide energy range, but it is only available at specialized facilities. Synchrotron radiation has several significant advantages over other sources of light and is therefore preferable for experiments. The most significant advantages compared to common sources are the high brilliance, tunable photon energy, high flux and stability.

Synchrotron radiation is generated by accelerated charged particles moving in curved orbits at relativistic speeds [133]. A storage ring, in which electrons circulate, consists of an assembly of deflecting bending magnets and focusing multipole magnet lenses, and straight sections [134, 135]. A schematic depiction of a storage ring is presented in Figure 3.8. One of the straight sections is reserved for the radio frequency (RF) cavity system, used to replace the energy lost by the electrons due to the emission of synchrotron radiation or to accelerate the electrons to higher energy. The storage ring is under UHV.
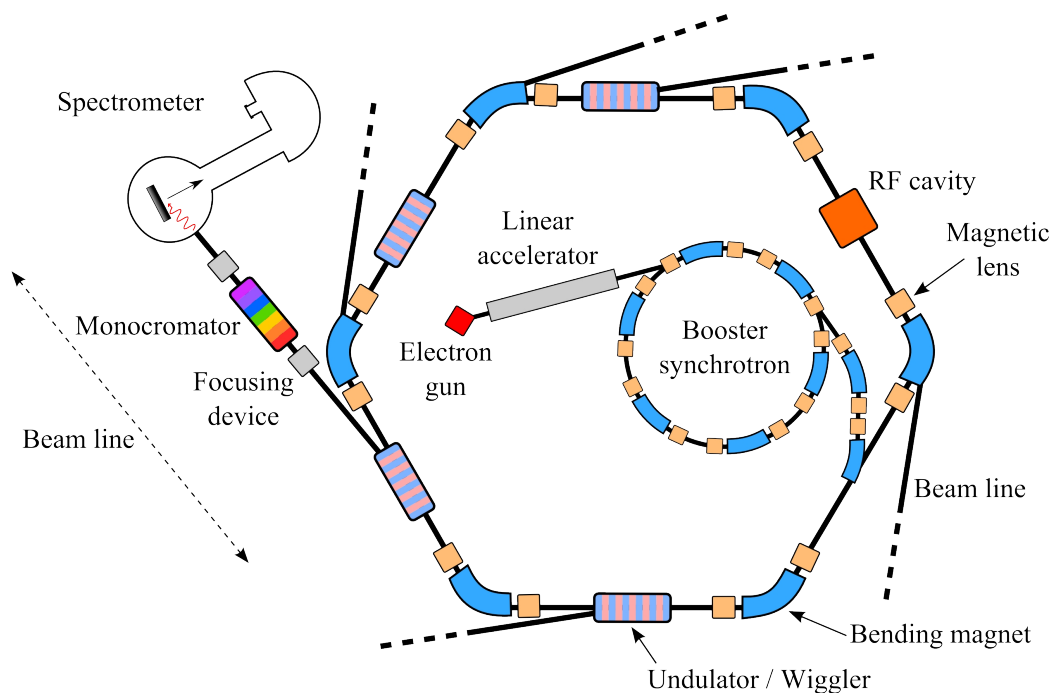
Figure 3.8: Schematic drawing of the main components of a synchrotron ring.

Synchrotron radiation is generated either by bending magnets, or by insertion devices, undulators and wigglers [134,135]. Figure 3.9 presents a schematic drawing of the three units and the characteristics of the light produced.

In bending magnets the magnetic field accelerates and forces the electrons into a curved (circular) trajectory, producing the so-called bending magnet radiation. Insertion devices, wigglers and undulators, generate more brilliant radiation and light at higher energies. These devices are placed in the straight sections of the storage ring. Undulators are composed of an array of magnets periodically disposed in such a way that an alternating magnetic field perpendicular to the storage ring plane is produced. This forces the electrons to execute oscillations in the horizontal plane. Construction of the device is possible such that the radiation emitted at each oscillation is in phase. The radiated waves add up to obtain the resulting intensity, yielding a narrow radiation cone with high brilliance. The wavelength of the emitted radiation can be tuned by changing the gap between the magnets in the array. The difference in performance between an undulartor and a wiggler arises from differences in the strength of the magnetic field, which translates into different amplitude of the electron oscillations in the horizontal plane. In the wigglers the magnetic field is stronger than in the undulator, and the radiated waves are not in phase, thus not interfering constructively, yielding a broader radiation
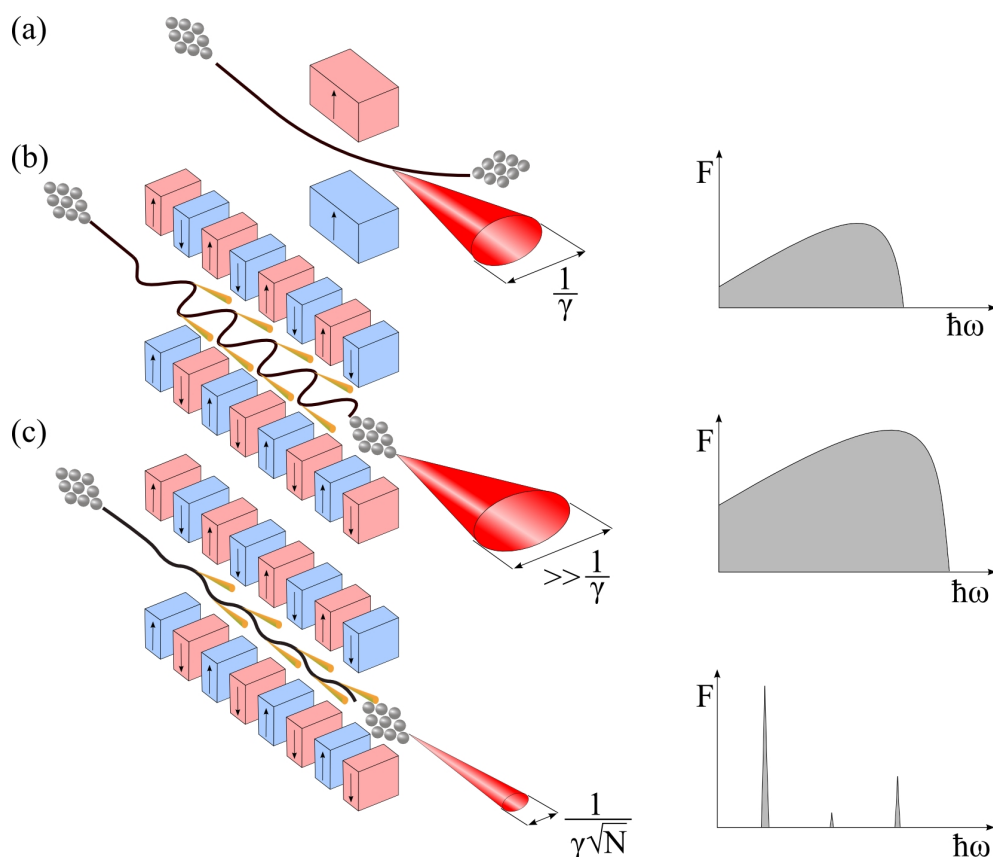
Figure 3.9: Schematic depiction of radiation from (a) bending magnet, (b) wiggler, and (c) undulator. The width of the emitted radiation cone is expressed by $\gamma = \frac{E_e}{mc^2} = 1957 E_e (\text{GeV})$, where E_e is the electron energy, N is the number of periods in the magnetic array, F is the photon flux (ph/sec), and $\hbar\omega$ is the photon energy, where $\hbar$ is Planck's constant and ω the frequency. Adapted from [134].

cone. The emitted light is collected at beam lines using focusing mirrors and monochromators, and utilized at end stations for experiments.

In this thesis all the XPS experiments where performed at synchrotron facilities. The high resolution XPS experiments in papers I, II, and III were performed at beam line I311 [136] of the MAX II storage ring at the MAX IV laboratory in Lund, Sweden. The high pressure XPS experiments in paper V were performed at beam line I511 [121], also at MAX IV laboratory in Lund, Sweden. The high pressure XPS experiments in article IV were performed at the Advanced Light Source (ALS), beam line 9.3.2, in Berkley, California, USA [119, 120].

3.4 Low Energy Electron Diffraction

In 1927 the physicists Clinton Davisson and Lester Germer accidentally observed the diffraction of electrons by crystals while performing electron scattering experiments with a nickel crystal [137, 138]. It was the first experimental observation of the wave nature of particles of matter such as electrons, proposed by Louis de Broglie in 1923 [139]. The modern apparatus for the observation of low energy electron diffraction (LEED) patterns from crystal surfaces was developed in 1960 [140].

LEED is a technique used to obtain information about the atomic structure of surfaces [85, 141–144]. It is based on diffraction of electrons with energies up to a few hundred eV. When a beam of electron impinges on a surface most of the electrons are either scattered inelastically or absorbed by the crystal, however, some undergo elastic scattering and are backscattered, contributing to a diffraction pattern characteristic of the surface structure. The electron mean free path in solids in this energy range is short, limited to a few Å, illustrated in Figure 3.1, thus the elastically backscattered electrons come only from a few surface layers, making LEED a very surface sensitive technique. Diffraction experiments require strict surface conditions for diffraction to be observed. A condition for the detection of a LEED pattern is a periodic surface structure. Thus, preparation of the surface to get a clean and ordered structure is necessary as a first step before using LEED.

3.4.1 Principles of Low Energy Electron Diffraction

Electrons display a wave and particle nature, the so called wave-particle dualism. Moving electrons therefore have a characteristic de Broglie wavelength λ given by [139, 143]

$$\lambda = \frac{h}{p}, \tag{3.12}$$

where h is Planck's constant and $p = \sqrt{2mE}$ is the momentum of the particle. After some manipulation it is possible to arrive at the following expression [141, 143]

$$\lambda(\text{Å}) = \frac{12.265}{\sqrt{E(eV)}}, \tag{3.13}$$

where E is the electron energy in eV. In LEED, electrons in the kinetic energy range 20-300 eV are applied, yielding wavelengths around 1Å, which is in the same order of magnitude as the periodicity of the atomic lattice, and corresponds
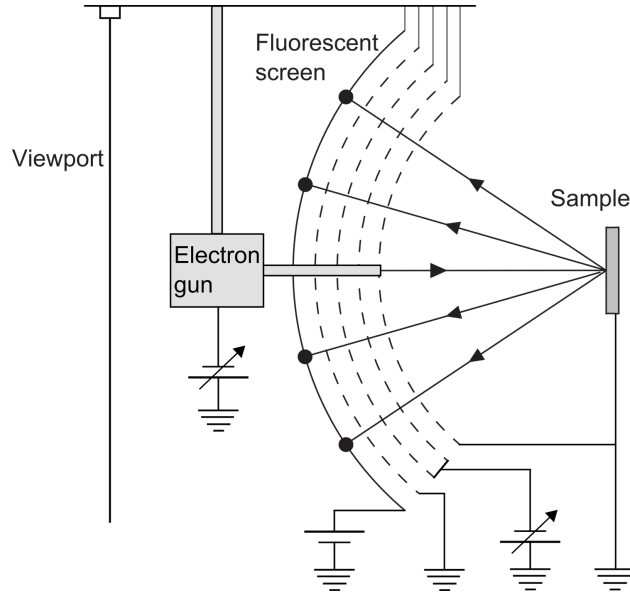
Figure 3.10: Schematic diagram of the LEED apparatus [85, 141–144]. An electron gun emits electrons that are diffracted at the sample surface and backscattered towards the screen. A series of grids energy-selects elastically scattered electrons only, which are then accelerated towards the fluorescent screen, producing a diffraction pattern.

to the interatomic distances in solids and molecules, making diffraction possible. It can provide information on average bond angles, nearest neighbor distances and translational symmetry. In addition, the sharpness of the diffraction pattern reflects the long range order of the surface. LEED is therefore often used to evaluate the cleanness of a surface, and to study surface reconstructions and overlayer structures.

In the kinematic approximation the electrons are assumed elastically scattered only once. From the principle of energy conservation, the incident, $\mathbf{k}$, and scattered, $\mathbf{k}'$, wave vectors must be equal in magnitude, $|\mathbf{k}'| = |\mathbf{k}|$. The wave vector consists of parallel and perpendicular components relative to the surface, denoted by the symbols $\parallel$ and $\perp$, respectively, $\mathbf{k} = \mathbf{k}_\parallel + \mathbf{k}_\perp$. For the case of 2D diffraction, the crystal periodicity in the direction normal to the surface is broken, and diffraction is governed by the translational symmetry of the surface. From the conservation of momentum it then follows

$$\mathbf{k}'_\parallel - \mathbf{k}_\parallel = \mathbf{G_{hk}} \tag{3.14}$$

which is the Laue condition for diffraction. The scattering angles of the diffracted beams are determined by this condition. After the diffractive scattering the parallel

component of the momentum can be equal to that of the incident electron beam, $\mathbf{k}'_\parallel = \mathbf{k}_\parallel$, or it can be equal to $\mathbf{k}_\parallel$ to within a reciprocal lattice vector $\mathbf{G_{hk}}$, $\mathbf{k}'_\parallel = \mathbf{k}_\parallel + \mathbf{G_{hk}}$. In a two dimensional lattice the reciprocal lattice vector is given by

$$\mathbf{G} = h\mathbf{a}^* + k\mathbf{b}^*, \tag{3.15}$$

where $\mathbf{a}^*$ and $\mathbf{b}^*$ are the reciprocal lattice vectors. The reciprocal lattice vectors are related to the real space unit cell vectors $\mathbf{a}$ and $\mathbf{b}$, by $\mathbf{a} \cdot \mathbf{a}^* = \mathbf{b} \cdot \mathbf{b}^* = 1$ and $\mathbf{a} \cdot \mathbf{b}^* = \mathbf{b} \cdot \mathbf{a}^* = 0$. [141]

Realistic surfaces often consist of overlayers or reconstructions on top of a substrate. To characterize superstructures formed by a reconstruction of the substrate surface or by adsorbed species, two notations are used. Let $\mathbf{a}_1$ and $\mathbf{a}_2$ define the real space lattice vectors for the substrate, and $\mathbf{b}_1$ and $\mathbf{b}_2$ define lattice vectors for adsorbate/reconstruction. The relation between the lattice vectors of the overlayer and substrate is given by [85, 142]

$$\begin{bmatrix} \mathbf{b}_1 \\ \mathbf{b}_2 \end{bmatrix} = \begin{bmatrix} G_{11} & G_{12} \\ G_{21} & G_{22} \end{bmatrix} \cdot \begin{bmatrix} \mathbf{a}_1 \\ \mathbf{a}_2 \end{bmatrix} = \mathbf{G} \begin{bmatrix} \mathbf{a}_1 \\ \mathbf{a}_2 \end{bmatrix} \tag{3.16}$$

An alternative and simplified representation, termed Wood-notation [145], is often used instead. It is defined as

$$p, c \left(\frac{|\mathbf{b}_1|}{|\mathbf{a}_1|} \times \frac{|\mathbf{b}_2|}{|\mathbf{a}_2|} \right) R\alpha, \tag{3.17}$$

where α is a rotation angle, and p and c denote either a primitive or a centered symmetry, respectively. The prefix p is often omitted for primitive symmetry. If $\alpha = 0$ the suffix $R\alpha$ is omitted. The two quotients are called elongation factors. This notation, however, does not directly indicate changes in the layer symmetry (e.g., square to hexagonal). Unreconstructed surfaces and saturated adlayers with one adsorbate species per one substrate site are denoted to have a (1×1) ordering.

A typical LEED apparatus is displayed in Figure 3.10 [85, 142]. The system main components are an electron gun with a variable accelerating potential producing a beam of monochromatic electrons, and a hemispherical retarding-field energy analyzer system to detect the elastically scattered electrons. Electrons produced in the electron gun are accelerated and focused by electrostatic lenses. Upon hitting the sample, which is grounded, some will undergo elastic scattering and reflect back. The detection system consists of four hemispherical concentric metal grids at different voltages and a fluorescent screen. The first grid is at the same potential as the sample, grounded, to ensure a field-free region between the sample and

screen. The next two grids are set at a potential slightly lower than the kinetic
energy of the electrons produced by the gun, in order to repel inelastically scat-
tered electrons. Elastically scattered electrons pass to the next grid which is set to
ground potential and are then accelerated towards the fluorescent screen which is
set to about 6 keV. The diffracted electrons hit the fluorescent screen, giving rise
to light emission, and the diffraction pattern can be observed or recorded with a
camera.

3.4.2   The $(\sqrt{5} \times \sqrt{5})$R27°-O Surface Oxide

In this thesis LEED was applied as a qualitative measure of surface structure, to
confirm that surfaces were well ordered, as a probe of sample surface quality, and
in order to identify surface structures such as surface oxides. As an example, Fig-
ure 3.11(a) and (c) display the LEED pattern for $\sqrt{5}$ surface oxide on Pd(100) and
$Pd_{75}Ag_{25}(100)$, respectively. The oxides were formed by exposing the surfaces to
oxygen at 320°C, using pressures 5×10^{-6} mbar for Pd(100) and about 5×10^{-4}
mbar for $Pd_{75}Ag_{25}(100)$.
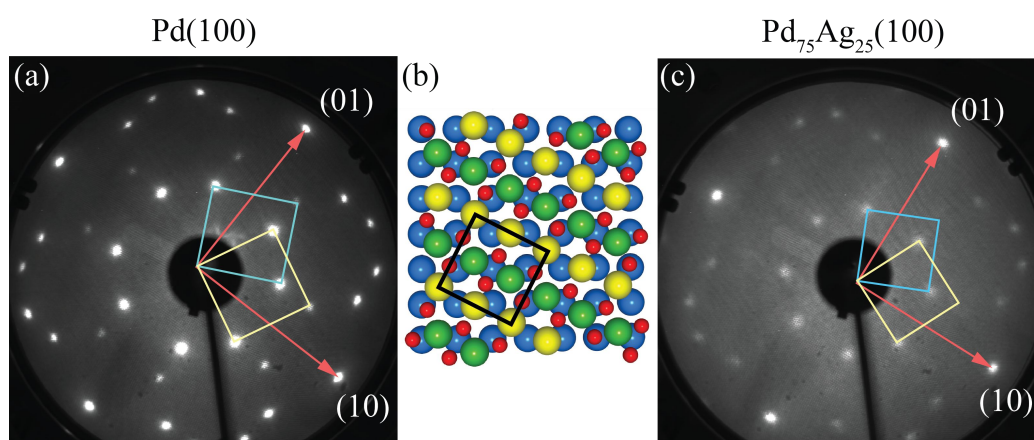
Figure 3.11: LEED pattern from the $(\sqrt{5} \times \sqrt{5})$R27° surface oxide on (a) Pd(100)
and (c) $Pd_{75}Ag_{25}(100)$. Both images were obtained at an electron energy of ap-
proximately 85 eV. The unit cell of two domains is indicated. (b) Model of the
PdO(101) structure on Pd(100) with the $(\sqrt{5} \times \sqrt{5})$R27° unit cell indicated.

The LEED pattern for the surface oxide structure on Pd(100) and $Pd_{75}Ag_{25}(100)$
displays a $(\sqrt{5} \times \sqrt{5})$R27° structure with four fold symmetry. Two domains rela-
tive to four fold symmetry are identified in the Figure 3.11. The LEED pattern can
be interpreted as a square lattice from a single PdO(101) layer on top of the square

substrate lattice. Figure 3.11(b) shows a model of a PdO(101) layer on Pd(100), with the unit cell identified by a black color square.

3.5 Scanning Tunneling Microscopy

Although the Scanning tunneling microscopy (STM) was first realized in 1980's, the physics concepts in which the instrument is based on, the quantum tunneling effect, was first conceptualized much earlier, at the end of the XIX century in work related with radioactivity, and was first applied and investigated in the late 1920's. More specifically, physicist George Gamow in his studies to understand alpha radioactivity in 1928 proposed how an α-particle is able to escape the large potential energy barrier imposed by the nucleus on the basis of quantum tunneling, deriving a relationship between the half-life of the decay, and the energy of the emission that is dependent on the probability of tunneling [146]. The discovery of transistors in 1947 and the tunnel diode in 1957 proved the electron tunneling in solids conclusively [147]. Gerd Binnig, Heinrich Rohrer, and their colleagues at the IBM Zurich Research Laboratory applied successfully the concept of tunneling in 1981 [148]. The first surface topology images of a sample surface with atomic resolution were obtained shortly after [149, 150]. This accomplishment earned Binnig and Rohrer the Nobel Prize in Physics in 1986 for their design of an STM system.

3.5.1 Principles of Scanning Tunneling Microscopy

STM exploits the quantum tunneling effect between a sharp metallic tip and a conducting sample. The wave-particle dualism [139] allows an electron with energy E impinging onto a potential energy barrier, with height V and thickness L, to pass the barrier with a finite probability even if $E < V$. The probability that an electron can tunnel through an arbitrary potential barrier which exhibits spatial variation, illustrated in Figure 3.12, for example from the tip to the sample (or vice versa), can be determined using an approach known as the Wentzel-Kramers-Brillouin (WKB) approximation to solve the Schrödinger equation [146, 151]. In the case of a strongly attenuating barrier, the tunneling probability T can be written as [146]

$$T \propto e^{-2\gamma} \propto e^{-2\frac{1}{\hbar}\int_{x_1}^{x_2}|\sqrt{2m(E-V(x))}|dx} \tag{3.18}$$

where $\hbar = h/2\pi$, $V(x)$ is the spatially varying potential energy function. In the case of tunneling with vacuum barriers the energy height $E - V(x)$, corresponds
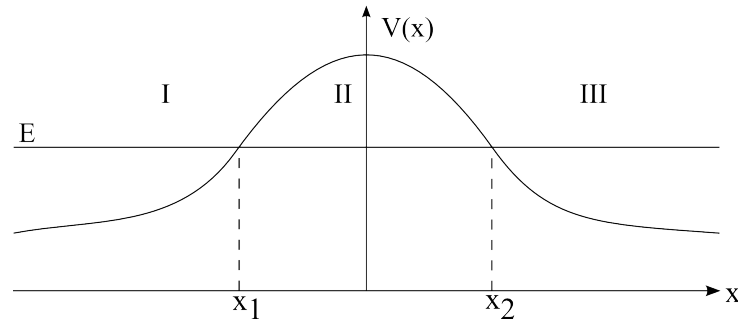
Figure 3.12: Generic spatially varying potential barrier $V(x)$ where a particle of energy E may tunnel through between x_1 and x_2.

to the energy needed to move an electron from the Fermi level to outside the material, the work function Φ. This result shows the exponential dependence of the tunneling probability on the width of the barrier, the separation between the tip and sample.

In the microscope, a bias voltage in the order of 10^{-2} V up to about 10 V is applied between the tip and a conducting sample, to create a preferential direction for current flow. A tunneling current I, generally in the order of 10^{-9} A, flows between the tip and the sample when they are approached to a distance typically in the nanometer to a few Å range. The exponential dependence makes the tunneling current very sensitive to the tip-sample distance. From scanning the tip over the sample surface while the tunneling current is controlled, a three dimensional image of the surface can be obtained. STM does not provide a direct image of the underlying geometrical atomic structure, but the tunneling current depends on the combined electronic structure of the tip and the sample. An exact theoretical description of the tunneling current can only be obtained if the correct wave functions of the sample and tip are known.

The theoretical understanding of STM is essential for a correct interpretation of characteristic features in the STM images. A discussion of methods for realistic theoretical description and modeling of tunneling in STM is presented elsewhere [152, 153]. The most accurate description of the process of electron tunneling between two contacts is the Keldysh formalism [154], also known as Nonequilibrium Green's Function approach (NEGF) [155], where the sample surface and the tip are treated as one interacting system and electron tunneling is described as an electron transport process. This method incorporates all inelastic effects such as electron-electron and electron-phonon scattering, which are usually negligible in STM [156, 157], making simulation of STM images from DFT calculations using this formalism very expensive. The most commonly used ap-
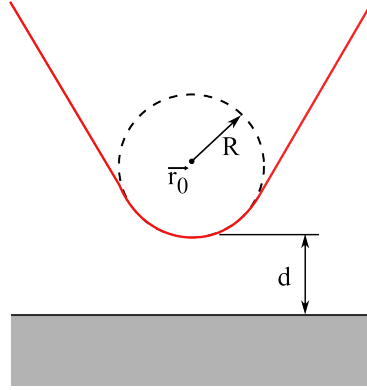
Figure 3.13: Schematic illustration of the geometry of the tip in the Tersoff-Hamann model. The tip is assumed to have local spherical symmetry, with curvature radius R, and with the center at distance $|\mathbf{r_0}|$ from the surface of the sample. The distance from the tip to the sample is d. Figure adapted from [158]

proximation was developed by Tersoff and Hamann [158], based on Bardeen's perturbation approach [159]. Since the transmission is small for a strongly attenuating barrier, assuming that the barrier is large enough, Bardeen proposed the separation of the total system into distinct subsystems, tip and sample, with known Hamiltonians and wave solutions. In this approach, the tunneling current is treated as first-order perturbation between the states of the sample and tip, coupled by a transition probability matrix.

Tersoff and Hamann proposed a method where the tip is approximated by a sphere of radius R centered at r_0, and distance d between the edge of sphere and the surface, as shown in Figure 3.13. The electronic structure of the tip is represented by a wave function which is assumed to be a spherically symmetrical s-wave. In this approximation, in the limit of small voltage and low temperature, the tunneling current is expressed as [158]

$$I \propto VR^2 \exp(-\sqrt{8m\Phi/\hbar}\,d) \sum_v |\psi_v(\mathbf{r_0})|^2 \delta(E_v - E_F), \qquad (3.19)$$

$$\sum_v |\psi_v(\mathbf{r_0})|^2 \delta(E_v - E_F) \equiv \rho(\mathbf{r_0}, E_F), \qquad (3.20)$$

where V is the applied voltage, E_v is the energy associated with the wave function of the sample ψ_v, and ϕ is the potential barrier height, which is equal to the work function of the surface. This equation shows that the tunneling current $I(V)$ is proportional to the local electron density of the sample states, $\rho(\mathbf{r_0}, E_F)$, at the center of the sphere, where contribution comes only from wave functions with an energy close to the Fermi energy E_F. The lateral resolution Δ_{lat} of the image can

be approximately related to the radius of the tip, R, the separation distance, d, and the work function of the sample, Φ, as [158]

$$\Delta_{lat} \approx \left(\frac{R+d}{\hbar^{-1}\sqrt{2m\Phi}} \right). \tag{3.21}$$

The Tersoff and Hamann method works well for metallic surfaces with bias voltages of the order of a few millivolt. However for many other surfaces of interest, for example metal oxides or semiconductors, higher bias voltages are often required for a meaningful tunneling current to be produced. A more general tunneling current expression has been proposed [151],

$$I \propto \int^{eV} \rho_t(\pm eV \mp E)\rho_s(E)T(E,eV)dE \tag{3.22}$$

where $\rho_t(E)$ and $\rho_s(E)$ are the density of states of the tip and sample, respectively, with the energy- and bias-dependent transmission coefficient $T(E,eV)$ given by

$$T(E,V) = \exp\left(-\frac{2(d+R)\sqrt{2m}}{\hbar}\sqrt{\frac{\Phi_s + \Phi_t}{2} + \frac{eV}{2} - E} \right) \tag{3.23}$$

where Φ_t and Φ_s denote the tip and sample surface work functions, respectively.

As previously discussed, the tunneling current is directly proportional to the local density of states (LDOS) of the sample surface, and depends mainly on the distance between the sample and probe. This makes it possible to obtain a topographic image of a sample. Figure 3.14 displays a schematic drawing of a typical STM setup, consisting of a sharp metal tip (the probe), a conducting sample, and control unit. The latter manages functions such as feedback loop and tip scanning. Between the tip and the sample there is an insulating barrier, usually a vacuum. A small bias-voltage is applied between the tip and the sample, and the resulting tunneling current is measured. The precise movement of the tip over the sample surface is accomplished using piezoelectric devices in the x, y, and z directions. The STM can produce images with resolution to the atomic scale both in the (x,y) plane and z direction. For probing the surface topography two main modes of operation are used, constant current imaging (CCI) and constant height imaging (CHI) [151, 160]. The most frequently used operation mode is CCI. In this mode the tip scans over the sample surface while the tunneling current is kept constant by continuously feedback-adjusting the vertical position of the tip. Provided that the LDOS is homogeneous, by monitoring z as a function of the lateral tip position (x,y), $z = f(x,y)$, a three dimensional image of the surface may be deduced from the vertical shift of the probe. The finite response time of the feedback control sets
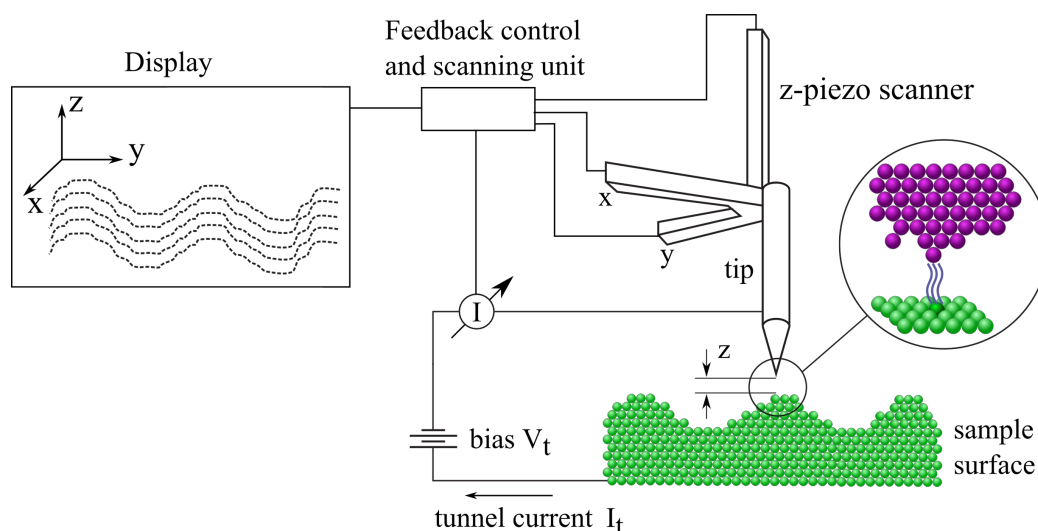
Figure 3.14: Schematic drawing of a generic STM setup, consisting of a sharp tip, conducting sample, and a control unit. The measurement of the tunneling current between the tip and sample, when a bias voltage V_t is applied, allows obtaining a topographic image of the sample surface, directly related to the electronic density of states at the surface.

a limit to the scanning speed [161]. In CHI mode the vertical position of the probe is kept constant, i.e., fixed tip-sample separation. The topographic image of the surface may be deduced from the measured tunneling current. The CHI scanning mode is faster than CCI because no feedback-adjustment process is necessary. However, irregularities in the sample surface may lead to tip crashing. Due to the very small time lag, this method can be used to capture a real-time evolution of surface processes. The STM can also operate in spectroscopic mode where local I(V) curves can be measured at selected points in space to obtain information on the LDOS [162, 163], however this operation mode was not of concern in this thesis.

To achieve atomic resolution, the vibrations of the STM environment must be efficiently decoupled from the STM device using, for example, a damping system in the vacuum chamber and/or damping springs to suspend the device while in operation. The STM unit was mounted in a UHV chamber with a pressure of less than 10^{-9} mbar. The experiments were performed at room temperature. The tip material used was tungsten. The method of electrochemical etching [164] in a solution of KOH was used for preparation of the tip. With this method a tip curvature radius of about 10 - 100 nm is achieved. The STM was operated in CCI mode.

3.5.2　STM Characterization of Oxidized Pd(100) and Pd$_{75}$Ag$_{25}$(100) Surfaces

The $\sqrt{5}$ surface oxide structure was previously presented in terms of its LEED and XPS signatures. Figure 3.15 displays STM images of the $\sqrt{5}$ surface oxide structure on Pd(100) and Pd$_{75}$Ag$_{25}$(100). Images (a) and (b) show the oxide structure on Pd(100) and images (c)-(f) on Pd$_{75}$Ag$_{25}$(100). The yellow rows in figures (b) and (d) indicate the location of two-fold oxygen coordinated Pd atom rows in the (101) PdO unit cell, represented as yellow atoms in the model shown in (g). The orange lines indicate domain boundaries between different translational domains of the oxide structure.

For Pd$_{75}$Ag$_{25}$(100) the number of domain boundaries is significantly larger compared to Pd(100). The $\sqrt{5}$ surface oxide consists of a strained PdO(101) layer on top of the Pd(100) surface. The stress is relieved by the formation of the domain boundaries. From image analysis, the average distance between the mismatch dislocations is $\approx 10\sqrt{5}$ unit cells for Pd(100) [67], and $\approx 3\sqrt{5}$ unit cells for Pd$_{75}$Ag$_{25}$(100). The higher number of domain boundaries on Pd$_{75}$Ag$_{25}$(100) indicates that the surface oxide is under higher stress on the Pd$_{75}$Ag$_{25}$ alloy compared to pure Pd, as result of the presence of silver. Calculations can be performed to evaluate the mismatch between a perfect PdO(101) overlayer and the $\sqrt{5}$ structure on Pd(100) and Pd$_{75}$Ag$_{25}$(100). Vegard's law [74, 75, 166], although with its accuracy limitations for metallic alloys [167, 168], provides an indication of the lattice constant of an alloy. Considering 3.89 Å and 4.08 Å for the lattice constants of Pd and Ag, for a Pd$_3$Ag alloy the lattice constant is 3.94 Å. From these values the unit cell size of the $\sqrt{5}$ structure on the two surfaces of interest can be calculated. Results are displayed in Table 3.1. The mismatch is larger on Pd$_{75}$Ag$_{25}$(100), and therefore the $\sqrt{5}$ oxide structure is under higher tensile stress on this surface, hence the increase in the number of domain boundaries.

Table 3.1: Unit cell size of the $(\sqrt{5} \times \sqrt{5})$R27° surface oxide on Pd(100) and Pd$_{75}$Ag$_{25}$(100) relative to the unperturbed structure, Pd(101) unit cell.

	PdO(101)	$\sqrt{5}$/Pd(100)	$\sqrt{5}$/Pd$_{75}$Ag$_{25}$(100)
Long side (Å)	6.13	6.15	6.21
Short side (Å)	3.03	3.08	3.11
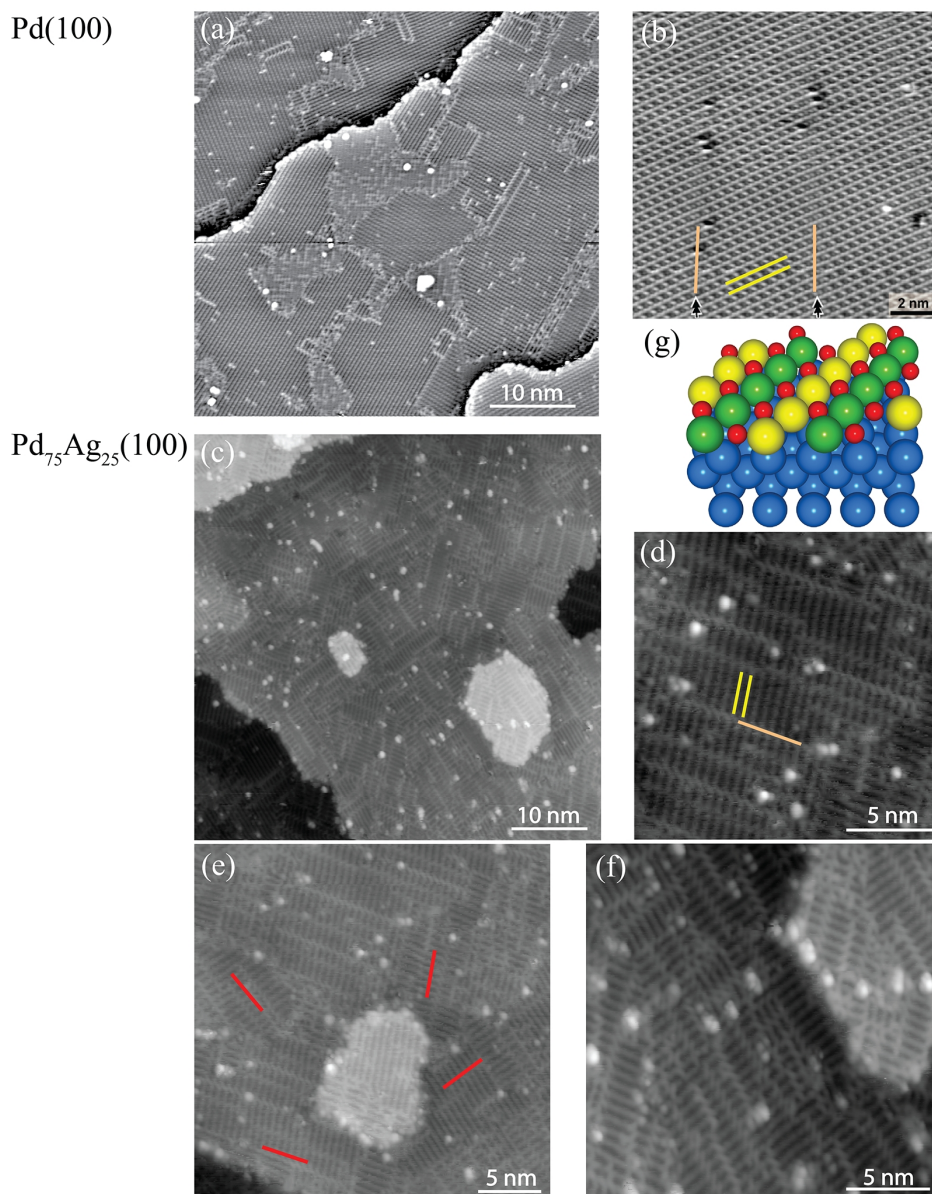
Pd(100)

Pd$_{75}$Ag$_{25}$(100)

Figure 3.15: STM images of the $(\sqrt{5} \times \sqrt{5})$R27° surface oxide structure on Pd(100), (a) and (b), and Pd$_{75}$Ag$_{25}$(100), (c) to (f). A model of the $(\sqrt{5} \times \sqrt{5})$R27° surface oxide is represented in (g). Four different domain orientations can be distinguished, indicated by red lines in image (e), for Pd$_{75}$Ag$_{25}$(100). In images (b) and (d) the two yellow lines highlight the rows of two-fold coordinated oxygen atoms in the (101) PdO unit cell, represented by the yellow atoms in the model (g). A translational domain boundary is indicated by the orange line. Image (a) was obtained from [165]. Image (b) was reproduced from [67].

3.6   Quadrupole Mass Spectrometry

In 1898, the physicist Wilhelm Wien, while studying streams of ionized gas, found that strong electric or magnetic fields deflected anode rays. He then constructed an apparatus capable of separating the positive anode rays by their mass-to-charge ratio, observing that the charge-to-mass ratio depended on the nature of the gas in the discharge tube. In his work he identified a positive particle equal in mass to the hydrogen atom, laying the foundation of mass spectrometry [169]. In the beginning of the 1910's, Sir Joseph John Thomson constructed the first mass spectrometer, at the time called a parabola spectrograph, and obtains the mass spectra of O_2, CO, CO_2, among others [170–172]. The first mass spectrometer based on Quadrupole ion traps was proposed in 1953 [173].

Quadrupole mass spectrometry (QMS) allows the identification of gas composition in a system by detection of ionized atoms and molecules. The total pressure of a sample atmosphere can be monitored, as well as the partial pressures of the gas components in the sample atmosphere.

3.6.1   Principles of Quadrupole Mass Spectrometry

A schematic illustration of the working principle of a QMS system is presented in Figure 3.16. Electrons are generated by Joule heating of a filament. The free electrons are accelerated by a potential difference applied between the filament and a source grid or trap electrode placed opposite to the filament. When molecules of a gas sample are introduced into the ion source unit, the electrons accelerating towards the electrode collide with the sample molecules, creating positive ions by removal of one or more electrons from the molecules. This ionization process is known as electron impact ionization (EI). The ion source box is grounded and to the lens unit is applied a negative DC voltage. The positive ions formed are extracted from the ion source region by the potential difference between the inside of the ion source box and the lens unit. The extracted ions are focused and further accelerated towards the quadrupole mass filter by the lens unit.

The quadrupole mass filter consists of four electrically conducting parallel rods arranged in a square, as illustrated in Figure 3.16. Two DC voltages, $\pm U$, with the same magnitude and opposite polarities are applied to the rods in pairs. A RF voltage, $V\cos(\omega t)$, is superimposed on the DC voltage, resulting in the final set of voltages $\pm U + V\cos(\omega t)$ to which the ions are subjected. This causes the ions to oscillate as they travel in the area between the rods. From the equations of motion
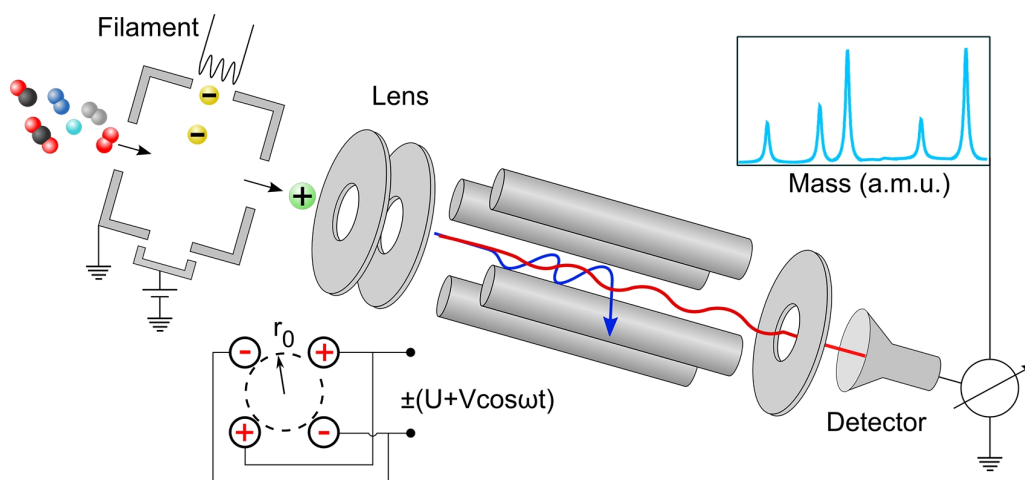
Figure 3.16: Schematic drawing of a quadrupole mass spectrometer.

one can derive the so called trapping parameters, a_u and q_u, where u denotes either x or y (plane perpendicular to the direction of the rods) [174–179]:

$$a_u = \frac{8zeU}{m\omega^2 r_0^2} \qquad and \qquad q_u = \frac{4zeV}{m\omega^2 r_0^2} \qquad (3.24)$$

where e is the electron charge, z is the charge of the ions, r_0 is the radius of the circle enclosed by the cylinders in the quadrupole, and m is the ion mass in atomic mass units. These equations define the stability areas, values of U and V that correspond to stable trajectories in the quadrupole mass filter for an ion with a given m/z ratio, i.e., the amplitude of oscillation lower than r_0, allowing the ion to be transmitted from the ion source to the detector. In the QMS system utilized in this thesis the detector was a Faraday cup with microchannel plate (MCP) electron multiplier. Ions approaching the MCP are attracted to the multiplier due to its negative charge. As the ions cascade down and strike the channel walls, they generate secondary electrons, amplifying the signal.

From equations 3.24 the voltages which set the criteria for the ions to pass through the quadrupole can be determined. Scanning U and V, while maintaining the U/V ratio constant at an appropriate value, in such a way that only a narrow range of mass-to-charge ratio is in resonance with the filter, allowing the successive detection of the different masses. This is illustrated in Figure 3.17. Ions with m/z ratios which do not fulfill the trapping condition eventually hit the rods and are not detected.
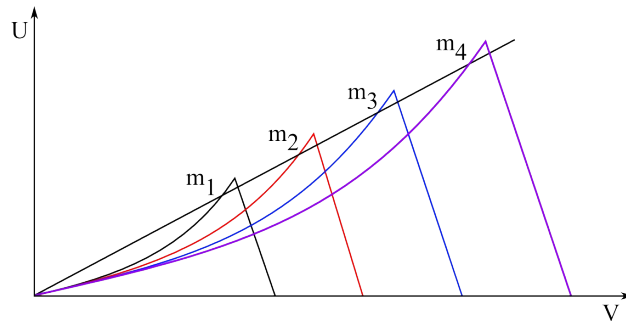
Figure 3.17: Stability areas as a function of U and V for ions with different masses $m_1 < m_2 < m_3 < m_4$ obtained from equations 3.24. By keeping the ratio U/V constant in a straight operating line, the so-called load line of the mass filter, allows the observation of the ions successively. A line with a higher slope results in higher resolution, as long as it intersects stability areas. $U = 0$ (no DC potential) yields zero resolution. All ions have a stable trajectory as long as V is within the limits of their stability area. Adapted from [178].

3.7 Theoretical Methods

Theoretical methods are important tools to analyze experimental data and complement experiments. This section briefly presents the theoretical formalism of solid state kinetics and density functional theory (DFT), which have been applied as modeling tools in this thesis.

3.7.1 Solid State Kinetics

Kinetic modeling was used to determine the character of the oxide reduction reactions, allowing to obtain information about the reaction mechanism and to determine reaction rate constants. In solid state kinetics the rate law of a transformation process at constant temperature is expressed in the form of a differential equation:

$$\frac{d\alpha}{dt} = kf(\alpha) \tag{3.25}$$

where α is the so-called degree of conversion, k is the rate constant, t is the time, and $f(\alpha)$ is the kinetic model, i.e., a mathematical expression describing the process. By definition the fractional extent of the reaction, α, changes progressively from reactants ($\alpha = 0$) to products ($\alpha = 1$). The rate equation can also be written in integral form as:

$$g(\alpha) = kt, \tag{3.26}$$

where $g(\alpha)$ represents the equation describing the kinetic model applied and k is the rate constant of the reaction. The functions $f(\alpha)$ and $g(\alpha)$ have the same meaning and represent the same, a model of the reaction. All models are written in differential form $f(\alpha)$. Most, but not all, models can be integrated analytically, being in this case expressed as $g(\alpha)$. The forms $f(\alpha)$ and $g(\alpha)$ are also termed conversion functions and depend on the system under consideration. In addition, some models can be written in its explicit form, i.e., α as a function of time t.

There are several kinetic models derived from the geometry of a reaction as well as empirical models to model the kinetics of a reaction. Some of the most widely used models are the model of contracting area, contracting volume, Johnson-Mehl-Avrami (JMA) (also known as Avrami-Erofeev), Prout-Tompkins (PT), reaction order, power and exponential laws, Jander equation (two-dimensional diffusion model), Ginstling-Brounstein (three-dimensional diffusion model), or Šesták-Berggren model. Derivations and considerations about these models and others can be found elsewhere [180–182].

All the models referred above have been considered in the present work. However, models based on nucleation and growth are the most probable contenders to adequately model the surface oxide reductions investigated in this thesis, in particular models based on Avrami theory. This is expected for processes where at the beginning and the end of the reaction the rate of transformation is lower than in between, i.e., an s-shaped or sigmoid curve. Here we will only refer to the relevant models for this work, which are the JMA and Šesták-Berggren models.

Avrami type models, such as JMA, are based on the formation and growth of nuclei, where the growing phases develop from different nuclei and come into contact after some time [180]. This model relies on the assumptions that nucleation occurs randomly in time and homogeneously distributed across the untransformed portion of the material and that growth occurs at the same rate in all directions and does not depend on the extent of transformation. The JMA equation is expressed in its differential, integral, and explicit forms, respectively, as

$$f(\alpha) = n(1-\alpha)[-ln(1-\alpha)]^{1-1/n}, \tag{3.27}$$

$$g(\alpha) = [-ln(1-\alpha)]^{1/n} = kt, \tag{3.28}$$

$$\alpha = 1 - \exp[-(kt)^n], \tag{3.29}$$

where n is denoted *index of reaction*. n usually has a value of 1.5, 2, 3 or 4 which reflects the nature of the transformation [180]. The exponent n is a combined term of β, the number of steps involved in the nucleation ($\beta = 0$ for instantaneous nucleation, $\beta = 1$ for constant nucleation rate), and λ, the number of dimensions in which the nuclei grow (1 for linear growth, 2 for disc or cylindric growth, and 3 for spherical or hemispherical growth). The form of n also depends on the kinetic behavior: for interface controlled reactions $n = \beta + \lambda$ while for diffusion controlled reactions $n = \beta + \lambda/2$ [180].

Although the limits of applicability of the JMA equation are known, in practice it is sometimes difficult to verify if all the criteria of applicability are met. Málek developed a procedure to test whether or not a process follows the JMA model [183]. The process starts by defining the functions $y(\alpha) = \phi$ and $z(\alpha) = \phi t$, where ϕ is the conversion rate on the process, i.e., $d\alpha/dt$, normalized to the interval $(0,1)$. These functions exhibit maxima at $\alpha_{max,y}$ and $\alpha_{max,z}$ for $y(\alpha)$ and $z(\alpha)$, respectively. For the JMA model, when $z(\alpha)$ is plotted as a function of α, its maximum is located at the constant value of $\alpha_{max,z} = 0.632$. This value is characteristic of this model [183, 184]. If the maximum $\alpha_{max,z}$ of the experimental data falls in the interval $0.61 < \alpha_{max,z} < 0.65$ it is likely to be a process described by the JMA model [183, 184].

A more general, empirical, rate equation has been proposed by Šesták and Berggren (SB) [185]:

$$f(\alpha) = \alpha^M (1-\alpha)^N [-ln(1-\alpha)]^P \qquad (3.30)$$

where M, N, and P are mathematical parameters. Depending on the value of these parameters, this equation can represent all common kinetic models [185]. Further mathematical analysis shows that two exponents are sufficient to describe a reaction process [186]. The SB equation in this case is

$$f(\alpha) = \alpha^M (1-\alpha)^N \qquad (3.31)$$

where the exponents M and N have the significance of the kinetic parameters of the reaction process. In the literature this model is sometimes referred to as extended PT equation [187]. The relative values of M and N determines the relative contribution of the acceleratory and decay regions in the process. It has also been shown that this model is physically meaningful only if $M < 1$ [188]. The SB equation includes the PT and JMA model for given M and N. When $M = N = 1$ the SB equation becomes the PT model. For $M = 0.72$ and $N = 0.76$ the SB equation corresponds to the JMA model with $n = 3$ and for $M = 0.77$ and $N = 0.69$ it corresponds to the JMA model with $n = 4$. The empirical SB model thus includes other models as special cases, being a plausible description of the nucleation and growth process [184, 185, 189]. However, the SB equation is a phenomenological description of kinetics, and the physical significance of the parameters M and N is limited.

3.7.2 Density Functional Theory

Density functional theory (DFT) is a theoretical framework to investigate the electronic structure of atoms, molecules, and condensed matter [190]. DFT calculations agree quite satisfactorily with experimental data, and computational costs are relatively low when compared to traditional methods, such as Hartree-Fock theory. This is because DFT only attempts to calculate total electronic energy and electronic density distribution, while Hartree-Fock theory calculates the full N-electron wave function of the system. Today, DFT has become the most used electronic structure calculation method. Due to the relevance of this method W. Kohn was awarded the Nobel Prize for his significant contribution in the development of DFT [191, 192]. In this work, DFT was used as a complementary approach to address the interaction of CO molecules with the Pd(100) and $Pd_{75}Ag_{25}(100)$ surfaces.

The electronic energy of a system and its quantum mechanical behavior are described by the Schrödinger equation

$$H\Psi = E\Psi, \tag{3.32}$$

where H is the Hamiltonian operator, E is the energy, and Ψ is the many-body wave function. The Hamiltonian operator consists of three terms, T the kinetic energy, V the potential energy from the external field due to positively charged nuclei, and U the electron-electron interaction energy. The Schrödinger equation for the N-electron system is then written as [190]

$$H\Psi = [T+V+U]\Psi = \left[\sum_i^N \left(-\frac{\hbar^2}{2m_i}\nabla_i^2\right) + \sum_i^N V(\mathbf{r}_i) + \sum_{i<j}^N U(\mathbf{r}_i,\mathbf{r}_j)\right]\Psi = E\Psi. \tag{3.33}$$

This equation is valid within the Born-Oppenheimer approximation, where nuclear motion is assumed to be decoupled from the electron motion due to the comparatively fast motion of the latter. The interaction term U does not allow the separation of this equation. This equation is computationally very expensive to solve using Hartree-Fock methods.

Hohenberg and Kohn showed that the ground state energy and other properties of the system were uniquely defined by the electron density, or in other words, E is a unique functional of $n(\mathbf{r})$ [191]. In DFT the energy functional is written as

$$E[n(\mathbf{r})] = F[n(\mathbf{r})] + \int v_{eff}(\mathbf{r})n(\mathbf{r})d\mathbf{r} \tag{3.34}$$

The first term, $F[n(\mathbf{r})]$, is the sum of the kinetic energy of the electrons and the contribution from the interelectronic interactions. The second term arises from the interaction of the electrons with an external effective potential $v_{eff}(\mathbf{r})$ (e.g., the potential of the nuclei in the crystal). Minimization of the energy functional will yield the ground-state density n_0 and thus all other ground-state observables.

The electron density of the system, written by Kohn and Sham as the sum of the square moduli of a set of one-electron orbitals [192], is given by

$$n(\mathbf{r}) = \sum_{i=1}^N |\psi_i(\mathbf{r})|^2, \tag{3.35}$$

were $\psi(\mathbf{r})$ is the wave function. The Kohn-Sham equations of non-interacting system of particles have the form [192]

$$\left[-\frac{\hbar^2}{2m}\nabla^2 + v_{eff}(\mathbf{r})\right]\psi_i(\mathbf{r}) = \varepsilon_i\psi_i(\mathbf{r}), \tag{3.36}$$

where ε_i is the orbital energy. The potential $v_{eff}(\mathbf{r})$, the effective single-particle potential, can be written as

$$v_{eff}(\mathbf{r}) = V_{ext}(\mathbf{r}) + \int \frac{n(\mathbf{r}')}{|\mathbf{r}' - \mathbf{r}|} d\mathbf{r}' + V_{XC}[n(\mathbf{r})], \qquad (3.37)$$

where $V_{ext}(\mathbf{r})$ is the external potential, the second term is the Hartree electrostatic energy, describing the electron-electron Coulomb repulsion, and $V_{XC}[n(\mathbf{r})]$ is the so-called exchange-correlation potential.

The difficulty of DFT is that $V_{XC}[n(\mathbf{r})]$ is not known exactly, and in practice approximations have to be taken. Several approximations for exchange-correlation functionals have been developed over the years [193–197]. The best functional to use depends on the problem under consideration.

To solve the Kohn-Sham equations an initial guess for the density $n(\mathbf{r})$ is provided and feed into equation 3.37. The calculated $V_{ext}(\mathbf{r})$ is used to solve equation 3.36, from which a set of orbitals ψ_i can be calculated, leading to an improved value of the density $n(\mathbf{r})$, equation 3.35. This iterative process is repeated until convergence is reached.

DFT has significant computational advantages over Hartree-Fock methods. To put it into perspective, the system size scaling in Hartree-Fock type methods is usually $O(N^4)$ to $O(N^7)$, where N is the number of basis functions. For DFT this is $O(N)$ to $O(N^3)$ [198]. However, DFT is less accurate for certain properties, for example, underestimated electronic band gaps and inability to properly describe Van der Waals interactions (which can be improved upon [199]). Nevertheless, it provides reliable predictions of atomic and electronic structures.

A more comprehensive description of DFT is presented elsewhere [190, 198, 200, 201]. Review articles include [202–204].

Chapter 4

Summary of papers

In this chapter a brief summary is given of the main results from the five papers included in this thesis. The chapter is divided in three sections concerning the oxidation of $Pd_{75}Ag_{25}(100)$ surface, reduction of surface oxides on $Pd(100)$ and $Pd_{75}Ag_{25}(100)$, and high-pressure studies of these surfaces.

4.1   Clean and oxidized $Pd_{75}Ag_{25}(100)$

Paper I
Surface composition of clean and oxidized $Pd_{75}Ag_{25}(100)$ from photoelectron spectroscopy and density functional theory calculations

In this paper we used high resolution photoelectron spectroscopy and density functional theory calculations to study the composition of clean and oxidized $Pd_{75}Ag_{25}(100)$. The results for the clean surface confirm earlier reports of surface segregation by Wouda et al. (1998), where the topmost layers are rich in Ag. The Pd 3d core level component from the surface region is observed at higher binding energies than the contribution from the bulk which is found to be a signature of Pd embedded in Ag. Low energy electron diffraction and scanning tunneling microscopy measurements reveal that oxidation of the $Pd_{75}Ag_{25}(100)$ surface results in a $(\sqrt{5} \times \sqrt{5})R27°$-O structure similar to the one reported for $Pd(100)$. The calculations suggest that the stable structure is a $PdO(101)$ monolayer supported on a (100) surface rich in Ag at the interface to the stoichiometric alloy. The calculated core level shifts for the oxidized surface are in good agreement with the

experimental observations.

4.2   Surface oxide reduction by CO and H$_2$

<div align="center">

Paper II

Reduction behavior of oxidized Pd(100) and Pd$_{75}$Ag$_{25}$(100) surfaces using CO

</div>

In this paper we report on the reduction of the $(\sqrt{5} \times \sqrt{5})$R27° surface oxide on Pd(100) and Pd$_{75}$Ag$_{25}$(100) surfaces by CO. The reduction process was investigated by high-resolution X-ray photoelectron spectroscopy in combination with kinetic analysis using Avrami-Erofeev theory. For both surfaces we observed that the reduction proceeds faster with increasing temperature. The results from kinetic analysis of the X-ray photoelectron spectroscopy data indicate that the reduction process is phase boundary controlled for Pd(100) in the temperature range investigated, from 30°C to 120°C. On Pd$_{75}$Ag$_{25}$(100) the surface oxide reduction is significantly slower compared to Pd(100). Also in this case, a phase boundary controlled reduction of the surface oxide is observed at temperatures of 120°C and above, while at $T \leq 70$°C the reduction is found to be diffusion limited. Density functional theory calculations were used to analyze the effect of silver atoms in the outermost surface layer in the diffusion CO molecule. The results show that the presence of silver significantly increases the CO diffusion barriers on the reduced areas, supporting a diffusion limited reduction process for Pd$_{75}$Ag$_{25}$(100) at lower temperatures.

Paper III
H_2 reduction of surface oxides on Pd-based membrane model systems - the case of Pd(100) and $Pd_{75}Ag_{25}$(100)

In this paper, using *in situ* high-resolution X-ray photoelectron spectroscopy, we studied the reduction of the $(\sqrt{5} \times \sqrt{5})$R27° surface oxide on Pd(100) and $Pd_{75}Ag_{25}$(100) surfaces by H_2 at pressures 5×10^{-9} mbar and 5×10^{-8} mbar and selected temperatures in the range 30°C to 170°C. We observe a slower reduction on $Pd_{75}Ag_{25}$(100) compared to Pd(100) for all temperatures and pressures investigated. For Pd(100) the surface oxide reduction is rather independent of temperature, while for $Pd_{75}Ag_{25}$(100) shows a non-monotonic variation. For the alloy surface the reduction is slowest at 30°C, increases at intermediate temperatures, and decreases at 170°C. Kinetic analysis indicates that reduction behavior is not well described by Avrami kinetics. The more general Šesták-Berggren equation was utilized to fit the experimental results. The dependence in temperature of the reduction rates for $Pd_{75}Ag_{25}$(100) correlates with the amount of surface Pd atoms.

4.3 High Pressure studies

Paper IV
In Situ X-Ray Photoelectron Spectroscopy of Model Catalysts: At the Edge of the Gap

This paper concerns the CO oxidation over a Pd(100) surface at different partial pressure of O_2 and CO. High-pressure x-ray photoelectron spectroscopy and first-principles kinetic Monte Carlo were used to address the nature of the active surface in CO oxidation over Pd(100). We observed both O-covered Pd(100) and a $(\sqrt{5} \times \sqrt{5})$R27° surface oxide as stable, highly active phases. No adsorbed CO can be detected during CO_2 production in the highly active phase of the catalyst, explained by a short residence time of the CO molecule on the surface and mass-transfer limitations in the present setup. It was concluded that at near stoichiometric O_2/CO pressure ratios 1.3 mbar is at the edge of the "pressure gap", above which formation of oxide phases on Pd(100) should be observed.

Paper V
Near-Ambient Pressure CO and H$_2$ Oxidation over Pd(100) and Pd$_{75}$Ag$_{25}$(100) Surfaces

We have used high pressure X-ray photoelectron spectroscopy and quadrupole mass spectrometry to compare the oxidation of CO and H$_2$ over Pd(100) and Pd$_{75}$Ag$_{25}$(100) surfaces under oxygen rich conditions at near-ambient pressure. For the CO oxidation and simultaneous CO and H$_2$ oxidation, below a critical temperature of about 185°C and 200°C for Pd(100) and Pd$_{75}$Ag$_{25}$(100), respectively, we observe low oxidation activity, controlled by CO poisoning on both surfaces. Above the critical temperature the activity is high and the chemistry of the surfaces changes. For Pd(100) the $(\sqrt{5} \times \sqrt{5})$R27° surface oxide is the active surface, while chemisorbed oxygen plays this role for Pd$_{75}$Ag$_{25}$(100). The activation for CO oxidation over Pd(100) was determined at 1.0 eV, while a value of 1.1 eV was obtained for Pd$_{75}$Ag$_{25}$(100). Regarding the oxidation of H$_2$ only, on Pd(100) the reaction is active from room temperature and a $(\sqrt{5} \times \sqrt{5})$R27° surface oxide is observed. Above 510°C the surface oxide is removed and chemisorbed oxygen phase is formed. This is accompanied by an small increase in water formation. For Pd$_{75}$Ag$_{25}$(100) the reaction is activated at 145°C. A chemisorbed oxygen phase is observed in this case. Overall, the presence of silver in the outermost surface layer significantly affects the surface chemistry during these reactions and thereby the reaction mechanism.

Chapter 5

Conclusions and Outlook

In this thesis Pd(100) and $Pd_{75}Ag_{25}$(100) surfaces were studied as model systems for catalytic Pd-based membranes and oxidation catalysts.

It was found that the $Pd_{75}Ag_{25}$(100) surface is silver rich and that a $(\sqrt{5} \times \sqrt{5})R27°$ surface oxide can form on the alloy surface, similar to that observed on Pd(100). Reduction of the surface oxide by CO is significantly slower on $Pd_{75}Ag_{25}$(100) compared to Pd(100), due to the presence of Ag. Increased temperature leads to faster reduction on both surfaces. Reduction by H_2 shows a complex temperature dependence. For the Pd(100) the reduction is faster at 30°C, while for $Pd_{75}Ag_{25}$(100) it is slowest at this temperature. Also for H_2 the reduction is slower on $Pd_{75}Ag_{25}$(100) compared to Pd(100).

In situ investigations at near-ambient pressures of the catalytic CO and H_2 oxidation over Pd(100) and $Pd_{75}Ag_{25}$(100) under oxygen rich conditions reveal that the catalytic activity of the surface at low temperature is controlled by CO poisoning. Above a critical temperature of approximately 185°C and 200°C for Pd(100) and $Pd_{75}Ag_{25}$(100), respectively, the oxidation activity is high. In the high activity regime the surface is covered by a $(\sqrt{5} \times \sqrt{5})R27°$ surface oxide on Pd(100) and a chemisorbed oxygen phase on $Pd_{75}Ag_{25}$(100). On the alloy surface CO oxidation shows a significant temperature dependence, while H_2 oxidation is not affected.

The studies presented show significant effects of the alloying element Ag on the catalytic properties of the system. In the case of $Pd_{75}Ag_{25}$(100) the active phase for catalytic oxidation of CO and H_2 is a chemisorbed oxygen phase, which is expected to change the reaction mechanism. Moreover, in the high activity regime, it was observed that CO oxidation to CO_2 over the alloy surface is influenced by

temperature.

The results obtained open a number of questions which may be of interest for further work. The significant temperature dependence of the surface oxide reduction using hydrogen requires further experiments at a finer temperature step in order to obtain a clearer picture. On the same note, the reaction mechanism leading to water formation during reduction of the $(\sqrt{5} \times \sqrt{5})R27°$ surface oxide is still unclear, in particular if the reaction involves OH groups. DFT calculations may assist in answering this question.

The high-pressure XPS investigation suggests that H_2 oxidation on Pd(100), follows a Mars van Krevelen mechanism. It is unclear in this case if the reaction path for water formation involves OH groups or if it is a result of direct reaction of the H_2 molecule with the oxygen atoms from the surface oxide. In the case of $Pd_{75}Ag_{25}(100)$ the reason for the significant temperature dependence for CO oxidation in the high activity regime may result from silver segregation or from the Langmuir-Hinshelwood mechanism. Which of these processes plays the major role is uncertain at this point. Investigation of oxidation reactions on the Pd(100) and $Pd_{75}Ag_{25}(100)$ surfaces at different ratios of O_2, CO, and H_2, as well XPS measurements focused on the segregation behavior of the alloy surface may provide further insight. In addition, CO and H_2 oxidation studies over the $Pd_{75}Ag_{25}(100)$ surface at gas pressures higher than 0.8 mbar are required to assess if a surface oxide phase forms in this case.

Bibliography

[1] H. Davy. *Phil. Trans. R. Soc. Lond.*, 107:77, 1817.

[2] J. J. Berzelius. *Edinburgh New Philosophical Journal*, 21:223, 1836.

[3] P. Serp and K. Philippot. *Nanomaterials in Catalysis*. John Wiley & Sons, 2012.

[4] J. M. Thomas and W. J. Thomas. *Principles and Practice of Heterogeneous Catalysis*. Wiley, 1997.

[5] A. C. Bose, editor. *Inorganic Membranes for Energy and Environmental Applications*, chapter 9. Springer, 2009.

[6] N. N. Li, A. G. Fane, W. S. Winston Ho, and T. Matsuura, editors. *Advanced Membrane Technology and Applications*, chapter 25. Jon Wiley & Sons, 2008.

[7] N. Itoh and R. Govind. *Ind. Eng. Chem. Res.*, 28(10):1554, 1989.

[8] G. J. Grashoff, C. E. Pilkington, and C. W. Corti. *Plat. Met. Rev.*, 27(4):157, 1983.

[9] J. Shu, B. P. A. Grandjean, A. Van Neste, and S. Kaliaguine1. *Can. J. Chem. Eng.*, 69(5):1036, 1991.

[10] S. Uemiya. *Separ. Purif. Rev.*, 28(1):51, 1999.

[11] S. N. Paglieri and J. D. Way. *Separ. Purif. Rev.*, 31(1):1, 2002.

[12] Ø. Hatlevik, S. K. Gade, M. K. Keeling, P. M. Thoen, A. P. Davidson, and J. D. Way. *Separ. Purif. Method.*, 73(1):59, 2010.

[13] P. Henry. *Palladium Catalyzed Oxidation of Hydrocarbons*. Springer, 1980.

[14] B. K. Warren and S. T. Oyama. *Heterogeneous hydrocarbon oxidation.* American Chemical Society, 1996.

[15] G. Centi. *J. Mol. Catal. A: Chem.*, 173(1-2):287, 2001.

[16] R.M. Heck and R.J. Farrauto. *Catalytic Air Pollution Control: Commercial Technology.* Van Nostrand Reinhold, 3 edition, 2009.

[17] A. F. Sammells and M. V. Mundschau, editors. *Nonporous Inorganic Membranes: for Chemical Processing*, chapter 3. Wiley, 2006.

[18] R. Dittmeyer, V. Höllein, and K. Daub. *J. Mol. Catal. A*, 173(1-2):135, 2001.

[19] D. Fort, J. P. G. Farr, and I. R. Harris. *J. Less Common Met.*, 39(2):293, 1975.

[20] J. N. Keuler and L. Lorenzen. *J. Membr. Sci.*, 195(2):203, 2002.

[21] A. L. Mejdell, H. Klette, A. Ramachandran, A. Borg, and R. Bredesen. *J. Membr. Sci.*, 307:96, 2008.

[22] W. M. Tucho, H. J. Venvik, M. Stange, J. C. Walmsley, R. Holmestad, and R. Bredesen. *Sep. Purif. Technol.*, 68:403, 2009.

[23] A. L. Mejdell, D. Chen, T. A. Peters, R. Bredesen, and H. J. Venvik. *J. Membr. Sci.*, 350:371, 2010.

[24] A. Ramachandran, W. M. Tucho, A. L. Mejdell, M. Stange, H. J. Venvik, J. C. Walmsley, R. Holmestad, R. Bredesen, and A. Borg. *Appl. Surf. Sci.*, 256:6121, 2010.

[25] F. Roa and J. D. Way. *Appl. Surf. Sci.*, 240(1-4):85, 2005.

[26] S. K. Gade, P. M. Thoen, and J. D. Way. *J. Membrane Sci.*, 316(1-2):112, 2008.

[27] P. T. Wouda, M. Schmid, B.E. Nieuwenhuys, and P. Varga. *Surf. Sci.*, 417(2-3):292, 1998.

[28] J. R. Kitchin, K. Reuter, and M. Scheffler. *Phys. Rev. B*, 77:075437, 2008.

[29] B. C. Khanra and M. Menon. *Physica B*, 291(3-4):368, 2000.

[30] M. Ropo, K. Kokko, L. Vitos, and J. Kollár. *Phys. Rev. B*, 71:045411, 2005.

[31] M. Ropo. *Phys. Rev. B*, 74:195401, 2006.

[32] O. M. Løvvik. *Surf. Sci.*, 583(1):100, 2005.

[33] H. Y. Kim, H. G. Kim, J. H. Ryu, and H. M. Lee. *Phys. Rev. B*, 75:212105, 2007.

[34] S. González, K. M. Neyman, S. Shaikhutdinov, H.-J. Freund, and F. Illas. *J. Phys. Chem. C*, 111(18):6852, 2007.

[35] T. Marten, O. Hellman, A. V. Ruban, W. Olovsson, C. Kramer, J. P. Godowski, L. Bech, Z. Li, J. Onsgaard, and I. A. Abrikosov. *Phys. Rev. B*, 77:125406, 2008.

[36] D. Tománek, S. Mukherjee, V. Kumar, and K. H. Bennemann. *Surf. Sci.*, 114(1):11, 1982.

[37] L. C. A. van den Oetelaar, O. W. Nooij, S. Oerlemans, A. W. Denier van der Gon, H. H. Brongersma, L. Lefferts, A. G. Roosenbrand, and J. A. R. van Veen. *J. Phys. Chem. B*, 102(18):3445, 1998.

[38] P. T. Wouda, M. Schmid, B. E. Nieuwenhuys, and P. Varga. *Surf. Sci.*, 423(1):229, 1999.

[39] I.-H. Svenum, J. A. Herron, M. Mavrikakis, and H. J. Venvik. *Catal. Today*, 193(1):111, 2012.

[40] J. Shu, B. E. W. Bongondo, B. P. A. Grandjean, A. Adnot, and S. Kaliaguine. *Surf. Sci.*, 291(1-2):129, 1993.

[41] O. M. Løvvik and R. A. Olsen. *J. Chem. Phys*, 118(7):3268–3276, 2003.

[42] O. M. Løvvik and S. M. Opalka. *Surf. Sci.*, 602(17):2840, 2008.

[43] H. Over, Y. D. Kim, A. P. Seitsonen, S. Wendt, E. Lundgren, M. Schmid, P. Varga, A. Morgante, and G. Ertl. *Science*, 287(5457):1474, 2000.

[44] B. L. M. Hendriksen and J. W. M. Frenken. *Phys. Rev. Lett.*, 89:046101, 2002.

[45] B. L. M. Hendriksen, S. C. Bobaru, and J. W. M. Frenken. *Surf. Sci.*, 552(1-3):229, 2004.

[46] M. D. Ackermann, T. M. Pedersen, B. L. M. Hendriksen, O. Robach, S. C. Bobaru, I. Popa, C. Quiros, H. Kim, B. Hammer, S. Ferrer, and J. W. M. Frenken. *Phys. Rev. Lett.*, 95:255505, 2005.

[47] J. Aßmann, D. Crihan, M. Knapp, E. Lundgren, E. Löffler, M. Muhler, V. Narkhede, H. Over, M. Schmid, A. P. Seitsonen, and P. Varga. *Angew. Chem. Int. Ed.*, 44(6):917, 2005.

[48] Y. B. He, M. Knapp, E. Lundgren, and H. Over. *J. Phys. Chem. B*, 109(46):21825, 2005.

[49] P.-A. Carlsson, V. P. Zhdanov, and M. Skoglundh. *Phys. Chem. Chem. Phys.*, 8:2703, 2006.

[50] M. A. Newton, A. J. Dent, S. Diaz-Moreno, S. G. Fiddy, B. Jyoti, and J. Evans. *Chem. Eur. J.*, 12(7), 2006.

[51] R. Westerström, J. G. Wang, M. D. Ackermann, J. Gustafson, A. Resta, A. Mikkelsen, J. N. Andersen, E. Lundgren, O. Balmes, X. Torrelles, J. W. M. Frenken, and B. Hammer. *J. Phys.: Condens. Matter*, 20(18):184018, 2008.

[52] M. E. Grass, Y. Zhang, D. R. Butcher, J. Y. Park, Y. Li, H. Bluhm, K. M. Bratlie, T. Zhang, and G. A. Somorjai. *Angew. Chem. Int. Ed.*, 47(46):8893, 2008.

[53] J. Gustafson, R. Westerström, A. Mikkelsen, X. Torrelles, O. Balmes, N. Bovet, J. N. Andersen, C. J. Baddeley, and E. Lundgren. *Phys. Rev. B*, 78:045423, 2008.

[54] J. Gustafson, R. Westerström, A. Resta, A. Mikkelsen, J. N. Andersen, O. Balmes, X. Torrelles, M. Schmid, P. Varga, and B. Hammer. *Catal. Today*, 145(3-4):227, 2009.

[55] H. Over, O. Balmes, and E. Lundgren. *Catal. Today*, 145(3-4):236, 2009.

[56] J. Gustafson, R. Westerström, O. Balmes, A. Resta, R. van Rijn, X. Torrelles, C. T. Herbschleb, J. W. M. Frenken, and E. Lundgren. *J. Phys. Chem. C*, 114(10):4580, 2010.

[57] R. van Rijn, O. Balmes, R. Felici, J. Gustafson, D. Wermeille, R. Westerström, E. Lundgren, and J. W. M. Frenken. *J. Phys. Chem. C*, 114(14):6875, 2010.

[58] J. Rogal, K. Reuter, and M. Scheffler. *Phys. Rev. Lett.*, 98:046101, 2007.

[59] J. Rogal, K. Reuter, and M. Scheffler. *Phys. Rev. B*, 75(20):205433, 2007.

[60] R. W. G. Wyckoff. *Crystal structures*, volume 1. Interscience Publ., 1964.

[61] D. R. Lide. *CRC Handbook of Chemistry and Physics: A Ready-reference Book of Chemical and Physical Data*. CRC Press, 2004.

[62] T. W. Orent and S. D. Bader. *Surf. Sci.*, 115:323, 1982.

[63] G. Zheng and E. I. Altman. *J. Phys. Chem. B*, 106(5):1048, 2002.

[64] D. T. Vu, K. A. R. Mitchell, O. L. Warren, and P. A. Thiel. *Surf. Sci.*, 318:129, 1994.

[65] M. Saidy, O. L. Warren, P. A. Thiel, and K. A. R. Mitchell. *Surf. Sci.*, 494:L799, 2001.

[66] M. Todorova, E. Lundgren, V. Blum, A. Mikkelsen, S. Gray, J. Gustafson, M. Borg, J. Rogal, K. Reuter, J. N. Andersen, and M. Scheffler. *Surf. Sci.*, 541:101, 2003.

[67] P. Kostelník, N. Seriani, G. Kresse, A. Mikkelsen, E. Lundgren, V. Blum, T. Šikola, P. Varga, and M. Schmid. *Surf. Sci.*, 601(6):1574, 2007.

[68] E. Lundgren, J. Gustafson, A. Mikkelsen, J. N. Andersen, A. Stierle, H. Dosch, M. Todorova, J. Rogal, K. Reuter, and M. Scheffler. *Phys. Rev. Lett.*, 92:046101, 2004.

[69] R. Westerström, M. E. Messing, S. Blomberg, A. Hellman, H. Grönbeck, J. Gustafson, N. M. Martin, O. Balmes, R. van Rijn, J. N. Andersen, K. Deppert, H. Bluhm, Z. Liu, M. E. Grass, M. Hävecker, and E. Lundgren. *Phys. Rev. B*, 83:115440, 2011.

[70] R. Feenstra, R. Griessen, and D. G. de Groot. *J. Phys. F: Metal Phys.*, 16(12):1933, 1986.

[71] T. McMullen, M. J. Stott, and E. Zaremba. *Phys. Rev. B*, 35:1076, 1987.

[72] W. Zhong, Y. Cai, and D. Tománek. *Phys. Rev. B*, 46:8099, Oct 1992.

[73] E. Salomons, H. Hemmes, and R. Griessen. *J. Phys.: Condens. Matter*, 2(4):817, 1990.

[74] L. Vegard. *Z. Phys.*, 5(1):17, 1921.

[75] L. Vegard. *Z. Kristallogr.*, 67(2):239, 1928.

[76] L. E. Walle, H. Grönbeck, V. R. Fernandes, S. Blomberg, M. H. Farstad, K. Schulte, J. Gustafson, J. N. Andersen, E. Lundgren, and A. Borg. *Surf. Sci.*, 606(23-24):1777, 2012.

[77] V. R. Fernandes, J. Gustafson, I.-H. Svenum, M. H. Farstad, L. E. Walle, S. Blomberg, E. Lundgren, and A. Borg. *Surf. Sci.*, 621(1):31, 2014.

[78] S. Ouannasser, J. Eugène, H. Dreyssé, C. Wolverton, and D. de Fontaine. *Surf. Sci.*, 307:826, 1994.

[79] L. Z. Mezey and J. Giber. *Jpn. J. Appl. Phys.*, 21(Part 1, No. 11):1569, 1982.

[80] L. Z. Mezey and J. Giber. *Surf. Sci.*, 117:220, 1982.

[81] H. L. Skriver and N. M. Rosengaard. *Phys. Rev. B*, 46:7157, 1992.

[82] M. Methfessel, D. Hennig, and M. Scheffler. *Phys. Rev. B*, 46:4816, Aug 1992.

[83] L. Vitos, A. V. Ruban, H. L. Skriver, and J. Kollár. *Surf. Sci.*, 411(1-2):186, 1998.

[84] A. V. Ruban, S. I. Simak, P. A. Korzhavyi, and B. Johansson. *Phys. Rev. B*, 75:054113, 2007.

[85] D. P. Woodruff and T. A. Delchar. *Modern techniques of Surface Science*. Cambridge University Press, Cambridge, 2 edition, 1994.

[86] A. Zangwill. *Physics at Surfaces*. Cambridge University Press, Cambridge, 1988.

[87] D. R. Penn. *J. Electron. Spectrosc. Relat. Phenom.*, 9(1):29, 1976.

[88] D. R. Penn. *Phys. Rev. B*, 13:5248, 1976.

[89] D. R. Penn. *J. Vac. Sci. Technol.*, 13(1):221, 1976.

[90] H. Hertz. *Annalen der Physik*, 267(8):983, 1887.

[91] A. Einstein. *Annalen der Physik*, 322(6):132, 1905.

[92] K. Siegbahn, C. Nordling, A. Fahlman, R. Nordberg, K. Hamrin, J. Hedman, G. Johansson, T. Bergmark, S.-E. Karlsson, and I. Lindgren. *Nova Acta Regiae Soc. Sci. Upsaliensis, Ser. IV, (Almquist & Wiksell, Uppsala, 1967), Vol. 20.*, 1967.

[93] F. Reinert and S. Hüfner. *New Journal of Physics*, 7(1):97, 2005.

[94] S. Hüfner. *Photoelectron spectroscopy: principles and applications*. Springer-Verlag, 1996.

[95] K. S. Kim and N. Winograd. *Chem. Phys. Lett.*, 30(1):91, 1975.

[96] H. J. Lewerenz. *Photons in Natural and Life Sciences: An Interdisciplinary Approach*. Springer, 2012.

[97] S. P. Kowalczyk, L. Ley, R. L. Martin, F. R. McFeely, and D. A. Shirley. *Faraday Discuss. Chem. Soc.*, 60:7, 1975.

[98] S. Kohiki. *Spectrochi. Acta B*, 54(1):123, 1999.

[99] A. M. Venezia. *Catal. today*, 77(4):359, 2003.

[100] E. Madelung. *Physikalische Zeitschrift*, 19:524, 1918.

[101] K. Hübner. *Phys. Status Solidi A*, 42(2):501, 1977.

[102] R. E. Crandall and J. F. Delord. *J. Phys. A: Math. Gen.*, 20(9):2279, 1987.

[103] M. J. Guittet, J. P. Crocombette, and M. Gautier-Soyer. *Phys. Rev. B*, 63:125117, 2001.

[104] N. F. Mott and R. W. Gurney. *Electronic processes in ionic crystals*. Clarendon Press, 1948.

[105] S. Doniach and M. Šunjić. *J. Phys. C: Solid State Phys.*, 3(2):285, 1970.

[106] J. W. Gadzuk and M. Šunjić. *Phys. Rev. B*, 12:524, 1975.

[107] S. Hüfner and G. K. Wertheim. *Phys. Rev. B*, 11:678, 1975.

[108] D. C. Langreth. *Phys. Rev. Lett.*, 54:126, 1985.

[109] F. de Groot and A. Kotani. *Core Level Spectroscopy of Solids*. Taylor & Francis, 2008.

[110] G. Rupprechter and C. Weilach. *Nano Today*, 2(4):20, 2007.

[111] G. Rupprechter and C. Weilach. *J. Phys.: Condens. Matter*, 20(18):184019, 2008.

[112] K. Siegbahn, C. Nordling, G. Johansson, J. Hedman, P. F. Heden, K. Hamrin, U. Gelius, T. Bergmark, L. O. Werme, R. Manne, and Y. Baer. *ESCA applied to free molecules*. North-Holland Pub. Co., 1969.

[113] H. Siegbahn and K. Siegbahn. *J. Electron Spectrosc. Relat. Phenom.*, 2(3):319, 1973.

[114] R. W. Joyner, M. W. Roberts, and K. Yates. *Surf. Sci.*, 87(2):501, 1979.

[115] H. Siegbahn. *J. Phys. Chem.*, 89(6):897, 1985.

[116] H. J. Ruppender, M. Grunze, C. W. Kong, and M. Wilmers. *Surf. Interface Anal.*, 15(4):245, 1990.

[117] M. Grunze, D. J. Dwyer, M. Nassir, and Y. Tsai. *Controlled-Atmosphere Photoelectron Spectroscopy*, chapter 12, page 169. American Chemical Society, 1992.

[118] D. F. Ogletree, H. Bluhm, D. H. Eleonore, and M. Salmeron. *Nucl. Instr. Meth. Phys. Res. A*, 601(1):151, 2009.

[119] M. E. Grass, P. G. Karlsson, F. Aksoy, M. Lundqvist, B. Wannberg, B. S. Mun, Z. Hussain, and Z. Liu. *Rev. Sci. Instrum.*, 81(5):053106, 2010.

[120] R. Chang, Y. P. Hong, S. Axnanda, B. Mao, N. Jabeen, S. Wang, R. Tai, and Z. Liu. *Curr. Appl. Phys.*, 12(5):1292, 2012.

[121] J. Schnadt, J. Knudsen, J. N. Andersen, H. Siegbahn, A. Pietzsch, F. Hennies, N. Johansson, N. Mårtensson, G. Öhrwall, S. Bahr, S. Mähl, and O. Schaff. *J. Synchrotron Rad.*, 19(5):701, 2012.

[122] S. Kaya, H. Ogasawara, L.-Å. Näslund, J.-O. Forsell, H. S. Casalongue, D. J. Miller, and A. Nilsson. *Catal. Today*, 205:101, 2013.

[123] M. Salmeron and R. Schlögl. *Surf. Sci. Rep.*, 63(4):169, 2008.

[124] R. Shankar. *Principles of quantum mechanics*. Springer, 2 edition.

[125] J. N. Andersen and C.-O. Almbladh. *J. Phys.: Condens. Matter*, 13(49):11267, 2001.

[126] G. D. Mahan. *Phys. Rev.*, 163:612, 1967.

[127] P. Nozières and C. T. De Dominicis. *Phys. Rev.*, 178:1097, 1969.

[128] S. Hüfner, G. K. Wertheim, D. N. E. Buchanan, and K. W. West. *Phys. Lett. A*, 46(6):420, 1974.

[129] D. A. Shirley. *Phys. Rev. B*, 5:4709, 1972.

[130] S. Tougaard. *Surf. Sci.*, 216(3):343, 1989.

[131] S. Tougaard and C. Jansson. *Surf. Interface Anal.*, 20(13):1013, 1993.

[132] G. Leclerc and J. J. Pireaux. *J. Electron Spectrosc. Relat. Phenom.*, 71(2):141, 1995.

[133] J. D. Jackson. *Classical Electrodynamics*. Wiley, 1998.

[134] D. Attwood. *Soft X-Rays and Extreme Ultraviolet Radiation*. Cambridge University Press, 1999.

[135] A. Hofmann. *The Physics of Synchrotron Radiation*. Cambridge University Press, 2004.

[136] R. Nyholm, J. N. Andersen, U. Johansson, B. N. Jensen, and I. Lindau. *Nucl. Instr. and Meth. in Phys. Res. A*, 467-468, Part 1:520, 2001.

[137] C. Davisson and L. H. Germer. *Phys. Rev.*, 30:705, 1927.

[138] C. Davisson and L. H. Germer. *Nature*, 119:558, 1927.

[139] L. de Broglie. *Nature*, 112:540, 1923.

[140] E. J. Scheibner, L. H. Germer, and C. D. Hartman. *Rev. Sci. Instrum.*, 31(2):112, 1960.

[141] L. J. Clarke. *Surface Crystallography: An Introduction to Low Energy Electron Diffraction*. John Wiley & Sons, 1985.

[142] M. A. van Hove, W. H. Weinberg, and C.-M. Chan. *Low-Energy Electron Diffraction. Experiment, Theory and Surface Structure Determinations*. Springer, 1986.

[143] K. Oura, V. G. Lifshits, A. A. Saranin, A. V. Zotov, and M. Katayama. *Surface Science: An Introduction*. Springer, 2003.

[144] F. Bechstedt. *Principles of surface physics*. Springer, 2003.

[145] E. A. Wood. *J. Appl. Phys.*, 35(4):1306, 1964.

[146] M. Razavy. *Quantum Theory of Tunneling*. World Scientific, 2003.

[147] L. Esaki. *Proceedings of the IEEE*, 62(6):825, 1974.

[148] G. Binnig, H. Rohrer, Ch. Gerber, and E. Weibel. *Appl. Phys. Lett.*, 40(2):178, 1982.

[149] G. Binnig, H. Rohrer, Ch. Gerber, and E. Weibel. *Phys. Rev. Lett.*, 49:57, 1982.

[150] G. Binnig and H. Rohrer. *Surf. Sci.*, 126(1-3):236, 1983.

[151] R. Wiesendanger. *Scanning Probe Microscopy and Spectroscopy: Methods and Applications*. Cambridge University Press, 1994.

[152] A. S. Foster, W. A. Hofer, and A. L. Shluger. *Current Opinion in Solid State and Materials Science*, 5(5):427, 2001.

[153] Theories of scanning probe microscopes at the atomic scale. *Rev. Mod. Phys.*, 75:1287, 2003.

[154] L. V. Keldysh. *Sov. Phys. JETP*, 20(4):1018, 1965.

[155] Y. Meir and N. S. Wingreen. *Phys. Rev. Lett.*, 68(16):2512, 1992.

[156] K. Palotás and W. A. Hofer. *J. Phys.: Condensed Matter*, 17(17):2705, 2005.

[157] A. Foster and W. Hofer. *Scanning Probe Microscopy: Atomic Scale Engineering by Forces and Currents*. Springer, 2006.

[158] J. Tersoff and D. R. Hamann. *Phys. Rev. B*, 31:805, 1985.

[159] J. Bardeen. *Phys. Rev. Lett.*, 6:57, 1961.

[160] P. K. Hansma and J. Tersoff. *J. Appl. Phys.*, 61(2):R1, 1987.

[161] A. Bryant, D. P. E. Smith, and C. F. Quate. *Appl. Phys. Lett.*, 48(13):832, 1986.

[162] R. M. Feenstra, W. A. Thompson, and A. P. Fein. *Phys. Rev. Lett.*, 56:608, 1986.

[163] R. M. Feenstra and J. A. Stroscio. *Phys. Scr.*, 1987(T19A):55, 1987.

[164] P. J. Bryant, H. S. Kim, Y. C. Zheng, and R. Yang. *Rev. Sci. Instrum.*, 58(6):1115, 1987.

[165] Courtesy of Edvin Lundgren, Lund University, Lund, Sweden.

[166] A. R. Denton and N. W. Ashcroft. *Phys. Rev. A*, 43:3161, 1991.

[167] H. J. Axon and W. Hume-Rothery. *Proc. R. Soc. Lond. A*, 193:1, 1948.

[168] W. Hume-Rothery, R. E. Smallman, and C. W. Haworth. *The structure of metals and alloys*, volume 1. Metals & Metallurgy Trust, 1969.

[169] W. C. Wien. *Verhandlungen der Physikalischen Gesellschaft zu Berlin*, 17:10, 1898.

[170] J. J. Thomson. *Philosophical Magazine Series 6*, 21(122):225, 1911.

[171] J. J. Thomson. *Philosophical Magazine Series 6*, 24(140):209, 1912.

[172] J. J. Thomson. *Rays of Positive Electricity and Their Application to Chemical Analysis*. Longmans Green, London, 1913.

[173] W. Paul and H. Steinwedel. *Z. Naturforsch.*, 8a:448, 1953.

[174] J. E. Campana. *Int. J. Mass Spectrom. Ion Phys.*, 33(2):101, 1980.

[175] P. E. Miller and M. B. Denton. *J. Chem. Educ.*, 63(7):617, 1986.

[176] P. E. Miller and M. B. Denton. *Int. J. Mass Spectrom. Ion Process.*, 72(3):223, 1986.

[177] R. E. March. *J. Mass Spectrom.*, 32(4):351, 1997.

[178] R. E. March and J. F. Todd. *Quadrupole Ion Trap Mass Spectrometry*. Wiley, 2005.

[179] E. de Hoffmann and V. Stroobant. *Mass Spectrometry: Principles and Applications*. Wiley, 2007.

[180] M.E. Brown, D. Dollimore, and A.K. Galwey. *Reactions in the Solid State*, volume 22 of *Comprehensive Chemical Kinetics*. Elsevier Science, 1980.

[181] J. W. Christian. *The Theory of Transformations in Metals and Alloys: Part I*. Pergamon Press, 3 edition, 2002.

[182] J. Šesták. *Science of Heat and Thermophysical Studies A Generalized Approach to Thermal Analysis*. Elsevier Science, 2005.

[183] J. Málek. *Thermochim. Acta*, 138(2):337, 1989.

[184] J. Málek. *J. Therm. Anal. Calorim.*, 56(2):763, 1999.

[185] J. Šesták and G. Berggren. *Thermochim. Acta*, 3:1, 1971.

[186] V. M. Gorbachev. *J. Therm. Anal. Calorim.*, 18(1):193, 1980.

[187] P. Šimon. *Thermochim. Acta*, 520(1-2):156, 2011.

[188] J. Málek, J. M. Criado, J. Šesták, and J. Militký. *Thermochim. Acta*, 153:429, 1989.

[189] J. Šesták and J. Málek. *Solid State Ionics*, 63:245, 1993.

[190] Andrew R. Leach. *Molecular Modelling: Principles and Applications*. Prentice Hall, 2001.

[191] P. Hohenberg and W. Kohn. *Phys. Rev.*, 136:B864, 1964.

[192] W. Kohn and L. J. Sham. *Phys. Rev.*, 140:A1133, 1965.

[193] C. Lee, W. Yang, and R. G. Parr. *Phys. Rev. B*, 37:785, 1988.

[194] J. P. Perdew and Y. Wang. *Phys. Rev. B*, 45:13244, 1992.

[195] J. P. Perdew, J. A. Chevary, S. H. Vosko, K. A. Jackson, M. R. Pederson, D. J. Singh, and C. Fiolhais. *Phys. Rev. B*, 46:6671, 1992.

[196] J. P. Perdew, K. Burke, and M. Ernzerhof. *Phys. Rev. Lett.*, 77:3865, 1996.

[197] J. Tao, J. P. Perdew, V. N. Staroverov, and G. E. Scuseria. *Phys. Rev. Lett.*, 91:146401, 2003.

[198] E. Engel and R. M. Dreizler. *Density Functional Theory: An Advanced Course*. Springer, 2011.

[199] J. Klimes and A. Michaelides. *J. Chem. Phys.*, 137(12):120901, 2012.

[200] R. G. Parr and W. Yang. *Density-functional theory of atoms and molecules*. Oxford university press, 1989.

[201] R. M. Martin. *Electronic Structure: Basic Theory and Practical Methods*. Cambridge University Press, 2008.

[202] W. Kohn. *Rev. Mod. Phys.*, 71:1253, 1999.

[203] P. Geerlings, F. De Proft, and W. Langenaeker. *Chem. Rev.*, 103(5):1793, 2003.

[204] K. Burke. *J. Chem. Phys.*, 136(15):150901, 2012.

Part II

Papers

Paper I

Surface composition of clean and oxidized Pd$_{75}$Ag$_{25}$(100) from photoelectron spectroscopy and density functional theory calculations

L.E. Walle, H. Grönbeck, V.R. Fernandes, S. Blomberg, M.H. Farstad, K. Schulte, J. Gustafson, J. N. Andersen c, d, E. Lundgren, A. Borg

Contents lists available at SciVerse ScienceDirect

Surface Science

journal homepage: www.elsevier.com/locate/susc

Surface composition of clean and oxidized $Pd_{75}Ag_{25}(100)$ from photoelectron spectroscopy and density functional theory calculations

L.E. Walle [a], H. Grönbeck [b], V.R. Fernandes [a], S. Blomberg [c], M.H. Farstad [a], K. Schulte [d], J. Gustafson [c], J.N. Andersen [c,d], E. Lundgren [c], A. Borg [a,*]

[a] Dept. of Physics, Norwegian Univ. of Science and Technology, NO-7491 Trondheim, Norway
[b] Competence Centre for Catalysis and Dept. of Applied Physics, Chalmers Univ. of Technology, SE-412 96 Göteborg, Sweden
[c] Div. of Synchrotron Radiation Research, Lund Univ., Box 117, SE-221 00 Lund, Sweden
[d] MAX IV Laboratory, Lund Univ., Box 118, SE-221 00 Lund, Sweden

ARTICLE INFO

ABSTRACT

High resolution photoelectron spectroscopy and density functional theory calculations have been used to study the composition of clean and oxidized $Pd_{75}Ag_{25}(100)$. The results for the clean surface confirm earlier reports of surface segregation by Wouda et al. (1998), where the top most layers are rich in Ag. The Pd 3d core level component from the surface region is observed at higher binding energies than the contribution from the bulk which is found to be a signature of Pd embedded in Ag. Low energy electron diffraction and scanning tunneling microscopy measurements reveal that oxidation of the $Pd_{75}Ag_{25}(100)$ surface results in a $\left(\sqrt{5} \times \sqrt{5}\right)R27°$-O structure similar to the one reported for Pd(100). The calculations suggest that the stable structure is a PdO(101) monolayer supported on a (100) surface rich in Ag at the interface to the stoichiometric alloy. The calculated core level shifts for the oxidized surface are in good agreement with the experimental observations.

1. Introduction

Palladium has high solubility, permeability and selectivity for hydrogen, thus being a suitable membrane material for hydrogen separation. To prevent embrittlement occurring in pure Pd due to formation of hydride phases [1,2], Pd-based alloys are often utilized in membrane applications. Alloying palladium with silver has been found to increase the permeability and durability of the membrane, with a maximum permeability at 23 wt.% Ag [3]. Moreover, heat treatment of Pd/Ag alloy membranes in air has been reported to enhance the hydrogen permeation [4–7]. Formation of a surface oxide is part of this picture [8]. Recently, it has also been reported that surface oxide formation on Pd/Ag membrane surfaces may reduce the inhibition effect of CO on the hydrogen permeation of such membranes [9]. However, full understanding of the thermal treatment effects is still lacking. In the present work, we investigate the $Pd_{75}Ag_{25}(100)$ surface as a Pd/Ag alloy model system to address surface composition and oxide formation.

The composition of alloy surfaces affects their physical and chemical behaviors. Understanding and controlling these properties are essential for applications. For the Pd/Ag alloy system lowering surface energy favors a silver terminated surface. The surface composition and segregation profile of Pd/Ag alloys have been subject of a number

of experimental and theoretical investigations [10–18]. Wouda et al. [11], applying scanning tunneling microscopy (STM), determined the surface composition at the atomic level of the clean (111) and (100) surfaces of a $Pd_{67}Ag_{33}$ alloy as a function of annealing temperature in the range of 720–920 K. On $Pd_{67}Ag_{33}(111)$, a Pd surface concentration of 5–11% was observed with a tendency of isolated palladium sites. In comparison, the palladium concentration on $Pd_{67}Ag_{33}(100)$ was found to be extremely low except when the system was forced into non-equilibrium. Theoretical calculations have shown a first layer surface composition of (111) oriented 50/50 alloys varying from 100% Ag at 0 K to 72% at 1200 K with a corresponding Pd enrichment in the second layer ranging from 100% at 0 K to 66% at 1200 K [17]. Similar trends were reported for alloys with silver content varying from 10% to 100% [18], namely silver enrichment in the outermost surface layer and depletion in the second layer as compared to the stoichiometric alloy composition.

On the close-packed (111) and (100) surfaces of pure palladium ordered oxygen induced phases are formed prior to onset of bulk oxide formation. Exposing Pd(111) to oxygen above 300 K yields three ordered surface structures [19–24], a p(2×2) oxygen overlayer at a coverage of 0.25 ML, a high coverage metastable structure [22] and a complex almost coplanar, two-dimensional Pd_5O_4 oxide overlayer [24–26]. Turning to the Pd(100) surface, four different oxygen induced structures at coverages below 1 ML are identified, namely p(2×2), c(2×2), p(5×5) and $\left(\sqrt{5} \times \sqrt{5}\right)R27°$ [27,28]. The latter of these structures has been subject to detailed investigations over the

years [29–33]. From a combination of experimental investigations and theoretical modeling [31,32], the $\left(\sqrt{5} \times \sqrt{5}\right)$R27° structure is known to be a PdO(101) monolayer on top of the underlying Pd(100) substrate. Evidence for similar oxides being formed on single crystal Pd/Ag alloy surfaces has not been reported.

In the present work, high resolution photoelectron spectroscopy (HR-PES) measurements and density functional theory (DFT) calculations have been used to explore the surface chemical composition for the clean and oxidized Pd$_{75}$Ag$_{25}$(100) surface. Our combined investigation strongly supports the findings in Ref. [11] for the clean surface. Furthermore, by comparing to the $\left(\sqrt{5} \times \sqrt{5}\right)$R27° surface oxide structure formed on Pd(100), strong evidence is reported for formation of a similar ordered Pd-oxide on the Pd$_{75}$Ag$_{25}$(100) surface upon exposure to molecular oxygen at elevated temperatures. This conclusion is supported by low energy electron diffraction (LEED) and STM measurements. Moreover, the present investigation suggests that the layer below the $\left(\sqrt{5} \times \sqrt{5}\right)$R27° structure consists mostly of Ag. The effect of oxide formation on the durability of PdAg membranes is briefly discussed.

2. Experimental methods

High-resolution photoelectron spectroscopy experiments were performed at beam line I311 of MAX-lab, the Swedish national synchrotron facility in Lund, Sweden. This beam line is equipped with a modified SX-700 monochromator and a large Scienta type hemispherical electron energy analyzer (SCIENTA SES200) [34]. The base pressure in the UHV system was $<2 \times 10^{-10}$ mbar. Complementary STM investigations were performed applying a commercial, room temperature Omicron UHV STM1 system.

Pd$_{75}$Ag$_{25}$(100), Pd(100) and Ag(110) single crystals, the latter two studied for comparison,[1] were cleaned by cycles of sputtering, oxygen treatment and annealing to selected temperatures. An annealing temperature of 900 K was applied as standard for the Pd$_{75}$Ag$_{25}$(100) sample, while 980 K and 670 K were used for Pd(100) and Ag(110), respectively. This procedure gave well-defined, clean surfaces as judged from LEED patterns and photoemission measurements of the C 1s core level region.

The Pd 3d core level spectra were recorded at 400 eV and the Ag 3d levels at 450 eV yielding an overall spectral resolution of about 80 meV and 100 meV, respectively. O 1s spectra were measured at photon energy of 630 eV with a spectral resolution of 180 meV. All spectra were measured at normal emission. The binding energy was calibrated by recording the Fermi edge immediately after the core level regions. All spectra have been normalized to the background on the low binding energy side of the core level peaks. Linear background subtraction has been applied and Doniach-Sunjic line shapes used for fitting the spectra [35].

3. Computational method

DFT was employed in the implementation with plane-waves and pseudo-potentials [36,37]. The spin polarized Perdew–Burke–Ernzerhof (PBE) approximation [38] was used for the exchange and correlation (xc) functional and ultrasoft scalar-relativistic pseudo potentials [39] were used to describe the interaction between the valence electrons and the core. The number of electrons treated variationally for each element was Ag(11), Pd(10) and O(6). A plane-wave kinetic energy cut-off of 28 Ry was used to expand the Kohn–Sham orbitals. With this approach, the fcc lattice constants of Pd, Pd$_3$Ag, and Ag are calculated to be 3.93, 3.97 and 4.14 Å, respectively. The clean (100) surfaces were investigated in p(2×2) surface cells with ten atomic layers. The Ag(110) surface was considered in a

p(2×2) surface cell with eleven atomic layers. The $\left(\sqrt{5} \times \sqrt{5}\right)$R27° surface oxide was modeled with the PdO(101) monolayer supported on five atomic metal layers. Repeated slabs were in all cases separated by at least 12 Å of vacuum. Reciprocal space integration over the Brillouin zone was approximated with a finite sampling of 8 [6 for Ag(110)] special k-points by use of the Monkhorst-Pack scheme [40,41]. Structural optimization was performed without any constraints and the structures were regarded converged when the largest element of the gradient was lower than 0.05 eV/Å and the displacement smaller than 0.002 Å. All atoms in the cell were relaxed in order to reduce effects of strain in the evaluation of the core level shifts.

The surface core level shifts (SCLS) for Pd 3d, Ag 3d and O 1s levels were evaluated by the use of pseudo-potentials that were generated with an electron hole in respective shell [42]. With this methodology, shifts in core levels are calculated as total energy differences by placing the pseudo-potential with a core hole at different sites. For the metals, a core hole in the center of the slab was used to model the bulk reference. This approach includes initial as well as final state effects. Convergence tests with respect to plane-wave kinetic energy cut-off, k-point sampling and vacuum width were performed and the accuracy of the reported core level shifts (CLS) are found to be ~0.01 eV.

4. Results and discussion

4.1. Clean Pd$_{75}$Ag$_{25}$(100)

3d$_{5/2}$ core level spectra of Pd and Ag measured for the clean Pd$_{75}$Ag$_{25}$(100) surface are presented in Fig. 1 together with the corresponding spectra from Pd(100) and Ag(110), respectively. The Pd 3d$_{5/2}$ spectra for both Pd(100) and Pd$_{75}$Ag$_{25}$(100) have two contributions. Comparing the binding energy of the bulk contribution for the Pd/Ag alloy to elemental Pd, a shift of −0.12 eV to lower binding energy is observed. The Pd 3d$_{5/2}$ surface component for Pd(100) is shifted −0.47 eV with respect to the bulk component. This surface core level shift is in good agreement with previous reports [43,44]. In contrast, the Pd 3d$_{5/2}$ spectrum from Pd$_{75}$Ag$_{25}$(100) reveals a surface contribution of different nature located at a *higher* binding energy (+0.52 eV) relative to the bulk component (at 334.84 eV). Noteworthy is that this peak is broader in width as compared to the bulk contribution indicative of a mixed Pd environment.

Turning to the Ag 3d$_{5/2}$ core level spectra, Fig. 1c and d, one highly asymmetric contribution is observed for both Ag(110) and Pd$_{75}$Ag$_{25}$(100). However, the spectrum is broader for Pd$_{75}$Ag$_{25}$(100). The decomposition of these spectra into two contributions relies in part on our DFT calculations presented below. Comparing the fitted core level spectra gives for the bulk contribution a shift of −0.72 eV to lower binding energy for Pd$_{75}$Ag$_{25}$(100) as compared to pure Ag. Previous studies of Pd$_{1−x}$Ag$_x$ alloy thin films with $0 \leq x \leq 1$ have shown that the binding energy of the Ag 3d core levels varies linearly with the silver content [45]. A shift of −0.95 ± 0.05 eV to lower binding energy was reported upon changing from pure Ag to a Pd film with about 5% Ag.

We note that both the Pd and Ag 3d bulk contributions are shifted to lower binding energies for Pd$_{75}$Ag$_{25}$(100) compared to elemental Pd and Ag. This is remarkable in view of the electrostatic potential model that often has been used to interpret chemical shifts [46]. DFT calculations have, however, recently rationalized the observation in terms of final state effects and intra-atomic charge redistribution [47].

The surface component for Ag(110) is shifted to lower binding energies with respect to the bulk by −0.15 eV. The reversed trend is observed in the case of Pd$_{75}$Ag$_{25}$(100). For this surface, the stronger component at higher binding energy is associated with the surface contribution, shifted by +0.23 eV (to higher binding energy) relative to the bulk component. Similar relative spectral weight of the bulk and

---

[1] Though Ag(110) has a different surface orientation the bulk core level binding energy is independent of the surface orientation.
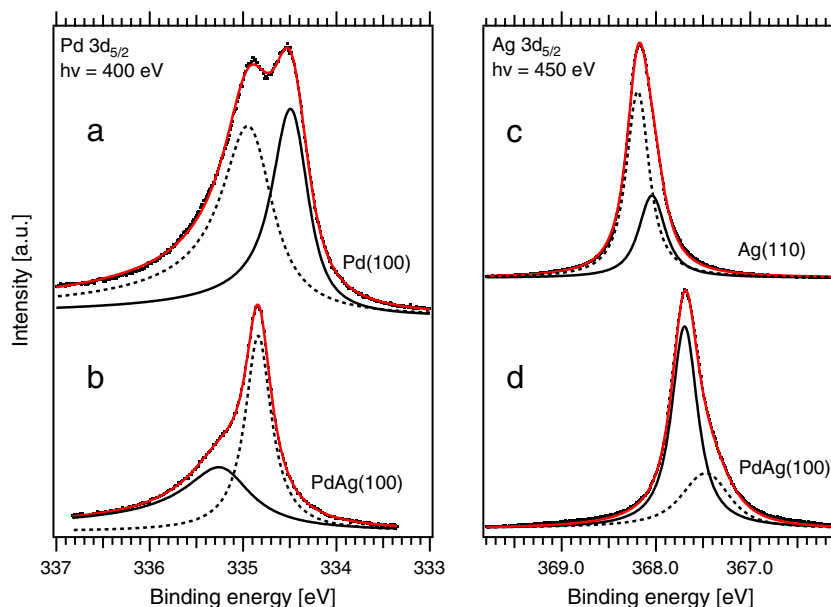
Fig. 1. Pd $3d_{5/2}$ spectra of a) clean Pd(100) and b) clean $Pd_{75}Ag_{25}$(100) measured at photon energy of 400 eV. Ag $3d_{5/2}$ spectra for c) the clean Ag(110) surface and d) the clean $Pd_{75}Ag_{25}$(100) surface, both measured at photon energy of 450 eV. Surface (bulk) components are reported with solid (dashed) lines.

surface components has previously been reported by Westerström et al. for a PtRh alloy where Pt segregates to the surface [48].

A set of model calculations was performed to understand why the surface components in the Pd 3d and Ag 3d spectra are shifted to lower binding energy in the case of the mono metallic surfaces, whereas the corresponding shifts are to higher binding energy for $Pd_{75}Ag_{25}$(100). The exact atomic composition in the surface region of the alloy is not known. However, the calculated surface energy[2] of Ag(100) is 49 eV/Å^2, whereas it is 100 eV/Å^2 for Pd(100) which implies that the surface is rich in Ag. Silver enrichment at the surface is, furthermore, indicated by the relative intensity of the Pd 3d and Ag 3d contributions measured after the annealing step. For the alloy, the Pd 3d intensity of the surface component is weaker than the bulk component, whereas the reversed situation applies for Ag 3d.

The models are selected in order to probe how enrichment of Ag at the surface affects SCLS. No attempt has been done to calculate the Ag concentration profile close to the surface from first principles. Schematic sketches of considered models are shown in Fig. 2. Model 1 has been constructed with a lattice constant that corresponds to pure Pd, Models 2–6 use the lattice constant of Pd_3Ag, whereas Models 7 and 8 use the lattice constant of elemental Ag. The choices are done so as to evaluate the bulk reference in a strain free environment. Explicit tests with varying the lattice constants indicate that the induced errors with the applied procedure are within ~0.1 eV.

It is possible with Model 1 to calculate the shift in Pd 3d binding energy between bulk Pd_3Ag and bulk Pd. We find that the bulk component of Pd_3Ag is shifted to lower binding energies by −0.19 eV, which is in good agreement with the experimental result. The SCLS of pure Pd(100) is calculated to be −0.36 eV, which is a slightly lower shift than the experimental. The SCLS for the alloy side of Model 1 has a clear negative shift with respect to the alloy bulk (−0.33 eV), which strongly suggests that the experimental $Pd_{75}Ag_{25}$(100) surface has another composition. Enrichment of Ag at the surface leads to a reduction of the shift (Models 2 and 3), however, it is still negative. A SCLS close to zero is calculated for the case with Pd in the second layer with a complete Ag surface layer (Model 4). Clear positive shifts are obtained for

models with Pd atoms close to the surface embedded in Ag (Models 5 and 6). The calculations show strong SCLS dependence on the silver environment of the Pd atoms in the surface region, which supports the broader surface component in the Pd $3d_{5/2}$ core level spectrum for $Pd_{75}Ag_{25}$(100).

The corrugated Ag(110) surface is calculated to have SCLS of −0.21 eV and −0.09 eV, with the lowest value for the outermost surface layer. The mean of these values (−0.15 eV) is in good agreement with the experimental shift. The shift of Ag 3d for the $Pd_{75}Ag_{25}$ alloy is investigated in Models 4, 7 and 8. The bulk component of the alloy is calculated to be shifted to lower binding energies by −0.77 eV with respect to the bulk component of elemental Ag. Furthermore, the calculations confirm that the surface is rich in Ag. A positive shift of the surface component with respect to the bulk alloy is present only in Model 4 (+0.30 eV), whereas a negative shift is predicted for a stoichiometric surface layer (Model 7). The shifts calculated for Model 8 (with respect to elemental Ag in this case) support this picture.
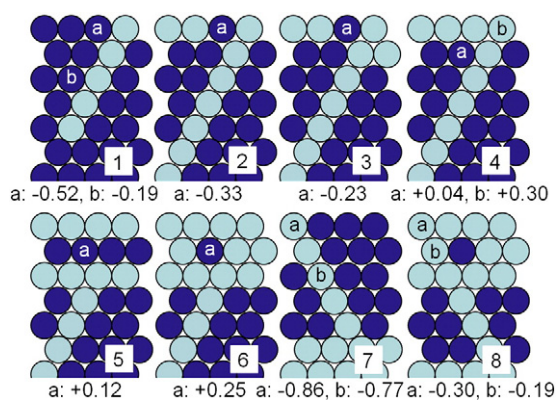

Fig. 2. Sketches of the models used to determine Pd 3d (Models 1–6) and Ag 3d (Models 4, 7, 8) SCLS. The calculations are done in p(2×2) surface cells with ten atomic layers. In order to show the elemental composition, the sketches display all atoms in each layer. The shifts for the indicated atoms are calculated with respect to an atom in bulk environment and reported in eV. Atomic color codes: Dark blue (Pd) and bright blue (Ag).

---

[2] The surface energy is calculated as $(E_{slab} - NE_{bulk})/2A$. E_{slab} and E_{bulk} are the total energies of the slab model and an atom in the bulk, respectively. N is the number of atoms in the slab and A is the surface area. The factor of 2 enters as the slab has two surfaces.

Our spectroscopic and calculated results for the observed core level shifts in the surface region of $Pd_{75}Ag_{25}(100)$ are consistent with the STM results by Wouda et al. reporting a silver terminated $Pd_{67}Ag_{33}(100)$ surface [11]. The shift to higher binding energy for the Pd $3d_{5/2}$ surface contribution of $Pd_{75}Ag_{25}(100)$ originates from such a surface termination. The DFT calculations show a range of chemical shifts both in the Pd 3d and Ag 3d core levels depending on the surface composition. Experimentally this is reflected in the wide features observed for some of the spectral contributions.

4.2. Oxidized $Pd_{75}Ag_{25}(100)$

On the Pd(100) surface, several surface oxide phases form at temperatures above 400 K, with the $\left(\sqrt{5} \times \sqrt{5}\right)$R27°-O being the phase occurring before three-dimensional oxide growth is initiated at higher pressures [28]. This structure can be described as a PdO(101) monolayer supported on the Pd(100) surface [31,32]. The Pd $3d_{5/2}$ core level spectrum for the $\left(\sqrt{5} \times \sqrt{5}\right)$R27°-O structure is displayed in Fig. 3a along with the corresponding LEED pattern shown in the inset. The three oxide induced contributions are four-fold coordinated (at binding energy of 336.22 eV), two-fold coordinated (at binding energy of 335.32 eV) and interface Pd atoms (at 334.66 eV) [31].

Exposing the Ag-terminated $Pd_{75}Ag_{25}(100)$ surface to oxygen at 600 K yields a photoemission spectrum shown in Fig. 3b and a corresponding LEED pattern, displayed in the inset, consistent with a $\left(\sqrt{5} \times \sqrt{5}\right)$R27° structure also formed on the Pd/Ag alloy surface. The photoemission spectrum contains two oxide induced contributions, shifted by +1.34 eV and +0.55 eV relative to the bulk contribution. The binding energies of these contributions are similar to those observed for the $\left(\sqrt{5} \times \sqrt{5}\right)$R27°-O structure on Pd(100). Noteworthy is that the interface component at lower binding energy observed in the case of Pd(100) is missing for $Pd_{75}Ag_{25}(100)$. In addition, the contribution due to two-fold coordinated Pd atoms has higher spectral weight compared to the four-fold contribution for $Pd_{75}Ag_{25}(100)$. The origin of this increased intensity is not fully understood. Chemisorbed oxygen on Pd atoms in the surface may contribute as may Pd atoms embedded in a silver rich layer underneath the surface oxide layer. Furthermore, photoelectron diffraction effects cannot be ruled out.

Our DFT-calculations show that the Pd–O distances in the PdO(101) are similar (within 0.01 Å) for the oxide on Pd(100) and $Pd_3Ag(100)$. However, the average metal–metal distance between the PdO(101) layer and the first unreconstructed surface layer is 2.95 Å for Pd(100) and 3.01 Å for $Pd_3Ag(100)$. This, together with possible differences in the scattering cross sections for Pd and Ag in the layer underneath the oxide, may affect the relative intensity of the oxide contributions. The corresponding O 1s spectra are displayed in Fig. 3c and d, for Pd(100) and $Pd_{75}Ag_{25}(100)$, respectively. In addition to the broad Pd 3p structure, two peaks at the low binding energy side reflecting the two different oxygen environments present for the $\left(\sqrt{5} \times \sqrt{5}\right)$R27° oxide can be observed for Pd(100), whereas one, broader main oxide contribution is observed for the same oxide structure on $Pd_{75}Ag_{25}(100)$. In the latter case an additional shoulder at ~529.50 eV is also present. The binding energies and corresponding core level shifts of the spectra in Fig. 3 are summarized in the left part of Table 1.

DFT calculations were performed to explore the composition of the oxidized $Pd_{75}Ag_{25}(100)$ surface in an unbiased manner. Using the $\left(\sqrt{5} \times \sqrt{5}\right)$R27°-O structure as initial structure, 25% of the Pd atoms were randomly replaced by Ag. In this way, about 100 structures were structurally relaxed. This approach was applied to get ideas about relevant structural motifs rather than actually finding the low energy structures, see Supplementary material for further details. It was found that the low energy structures were all composed of an PdO(101) layer and Ag at the interface towards the slab. This finding explains the lack of an interface component in the Pd $3d_{5/2}$ core level spectrum for the $\left(\sqrt{5} \times \sqrt{5}\right)$R27°-O structure on the $Pd_{75}Ag_{25}(100)$ surface.

On the basis of the calculated energetics, two models were considered for CLS calculations; the $\left(\sqrt{5} \times \sqrt{5}\right)$R27°-O structure on Pd(100), shown in Fig. 4a (top view) and Fig. 4c (side view), and a model for $Pd_{75}Ag_{25}(100)$ where the monolayer is PdO(101), the first unreconstructed layer is Ag and the rest is a stoichiometric Pd_3Ag alloy, illustrated in Fig. 4b (top view) and Fig. 4d (side view). The alloy system has been evaluated with the lattice constant of Pd_3Ag. The calculated CLS are summarized in the right part of Table 1.

For the oxidized surface of elemental Pd, the atoms in the first surface layer of Pd(100) are calculated to have shifts grouped at −0.2 eV and +0.2 eV with an average at −0.15 eV. Atoms in the surface
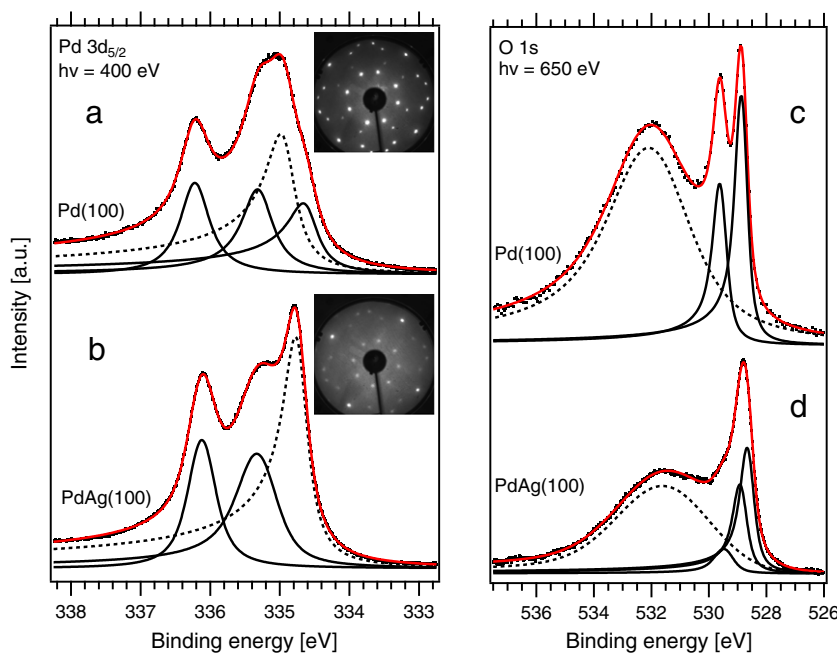

Fig. 3. Pd $3d_{5/2}$ and O 1s spectra from oxidized Pd(100) (upper panels) and $Pd_{75}Ag_{25}(100)$ (lower panels). Corresponding LEED patterns, showing $\left(\sqrt{5} \times \sqrt{5}\right)$R27° oxide structures formed on both surfaces, are displayed in the insets. Oxide induced components in the Pd $3d_{5/2}$ spectra in a) and b) are shown with solid lines, while bulk contributions are reported with dashed lines. In c) and d) the O 1s and Pd 3p contributions are shown with solid and dashed lines, respectively.

Table 1

Measured binding energies and measured and calculated core level shifts for the oxidized surfaces of Pd(100) and Pd$_{75}$Ag$_{25}$(100).

	Experimental				Theoretical core level shift (eV)	
	Binding energy (eV)		Core level shift (eV)			
	Pd 3d$_{5/2}$	O 1s	Pd 3d$_{5/2}$	O 1s	Pd 3d$_{5/2}$	O 1s
Pd(100)	334.98		0		0	
	334.66		−0.32		−0.15	
	335.32	528.88	0.34	0	0.4	0
	336.22	529.63	1.24	0.75	1.19	0.69
Pd$_{75}$Ag$_{25}$(100)	334.78		0		0	
	335.33	528.68	0.55	0	0.35	0
	336.12	528.93	1.34	0.25	1.17	0.24
		529.50		0.82		

oxide that are coordinated to two oxygen atoms have CLS of +0.33 and +0.45 eV, respectively. The Pd atoms that coordinate to four oxygen atoms have the largest shifts, namely +1.17 and +1.21 eV. The results are in good agreement with the experimental results, as well as previous theoretical reports [31].

For O 1s, the shift between the oxygen atoms close and far from the unreconstructed surface, seen in the side views in Fig. 4, is calculated to be 0.69 eV with the highest binding energy occurring for the two atoms close to the Pd(100) surface, in good agreement with the experimentally observed shift.

For the alloy surface, Pd atoms in the surface oxide coordinated to two oxygen atoms have theoretical CLS of +0.33 and +0.38 eV, respectively. Pd atoms coordinated to four oxygen atoms have shifts of +1.13 and +1.21 eV, respectively, slightly lower than the experimental observations. Here, the shifts are calculated with respect to a Pd atom in the Pd$_3$Ag bulk. Turning to the O 1s spectrum, the slightly broader oxygen structure at ~528.8 eV cannot be deconvoluted unambiguously from the experimental results alone. Therefore, a fitting into two main oxygen contributions has been performed based on the calculated shift of 0.24 eV between the oxygen species. The widths
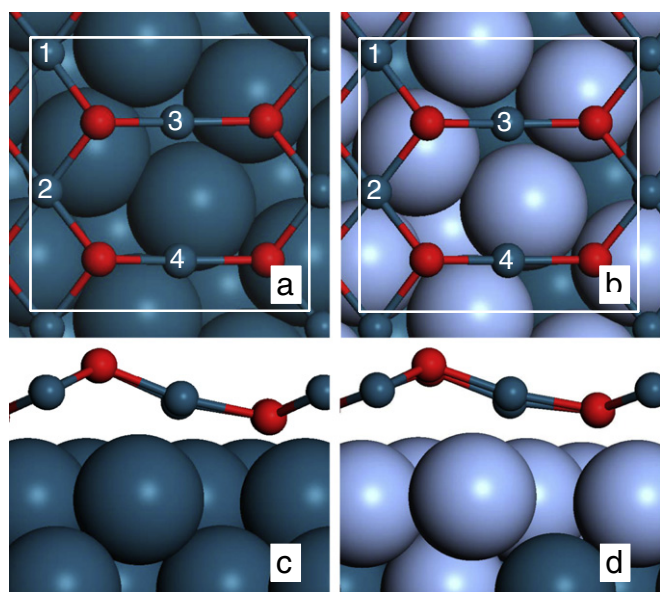
and relative intensity of these two peaks are similar to that observed for Pd(100). In addition, the oxygen structure on Pd$_{75}$Ag$_{25}$(100) has a shoulder at ~529.50 eV, which has been fitted with a separate peak. The origin of this contribution is currently unclear, but because of its low intensity, it is not believed to originate from the two different oxygen species in the $\left(\sqrt{5}\times\sqrt{5}\right)$R27° oxide. Possible explanations could be the presence of chemisorbed oxygen or OH groups on the surface. Alternatively, oxygen atoms at domain boundaries frequently occurring for this oxide (see Fig. 5) may also be the source of this O 1s contribution. As the binding energy of the shoulder is similar to that of the high binding energy O 1s component for the oxide on Pd(100), it is also possible that the shoulder may originate from patches of oxide with Pd instead of Ag in the first surface layer.

Fig. 5 displays STM images recorded for the oxidized Pd$_{75}$Ag$_{25}$(100) surface. The oxide is covering the entire surface and is characterized by small surface domains with different orientations. The $\left(\sqrt{5}\times\sqrt{5}\right)$R27°-O structure has 8 possible orientations with respect to the underlying (100) surface. In Fig. 5a four different domain orientations are identified as indicated by the red lines in the figure. The bright protrusions (indicated by red lines) dominating the STM image in Fig. 5b are due to the rows of two-fold coordinated oxygen atoms in the PdO(101) layer [31,32]. The line protrusions, marked by the yellow line, intersecting the atomic oxygen rows have for the $\left(\sqrt{5}\times\sqrt{5}\right)$R27°-O structure on Pd(100) been identified as domain boundaries between different translational domains of the reconstruction [32]. The formation of these domain boundaries is caused by mismatch due to the short side of the PdO(101) unit cell being smaller than an unperturbed $\left(\sqrt{5}\times\sqrt{5}\right)$R27°-O structure on Pd(100). This effect is expected to be stronger for the Pd$_{75}$Ag$_{25}$(100) surface due to the larger mismatch compared to pure palladium. Indeed, the translational domain boundaries are more abundant within the ordered rotational domains of the surface oxide on Pd$_{75}$Ag$_{25}$(100) as compared to $\left(\sqrt{5}\times\sqrt{5}\right)$R27°-O on the pure Pd(100) surface. In addition to the ordered $\left(\sqrt{5}\times\sqrt{5}\right)$R27°-O structure on the Pd$_{75}$Ag$_{25}$(100) surface, the STM images display some irregular bright protrusions, indicated by the arrow in Fig. 5b. The chemical origin of these features is not known and we cannot rule out that these are silver present on top of the Pd-oxide layer. The amount is however very low. Less than 2% of the surface area is covered by these protrusions.

The presented experimental and theoretical results clearly show that Ag segregates to the surface when heating Pd$_{75}$Ag$_{25}$(100) under UHV conditions, while Pd segregates in the presence of oxygen. A surface oxide very similar to the $\left(\sqrt{5}\times\sqrt{5}\right)$R27°-O on Pd(100) is formed on the surface, although a significantly higher pressure of oxygen is needed. Another difference from pure Pd is that an almost complete Ag layer resides underneath the $\left(\sqrt{5}\times\sqrt{5}\right)$R27°-O in the
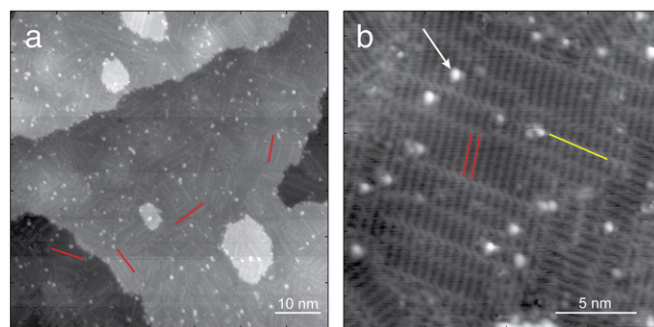

Fig. 4. Top and side views of the atomistic models for oxidized Pd(100) (a,c) and Pd$_{75}$Ag$_{25}$(100) (b,d). Atomic color codes: Red (O), dark blue (Pd) and bright blue (Ag). The CLS in the oxide layer with respect to Pd atoms in the bulk of Pd (a) are 1.17 (1), 1.21 (2), 0.33 (3), and 0.45 (4) eV. The CLS in the oxide layer with respect to Pd atoms in the bulk of Pd$_3$Ag (b) are 1.13 (1), 1.21 (2), 0.38 (3), and 0.33 (4) eV.

Fig. 5. STM images of the $\left(\sqrt{5}\times\sqrt{5}\right)$R27°-O structure on Pd$_{75}Ag_{25}$(100). a) Large scale image (70 nm×70 nm) showing the domain structure of the oxide. Four different domain orientations can be distinguished, indicated by red lines. b) High resolution image with two red lines highlighting the rows of two-fold coordinated oxygen atoms in the (101) Pd–O unit cell. A translational domain boundary is indicated by the yellow line.

$Pd_{75}Ag_{25}(100)$ case. The Ag layer may have some important consequences. Firstly, as the surface oxide on the $Pd_{75}Ag_{25}(100)$ is reduced by CO, and if the temperature is too low for segregation, areas of pure Ag (20%) and pure Pd (80%) will be present as islands on the surface. This is expected to lower the reduction speed, as CO will not adsorb on the Ag areas [49] and can therefore not diffuse to a surface oxide island border and react with the oxygen in the surface oxide. Thus, the oxide on $Pd_{75}Ag_{25}(100)$ will be more difficult to remove with CO than the oxide on pure Pd. Secondly, although the Pd areas will most likely be covered by CO after a complete reduction, the CO will not stick on the Ag areas [49]. One may speculate if the presence of silver atoms in the surface layer in this case may reduce the ability of CO to bond to nearby Pd atoms, leaving uncovered Pd sites for hydrogen dissociation, which could explain the reduced CO inhibition of Pd/Ag membrane surfaces. In addition, a reduced ability for CO to bond to Pd atoms embedded in Ag would mainly be due to a geometrical effect as CO is adsorbed preferably in a bridge position on Pd(100). In fact, explicit calculations within the present scheme indicate that the binding energy of CO on a Pd surface atom embedded in Ag is 1.57 eV (atop adsorption), whereas the stable (bridge) configuration on Pd(100) has a binding energy of 2.07 eV.

5. Conclusions

Whereas clean Pd(100) displays a surface core level shift to lower binding energies in Pd 3d photoemission spectra, a shift to higher binding energies relative to the bulk contribution is observed for $Pd_{75}Ag_{25}(100)$. Density functional theory calculations show that this contribution originates from Pd atoms embedded in the surface region of a silver terminated $Pd_{75}Ag_{25}(100)$ surface. These results confirm the segregation behavior at this surface earlier observed by scanning tunneling microscopy by Wouda et al. [11]. Oxidation of the $Pd_{75}Ag_{25}(100)$ surface yields a $\left(\sqrt{5} \times \sqrt{5}\right)R27°$-O structure similar to that reported for Pd(100). Our DFT calculations show that the most stable oxide structure on $Pd_{75}Ag_{25}(100)$ consists of a $\left(\sqrt{5} \times \sqrt{5}\right)R27°$-O surface layer supported on an almost complete silver layer at the interface to the stoichiometric alloy bulk structure. The calculated core level shifts for the oxide structure are in good agreement with the experimental observations.

Acknowledgments

Appendix A. Supplementary data

Supplementary data to this article can be found online at http://dx.doi.org/10.1016/j.susc.2012.07.006.

References

[1] G. Grashoff, C. Pilkington, C. Corti, Platin. Met. Rev. 27 (1983) 157.
[2] A. Fazle Kibria, T. Tanaka, Y. Sakamoto, Int. J. Hydrog. Energy 23 (1998) 891.
[3] S. Uemiya, T. Matsuda, E. Kikuchi, J. Membr. Sci. 56 (1991) 315.
[4] A.L. Mejdell, H. Klette, A. Ramachandran, A. Borg, R. Bredesen, J. Membr. Sci. 307 (2008) 96.
[5] J.N. Keuler, L. Lorenzen, J. Membr. Sci. 195 (2002) 203.
[6] D. Fort, J.P.G. Farr, I.R. Harris, J. Less-Common Met. 39 (1975) 293.
[7] W.M. Tucho, H.J. Venvik, M. Stange, J.C. Walmsley, R. Holmestad, R. Bredesen, Sep. Purif. Technol. 68 (2009) 403.
[8] A. Ramachandran, W.M. Tucho, A.L. Mejdell, M. Stange, H.J. Venvik, J.C. Walmsley, R. Holmestad, R. Bredesen, A. Borg, Appl. Surf. Sci. 256 (2010) 6121.
[9] A.L. Mejdell, D. Chen, T.A. Peters, R. Bredesen, H.J. Venvik, J. Membr. Sci. 350 (2010) 371.
[10] F. Reniers, Surf. Interface Anal. 23 (1995) 374.
[11] P.T. Wouda, M. Schmid, B.E. Nieuwenhuys, P. Varga, Surf. Sci. 417 (1998) 292.
[12] S. Crampin, J. Phys. Condens. Matter 5 (1993) L443.
[13] G.H. Vurens, F.C.M.J.M. Van Delft, B.E. Nieuwenhuys, Surf. Sci. 192 (1987) 438.
[14] L.Z. Mezey, J. Giber, Surf. Sci. 117 (1982) 220.
[15] S.M. Foiles, J. Vac. Sci. Technol. A 5 (1987) 889.
[16] O.M. Løvvik, Surf. Sci. 583 (2005) 100.
[17] M. Ropo, K. Kokko, L. Vitos, J. Kollár, Phys. Rev. B 71 (2005) 045411.
[18] M. Ropo, K. Kokko, L. Vitos, J. Kollár, B. Johansson, Surf. Sci. 600 (2006) 904.
[19] H. Conrad, G. Ertl, J. Küppers, E.E. Latta, Surf. Sci. 65 (1977) 245.
[20] P. Légaré, L. Hilaire, G. Maire, G. Krill, A. Amamou, Surf. Sci. 107 (1981) 533.
[21] D.L. Weissman-Wenocur, M.L. Shek, P.M. Stefan, I. Lindau, W.E. Spicer, Surf. Sci. 127 (1983) 513.
[22] G. Zheng, E.I. Altman, Surf. Sci. 462 (2000) 151.
[23] A.P. Seitsonen, Y.D. Kim, S. Schwegmann, H. Over, Surf. Sci. 468 (2000) 176.
[24] E. Lundgren, G. Kresse, C. Klein, M. Borg, J.N. Andersen, M. De Santis, Y. Gauthier, C. Konvicka, M. Schmid, P. Varga, Phys. Rev. Lett. 88 (2002) 246103.
[25] G. Ketteler, D.F. Ogletree, H. Bluhm, H. Liu, E.L.D. Hebenstreit, M. Salmeron, J. Am. Chem. Soc. 127 (2005) 18269.
[26] J. Klikovits, E. Napetschnig, M. Schmid, N. Seriani, O. Dubay, G. Kresse, P. Varga, Phys. Rev. B 76 (2007) 045405.
[27] T.W. Orent, S.D. Bader, Surf. Sci. 115 (1982) 323.
[28] G. Zheng, E.I. Altman, Surf. Sci. 504 (2002) 253.
[29] D.T. Vu, K.A.R. Mitchell, O.L. Warren, P.A. Thiel, Surf. Sci. 318 (1994) 129.
[30] M. Saidy, O.L. Warren, P.A. Thiel, K.A.R. Mitchell, Surf. Sci. 494 (2001) L799.
[31] M. Todorova, E. Lundgren, V. Blum, A. Mikkelsen, S. Gray, J. Gustafson, M. Borg, J. Rogal, K. Reuter, J.N. Andersen, M. Scheffler, Surf. Sci. 541 (2003) 101.
[32] P. Kostelník, N. Seriani, G. Kresse, A. Mikkelsen, E. Lundgren, V. Blum, T. Sikola, P. Varga, M. Schmid, Surf. Sci. 601 (2007) 1574.
[33] R. Westerström, M.E. Messing, S. Blomberg, A. Hellman, H. Grönbeck, J. Gustafson, N.M. Martin, O. Balmes, R. van Rijn, J.N. Andersen, K. Deppert, H. Bluhm, Z. Liu, M.E. Grass, M. Hävecker, E. Lundgren, Phys. Rev. B 83 (2011) 115440.
[34] R. Nyholm, J.N. Andersen, U. Johansson, B.N. Jensen, I. Lindau, Nucl. Instrum. Methods Phys. Res. Sect. A 467468 (2001) 520 (Part 1).
[35] S. Doniach, M. Šunjić, J. Phys. C: Solid State Phys. 3 (1970) 285.
[36] S. Clark, M. Segall, C. Pickard, P. Hasnip, M. Probert, K. Refson, M. Payne, Z. Kristallogr. 220 (2005) 567.
[37] We use the CASTEP program, Version 5.0.
[38] J.P. Perdew, K. Burke, M. Ernzerhof, Phys. Rev. Lett. 77 (1996) 3865.
[39] D. Vanderbilt, Phys. Rev. B 41 (1990) 7892.
[40] H.J. Monkhorst, J.D. Pack, Phys. Rev. B 13 (1976) 5188.
[41] J.D. Pack, H.J. Monkhorst, Phys. Rev. B 16 (1977) 1748.
[42] E. Pehlke, M. Scheffler, Phys. Rev. Lett. 71 (1993) 2338.
[43] R. Nyholm, M. Qvarford, J.N. Andersen, S.L. Sorensen, C. Wigren, J. Phys. Condens. Matter 4 (1992) 277.
[44] J.N. Andersen, D. Hennig, E. Lundgren, M. Methfessel, R. Nyholm, M. Scheffler, Phys. Rev. B 50 (1994) 17525.
[45] P. Steiner, S. Hüfner, Solid State Commun. 37 (1981) 79.
[46] B.J. Lindberg, K. Hamrin, G. Johansson, U. Gelius, A. Fahlman, C. Nordling, K. Siegbahn, Phys. Scr. 1 (1970) 286.
[47] I.A. Abrikosov, W. Olovsson, B. Johansson, Phys. Rev. Lett. 87 (2001) 176403.
[48] R. Westerström, J.G. Wang, M.D. Ackermann, J. Gustafson, A. Resta, A. Mikkelsen, J.N. Andersen, E. Lundgren, O. Balmes, X. Torrelles, J.W.M. Frenken, B. Hammer, J. Phys. Condens. Matter 20 (2008) 184018.
[49] G. McElhiney, H. Papp, J. Pritchard, Surf. Sci. 54 (1976) 617.

Paper II

Reduction behavior of oxidized Pd(100) and Pd$_{75}$Ag$_{25}$(100) surfaces using CO

V.R. Fernandes, J. Gustafson, I.-H. Svenum, M.H. Farstad, L.E. Walle, S. Blomberg, E. Lundgren, A. Borg

Reduction behavior of oxidized Pd(100) and Pd$_{75}$Ag$_{25}$(100) surfaces using CO

V.R. Fernandes [a], J. Gustafson [b], I.-H. Svenum [c], M.H. Farstad [a], L.E. Walle [a], S. Blomberg [b], E. Lundgren [b], A. Borg [a,*]

[a] Dept. of Physics, Norwegian Univ. of Science and Technology, NO-7491 Trondheim, Norway
[b] Div. of Synchrotron Radiation Research, Lund Univ., Box 118, SE-221 00 Lund, Sweden
[c] Dept. of Chemical Engineering, Norwegian Univ. of Science and Technology, NO-7491 Trondheim, Norway

ABSTRACT

The reduction of the $\left(\sqrt{5}\times\sqrt{5}\right)$R27° surface oxide on Pd(100) and Pd$_{75}$Ag$_{25}$(100) surfaces by CO has been investigated by high-resolution X-ray photoelectron spectroscopy in combination with kinetic analysis using the Avrami–Erofeev theory. For both surfaces we observed faster reduction with increasing temperature. Kinetic analysis indicates that the reduction process is phase boundary controlled for Pd(100) in the temperature range investigated, from 30 °C to 120 °C. On Pd$_{75}$Ag$_{25}$(100) the surface oxide reduction is significantly slower compared to Pd(100). Also in this case, a phase boundary controlled reduction of the surface oxide is observed at temperatures of 120 °C and above, while at $T \leq 70$ °C the reduction is found to be diffusion limited. Density functional theory calculations show that the presence of silver in the outermost surface layer significantly increases the CO diffusion barriers on the reduced areas, supporting a diffusion limited reduction process for Pd$_{75}$Ag$_{25}$(100) at lower temperatures.

© 2013 Elsevier B.V. All rights reserved.

1. Introduction

In recent years, the structure and chemical properties of thin surface oxides formed on many catalytically active metals have been extensively studied [1,2]. In several cases, it has been reported that these oxides are in fact more active in oxidation reactions than the metal surfaces themselves [3–20]. One such metal is palladium, which is used, for instance, as oxidation catalyst for the removal of CO in car exhaust converters. The high oxidation activity of Pd under oxygen-rich conditions has been attributed to oxides formed on the surface [6,20–22]. Kinetic Monte-Carlo simulations also indicate that the surface oxide on Pd(100) could be responsible for a higher reactivity [18,23].

Exposing the Pd(100) surface to oxygen in ultra-high vacuum (UHV) results in the formation of up to four different oxygen induced structures at coverages below 1 ML, namely $p(2 \times 2)$, $c(2 \times 2)$, $p(5 \times 5)$, and $\left(\sqrt{5}\times\sqrt{5}\right)$R27° (henceforth denoted $\sqrt{5}$) [24,25]. The latter of these structures has been subject to detailed investigations over the years [26–29].

Furthermore, bimetallic systems are commonly applied in order to tailor catalyst reactivity, selectivity and stability. For such systems surface segregation effects may influence the chemisorption and reaction behavior as well as the formation of thin surface oxides. Understanding the influence of a less reactive alloying element in surface reactions is

well motivated in this context. For this purpose we have chosen silver as alloying element in Pd.

In PdAg alloys, several studies have reported that silver segregates to the surface under UHV conditions [30–38]. This can be understood by the lower surface energy of Ag compared to Pd [33,35,39,40], and the fact that the slightly larger Ag atoms induce less strain at the surface than in the subsurface region. In the presence of adsorbates interacting with the alloy surface the situation may change, resulting in adsorbate-induced segregation due to differences in chemisorption energies of the interacting molecules [41,42]. For instance, we have recently reported that a $\sqrt{5}$ Pd surface oxide, similar to the one formed on Pd(100), is formed on Pd$_{75}$Ag$_{25}$(100) when heated in an oxygen atmosphere [43]. While Pd segregates to the surface to form the oxide structure, we find an enrichment of Ag in the interface layer between the surface oxide and the Pd$_{75}$Ag$_{25}$ bulk.

On pure Pd, the reduction behavior of different oxygen and oxide structures have been previously reported [25,44–46]. Veser et al. [44], combining X-ray photoelectron spectroscopy (XPS) and kinetic modeling, observed that time traces of the fractional amount of oxide on polycrystalline Pd during reduction by annealing were best fit by a first-order rate law. A desorption-controlled reduction process was found at temperatures $T < 230$ °C and a diffusion-controlled process at $T > 450$ °C. A similar behavior was reported by Ketteler et al. during reduction by annealing of bulk-like PdO on Pd(111). Applying near-ambient pressure photoelectron spectroscopy measurements they observed the reaction to follow a first-order rate law. Investigations of CO adsorption on a $p(2 \times 2)$ oxygen overlayer on Pd(111) by Nakai et al. [46] revealed

* Corresponding author.
E-mail address: anne.borg@ntnu.no (A. Borg).

that CO adsorption initially results in compression of the $p(2 \times 2)$ structure into a $\left(\sqrt{3} \times \sqrt{3}\right)$R30° structure, where the reaction with CO occurs at island peripherals. With increasing CO coverage a $p(2 \times 1)$ structure evolves, where the reaction occurs inside the oxygen islands. The $p(2 \times 2)$ phase does not react with CO at surface temperatures below 290 K. Above 290 K the surface oxygen reacts with diffusing CO molecules [46].

The reactivity of different surface oxygen phases on Pd(100) towards reduction by CO was investigated by Zheng et al. [25]. They reported that the $\sqrt{5}$ and bulk PdO were relatively inert towards reaction with CO, while the p(5 × 5) and p(2 × 2) were the most reactive phases. Additionally they observed that the reduction rate increased with increasing temperature for all oxygen coverages over the range studied (335 K to 850 K).

In the present work, high resolution XPS (HRXPS) measurements have been used to monitor the reduction of $\sqrt{5}$ surface oxide on the Pd(100) and $Pd_{75}Ag_{25}(100)$ surfaces during exposure to CO at different temperatures. Kinetic modeling of the HRXPS data was employed to characterize the reaction mechanism and evaluate the influence of silver in the alloy case. We find that increasing the temperature leads to faster reduction on both surfaces. On the Pd(100) surface oxide reduction is a phase boundary controlled process in the temperature range investigated. For $Pd_{75}Ag_{25}(100)$ kinetic modeling indicates a phase boundary limited reaction at temperatures above 120 °C. At and below 70 °C the reduction is diffusion limited. On $Pd_{75}Ag_{25}(100)$ the reduction rates were found to be significantly slower compared to Pd(100). This is addressed by density functional theory (DFT) calculations which show weaker binding and higher activation barriers for diffusion of CO in the presence of silver.

2. Methods

2.1. Experimental

The HRXPS experiments were performed at beamline I311 at the MAX II storage ring of the MAX IV Laboratory, in Lund, Sweden. This beamline is equipped with a modified SX-700 monochromator and a large Scienta hemispherical electron energy analyzer (SCIENTA SES200) [47]. The base pressure in the UHV system was $< 2 \times 10^{-10}$ mbar.

Pd(100) and $Pd_{75}Ag_{25}(100)$ single crystals were cleaned by cycles of sputtering, oxygen treatment, and annealing to 705 °C for Pd(100) and 625 °C for the $Pd_{75}Ag_{25}(100)$. This procedure gave well-defined, clean surfaces as judged from LEED patterns and photoemission measurements of the C 1s core level region. The oxides were formed by exposing the surfaces to oxygen at 320 °C, using pressures 5×10^{-6} mbar for Pd(100) and about 5×10^{-4} mbar for $Pd_{75}Ag_{25}(100)$.

The reduction of the $\sqrt{5}$ surface oxide was monitored in-situ by recording the Pd $3d_{5/2}$ and C 1s core level spectra during exposure to 5×10^{-8} mbar CO at selected temperatures, in the range 30 °C to 170 °C. A photon energy of 400 eV was used and the overall spectral resolution was about 200 meV. All spectra were measured at normal emission. The binding energy was calibrated against the Fermi edge. All spectra have been normalized to the background at the low binding energy side of the core level peaks. Linear background subtraction has been applied and Doniach–Sunjic line shapes were used for fitting the spectra [48].

The fitting of the Pd $3d_{5/2}$ core level spectra recorded continuously during the reduction, along with C 1s core level spectra, was performed in a two-step process. We began by analyzing the first and last scan of a given measurement series to obtain the value of the Gaussian and Lorentzian widths for all the components due to the $\sqrt{5}$ oxide and CO covered reduced surfaces, i.e. contributions from two-fold and four-fold oxygen coordinated Pd, Pd bulk, adsorbed CO and interface Pd (for Pd(100)). Next, fitting was performed for all the scans, where the Gaussian and Lorentzian widths were allowed a 2% variation. The height of the CO component in the Pd $3d_{5/2}$ core level spectra was determined

utilizing the C 1s spectra and assuming linear dependence between the intensity of the CO components in the Pd $3d_{5/2}$ and C 1s spectra. Thus, the height, H, of the CO contribution in the ith scan of the Pd $3d_{5/2}$ core level spectra was calculated as $H_{CO, i}^{Pd3d} = (H_{CO, i}^{C1s} \times H_{CO, last}^{Pd3d})/H_{CO, last}^{C1s}$, where $H_{CO, i}^{C1s}$ is the height of the CO contribution in the ith scan of the C 1 s core level spectra, $H_{CO, last}^{Pd3d}$ the height of the CO component in the last scan of the Pd $3d_{5/2}$ core level spectra, and $H_{CO, last}^{C1s}$ the height of the CO peak in the last scan of the C 1 s core level spectra. The calculated $H_{CO, i}^{Pd3d}$ was allowed a 10% variation interval in the optimization routine to account for possible intensity variations.

2.2. Kinetic modeling

Kinetic modeling was used to determine the character of the oxide reduction reactions. By definition the fractional extent of the reaction, α, changes progressively from reactants ($\alpha = 0$) to products ($\alpha = 1$). In solid state reactions the rate equation of a process at constant T can be written in its integral form as:

$$g(\alpha) = kt, \tag{1}$$

where $g(\alpha)$ represents the equation describing the kinetic model applied and k is the rate constant of the reaction. $g(\alpha)$ is also denoted the conversion function and it depends on the system under consideration.

We have tried to apply several different models for $g(\alpha)$, such as contracting area and contracting volume, Prout–Tompkins, Avrami–Erofeev (AE), two-dimensional diffusion, second and third order reactions, and power and exponential laws [49]. As will be presented in the Results part, the AE model fitted our measurements best, which is also expected for this kind of process, where at the initial and the final stages of the reaction the rate of transformation is lower than during the intermediate stage.

The AE model (also known as the Johnson–Mehl–Avrami (JMA) equation) is based on the formation and growth of nuclei, where the growing phases develop from different nuclei and come into contact after some time [49]. This model relies on the assumptions that nucleation occurs randomly in time and homogeneously distributed across the untransformed portion of the material, and growth occurs at the same rate in all directions and does not depend on the extent of transformation. The AE equation is expressed as:

$$g(\alpha) = [-ln(1-\alpha)]^{1/n} = kt, \tag{2}$$

where n is denoted as the index of reaction. n usually has a value of 1.5, 2, 3 or 4 which reflects the nature of the transformation [49]. The exponent n is a combined term of β, the number of steps involved in the nucleation ($\beta = 0$ for instantaneous nucleation, $\beta = 1$ for constant nucleation rate), and λ, the number of dimensions in which the nuclei grow (1 for linear growth, 2 for disks or cylinders and 3 for spheres or hemispheres). The form of n also depends on the kinetic behavior, for interface controlled reactions $n = \beta + \lambda$ while for diffusion controlled reactions $n = \beta + \lambda / 2$ [49].

2.3. Density functional theory calculations

Periodic, self-consistent density functional theory (DFT) calculations were performed using the DACAPO code [50,51]. The exchange-correlation effects were described by the generalized gradient approximation with the GGA-PW91 functional [52,53], and the ionic cores were represented by ultrasoft pseudo-potentials [54]. A plane-wave basis expansion with an energy cutoff of 400 eV was applied.

Pd and Pd_3Ag surfaces oriented in the (100) direction were modeled by a six layer slab using a (2×2) surface unit cell. The Brillouin zone was sampled using a Monkhorst–Pack [55] grid with $(6 \times 6 \times 1)$ k-points. The four topmost layers were free to relax during structural optimizations, whereas the two bottom layers were kept fixed. Calculated

bulk lattice constants of 3.985 Å and 4.014 Å were used for Pd(100) and Pd$_3$Ag(100), respectively. The slabs were separated by a vacuum region equivalent to about 14 Å. The (100) surface of Pd$_3$Ag has two different terminations, one with 50% Ag in the top layer and a pure Pd layer underneath and one where these two layers have the reverse order. Here, we focus on the termination with mixed composition as both components are found in the surface experimentally. A surface configuration of the Pd$_3$Ag(100) slab with only Ag in the second layer instead of pure Pd was also explored. For completeness, a full layer of Pd on top of Ag(100) was included in the calculations. Adsorption of CO was allowed on one side of the slab with no imposed restrictions during optimization, and the electrostatic potential was adjusted accordingly [56,57]. CO adsorption energies were calculated by $E_{ads} = E_{CO/slab} - E_{slab} - E_{CO}$, where $E_{CO/slab}$, E_{slab} and E_{CO} are the total energy of the slab with one adsorbed CO molecule, the slab without CO, and the CO molecule in the gas phase, respectively.

Diffusion of CO on the surfaces was investigated using climbing image nudged elastic band (CI-NEB) calculations [58]. Transition states were verified by vibrational analysis yielding a single imaginary frequency.

3. Results

3.1. The $\left(\sqrt{5} \times \sqrt{5}\right)$R27° surface oxide on Pd(100) and PdAg(100)

The formation of the $\sqrt{5}$ surface oxide on Pd(100) is well understood and has been thoroughly discussed [28,29]. Recently, we reported the formation of a similar $\sqrt{5}$ surface oxide on Pd$_{75}$Ag$_{25}$(100) [43]. Here we briefly present the HRXPS spectral signatures of the $\sqrt{5}$ surface oxide on these surfaces. The Pd $3d_{5/2}$ core level spectrum for the $\sqrt{5}$ structure on Pd(100), which can be described as a PdO(101) monolayer supported on the Pd(100) surface [28,29], is displayed in Fig. 1(bottom). In addition to the bulk component, at binding energy 334.98 eV, the spectrum displays three oxide-induced contributions, one from 4-fold oxygen coordinated Pd atoms (336.22 eV), one from 2-fold oxygen coordinated Pd atoms (335.32 eV) and finally one from Pd atoms located at the interface between the surface oxide and the bulk crystal (334.66 eV) [28].

The corresponding Pd $3d_{5/2}$ core level spectrum recorded for the $\sqrt{5}$ surface oxide on Pd$_{75}$Ag$_{25}$(100) is shown in Fig. 1(top). Because of an Ag enrichment in the interface layer underneath the surface oxide, no interface component can be observed [43]. In Pd$_{75}$Ag$_{25}$(100) the bulk component has a binding energy of 334.78 eV, while the binding energies of the two oxide contributions are similar (336.12 eV and 335.33 eV, respectively) to those observed for the $\sqrt{5}$ oxide on Pd(100). In general, the $\sqrt{5}$ surface oxide on Pd$_{75}$Ag$_{25}$(100) is characterized by a larger number of misfit dislocations and smaller ordered domains as compared to the $\sqrt{5}$ surface oxide on Pd(100) [43].

3.2. Surface oxide reduction by CO

Fig. 2 presents an example of the recorded Pd $3d_{5/2}$ and C *1s* core level spectra as a function of CO exposure time during the oxide reduction experiments for Pd$_{75}$Ag$_{25}$(100) exposed to 5×10^{-8} mbar CO at temperature 70°C, along with the resulting changes in spectral intensities due to the oxide and CO induced Pd $3d_{5/2}$ contributions. Fig. 2(a) and (b) display the evolution of the Pd $3d_{5/2}$ and C *1s* core level spectra, respectively. The numbers 1–3 indicate three different stages during the reduction experiments. Fig. 2(c) and (d) present fitted spectra for the Pd $3d_{5/2}$ and C *1s* regions, respectively, at these three stages. The spectra labeled 1 are recorded of the oxidized surface before the onset of oxide reduction. At an intermediate stage, labeled 2, the oxide is partially reduced. Spectrum 2 in Fig. 2(c) consists of both oxide and CO-induced Pd $3d_{5/2}$ contributions illustrating coexistence of oxide and CO-covered areas on the surface. The presence of adsorbed CO is confirmed by the C *1s* signal in the corresponding spectrum in Fig. 2(d). For Pd$_{75}$Ag$_{25}$(100) the CO-induced contribution in the Pd $3d_{5/2}$ core
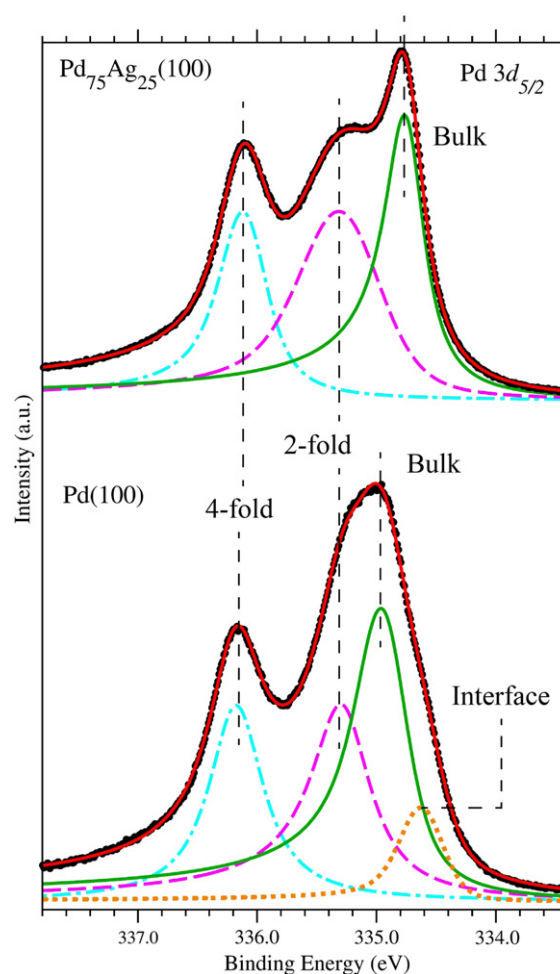

Fig. 1. Pd $3d_{5/2}$ core level spectra from the $\left(\sqrt{5} \times \sqrt{5}\right)$R27° surface oxide structures on Pd(100) and Pd$_{75}$Ag$_{25}$(100). Oxide induced components due to 4-fold and 2-fold oxygen coordinated Pd are shown with dash–dot and dashed lines, respectively. The component due to Pd atoms between the surface oxide and the bulk Pd(100) crystal is shown with dotted line. The bulk contributions are presented with solid lines.

level spectrum is shifted approximately $+0.70$ eV relative to the bulk Pd$_{75}$Ag$_{25}$ peak. On Pd(100) the component due to adsorbed CO is shifted approximately $+0.45$ eV relative to the bulk Pd component (not shown). When the reduction is completed only the bulk and CO induced Pd $3d_{5/2}$ components are present, as displayed in spectrum 3 in Fig. 2(c). The CO coverage (C *1s* signal) is at its maximum as seen in Fig. 2(e) and curve 3 in Fig. 2(d).

Through fitting all the measured HRXPS data, illustrated in Fig. 2(a) and (b), the development of the components related to the surface oxide and adsorbed CO as function of time was obtained. Fig. 2(e) displays the intensity of the Pd $3d_{5/2}$ component due to Pd atoms 4-fold coordinated to oxygen in the surface oxide and the CO induced contribution in the Pd $3d_{5/2}$ core level spectra as a function of CO exposure time. The component due to 4-fold oxygen coordinated Pd atoms provides a cleaner signature of oxide removal compared to the component due to 2-fold oxygen coordinated Pd atoms and is therefore used in our analysis. The data presented has been normalized relative to the maximum intensity observed for each of these two contributions.

Reduction experiments analogous to the one presented in Fig. 2 were performed for Pd(100) and Pd$_{75}$Ag$_{25}$(100) at a CO pressure of 5×10^{-8} mbar and selected temperatures in the range 30 °C to 170 °C. Fig. 3 presents extracted intensity curves from the corresponding recorded HRXPS Pd $3d_{5/2}$ core level spectra.

Two distinct features of the reduction behavior can be extracted from Fig. 3, the initial period before onset of the reaction, where there
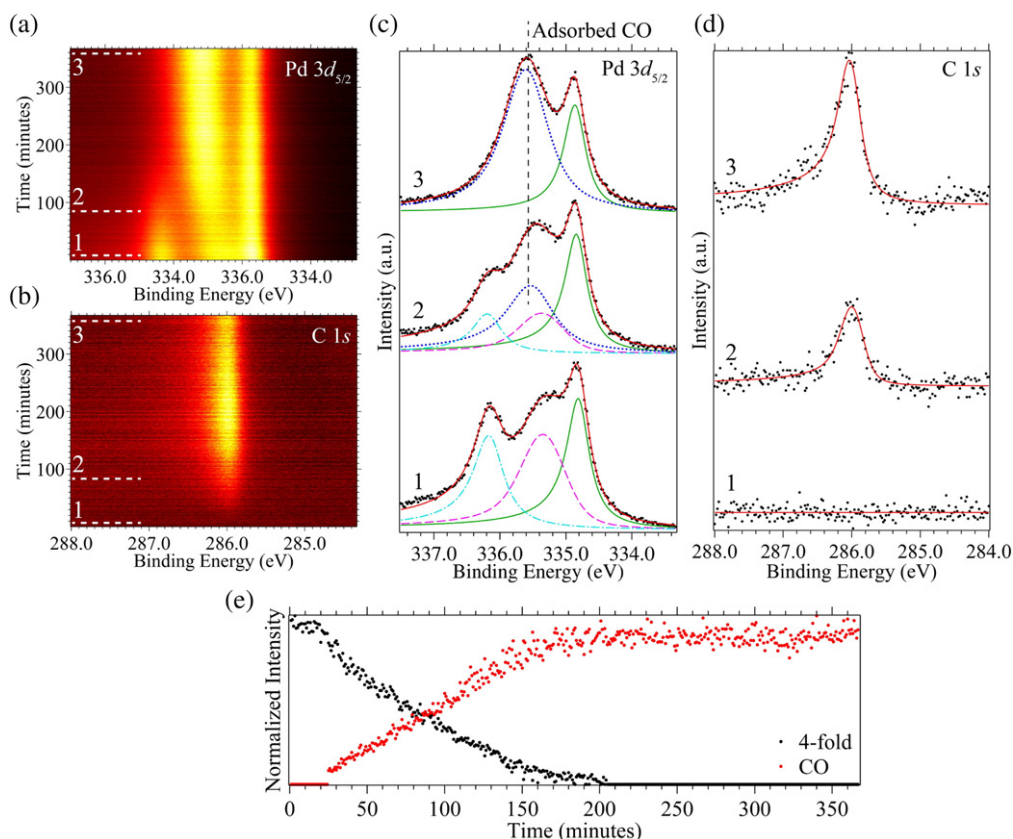
Fig. 2. Reduction of the surface oxide on $Pd_{75}Ag_{25}(100)$ upon 5×10^{-8} mbar CO exposure at 70 °C monitored using HRXPS. (a) and (b): Evolution of the Pd $3d_{5/2}$ and C $1s$ core level spectra during the reduction reaction, respectively. (c) and (d): Decomposition of the spectra for Pd $3d_{5/2}$ and C $1s$, respectively, at three stages in the reduction, oxidized (1), partially reduced (2), and fully reduced surface (3). (e): Intensity of the components due to 4-fold oxygen coordinated Pd atoms in the $\left(\sqrt{5} \times \sqrt{5}\right) R27°$ surface oxide and adsorbed CO as a function of CO exposure time obtained by fitting the spectra in (a).

is no significant variation in the intensity of the surface oxide contribution, and surface oxide reduction where the intensity of the oxide component decreases. The onset of the reaction varies between different experiments and depends on the quality of the surface oxide prepared. As mentioned above, there is generally a larger number of misfit dislocations, and hence smaller well ordered domains of the surface oxide on $Pd_{75}Ag_{25}(100)$ as compared to Pd(100).

After the onset of the reduction reaction, at any given temperature, the time required to fully reduce the surface oxide on $Pd_{75}Ag_{25}(100)$ is significantly longer than for pure Pd(100) irrespective of the sample temperature applied. Increasing the temperature leads to faster reduction on both surfaces. For Pd(100) at a temperature of 170 °C the reduction is so fast that our HRXPS measurement cannot follow the transition from oxidized to reduced surface.

The shape of the intensity curve due to adsorbed CO and 4-fold oxygen coordinated Pd atoms in the Pd $3d_{5/2}$ spectra of $Pd_{75}Ag_{25}(100)$ at 70 °C differs from the remaining experiments, as it reaches the final value more gradually (asymptotically). This suggests different mechanisms for the oxide reduction for the two surfaces. Kinetic modeling was utilized to assess possible differences in the reaction mechanism.

The reduction of the $\sqrt{5}$ surface oxide on $Pd_{75}Ag_{25}(100)$ and Pd(100) by CO is a gas–solid reaction where one phase, the surface oxide, is consumed and a new phase, the CO covered metal surface, is formed. The intensity of the oxide components in the HRXPS spectra is proportional to the amount of $\sqrt{5}$ surface oxide remaining on the surfaces, indicating the progress of the reaction. Therefore, the fractional extent of reduced surface α at time t is defined as the reduced area fraction, $\alpha = 1 - \text{Intensity}_{4-\text{fold}}$.

Various experimental and theoretical studies point out that the reduction of surface oxides on both Rh and Pd upon exposure to H_2 or CO are initiated at defects [59–63], where the reducing agent can adsorb

and nucleate, initiating the reduction process. In the present work, the defects in the surface oxide are the nucleation centers where CO adsorbs and initiates the reduction, as CO is not expected to adsorb on the surface oxide at the gas pressures and temperatures utilized in this study [64,65]. These observations suggest that the AE model is the appropriate kinetic model for our experiments.

Nevertheless, to address the reduction process in an unbiased manner we have tested a range of models for the reduction process, namely contracting area and contracting volume, Prout–Tompkins, AE, two-dimensional diffusion, second and third order reactions, and power and exponential laws [49]. Using the data for the Pd $3d_{5/2}$ component corresponding to 4-fold oxygen coordinated Pd atoms from Fig. 3 to obtain $\alpha = 1 - \text{Intensity}_{4-\text{fold}}$ and Eq. (2), the linearity of plots of $g(\alpha)$ for different models as a function of time t can be used to determine which kinetic model is best for describing the experiment. From this fitting the nature of the reaction can be inferred. Intensity values in the range 2% to 95% in Fig. 3 were selected for determining α, in order to avoid induction effects [49] and values at low intensities, where peak fitting is less accurate.

Linear regression was applied for choosing the best fitting model through evaluating the correlation parameter R^2, which describes the quality of the fit and which has a value of 1 for a perfect fit. For all temperatures investigated, the results yield an AE type equation, with varying n, as the model that best describes the observations. Fig. 4 displays plots of the obtained best fits to the experimental data. Table 1 presents the corresponding obtained values of n, k, and R^2 for the best fitting AE model.

The values of the rate constant k given in Table 1 quantify the differences in the reduction rate of the $\sqrt{5}$ surface oxide on Pd(100) and $Pd_{75}Ag_{25}(100)$. It should be noted that for Pd(100) at temperature 120 °C, the number of available data points is just three, which does
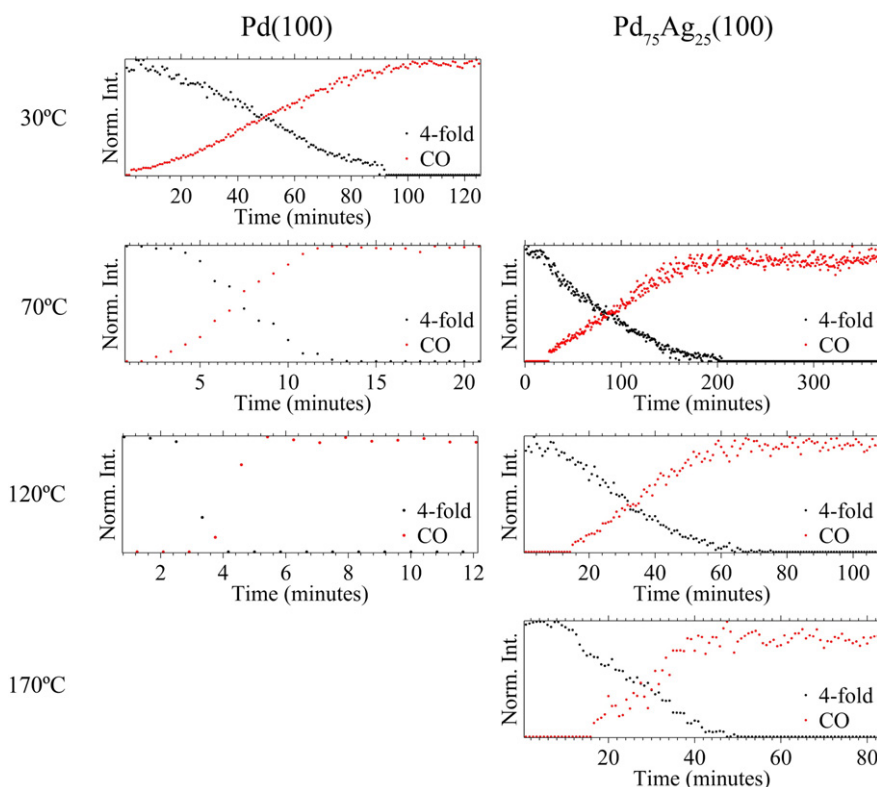
Fig. 3. Intensity of the components due to 4-fold oxygen coordinated Pd atoms (i.e., the surface oxide) and adsorbed CO obtained by fitting the Pd $3d_{5/2}$ core level spectra recorded *in-situ* during reduction of the $\left(\sqrt{5} \times \sqrt{5}\right)$R27° surface oxide structure for Pd(100), left panel, and Pd$_{75}$Ag$_{25}$(100), right panel. Reduction was performed at selected temperatures during exposure to 5×10^{-8} mbar CO.

not allow for a meaningful evaluation of n, but gives an approximate value for k of $\approx 1(\text{min}^{-1})$. The fits display good linear correlation, with the lowest R^2 value of 0.959 obtained for Pd$_{75}$Ag$_{25}$(100) and 170 °C.

The ratio between the rate constants k_{Pd}/k_{PdAg} is about 13 at 70 °C and increases to about 50 at 120 °C. This may be rationalized in terms of the amount of adsorbed CO on the reduced areas. Fig. 5 displays the intensity of the component corresponding to adsorbed CO after surface oxide reduction on Pd(100) and Pd$_{75}$Ag$_{25}$(100) as a function of temperature. The data was normalized to the highest intensity for each sample. On Pd$_{75}$Ag$_{25}$(100) there is a substantial decrease in the intensity of the component corresponding to adsorbed CO, in particular at 170 °C. On Pd(100) the variation between 30 °C and 120 °C is small, but a significant decrease is expected at 170 °C, which is close to the desorption temperature of CO on the Pd(100) surface, reported at approximately 190 °C [66–68]. The amount of CO residing on the Pd$_{75}$Ag$_{25}$(100) surface at 170 °C is considerably less than for lower temperatures, yielding higher uncertainty in the fitting procedure.

Table 1 shows that an index of reaction $n = 3$ is obtained for all the experimental data except for the reduction of the $\sqrt{5}$ surface oxide on Pd$_{75}$Ag$_{25}$(100) at 70 °C. As explained in the Methods part, the exponent n in Eq. (2) is a combined term of β, the number of steps involved in the nucleation, and λ, the number of dimensions in which the nuclei grow. In the present work, the reduction reaction is a two dimensional process, corresponding to $\lambda = 2$. From our experimental data we cannot establish the value of β directly. Since CO does not adsorb on the surface oxide at the pressures applied in the present study [64,65], it is expected that the nucleation proceeds similarly to that observed during reduction of the surface oxide on Rh(111), where Klikovits et al. determined a constant rate of nuclei formation [61]. In all cases the reduction process was initiated at steps and imperfections in the surface oxide and instantaneous nucleation was not expected in this case. Thus, we assume a

constant nucleation rate during the reduction, which implies $\beta = 1$. Considering these values of λ and β, for Pd(100) AE analysis indicates a phase-boundary controlled process, $n = \beta + \lambda = 1 + 2 = 3$, in the temperature range investigated. For Pd$_{75}$Ag$_{25}$(100) and a temperature of 70 °C, the AE analysis points to a diffusion controlled reaction, $n = \beta + \lambda / 2 = 1 + 2 / 2 = 2$ [49], as the reduction process is best fitted by a value of $n = 2$ in this case. Increasing the temperature of the Pd$_{75}$Ag$_{25}$(100) surface leads to a change in the best fitting parameter to $n = 3$, which corresponds to a phase-boundary controlled process, where the reaction at the border of the surface oxide islands is the rate limiting step.

To address the observed difference in reduction behavior between Pd(100) and Pd$_{75}$Ag$_{25}$(100), and in particular the indicated diffusion limited reduction for Pd$_{75}$Ag$_{25}$(100) and temperature 70 °C, DFT calculations to determine the adsorption and diffusion properties of CO on selected model surfaces were performed. A coverage of 0.25 ML CO was investigated. For Pd(100), DFT provides similar adsorption energies for the bridge and hollow sites of about −2.00 eV, similar to previous results [69]. Experimentally, CO adsorbs in Pd–Pd bridge sites [66,70–76]. The discrepancy can be related to inaccuracy of the functional describing CO, and can be overcome using different approaches [77–80]. This should, however, not affect the overall trends in CO diffusion between Pd and PdAg alloys. CO shows similar adsorption behavior on a Pd-overlayer on Ag(100) as on the Pd(100) surface and the binding to Pd is in this case not significantly affected by the underlying Ag for the most stable sites. For the Pd$_3$Ag(100) surface cut with Pd-Ag in the topmost surface layer, CO adsorption is stable in Ag top (−0.54 eV), Pd top (−1.51 eV) and Pd–Ag hollow sites (−1.68 eV). The most stable adsorption geometry is shown in Fig. 6. When situated in the preferred Pd–Ag hollow site, the surface undergoes structural changes. The two Pd atoms are pulled closer to CO and the Ag atoms move away from the CO molecules. Simulating the experimentally
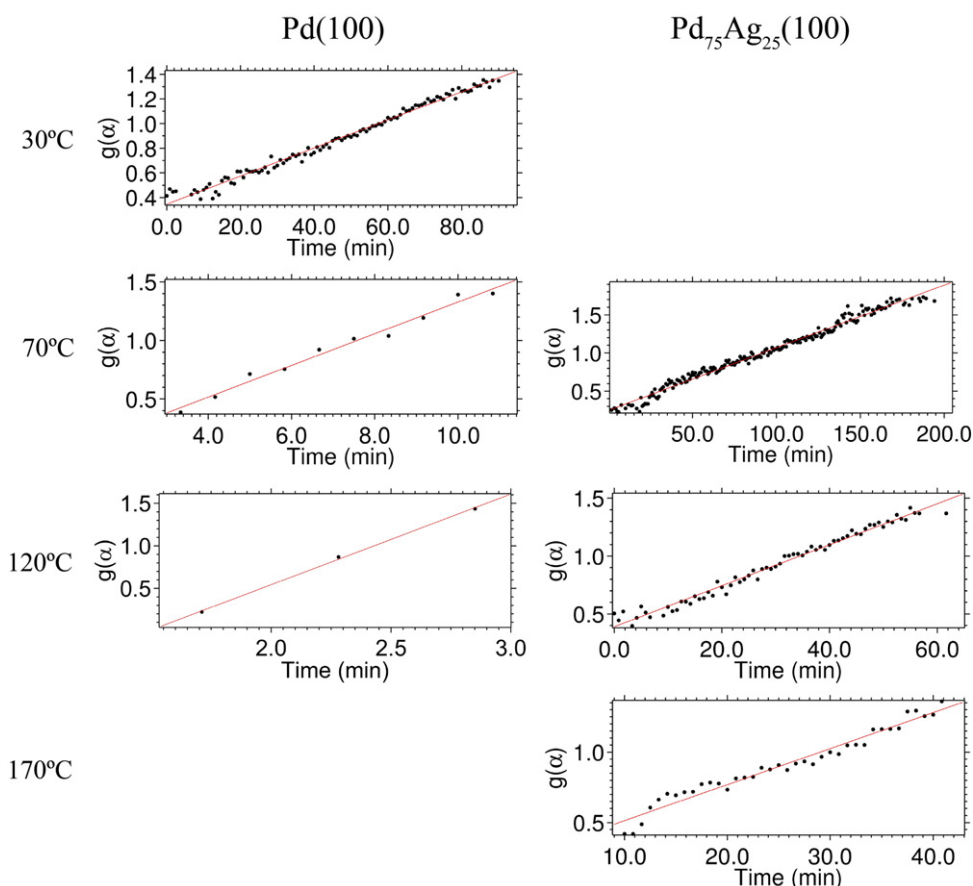
Pd(100)   Pd$_{75}$Ag$_{25}$(100)

Fig. 4. Kinetic analysis of the intensity curves for the Pd 3$d_{5/2}$ component corresponding to Pd atoms 4-fold coordinated to oxygen in Fig. 3 by linear regression of the equation $g(\alpha) = kt$ for Pd(100), left panel, and Pd$_{75}$Ag$_{25}$(100), right panel. For all cases the best fitting kinetic model is Avrami–Erofeev, where $g(\alpha) = [-ln(1-\alpha)]^{1/n}$. The fit parameters obtained are given in Table 1.

observed enrichment in the surface region by replacing the Pd layer underneath the first Pd–Ag layer of the Pd$_3$Ag(100) surface with Ag yields a weakening of the CO binding for all three stable sites.

Turning to the diffusion behavior, the diffusion path of CO on the Pd(100) surface exhibits a low barrier. The path from bridge to bridge sites over a hollow site, which is the path with the lowest barrier, has a barrier of 0.07 eV, indicating that CO diffusion is relatively fast on this surface. This value is comparable to previously reported results for CO diffusion on Pd(100) where a barrier of 0.13 eV was obtained [81]. For the Pd$_3$Ag(100) surface with PdAg termination, the favored CO diffusion path from a Pd–Ag hollow site to another hollow site occurs via a Pd top site. The diffusion from the Pd–Ag hollow site to a Pd top site exhibits an activation barrier of 0.31 eV, and diffusion from the Pd top site to a Pd–Ag hollow site is associated with a barrier of 0.14 eV. The favored diffusion path involves the surface Pd-atoms only. Diffusion over a surface Ag atom results in a larger activation barrier compared

to Pd. The lowest diffusion barrier involving Ag is about 1.0 eV. Thus, the diffusion paths are much more limited on the Pd$_{75}$Ag$_{25}$(100) surface compared to Pd(100). The increased activation barrier for CO diffusion suggests that surface Ag atoms, in addition to being less favorable adsorption sites, impede the diffusion of CO on Pd$_{75}$Ag$_{25}$(100) compared to Pd(100). Changing the second layer from Pd to Ag gives a similar picture.

4. Discussion

Both in the case of Pd(100) and Pd$_{75}$Ag$_{25}$(100) we observe a reduction of the $\sqrt{5}$ surface oxide upon exposure to CO. Unlike the reported results by Zheng et al. that the $\sqrt{5}$ and PdO on Pd(100) are relatively inert towards CO [25], we observe a reduction rate for the $\sqrt{5}$ surface oxide on Pd(100) which is increasing with increasing temperature. The current results for the (100) surface of Pd follow the same trend as reported for oxides on Pd(111) [45,62], where an increased reduction rate with temperature was observed. The temperature dependence of the reduction rate for the $\sqrt{5}$ surface oxide follows a similar trend for Pd$_{75}$Ag$_{25}$(100).

The reduction behavior observed in this study compares well with the reduction of the surface oxide on Rh(111) by H$_2$ analyzed using Avrami kinetics [61]. Klikovits et al. found that the reduction of the surface oxide can only be initiated at defects and consists of a two regime process, where reduction speed is determined initially by hydrogen adsorption on the already reduced areas and later by processes at the border between oxidized and reduced areas [61]. A similar behavior was observed for the reduction of oxidized Rh(110) by hydrogen [82]. Our results also show several similarities with the CO induced reduction of the (9 × 9) surface oxide on Rh(111) [60]. As for the Rh(111) case, CO does not adsorb on the $\sqrt{5}$ surface oxide on Pd(100) [64,65].

Table 1
Kinetic analysis results for the $(\sqrt{5} \times \sqrt{5})$R27° surface oxide reduction on Pd(100) and Pd$_{75}$Ag$_{25}$(100) obtained using the Avrami–Erofeev kinetic model $[-ln(1-\alpha)]^{1/n} = kt$ and data presented in Fig. 4. The calculated parameters are the index of reaction n, the rate constant k, and the correlation coefficient of the linear regression R^2.

T (°C)	n		k(min^{-1})		R^2		k_{Pd}/k_{PdAg}
	Pd	PdAg	Pd	PdAg	Pd	PdAg	
30	3		0.01		0.987		
70	3	2	0.1	0.008	0.983	0.984	13
120		3	~1[a]	0.02		0.981	50
170		3		0.03		0.959	

[a] The value is calculated using three experimental points only and therefore represents an approximate value for the rate constant in this case.
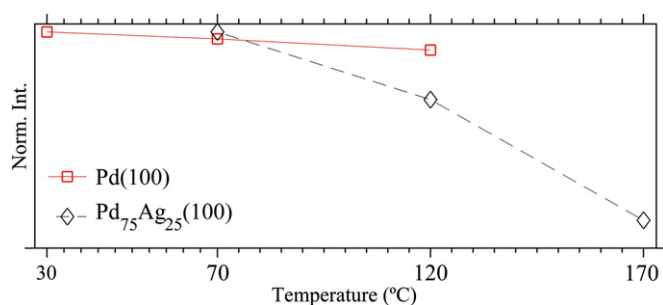
Fig. 5. Peak areas of the component due to adsorbed CO in the Pd $3d_{5/2}$ core level spectra after surface oxide reduction on Pd(100) and Pd$_{75}$Ag$_{25}$(100) at selected temperatures.

Domain boundaries in the surface oxide, steps, and other defects may provide Pd sites that are oxygen under coordinated. Such sites are accessible for CO adsorption, thus initiating the reaction with the surface oxide to produce CO$_2$, which desorbs from the surface and leaves metallic areas accessible for further CO adsorption and diffusion. The preparation dependent onset of the reduction process supports this picture. The time before onset of the reduction differs in all the experiments, indicating that surface quality, i.e., defect density, is important for the reaction onset. Before the oxide reduction starts, the C $1s$ peak due to adsorbed CO is absent. Moreover, since all experiments were best fitted by the AE model, which is based on nucleation theory, our results support the notion that CO does not adsorb on the surface oxide at the pressures and temperatures used in this study.

The surface oxide reduction process on both Pd(100) and Pd$_{75}$Ag$_{25}$(100) consists of a two regime process. The first regime is characterized by adsorption of CO at steps and defects, where it can react with nearby oxygen atoms of the surface oxide to produce CO$_2$. In the second regime the reduction proceeds by propagation of the reaction front. AE analysis of the HRXPS data for the √5 surface oxide reduction on Pd(100) indicates a phase-boundary limited reaction in the temperature range investigated. The same is observed for Pd$_{75}$Ag$_{25}$(100) at temperatures ≥ 120 °C, while at temperatures ≤ 70 °C diffusion is the rate limiting step.

These results can be understood from previous reports in combination with our DFT calculations. In general CO favors adsorption in highly coordinated sites on ensembles of Pd atoms on PdAg alloy surfaces [83–87]. The presence of Ag in the surface leads to changes in the CO bond strength and may alter adsorption sites due to variations in available Pd ensembles [85,87]. Our DFT calculations show that the CO bond strength is weaker for the Pd$_3$Ag(100) alloy surfaces compared to Pd(100). The destabilizing effect increases with the amount of Ag in
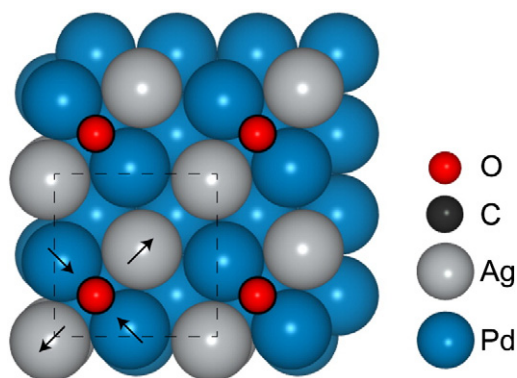
the subsurface region. Even though the binding of CO is weaker on the Pd$_{75}$Ag$_{25}$(100) surface, the diffusion of CO is associated with a higher activation barrier compared to Pd(100). On the alloy surface CO diffuses preferentially to and from Pd atoms, as diffusion over Ag atoms results in a higher activation barrier. Thus, the diffusion paths are more limited on Pd$_3$Ag(100) compared to Pd(100) and the latter has a lower activation barrier for diffusion compared to the former. Hence, the presence of silver in the reduced areas affects the availability of CO near √5 oxide islands, where the reaction takes place, leading to a significantly slower reduction for Pd$_{75}$Ag$_{25}$(100) compared to Pd(100), in agreement with our experimental results. Furthermore, increasing the temperature facilitates diffusion, which explains why the reduction of the surface oxide on the alloy is diffusion limited at low, but not at high temperatures.

Our experimental observations show that the reduction time is substantially decreased with increased temperature. Results show a considerably larger ratio of the rate constant between Pd(100) and Pd$_{75}$Ag$_{25}$(100) at 120 °C compared to 70 °C, meaning that reduction speed increases faster with temperature on Pd(100). At higher temperatures the reduction is not rate limited by diffusion. However, increased temperature leads to less adsorbed CO on the surface, particularly for Pd$_{75}$Ag$_{25}$(100), as shown in Fig. 5. The DFT results support this picture in which CO binds more weakly on Pd$_{75}$Ag$_{25}$(100) compared to Pd(100). Noordermeer et al. showed that CO desorption occurs at lower temperature for Pd$_{67}$Ag$_{33}$(111) compared to Pd(111), and the amount of CO per unit surface area that can be adsorbed on Pd$_{67}$Ag$_{33}$(111) is less than on Pd(111) [88]. Our HRXPS data provides the same picture.

The main features of the CO induced reduction process of the √5 surface oxide on Pd(100) and Pd$_{75}$Ag$_{25}$(100) are illustrated in Fig. 7. The amount of Pd atoms in the √5 surface oxide is about 80% of a full monolayer on the (100) surface. As a result, upon reduction, areas of the layer underneath the oxide layer will be exposed. For Pd(100), Pd atoms in the interface layer will be available for CO adsorption in addition to reduced Pd areas from the oxide layer, as indicated in Fig. 7(a). In comparison, a Ag rich layer will be exposed for Pd$_{75}$Ag$_{25}$(100). As CO does not adsorb on Ag [83–85,87–89], illustrated in Fig. 7(b), these areas will lead to less CO available for the surface oxide reduction. Furthermore, possible mixing of Ag into the reduced areas in the surface oxide layer weakens the adsorption energy of CO and significantly increases the CO diffusion barriers and thus possible diffusion paths.

Our experiments illustrate that alloying of Pd with Ag strongly diminishes the reduction rate of the √5 surface oxide upon exposure to CO. This finding may have implications on CO poisoning effects on these surfaces. In fact, Mejdell et al. [90] showed that the inhibition effect by CO on the hydrogen permeation through thin PdAg (23 wt.%) membranes was significantly reduced after heat treatment in air, where a 2–3 nm thick surface oxide is formed [91].

5. Conclusions

In-situ high resolution photoelectron spectroscopy measurements during CO induced reduction of the √5 surface oxide on Pd$_{75}$Ag$_{25}$(100) and Pd(100) revealed that the reduction proceeds much slower on Pd$_{75}$Ag$_{25}$(100) compared to Pd(100). For both surfaces increasing the temperature leads to faster reduction. Kinetic analysis using AE equation suggests a phase-boundary controlled process for Pd(100) in the temperature range investigated. For Pd$_{75}$Ag$_{25}$(100) the reduction process is diffusion limited at temperatures at and lower than 70 °C. At higher temperatures the mechanism changes to a phase-boundary controlled process also for this surface.

Density function theory calculations show that the presence of silver in the outermost surface layer significantly increases the CO diffusion barriers on the metallic Pd$_{75}$Ag$_{25}$(100) surface compare to Pd(100) and weakens the CO binding. These effects of Ag may explain the slower reduction of the √5 surface oxide on Pd$_{75}$Ag$_{25}$(100) relative to Pd(100).

Fig. 6. 0.25 ML CO adsorbed on Pd$_3$Ag(100) where the (2 × 2) unit cell is indicated. The arrows represent the direction of the structural movement of the surface Pd and Ag atoms after CO adsorption compared to the clean surface. Pd atoms are represented as blue spheres, and silver atoms as gray.
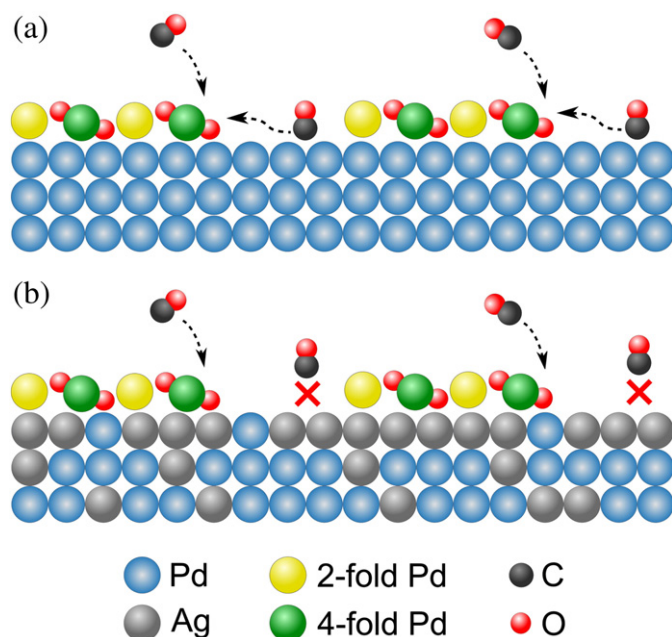
Fig. 7. Schematic depiction of the surface oxide reduction by CO for (a) Pd(100) and (b) Pd$_{75}$Ag$_{25}$(100). (The true orientation of the oxide relative to the substrate is not correctly represented in the illustration).

Acknowledgments

References

[1] E. Lundgren, A. Mikkelsen, J.N. Andersen, G. Kresse, M. Schmid, P. Varga, J. Phys. Condens. Matter 18 (30) (2006) R481.
[2] H. Over, Chem. Rev. 112 (6) (2012) 3356.
[3] R. Westerström, J.G. Wang, M.D. Ackermann, J. Gustafson, A. Resta, A. Mikkelsen, J.N. Andersen, E. Lundgren, O. Balmes, X. Torrelles, J.W.M. Frenken, B. Hammer, J. Phys. Condens. Matter 20 (18) (2008) 184018.
[4] B.L.M. Hendriksen, J.W.M. Frenken, Phys. Rev. Lett. 89 (2002) 046101.
[5] M.D. Ackermann, T.M. Pedersen, B.L.M. Hendriksen, O. Robach, S.C. Bobaru, I. Popa, C. Quiros, H. Kim, B. Hammer, S. Ferrer, J.W.M. Frenken, Phys. Rev. Lett. 95 (2005) 255505.
[6] B.L.M. Hendriksen, S.C. Bobaru, J.W.M. Frenken, Surf. Sci. 552 (1–3) (2004) 229.
[7] R. van Rijn, O. Balmes, R. Felici, J. Gustafson, D. Wermeille, R. Westerstroöm, E. Lundgren, J.W.M. Frenken, J. Phys. Chem. C 114 (14) (2010) 6875.
[8] J. Gustafson, R. Westerström, A. Mikkelsen, X. Torrelles, O. Balmes, N. Bovet, J.N. Andersen, C.J. Baddeley, E. Lundgren, Phys. Rev. B 78 (2008) 045423.
[9] J. Gustafson, R. Westerström, A. Resta, A. Mikkelsen, J.N. Andersen, O. Balmes, X. Torrelles, M. Schmid, P. Varga, B. Hammer, Catal. Today 145 (3–4) (2009) 227.
[10] J. Gustafson, R. Westerström, O. Balmes, A. Resta, R. van Rijn, X. Torrelles, C.T. Herbschleb, J.W.M. Frenken, E. Lundgren, J. Phys. Chem. C 114 (10) (2010) 4580.
[11] H. Over, Y.D. Kim, A.P. Seitsonen, S. Wendt, E. Lundgren, M. Schmid, P. Varga, A. Morgante, G. Ertl, Science 287 (5457) (2000) 1474.
[12] Y.B. He, M. Knapp, E. Lundgren, H. Over, J. Phys. Chem. B 109 (46) (2005) 21825.
[13] H. Over, O. Balmes, E. Lundgren, Catal. Today 145 (3–4) (2009) 236.
[14] J. Aßmann, D. Crihan, M. Knapp, E. Lundgren, E. Löffler, M. Muhler, V. Narkhede, H. Over, M. Schmid, A.P. Seitsonen, P. Varga, Angew. Chem. Int. Ed. 44 (6) (2005) 917.
[15] P.-A. Carlsson, V.P. Zhdanov, M. Skoglundh, Phys. Chem. Chem. Phys. 8 (2006) 2703.
[16] M.A. Newton, A.J. Dent, S. Diaz-Moreno, S.G. Fiddy, B. Jyoti, J. Evans, Chem. Eur. J. 12 (7) (2006) 1975.
[17] M.E. Grass, Y. Zhang, D.R. Butcher, J.Y. Park, Y. Li, H. Bluhm, K.M. Bratlie, T. Zhang, G.A. Somorjai, Angew. Chem. Int. Ed. 47 (46) (2008) 8893.
[18] J. Rogal, K. Reuter, M. Scheffler, Phys. Rev. Lett. 98 (2007) 046101.
[19] A. Hellman, A. Resta, N.M. Martin, J. Gustafson, A. Trinchero, P.-A. Carlsson, O. Balmes, R. Felici, R. van Rijn, J.W.M. Frenken, J.N. Andersen, E. Lundgren, H. Grönbeck, J. Phys. Chem. Lett. 3 (6) (2012) 678.
[20] S. Blomberg, M.J. Hoffmann, J. Gustafson, N.M. Martin, V.R. Fernandes, A. Borg, Z. Liu, R. Chang, S. Matera, K. Reuter, E. Lundgren, Phys. Rev. Lett. 110 (2013) 117601.
[21] M. Ziauddin, G. Veser, L.D. Schmidt, Catal. Lett. 46 (3–4) (1997) 159.
[22] R. Westerström, M.E. Messing, S. Blomberg, A. Hellman, H. Grönbeck, J. Gustafson, N.M. Martin, O. Balmes, R. van Rijn, J.N. Andersen, K. Deppert, H. Bluhm, Z. Liu, M.E. Grass, M. Hävecker, E. Lundgren, Phys. Rev. B 83 (2011) 115440.
[23] J. Rogal, K. Reuter, M. Scheffler, Phys. Rev. B 75 (20) (2007) 205433.
[24] T.W. Orent, S.D. Bader, Surf. Sci. 115 (1982) 323.
[25] G. Zheng, E.I. Altman, J. Phys. Chem. B 106 (5) (2002) 1048.
[26] D.T. Vu, K.A.R. Mitchell, O.L. Warren, P.A. Thiel, Surf. Sci. 318 (1994) 129.
[27] M. Saidy, O.L. Warren, P.A. Thiel, K.A.R. Mitchell, Surf. Sci. 494 (2001) L799.
[28] M. Todorova, E. Lundgren, V. Blum, A. Mikkelsen, S. Gray, J. Gustafson, M. Borg, J. Rogal, K. Reuter, J.N. Andersen, M. Scheffler, Surf. Sci. 541 (2003) 101.
[29] P. Kostelník, N. Seriani, G. Kresse, A. Mikkelsen, E. Lundgren, V. Blum, T. Sikola, P. Varga, M. Schmid, Surf. Sci. 601 (6) (2007) 1574.
[30] P.T. Wouda, M. Schmid, B. Nieuwenhuys, P. Varga, Surf. Sci. 417 (2–3) (1998) 292.
[31] J.R. Kitchin, K. Reuter, M. Scheffler, Phys. Rev. B 77 (2008) 075437.
[32] B.C. Khanra, M. Menon, Physica B 291 (3–4) (2000) 368.
[33] M. Ropo, K. Kokko, L. Vitos, J. Kollár, Phys. Rev. B 71 (2005) 045411.
[34] M. Ropo, Phys. Rev. B 74 (2006) 195401.
[35] O.M. Løvvik, Surf. Sci. 583 (1) (2005) 100.
[36] H.Y. Kim, H.G. Kim, J.H. Ryu, H.M. Lee, Phys. Rev. B 75 (2007) 212105.
[37] S. González, K.M. Neyman, S. Shaikhutdinov, H.-J. Freund, F. Illas, J. Phys. Chem. C 111 (18) (2007) 6852.
[38] T. Marten, O. Hellman, A.V. Ruban, W. Olovsson, C. Kramer, J.P. Godowski, L. Bech, Z. Li, J. Onsgaard, I.A. Abrikosov, Phys. Rev. B 77 (2008) 125406.
[39] L. Vitos, A.V. Ruban, H.L. Skriver, J. Kollár, Surf. Sci. 411 (1–2) (1998) 186.
[40] A.V. Ruban, S.I. Simak, P.A. Korzhavyi, B. Johansson, Phys. Rev. B 75 (2007) 054113.
[41] D. Tománek, S. Mukherjee, V. Kumar, K.H. Bennemann, Surf. Sci. 114 (1) (1982) 11.
[42] L.C.A. van den Oetelaar, O.W. Nooij, S. Oerlemans, A.W. Denier van der Gon, H.H. Brongersma, L. Lefferts, A.G. Roosenbrand, J.A.R. van Veen, J. Phys. Chem. B 102 (18) (1998) 3445.
[43] L.E. Walle, H. Grönbeck, V.R. Fernandes, S. Blomberg, M.H. Farstad, K. Schulte, J. Gustafson, J.N. Andersen, E. Lundgren, A. Borg, Surf. Sci. 606 (23–24) (2012) 1777.
[44] G. Veser, A. Wright, R. Caretta, Catal. Lett. 58 (4) (1999) 199.
[45] G. Ketteler, D. Ogletree, H. Bluhm, H. Liu, E. Hebenstreit, M. Salmeron, J. Am. Chem. Soc. 127 (51) (2005) 18269.
[46] I. Nakai, H. Kondoh, T. Shimada, A. Resta, J.N. Andersen, T. Ohta, J. Chem. Phys 124 (2006) 224712.
[47] R. Nyholm, J.N. Andersen, U. Johansson, B.N. Jensen, I. Lindau, Nucl. Instrum. Methods Phys. Res., Sect. A (2001) 520(467–468, Part 1).

[48] S. Doniach, M. Sunjic, J. Phys. C: Solid State Phys. 3 (1970) 285.
[49] M.E. Brown, D. Dollimore, A.K. Galwey, Reactions in the solid state, Comprehensive Chemical Kinetics, vol. 22, Elsevier Science, 1980.
[50] B. Hammer, L.B. Hansen, J.K. Nørskov, Phys. Rev. B 59 (1999) 7413.
[51] J. Greeley, J.K. Nørskov, M. Mavrikakis, Annu. Rev. Phys. Chem. 53 (1) (2002) 319.
[52] J.P. Perdew, K. Burke, M. Ernzerhof, Phys. Rev. Lett. 77 (18) (1996) 3865.
[53] J.A. White, D.M. Bird, Phys. Rev. B 50 (1994) 4954.
[54] D. Vanderbilt, Phys. Rev. B 41 (1990) 7892.
[55] H.J. Monkhorst, J.D. Pack, Phys. Rev. B 13 (1976) 5188.
[56] J. Neugebauer, M. Scheffler, Phys. Rev. B 46 (1992) 16067.
[57] L. Bengtsson, Phys. Rev. B 59 (1999) 12301.
[58] G. Henkelman, B.P. Uberuaga, H. Jónsson, J. Chem. Phys. 113 (22) (2000) 9901.
[59] C.T. Williams, E.K.-Y. Chen, C.G. Takoudis, M.J. Weaver, J. Phys. Chem. B 102 (24) (1998) 4785.
[60] E. Lundgren, J. Gustafson, A. Resta, J. Weissenrieder, A. Mikkelsen, J.N. Andersen, L. Köhler, G. Kresse, J. Klikovits, A. Biederman, M. Schmid, P. Varga, J. Elect. Spectr. Rel. Phen. 144–147 (2005) 367.
[61] J. Klikovits, M. Schmid, J. Gustafson, A. Mikkelsen, A. Resta, E. Lundgren, J.N. Andersen, P. Varga, J. Phys. Chem. B 110 (20) (2006) 9966.
[62] H. Gabasch, A. Knop-Gericke, R. Schlögl, M. Borasio, C. Weilach, G. Rupprechter, S. Penner, B. Jenewein, K. Hayek, B. Klötzer, Phys. Chem. Chem. Phys. 9 (4) (2007) 533.
[63] M. Blanco-Rey, D.J. Wales, S.J. Jenkins, J. Phys. Chem. C 113 (38) (2009) 16757.
[64] F. Gao, M. Lundwall, D.W. Goodman, J. Phys. Chem. C 112 (15) (2008) 6057.
[65] M. J. Hoffmann, K. Reuter, Pre-print, arXiv:1301.3285v1 [cond-mat.mtrl-sci] 15 Jan 2013.
[66] R.J. Behm, K. Christmann, G. Ertl, M.A. Van Hove, J. Chem. Phys 73 (6) (1980) 2984.
[67] A. Ortega, F.M. Huffman, A.M. Bradshaw, Surf. Sci. 119 (1) (1982) 79.
[68] J. Szanyi, W.K. Kuhn, D.W. Goodman, J. Vac. Sci. Technol. A 11 (4) (1993) 1969.
[69] S.E. Mason, I. Grinberg, A.M. Rappe, Phys. Rev. B 69 (2004) 161401.
[70] A.M. Bradshaw, F.M. Hoffmann, Surf. Sci. 72 (3) (1978) 513.
[71] P. Uvdal, P.-A. Karlsson, C. Nyberg, S. Andersson, N. Richardson, Surf. Sci. 202 (1–2) (1988) 167.
[72] K. Yoshioka, F. Kitamura, M. Takeda, M. Takahashi, M. Ito, Surf. Sci. 227 (1–2) (1990) 90.
[73] F.M. Hoffmann, Surf. Sci. Rep. 3 (2–3) (1983) 107.
[74] R.J. Behm, K. Christmann, G. Ertl, M.A. Van Hove, P.A. Thiel, W.H. Weinberg, Surf. Sci. 88 (2–3) (1979) L59.
[75] W. Berndt, A.M. Bradshaw, Surf. Sci. 279 (1–2) (1992) L165.
[76] J.N. Andersen, M. Qvarford, R. Nyholm, S.L. Sorensen, C. Wigren, Phys. Rev. Lett. 67 (1991) 2822.
[77] G. Kresse, A. Gil, P. Sautet, Phys. Rev. B 68 (2003) 073401.
[78] X. Ren, P. Rinke, M. Scheffler, Phys. Rev. B 80 (2009) 045402.
[79] S.E. Mason, I. Grinberg, A.M. Rappe, Phys. Rev. B 69 (2004) 161401.
[80] M. Birgersson, C.-O. Almbladh, M. Borg, J.N. Andersen, Phys. Rev. B 67 (2003) 045402.
[81] D.R. Alfonso, Top. Catal. 55 (5–6) (2012) 267.
[82] P. Dudin, A. Barinov, L. Gregoratti, M. Kiskinova, F. Esch, C. Dri, C. Africh, G. Comelli, J. Phys. Chem. B 109 (28) (2005) 13649.
[83] Y. Soma-Noto, W.M.H. Sachtler, J. Catal. 32 (2) (1974) 315.
[84] N.A. Khan, A. Uhl, S. Shaikhutdinov, H.J. Freund, Surf. Sci. 600 (9) (2006) 1849.
[85] Y. Ma, T. Diemant, J. Bansmann, R.J. Behm, Phys. Chem. Chem. Phys. 13 (2011) 10741.
[86] I.-H. Svenum, J.A. Herron, M. Mavrikakis, H.J. Venvik, Catal. Today 193 (1) (2012) 111.
[87] L.A. Mancera, R.J. Behm, A. Groß, Phys. Chem. Chem. Phys. 15 (2013) 1497.
[88] A. Noordermeer, G.A. Kok, B.E. Nieuwenhuys, Surf. Sci. 165 (2–3) (1986) 375.
[89] G. McElhiney, H. Papp, J. Pritchard, Surf. Sci. 54 (3) (1976) 617.
[90] A.L. Mejdell, D. Chen, T.A. Peters, R. Bredesen, H.J. Venvik, J. Membr. Sci. 350 (2010) 371.
[91] A. Ramachandran, W.M. Tucho, A.L. Mejdell, M. Stange, H.J. Venvik, J.C. Walmsley, R. Holmestad, R. Bredesen, A. Borg, Appl. Surf. Sci. 256 (2010) 6121.

Paper III

H$_2$ reduction of surface oxides on Pd-based membrane model systems - the case of Pd(100) and Pd$_{75}$Ag$_{25}$(100)

V.R. Fernandes, J. Gustafson, M.H. Farstad, L.E. Walle, S. Blomberg, E. Lundgren, H.J. Venvik, A. Borg

In manuscript.

H$_2$ reduction of surface oxides on Pd-based membrane model systems - the case of Pd(100) and Pd$_{75}$Ag$_{25}$(100)

V.R. Fernandes[a], J. Gustafson[b], M.H. Farstad[a], L.E. Walle[a], S. Blomberg[b], E. Lundgren[b], H.J. Venvik[c], A. Borg[a]

[a]*Dept. of Physics, Norwegian Univ. of Science and Technology, NO-7491 Trondheim, Norway*
[b]*Div. of Synchrotron Radiation Research, Lund Univ., Box 117, SE-221 00 Lund, Sweden*
[c]*Dept. of Chemical Engineering, Norwegian Univ. of Science and Technology, NO-7491 Trondheim, Norway*

Abstract

Reduction of the $(\sqrt{5} \times \sqrt{5})R27°$ surface oxide on Pd(100) and Pd$_{75}$Ag$_{25}$(100) surfaces by H$_2$ has been studied using high-resolution photoelectron spectroscopy *in situ* at H$_2$ pressures 5×10^{-9} mbar and 5×10^{-8} mbar and selected temperatures in the range 30°C to 170°C. The reduction is slower on Pd$_{75}$Ag$_{25}$(100) compared to Pd(100) for all temperatures and pressures investigated. The surface oxide reduction is rather independent of temperature for Pd(100), while for Pd$_{75}$Ag$_{25}$(100) shows a non-monotonic variation. As indicated by kinetic analysis, the complex reduction behavior is not well described by Avrami kinetics. The more general Šesták-Berggren equation was utilized to fit the experimental results. The dependence in temperature of the reduction rates for Pd$_{75}$Ag$_{25}$(100) correlates with the amount of surface Pd atoms. The results may have implication for understanding the oxidation, reduction and hydrogen transport properties of Pd-Ag membranes.

Keywords: H$_2$ reduction, PdAg alloy, surface oxide, Pd$_{75}$Ag$_{25}$(100), photoelectron spectroscopy

1. Introduction

The interaction of hydrogen with transition metal (TM) surfaces has been extensively studied due to its relevance for heterogeneous catalysis and industrial applications. In particular, palladium has attracted significant attention due to its excellent catalytic ability in catalytic oxidation as well as for hydrogenation and dehydrogenation reactions. Furthermore, palladium has high solubility, permeability and selectivity for hydrogen, thus being a suitable membrane material for hydrogen separation [1–6].

To prevent embrittlement occurring in pure Pd due to formation of hydride phases [1, 7], Pd-based alloys are often utilized in commercial membrane applications to suppress the $\alpha \rightarrow \beta$ hydride phase transition during operation at elevated temperature ($\leq$ 300°C) and pressure ($\leq$ 2MPa). Alloying palladium with silver has been found to increase the permeability and durability of membranes, with a maximum hydrogen permeability observed at 23wt% Ag [8], while retaining the high selectivity for hydrogen. Moreover, heat treatment of PdAg alloy membranes in air has been reported to enhance the hydrogen permeation [9–12]. Formation of a surface oxide as a result of this heat treatment is part of this picture [13]. In addition, several studies have reported oxida-tion and subsequent reduction to increase hydrogen per-meation [9, 10, 13–15]. Recently, it has also been ob-served that surface oxide formation on PdAg membrane surfaces may reduce the inhibition effect of CO on the hy-drogen permeation of such membranes [16]. Full under-standing of the interaction of hydrogen with the oxide and its reduction behavior, the reason for the beneficial effects of thermal treatment, as well as effects of the alloying ele-ment silver in surface reactions, are still partially lacking. Investigation of palladium model systems provides a route to address these questions. In the present work the (100) surfaces of Pd and Pd$_{75}$Ag$_{25}$ have been selected for this purpose.

Segregation effects are likely to influence the perfor-mance of a Pd based alloy membrane or catalyst. In PdAg alloys silver segregates to the surface under vacuum con-ditions [17–26] due to the lower surface energy of Ag compared to Pd [21, 23, 27, 28], and geometric effects resulting from the slightly larger Ag atoms, which induce less stress at the surface. Reversed segregation of Ag in PdAg alloys has been found as a result of adsorption of oxygen [18, 20, 29, 30] and hydrogen [25, 30–33].

Exposing the Pd(100) surface to oxygen under ultra-high vacuum (UHV) conditions results in formation of

four different oxygen induced structures at coverages below 1 ML, namely the p(2 × 2), c(2 × 2), p(5 × 5) and (√5×√5)R27° (henceforth denoted √5) structure [34, 35]. The latter of these structures, consisting of a PdO(101) monolayer on top of the underlying Pd(100) substrate, has been subject to detailed investigations over the years [36–39]. At pressure above 1 Torr and temperature 300°C, bulk PdO is formed [40, 41]. Recently, we showed that $Pd_{75}Ag_{25}(100)$ forms a (√5×√5)R27° surface oxide, similar to the one observed on Pd(100) [18].

Interaction of H_2 with surfaces of bulk PdO(101) has been studied both experimentally and theoretically [42–44]. It was found that H_2 adsorbs molecularly at under-coordinated Pd sites, and dissociates to form Pd-H and O-H groups. The oxide is reduced by hydrogen at room temperate and water is formed in a reaction that, according to density functional theory (DFT), proceeds by disproportionation of the OH groups [44], $HO_u + HO_u \rightarrow H_2O + O_u$, where the subscript u refers to undercoordinated oxygen in the oxide. Blanco-Rey *et al.* [42], by means of DFT, analyzed the reduction of the √5 surface oxide on Pd(100) by H_2 and found significant differences to the case of bulk PdO(101). The authors concluded that despite the outer layers of these surfaces having similar atomic structure, the reduction follows different mechanisms. H_2 chemisorbs on the surface of bulk PdO(101) but not on the √5 surface oxide. Adsorption of atomic hydrogen was reported on both surfaces.

In the present work, we have investigated the H_2 induced reduction of the √5 surface oxide on Pd(100) and $Pd_{75}Ag_{25}(100)$ surfaces, as model systems for Pd based alloy membranes. High resolution X-ray photoelectron spectroscopy (HRXPS) measurements were used to monitor the reduction of the √5 surface oxide upon exposure to 5×10^{-9} and 5×10^{-8} mbar H_2 pressures at temperatures in the range 30°C to 170°C. Kinetic modeling was employed to gain insight into the reaction mechanism and evaluate the influence of silver on the surface oxide reduction behavior. We observe a complex temperature dependent behavior. The overall reduction rates were found to be slower on $Pd_{75}Ag_{25}(100)$ compared to Pd(100) for all temperature and pressures investigated. Kinetic modeling indicates that the reduction process deviates significantly from Avrami theory.

2. Experimental methods

Pd(100) and $Pd_{75}Ag_{25}(100)$ single crystals were cleaned by cycles of sputtering, oxygen treatment and annealing to selected temperatures. An annealing temperature of 705°C was used for Pd(100), while $Pd_{75}Ag_{25}(100)$ was heated to 625°C. This procedure yielded well-defined, contaminant free surfaces, as judged by LEED patterns and HRXPS measurements of the C $1s$ and S $2p$ core level regions. The oxides were formed by exposing the surfaces to oxygen at 320 °C, using pressures 5×10^{-6} mbar for Pd(100) and 5×10^{-3} mbar for $Pd_{75}Ag_{25}(100)$.

HRXPS experiments were performed at beam line I311 at the MAX II storage ring of the MAX IV Laboratory, in Lund, Sweden. This beam line is equipped with a modified SX-700 monochromator and a large Scienta type hemispherical electron energy analyzer (SCIENTA SES200) [45]. The base pressure in the UHV system was $< 2 \times 10^{-10}$ mbar.

The reduction of the √5 surface oxide was monitored *in situ* by recording the $Pd3d_{5/2}$ core level spectra during exposure to H_2 at 5×10^{-8} and 5×10^{-9} mbar and selected temperatures in the range 30°C to 170°C. One scan of the √5 surface oxide was recorded before hydrogen exposure. The core level spectra were recorded at photon energy 400 eV. The overall spectral resolution was about 200 meV. All spectra were measured at normal emission. The binding energy was calibrated against the Fermi edge. All spectra have been normalized to the background at the low binding energy side of the core level peaks. Linear background subtraction has been applied and Doniach-Sunjic line shapes used for fitting the spectra [46].

The fitting of the Pd $3d_{5/2}$ core level spectra, recorded continuously during the reduction, was performed in a two-step process. We began by analyzing the first and last scan of a given measurement series to obtain the value of the Gaussian and Lorentzian widths for all the contributions from the √5 oxide and reduced surfaces, the components due to two-fold and four-fold oxygen coordinated Pd, Pd bulk, interface Pd (for Pd(100)), and metallic surface components. Next, fitting was performed for all the scans of a reduction series, where the Gaussian and Lorentzian widths were allowed a 2% variation.

3. Kinetic Analysis

Kinetic modeling was utilized to model the reduction of the √5 surface oxide and infer about the character of the reaction. In solid state kinetics the rate law of a transformation process at constant temperature is expressed in the form of a differential equation:

$$\frac{d\alpha}{dt} = kf(\alpha), \tag{1}$$

where α is the so-called degree of conversion, k is the rate of the process, t is the time, and $f(\alpha)$ is a function repre-

senting the mathematical expression of the kinetic model describing the reaction. The degree of conversion of the reaction, α, changes progressively from reactants ($\alpha = 0$) to products ($\alpha = 1$).

We have tried to apply several different models for $f(\alpha)$, such as the models of contracting area, contracting volume, Johnson-Mehl-Avrami (JMA), Prout-Tompkins (PT), reaction order, Jander equation, Ginstling-Brounstein, or Šesták-Berggren (SB) [47]. However, as will be presented in the Results part, models based on nucleation and growth are the most adequate to model our experimental observations. Here we will only refer to the relevant models for this work, which are the JMA and SB.

The JMA model (also known as Avrami-Erofeev) is based on the formation and growth of nuclei and can generally be applied to any process that is governed by nucleation and/or growth and where the growing phases develop from different nuclei and come into contact after some time (preventing further growth) [47]. This model relies on the assumptions that nucleation occurs randomly in time and homogeneously distributed across the untransformed portion of the material, and that the growth occurs at the same rate in all directions and does not depend on the extent of transformation. The JMA model is expressed in its differential form as

$$f(\alpha) = n(1 - \alpha)[-ln(1 - \alpha)]^{1-1/n}, \qquad (2)$$

where n is denoted the index of reaction. The parameter n usually has a value of 1.5, 2, 3 or 4 which reflects the nature of the transformation [47]. Although the applicability of the JMA equation are known, in practice it is sometimes difficult to verify if all criteria are met. Málek developed a procedure to test whether or not a process is described by the JMA model [48]. The function $z(\alpha) = \phi t$ is defined, where ϕ is the conversion rate of the process, i.e. $d\alpha/dt$. When $z(\alpha)$ is normalized to the interval (0,1), for practicality, and plotted as a function α, it has its maximum located at the constant value of $\alpha_{max} = 0.632$. This value is characteristic of the JMA model [48, 49]. If the maximum α_{max} of the experimental data falls in the interval $0.61 < \alpha_{max} < 0.65$ it is likely to be a process described by this model [48, 49].

A more general, empirical rate equation has been proposed by Šesták and Berggren (SB) [50, 51]:

$$f(\alpha) = \alpha^M (1 - \alpha)^N \qquad (3)$$

where the exponents M and N represent the kinetic parameters of the process. In the literature this model is sometimes referred to as the extended PT equation [52]. The relative values of M and N determine the relative contribution of the acceleratory and decay regions in the process. It has also been shown that these two parameters are physically meaningful only if $M < 1$ [53]. The SB equation includes the PT and JMA models for given M and N. When $M = N = 1$ the SB equation becomes the PT model. For $M = 0.72$ and $N = 0.76$ the SB equation corresponds to the JMA model with $n = 3$ and for $M = 0.77$ and $N = 0.69$ it corresponds to the JMA model with $n = 4$. The empirical SB model thus includes other models as special cases, being a plausible description of nucleation and growth processes [49, 50, 54]. However, the SB equation is a phenomenological description of kinetics, and the physical significance of the parameters M and N is limited.

4. Results

4.1. Reduction of the $(\sqrt{5} \times \sqrt{5})R27°$ surface oxide by H_2

Reduction by hydrogen was preceded by the formation of the $\sqrt{5}$ surface oxide on Pd(100) and Pd$_{75}$Ag$_{25}$(100). The structure of the $\sqrt{5}$ oxide is well understood and has been discussed elsewhere for both Pd(100)[38, 39] and Pd$_{75}$Ag$_{25}$(100) [18]. Figure 1 presents recorded Pd $3d_{5/2}$ core level spectra, as a function of H_2 exposure time, during reduction experiments for Pd(100) and Pd$_{75}$Ag$_{25}$(100) at temperature 120°C and 5×10^{-8} mbar H_2. Figure 1(a) displays the evolution of the Pd $3d_{5/2}$ core level spectrum as a function of time for Pd(100). The labels 1 and 2 denote two different stages during the reduction experiments. Fitted spectra at these two stages are shown in Figure 1(b). Spectrum 1 was recorded of the oxidized Pd(100) before H_2 exposure. The spectrum consists of the bulk Pd component, at binding energy of 334.92 eV, and three oxide induced contributions [18, 38]. The oxide induced contributions, shifted +0.39 eV and +1.22 eV relative to the bulk component, are attributed to two-fold and four-fold oxygen coordinated palladium atoms, respectively. The third oxide induced contribution, shifted -0.33 eV relative to the Pd bulk peak, is due to interface Pd atoms between the surface oxide and the bulk Pd crystal. When the reduction is complete only the bulk Pd peak and a surface component, shifted -0.39 eV relative to the bulk component, are present, illustrated by spectrum 2 in Figure 1(b).

Figures 1(c) and (d) show the corresponding spectra recorded for Pd$_{75}$Ag$_{25}$(100). Spectrum 3, displayed in Figure 1(d), is consistent with a $\sqrt{5}$ surface oxide on Pd$_{75}$Ag$_{25}$(100) [18]. The spectrum contains the bulk Pd$_{75}$Ag$_{25}$ contribution, located at binding energy 334.76
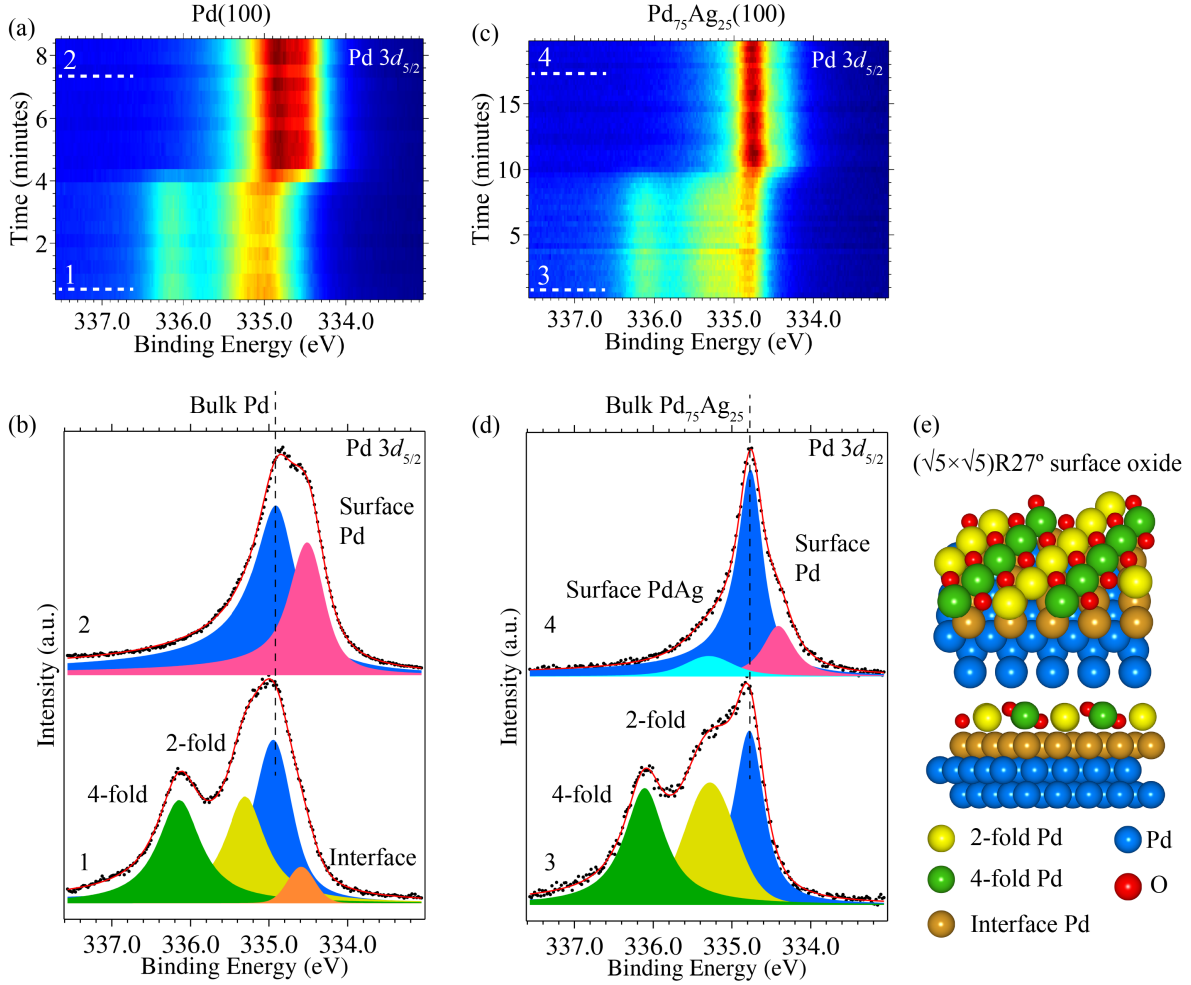
Figure 1: Reduction of the $(\sqrt{5} \times \sqrt{5})R27°$ surface oxide on Pd(100) and $Pd_{75}Ag_{25}(100)$ upon 5×10^{-8} mbar H_2 exposure at 120°C monitored using HRXPS. (a) and (c): Evolution of the Pd $3d_{5/2}$ core level spectra during the reduction reaction for Pd(100) and $Pd_{75}Ag_{25}(100)$, respectively. (b) and (d): Decomposition of the Pd $3d_{5/2}$ core level spectra for Pd(100) and $Pd_{75}Ag_{25}(100)$, respectively, at two stages in the reduction experiments, oxidized surface 1/3 and fully reduced surface 2/4. (e): Model of the $(\sqrt{5} \times \sqrt{5})R27°$ surface oxide on Pd(100).

eV, and two oxide induced contributions, shifted by +1.35 eV and +0.52 eV relative to the bulk component, attributed to the four-fold and two-fold oxygen coordinated Pd atoms, respectively. The absence of an interface component at lower binding energy in the case of $Pd_{75}Ag_{25}(100)$ has been attributed to the presence of a silver rich interface layer between the surface oxide and bulk $Pd_{75}Ag_{25}$ [18].

Spectrum 4 in Figure 1(d), recorded after complete oxide reduction, shows the bulk $Pd_{75}Ag_{25}$ component and two additional components. A small contribution, shifted +0.54 eV relative to the bulk peak, is observed along with a component with stronger spectral intensity, shifted -0.34 eV towards lower binding energy relative to the Pd $3d_{5/2}$ bulk contribution. As prepared clean $Pd_{75}Ag_{25}(100)$ is characterized by a surface related contribution in the Pd $3d_{5/2}$ core level spectrum at higher binding energy,

+0.52 eV, relative to the Pd $3d_{5/2}$ bulk component from $Pd_{75}Ag_{25}$, originating from Pd atoms embedded in the surface region of a silver terminated $Pd_{75}Ag_{25}(100)$ surface [18]. The component at lower binding energy relative to the bulk component is consistent with surface Pd atoms [18], indicating that the silver content in the outermost surface layer after oxide reduction is lower compared to as prepared, clean $Pd_{75}Ag_{25}(100)$. The presence of more palladium atoms on the surface after reduction can be understood by the fact that upon reduction of the surface oxide Pd atoms remain on the surface while oxygen atoms react with hydrogen to form H_2O, followed by desorption from the surface.

Comparing Figures 1(a) and 1(c) and noting the difference in time scales for the two experiments, a sharp transition from oxidized to reduced surface is observed for Pd(100), while $Pd_{75}Ag_{25}(100)$ shows a more gradual and
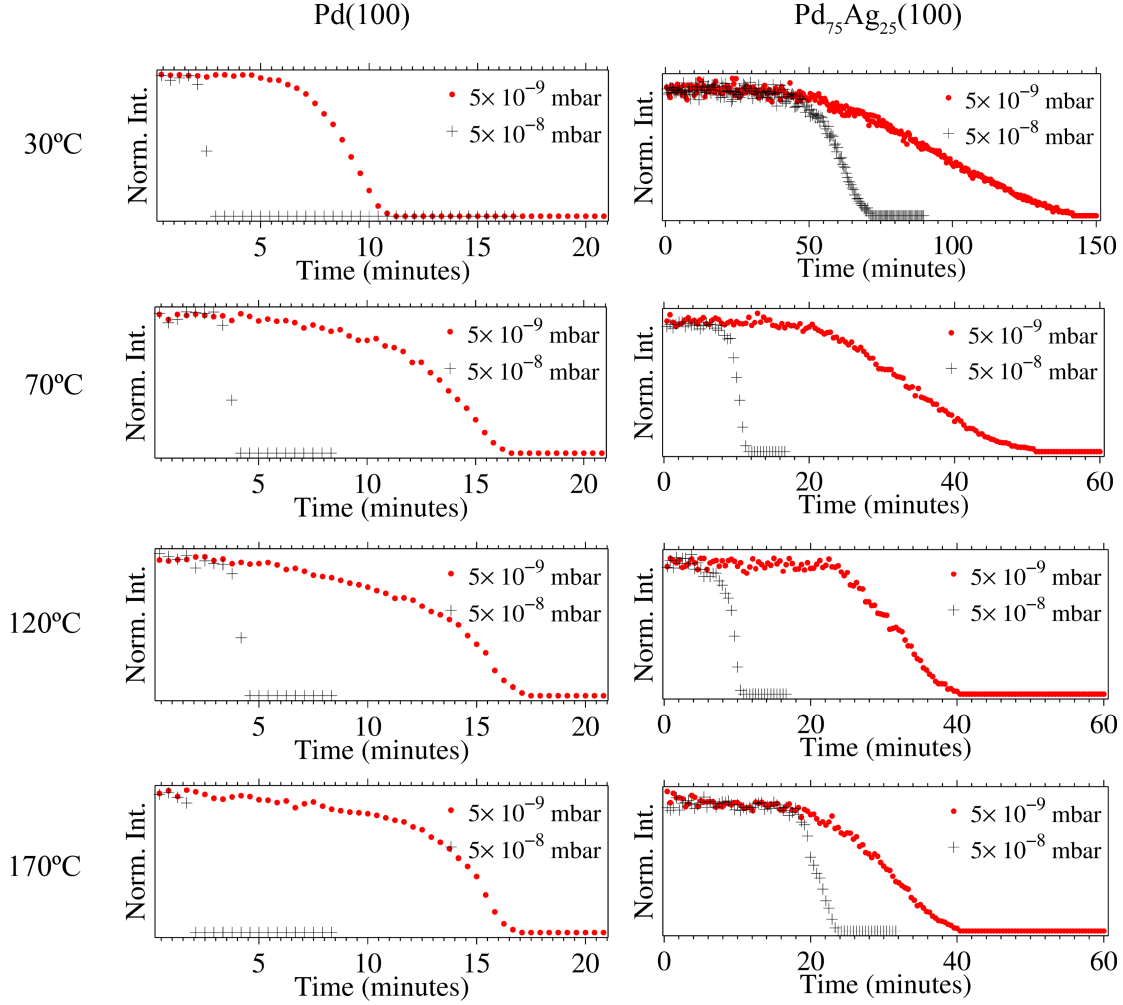
Figure 2: Intensity of the components due to 4-fold oxygen coordinated Pd atoms (i.e., the surface oxide) as a function of time, obtained by fitting the Pd $3d_{5/2}$ core level spectra recorded *in situ* during reduction of the $(\sqrt{5} \times \sqrt{5})$R27° surface oxide structure on Pd(100), left panels, and Pd$_{75}$Ag$_{25}$(100), right panels. Reduction was performed at selected temperatures by exposure to H_2 at pressures 5×10^{-9} mbar and 5×10^{-8} mbar. The time scale varies between the experiments.

slower reduction process. Reduction experiments analogous to the ones presented in Figure 1 were performed for both Pd(100) and Pd$_{75}$Ag$_{25}$(100) at H_2 pressures of 5×10^{-8} mbar and 5×10^{-9} mbar and at selected temperatures in the range 30°C to 170°C. Through fitting of all the data, exemplified in Figures 1(a) and (c), the development of the components related to the surface oxide as function of H_2 exposure time were obtained. The Pd $3d_{5/2}$ core level component due to 4-fold oxygen coordinated Pd atoms provides a cleaner signature of the amount of oxide present on the surface compared to that originating from 2-fold oxygen coordinated Pd atoms and is therefore used in our analysis. Figure 2 displays the intensity of this Pd $3d_{5/2}$ core level component as a function of time for all experiments performed. The data presented has been normalized relative to the maximum intensity observed for each experiment.

The time traces of the $\sqrt{5}$ surface oxide peak intensity (Figure 2) show a reduction behavior which can be divided into two stages. During the initial stage, there seems to an induction period of no or rather slow decrease on the intensity of the 4-fold $\sqrt{5}$ surface oxide component. A significantly faster second stage follows where the intensity of the $\sqrt{5}$ surface oxide component decreases faster until it vanishes completely. The length of the induction period (initial stage) varies between experiments, which is attributed to variations in oxide quality from different preparations. For Pd(100), at pressure $P_{H_2} = 5 \times 10^{-9}$ mbar, the length of the induction and the extent of reduction reached before the process accelerates is significantly longer for temperature of 70°C and above, compared to 30°C. Once the reaction enters the second stage the $\sqrt{5}$ surface oxide is quickly reduced. For Pd(100) and $P_{H_2} = 5 \times 10^{-8}$ mbar the second stage of the reduction

5

Table 1: Maximum experimental reduction rates for the H_2 induced $(\sqrt{5} \times \sqrt{5})R27°$ surface oxide reduction on Pd(100) and $Pd_{75}Ag_{25}(100)$.

	5×10^{-9} mbar		5×10^{-8} mbar	
	Pd(100)	$Pd_{75}Ag_{25}(100)$	Pd(100)[a]	$Pd_{75}Ag_{25}(100)$
30°C	0.29	0.014	1.1	0.055
70°C	0.20	0.040	1.1	0.46
120°C	0.21	0.072	1.0	0.45
170°C	0.27	0.058	2.2	0.21

[a] The values are calculated by linear approximation using three (two for 170°C) experimental points only, and therefore represent an approximate value for the maximum reduction rate in this case.

is notably faster. At 170°C the process is so fast that our HRXPS measurement can not follow the second stage of the reduction. The induction period increases also here for 70°C and 120°C, relative to 30°C, but decreases again at 170°C.

Turning to $Pd_{75}Ag_{25}(100)$, at P_{H_2} = 5×10^{-9} mbar, the $\sqrt{5}$ surface oxide intensity decay is similar to that of Pd(100), i.e. characterized by a two stage process. However, the time required to complete the reduction is significantly longer for the alloy surface, as can be seen from the time scales of the different panels in Figure 2. On $Pd_{75}Ag_{25}(100)$, using P_{H_2} = 5×10^{-8} mbar, yields faster reduction compared to P_{H_2} = 5×10^{-9} mbar. The length of both the first and second stages of the reduction is significantly longer on $Pd_{75}Ag_{25}(100)$ compared to Pd(100), for all pressures and temperatures investigated.

From the times traces of the $\sqrt{5}$ surface oxide reduction presented in Figure 2 the experimental maximum reduction rate can be obtained, and these are given in Table 1. For the alloy surface the maximum reduction rate is significantly lower compared to pure Pd, for all pressures and temperatures. In the case of Pd(100) and P_{H_2} = 5×10^{-9} mbar, the values of the maximum reduction rate display a relatively small temperature variation, while for $Pd_{75}Ag_{25}(100)$, at the same pressure, there is a significant variation with temperature. For P_{H_2} = 5×10^{-8} mbar the maximum reduction rates follow a similar trend. On the Pd(100) surface the rates are relatively similar, within the large experimental uncertainty due to the fast transition in these cases. On the $Pd_{75}Ag_{25}(100)$, there is a significant difference between 30°C and higher temperatures.

4.2. Kinetic Analysis

During the H_2 induced reduction of the $\sqrt{5}$ surface oxide on Pd(100) and $Pd_{75}Ag_{25}(100)$ oxygen atoms are removed by reaction with hydrogen. This is a gas-solid

reaction where the $\sqrt{5}$ surface oxide is consumed and a metallic surface accessible for molecular hydrogen adsorption and dissociation is formed. As the intensity of the oxide components in the HRXPS spectra is proportional to the amount of $\sqrt{5}$ surface oxide remaining on the surfaces, the fractional extent of the reaction, i.e. the amount of reduced surface can be defined from the normalized oxide intensity decay curves as $\alpha = 1 - \text{Intensity}_{4-\text{fold}}$.

Theoretical DFT calculations indicate that molecular H_2 does not adsorb on the $\sqrt{5}$ surface oxide on Pd(100) [42]. Imperfections such as steps and defects may play the role as H_2 adsorption sites at which the reduction process may nucleate. Further surface oxide reduction proceeds through growth of reduced areas where molecular hydrogen can adsorb, dissociate, and migrate to oxide island boarders. The reduction of surface oxides on both Rh and Pd upon exposure to H_2 has been reported to be initiated at defects [55–57], where the reducing agent can adsorb and nucleate the reduction process. This suggests that kinetic models based on nucleation and growth are adequate to describe our experiments.

We start by evaluating if the kinetics obtained from the HRXPS data are well described by the JMA model, following the procedure devised by Málek [48, 49]. Figure 3 displays the function $z(\alpha)$ *versus* α for three experiments at 70°C. We recall from Section 3 that if a process follows the JMA model, this curve has a maximum at the constant value α_{max} = 0.632, indicated in Figure 3 by the vertical dashed line. Table 2 displays the peak values for all the experiments performed at 70°C except for Pd(100) at P_{H_2} = 5×10^{-8} mbar, in which the very fast transition from oxidized to reduced surface does not allow a meaning full calculation.

The three example experiments in Figure 3 show that the maxima of the three curves are not within the acceptable interval for α_{max}. The curves peak at both lower and
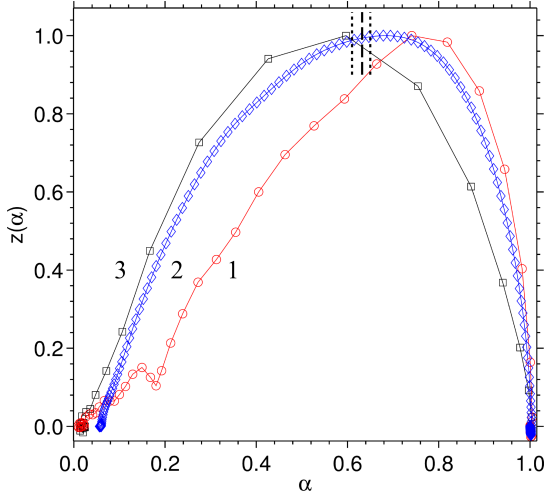
Figure 3: Normalized $z(\alpha)$ function for the $(\sqrt{5} \times \sqrt{5})R27°$ surface oxide reduction at 70°C for three experiments are displayed, namely (1) Pd(100) at $P_{H_2} = 5\times10^{-9}$ mbar, (2) $Pd_{75}Ag_{25}(100)$ at $P_{H_2} = 5\times10^{-9}$ mbar, and (3) $Pd_{75}Ag_{25}(100)$ at $P_{H_2} = 5 \times 10^{-8}$ mbar. The vertical dashed and dotted lines corresponds to the characteristic value for the JMA model $\alpha_{max} = 0.632$, and the acceptable interval $0.61 < \alpha_{max} < 0.65$ for the JMA model, respectively.

Table 2: Values of α corresponding to the maximum of the normalized $z(\alpha)$ function for the $(\sqrt{5} \times \sqrt{5})R27°$ surface oxide reduction for Pd(100) and $Pd_{75}Ag_{25}(100)$ based on the data presented in Figure 2. The characteristic value for the JMA model is 0.632.

	5×10^{-9} mbar		5×10^{-8} mbar
	Pd(100)	$Pd_{75}Ag_{25}(100)$	$Pd_{75}Ag_{25}(100)$
30°C	0.70	0.72	0.64
70°C	0.74	0.68	0.60
120°C	0.77	0.68	0.62
170°C	0.71	0.71	0.51

higher α values. Noteworthy is the shape of the curve for Pd(100), which shows significant asymmetry, with a peak value of 0.74. Table 2 shows that all values for both $Pd_{75}Ag_{25}(100)$ and Pd(100), are above the acceptable maximum for $P_{H_2} = 5 \times 10^{-9}$ mbar. This finding is related to the slow reduction taking place during the induction period. This behavior is less pronounced for $Pd_{75}Ag_{25}(100)$, where the average peak value is lower than for Pd(100). For $Pd_{75}Ag_{25}(100)$ at $P_{H_2} = 5 \times 10^{-8}$ mbar, the values are within the $0.61 < \alpha_{max} < 0.65$ range for 30°C and 120°C, and lower for the remaining temperatures. The results presented in Table 2 indicate that, in general, the reduction process does not follow a JMA model, with the exception of two experiments on $Pd_{75}Ag_{25}(100)$.

The shape of the $z(\alpha)$ function and the shift of its maximum to both higher and lower values relative of the characteristic JMA parameters suggest a complex reduction behavior, not accounted for by this model. A more flexible kinetic model has therefore been considered, namely the SB model, equation 3. This equation was adapted to the data by least squares fitting, in order to obtain the overall reduction rate k and the parameters M and N, and the results obtained are presented in Table 3. Figure 4 displays fitted data for the three experiments performed at 70°C, as used for Figure 3, again omitting the Pd(100) at $P_{H_2} = 5 \times 10^{-8}$ mbar because of uncertainty.
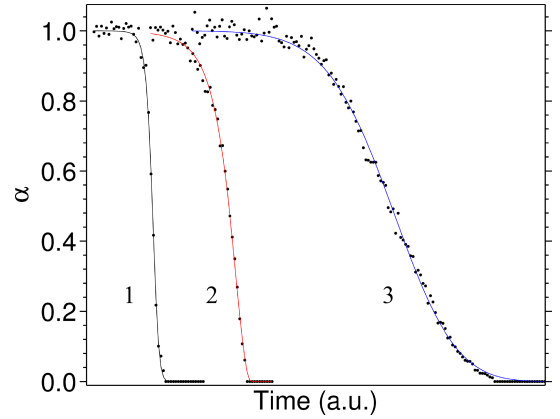

Figure 4: Least squares fitting of the intensity curves for the Pd $3d_{5/2}$ core level component corresponding to Pd atoms 4-fold coordinated to oxygen in the $(\sqrt{5} \times \sqrt{5})R27°$ using the equation $d\alpha/dt = kf(\alpha)$, where $f(\alpha) = \alpha^M(1-\alpha)^N$ corresponds to the Šesták-Berggren equation. Results from three experiments performed at temperature of 70°C are displayed, for (1) Pd(100) at $P_{H_2} = 5 \times 10^{-9}$ mbar, (2) $Pd_{75}Ag_{25}(100)$ at $P_{H_2} = 5 \times 10^{-9}$ mbar, and (3) $Pd_{75}Ag_{25}(100)$ at $P_{H_2} = 5 \times 10^{-8}$ mbar. The curves (2) and (3) are shifted in time.

The results for Pd(100) and $P_{H_2} = 5 \times 10^{-9}$ mbar show that the overall rate k of the reduction is relatively similar for all temperatures, but reflecting the somewhat slower reduction observed for intermediate temperatures. For $Pd_{75}Ag_{25}(100)$ and $P_{H_2} = 5 \times 10^{-9}$ mbar the overall reduction rate is lowest at 30°C, increases up to 120°C, and decreases at 170°C. A similar trend is observed for $P_{H_2} = 5 \times 10^{-8}$ mbar. The trends presented in Table 3 are in good agreement with the values maximum rate values displayed in Table 1.

For all the experiments the parameter $M < 1$ and is therefore within the limits of physical significance [53]. The results show that in general the decay region, exponent N, plays a significant role in the reduction, with its relative contribution in the reaction being larger than the acceleratory region, i.e. $N > M$, for all experiments. This can be understood by the significant induction periods in the reduction. In some cases the value of N is higher

Table 3: Kinetic analysis results of the H_2 induced $(\sqrt{5} \times \sqrt{5})R27°$ surface oxide reduction on Pd(100) and $Pd_{75}Ag_{25}(100)$ obtained by least square fitting of equation $d\alpha/dt = kf(\alpha)$. The function $f(\alpha) = \alpha^M(1 - \alpha)^N$ corresponds to the Šesták-Berggren equation.

| | 5×10^{-9} mbar | | | | | | 5×10^{-8} mbar | | |
| | Pd(100) | | | $Pd_{75}Ag_{25}(100)$ | | | $Pd_{75}Ag_{25}(100)$ | | |
	k (min^{-1})	M	N	k (min^{-1})	M	N	k (min^{-1})	M	N
30°C	0.86	0.55	1.01	0.029	0.45	0.70	0.17	0.60	1.11
70°C	0.54	0.50	1.19	0.13	0.67	0.87	1.58	0.57	1.13
120°C	0.46	0.49	1.15	0.22	0.59	0.92	1.40	0.52	1.19
170°C	0.61	0.50	1.19	0.16	0.54	0.93	0.62	0.52	1.10

than one, which indicates increased complexity. This is particularly evident for Pd(100), P_{H_2} = 5×10^{-9} mbar and temperatures at 70°C and above, and $Pd_{75}Ag_{25}(100)$, P_{H_2} = 5×10^{-8} , where the *M* parameter has values of about 0.50 and *N* has values about 1.15.

5. Discussion

The H_2 induced reduction of the $\sqrt{5}$ surface oxide for both Pd(100) and $Pd_{75}Ag_{25}(100)$, proceeding in two stages, with a slow initial stage, followed by a faster second stage where the intensity of the oxide components decreases significantly until complete removal, shows similarities with the reduction of surface oxide on (111) and (110) surfaces of Rh by H_2 [56–58]. Klikovits *et al.*, analyzing the reduction of surface oxide on Rh(111) by H_2 using STM and Avrami kinetics, found that the reduction of the surface oxide can only be initiated at steps and defects and consists of a two regime process. Initially, the rate of reduction is limited by hydrogen adsorption on the already reduced areas, and later by processes at the interface between oxidized and reduced areas [57]. Similar behavior was observed for the reduction of oxidized Rh(110) by hydrogen [56], and for the reduction of the $\sqrt{5}$ surface oxide Pd and $Pd_{75}Ag_{25}(100)$ by CO [59].

Theoretical DFT calculations predict that adsorption and dissociation of molecular hydrogen on the Pd(100) $\sqrt{5}$ surface oxide is not energetically favored [42]. Our results are in agreement with these findings. The extent of the first stage of the reduction differs in all the experiments, indicating that surface quality, i.e. defect density, is relevant to the onset of the second stage of the reduction. Defects in the surface oxide, steps, and domain boundaries may provide undercoordinated sites where H_2 can adsorb and dissociate, thus enabling the reaction with the surface oxide to produce H_2O, which immediately desorbs [60–68], leaving Pd sites available for further H_2 adsorption and subsequent oxide reduction. Comparing Pd(100) and $Pd_{75}Ag_{25}(100)$, it should be noted that the $\sqrt{5}$ surface oxide on $Pd_{75}Ag_{25}(100)$ has, in general, a larger number of misfit dislocations, and hence larger number of defects [18]. Still, the induction periods for this surface are longer. This findings may indicate that not all types of defects are facilitating H_2 adsorption and dissociation, or that Ag in the layer beneath the $\sqrt{5}$ surface oxide inhibits the progress of the reaction.

The reduction behavior has a complex temperature dependence. For Pd(100) the maximum experimental reduction rate is relatively independent of the temperature, while it displays significantly stronger variations with temperature for $Pd_{75}Ag_{25}(100)$. The observed reaction kinetics may be an interplay between temperature dependent factors such as H_2 sticking probability, adsorption of hydrogen on the reduced areas, hydrogen diffusion, as well as the influence of silver in the case of the $Pd_{75}Ag_{25}(100)$ surface.

On Pd surfaces, the sticking probability for hydrogen is reported as high, usually in the range 0.1 to 0.5 [60, 69–81], and thus not expected to significantly impact the surface oxide reduction. The amount of hydrogen adsorbed on the surface also depends on temperature. HRXPS analysis of the Pd(100) surface after complete reduction of the $\sqrt{5}$ surface oxide reveals that the final state of the surface under H_2 depends strongly on temperature. Figure 5(a) and (b) display fitted spectra of the Pd $3d_{5/2}$ core level after complete reduction of the $\sqrt{5}$ surface oxide using P_{H_2} = 5×10^{-8} mbar, for Pd(100) and $Pd_{75}Ag_{25}(100)$, respectively. For pure Pd, at 170°C and 120°C the Pd $3d_{5/2}$ core level spectra shows a clear surface core level shift contribution at lower binding energy relative to the bulk Pd. At and below 70°C no surface core level shift is observed, due high hydrogen coverage on the surface. Adsorbed hydrogen leads to a Pd $3d_{5/2}$ core level bind-

8

ing energy similar to bulk Pd and can not be resolved in the HRXPS spectra. The same behavior is observed for $P_{H_2} = 5 \times 10^{-9}$ mbar (not shown). This observations are in agreement with temperature programmed desorption (TPD) studies of hydrogen adsorption on Pd surfaces, showing a main desorption peak at about 360 K (87°C) for hydrogen. [82–84]. Diffusion of hydrogen over Pd surfaces is facile and expectedly proceeds faster with increasing temperature, and may counteract the decrease in amount of hydrogen adsorbed on the surface to give a rather temperature independent reduction.

For the case of Pd$_{75}$Ag$_{25}$(100), the effect of silver is apparent in the slower reduction on the alloy surface compared to Pd(100). This may be partially understood by the nature of the interaction between hydrogen and the Ag atoms. Molecular hydrogen readily dissociates on Pd, while the adsorption of H$_2$ on silver is weak [30, 31, 83, 85]. Moreover, TPD investigations also indicate that PdAg surfaces adsorb less hydrogen than pure Pd surfaces, under the same exposure conditions [83]. Diffusion of hydrogen on the alloy surface is expected to be slower as compared to pure Pd [59].

Figure 5(b), shows that for temperature 120°C the Pd $3d_{5/2}$ core level spectrum has two contributions in addition to the bulk component, where the contribution at higher binding energy primarily originates from Pd atoms embedded in a silver rich surface region [18]. Furthermore, the contribution at lower binding energy can be attributed to surface Pd atoms left at the surface upon the reduction of the $\sqrt{5}$ surface oxide. Comparing to the corresponding spectrum for Pd(100), only a minor amount of hydrogen, if any, is expected adsorbed at the surface at this point. The intensity of the surface contribution for PdAg shows significantly less surface Pd atoms being available for H$_2$ adsorption, in part explaining the much slower reaction rate at this surface. As the temperature is lowered the surface Pd contribution reduces and disappears at 30°C, at which the high binding energy contribution is stronger. At low temperature less intermixing of Pd and Ag during the reaction is expected, which means that surface Pd is expected to be present. The stronger spectral weight of the peak at higher binding energy is for this reason attributed both to Pd embedded in a Ag rich surface region and adsorbed hydrogen. The binding energy of this peak is close to the binding energy observed for the single peak in the Pd $3d_{5/2}$ core level spectrum Pd(100) at the same temperature. The slowing down of the reduction of the surface oxide on Pd$_{75}$Ag$_{25}$(100) at 30°C compared to at 70 °C and 120 °C, is probably a result of several temperature depending factors, including adsorption energy

and diffusion rate depending on the presence of Ag. Also the activation energy for the reaction must be taken into account.

The spectrum in Figure 5(b) recorded after reduction at 170°C display an interesting feature. Compared to the spectrum measured at 120°C, the surface contribution is clearly reduced, indicating that the amount of Pd atoms in the outermost surface layer is reduced, leaving a more silver rich surface. This finding may explain why a small reduction in the maximum reduction rate is observed at this temperature. A same behavior is observed for the surface oxide reduction on the alloy surface at $P_{H_2} = 5 \times 10^{-9}$ mbar (not shown).

Even though the intensity of $\sqrt{5}$ surface oxide as a function time displays a sigmoid-like shape, the complex reduction behavior is not well described by the nucleation and growth JMA model. The validity of the JMA model partially relies on the assumption of uniform nucleation and random distribution of nuclei. A non-random distribution of nuclei leads to deviations from the Avrami kinetics, with slower kinetics and a tail at the end of the reaction [86–88]. Such an effect may explain the deviation from JMA kinetics in some experiments, e.g. Pd$_{75}$Ag$_{25}$(100) at 30°C and $P_{H_2} = 5 \times 10^{-9}$.

Effects such as the removal of an appreciable amount of $\sqrt{5}$ surface oxide in the experiments on Pd(100) at $P_{H_2} = 5 \times 10^{-9}$ and temperatures of 70° and above may not be completely rationalized in the context of a non-random distribution of nuclei. The reaction mechanism leading to water formation may also play a role in this case.

The path for H$_2$O formation likely involves intermediate species such OH. For example, a number of theoretical DFT studies report that reduction of bulk PdO(101) involves OH groups [42–44]. Blanco-Rey *et al.* report a favorable mechanism for H$_2$O formation in the presence of hydroxyl where H$_2$ adsorbs on an undercoordinated Pd^u atom and reacts directly with HO^u to form H$_2$O^u, which desorbs from the surface, leaving a H-Pd^u site and O^u vacancy. The H atom diffuses to a near O^u and leaves the Pd^u available for a new H$_2$ molecule. Martin *et al.* find that the most favorable path for water formation upon reduction of PdO(101) consists of molecular H$_2$ adsorption on Pd^u atoms, dissociation to form HPd^u and HO^u groups and subsequently HO^u and HO^u, and finally disproportionation of the HO groups to form water in the reaction HO^u + HO$^u \rightarrow$ H$_2$O + O^u [44]. On Pd(100), experimental studies concluded that the water molecules are formed by disproportionation of OH radicals, OH + OH $\rightarrow$ H$_2$O + O, at temperatures around 200 K [61]. Furthermore, on Pd(100), H$_2$O formation proceeds much faster through
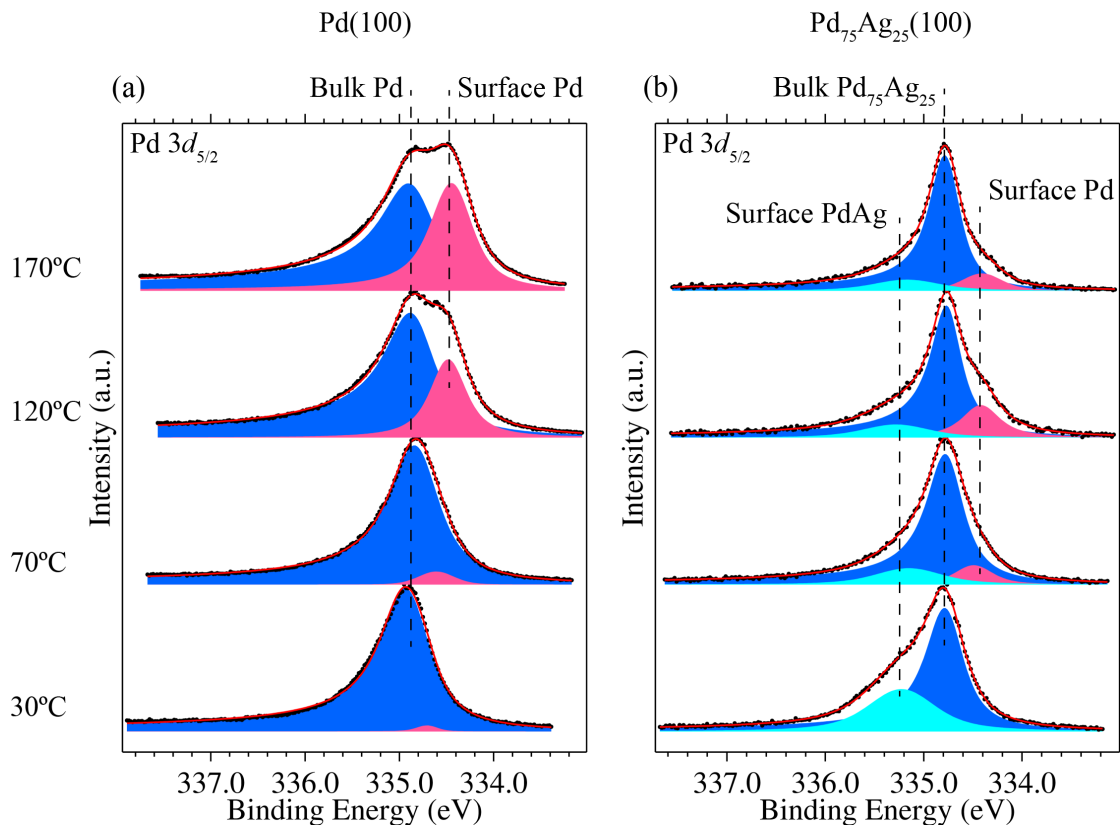
Figure 5: Decomposition of the Pd $3d_{5/2}$ core level spectra after complete reduction of the $(\sqrt{5} \times \sqrt{5})R27°$ surface oxide using $P_{H_2} = 5 \times 10^{-8}$ mbar, for (a) Pd(100) and (b) Pd$_{75}$Ag$_{25}$(100).

disproportionation than through combination of OH with another H atom [62, 89]. The formation of the OH is rate-limiting for the overall reaction. Once OH is formed rapidly reacts further to water, which immediately desorbs [60–62, 68, 89].

Based on this evidence it is reasonable to assume that water formation during reduction of the $\sqrt{5}$ surface oxide proceeds by formation of the OH groups upon adsorption and dissociation of H_2 at steps and defects, and reaction between two OH groups will result in H_2O formation and desorption. This leaves an undercoordinated oxygen atom on the surface, which will eventually be consumed in another reaction event. Under constant supply of hydrogen this mechanism can be regarded as autocatalytic, since new sites are generated both as reduced Pd and undercoordinated O. The net effect of the defect density and the amount of OH formed is likely to influence the onset of the second stage of the reduction, and consequently the amount of $\sqrt{5}$ surface oxide removed in the first stage of the reaction.

Our findings may have implications to the explanation of hydrogen permeation properties of thin Pd-Ag membranes, in particular the effect of oxidation and subsequent reduction leading to improved permeance and reduced CO inhibition [9, 10, 13–15]. Since H_2 readily dissociates on Pd while the adsorption on Ag is weak [30, 31, 83, 85], the ratio of Pd to Ag in the outermost surface layer affects the number of sites available for H_2 dissociation and hence the hydrogen permeation if the thickness is low enough for the surface to become rate determining. The Pd$_{75}$Ag$_{25}$(100) core level spectra after reduction confirm that more palladium atoms reside on the surface after reduction of the $\sqrt{5}$ surface oxide compared to the Ag-terminated surface equilibrated under vacuum conditions or inert gas. The reduction of the $\sqrt{5}$ surface oxide is found to be a complex process where the impact of the different phenomena involved - adsorption, dissociation, diffusion and reaction to form reduced Pd - is dependent on the conditions and the structure and composition of the oxide, particularly the density and the nature of the defects in the oxide layer and the presence Ag beneath it. Figure 5 indicates that the conditions under which the reduction takes place therefore affect the final state of the surface in particular the distribution of Ag in, and possibly near, the topmost surface layer, which is expected to affect the dissociative H_2 adsorption as well as the transfer

10

of atomic hydrogen from the surface to the bulk of PdAg membranes.

6. Conclusions

In-situ high resolution photoelectron spectroscopy measurements during reduction of the $(\sqrt{5} \times \sqrt{5})R27°$-O surface oxide on Pd(100) and Pd$_{75}$Ag$_{25}$(100) using H$_2$ revealed that the reduction proceeds slower on Pd$_{75}$Ag$_{25}$(100) compared to Pd(100). The reduction shows a complex temperature dependent behavior that cannot be fitted by Avrami kinetics based on nucleation and growth theory in a satisfactory way. For Pd(100) the experimentally observed reduction rate is rather independent of temperature in the range investigated. For Pd$_{75}$Ag$_{25}$(100) the reduction is slowest at 30°C, increases at intermediate temperatures and decreases at 170°C.

Differences between Pd and Pd$_{75}$Ag$_{25}$(100) are attributed to the impact of Ag atoms present at the surface, which affects the adsorption of H$_2$, both in terms of number of available sites for dissociation and bond strength, as well as diffusion over the surface. The results show that enhanced reaction kinetics on the alloy surface correlates with the amount of surface Pd atoms, which again is influenced by the temperature of the reduction. The results may have implication for understanding the oxidation, reduction and hydrogen transport properties of Pd-Ag membranes.

References

[1] G. J. Grashoff, C. E. Pilkington, C. W. Corti, Plat. Met. Rev. 27 (4) (1983) 157.

[2] J. Shu, B. P. A. Grandjean, A. V. Neste, S. Kaliaguine1, Can. J. Chem. Eng. 69 (5) (1991) 1036.

[3] S. N. Paglieri, J. D. Way, Separ. Purif. Rev. 31 (1) (2002) 1.

[4] O. Hatlevik, S. K. Gade, M. K. Keeling, P. M. Thoen, A. P. Davidson, J. D. Way, Separ. Purif. Method. 73 (1) (2010) 59.

[5] S. Yun, S. T. Oyama, J. Membr. Sci. 375 (1-2) (2011) 28.

[6] R. Bredesen, T. A. Peters, M. Stange, N. Vicinanza, H. J. Venvik, Chapter 11 palladium-based membranes in hydrogen production, in: Membrane Engineering for the Treatment of Gases: Volume 2: Gas-separation Problems Combined with Membrane Reactors, Vol. 2, The Royal Society of Chemistry, 2011, p. 40.

[7] A. K. M. Fazle Kibria, T. Tanaka, Y. Sakamoto, Int. J. Hydrogen Energy 23 (1998) 891.

[8] S. Uemiya, T. Matsuda, E. Kikuchi, J. Membr. Sci. 56 (1991) 315.

[9] D. Fort, J. P. G. Farr, I. R. Harris, J. Less Common Met. 39 (2) (1975) 293.

[10] J. N. Keuler, L. Lorenzen, J. Membr. Sci. 195 (2) (2002) 203.

[11] A. L. Mejdell, H. Klette, A. Ramachandran, A. Borg, R. Bredesen, J. Membr. Sci. 307 (2008) 96.

[12] W. M. Tucho, H. J. Venvik, M. Stange, J. C. Walmsley, R. Holmestad, R. Bredesen, Sep. Purif. Technol. 68 (2009) 403.

[13] A. Ramachandran, W. M. Tucho, A. L. Mejdell, M. Stange, H. J. Venvik, J. C. Walmsley, R. Holmestad, R. Bredesen, A. Borg, Appl. Surf. Sci. 256 (2010) 6121.

[14] F. Roa, J. D. Way, Appl. Surf. Sci. 240 (1-4) (2005) 85.

[15] S. K. Gade, P. M. Thoen, J. D. Way, J. Membrane Sci. 316 (1-2) (2008) 112.

[16] A. L. Mejdell, D. Chen, T. A. Peters, R. Bredesen, H. J. Venvik, J. Membr. Sci. 350 (2010) 371.

[17] P. T. Wouda, M. Schmid, B. Nieuwenhuys, P. Varga, Surf. Sci. 417 (2-3) (1998) 292.

[18] L. E. Walle, H. Grönbeck, V. R. Fernandes, S. Blomberg, M. H. Farstad, K. Schulte, J. Gustafson, J. N. Andersen, E. Lundgren, A. Borg, Surf. Sci. 606 (23-24) (2012) 1777.

[19] J. R. Kitchin, K. Reuter, M. Scheffler, Phys. Rev. B 77 (2008) 075437.

[20] B. C. Khanra, M. Menon, Physica B 291 (3-4) (2000) 368.

[21] M. Ropo, K. Kokko, L. Vitos, J. Kollár, Phys. Rev. B 71 (2005) 045411.

[22] M. Ropo, Phys. Rev. B 74 (2006) 195401.

[23] O. M. Løvvik, Surf. Sci. 583 (1) (2005) 100.

[24] H. Y. Kim, H. G. Kim, J. H. Ryu, H. M. Lee, Phys. Rev. B 75 (2007) 212105.

[25] S. González, K. M. Neyman, S. Shaikhutdinov, H.-J. Freund, F. Illas, J. Phys. Chem. C 111 (18) (2007) 6852.

[26] T. Marten, O. Hellman, A. V. Ruban, W. Olovsson, C. Kramer, J. P. Godowski, L. Bech, Z. Li, J. Onsgaard, I. A. Abrikosov, Phys. Rev. B 77 (2008) 125406.

[27] L. Vitos, A. V. Ruban, H. L. Skriver, J. Kollár, Surf. Sci. 411 (1-2) (1998) 186.

[28] A. V. Ruban, S. I. Simak, P. A. Korzhavyi, B. Johansson, Phys. Rev. B 75 (2007) 054113.

[29] P. T. Wouda, M. Schmid, B. E. Nieuwenhuys, P. Varga, Surf. Sci. 423 (1) (1999) 229.

[30] I.-H. Svenum, J. A. Herron, M. Mavrikakis, H. J. Venvik, Catal. Today 193 (1) (2012) 111.

[31] J. Shu, B. E. W. Bongondo, B. P. A. Grandjean, A. Adnot, S. Kaliaguine, Surf. Sci. 291 (1-2) (1993) 129.

[32] O. M. Løvvik, R. A. Olsen, J. Chem. Phys 118 (7) (2003) 3268–3276.

[33] O. M. Løvvik, S. M. Opalka, Surf. Sci. 602 (17) (2008) 2840.

[34] T. W. Orent, S. D. Bader, Surf. Sci. 115 (1982) 323.

[35] G. Zheng, E. I. Altman, J. Phys. Chem. B 106 (5) (2002) 1048.

[36] D. T. Vu, K. A. R. Mitchell, O. L. Warren, P. A. Thiel, Surf. Sci.

318 (1994) 129.

[37] M. Saidy, O. L. Warren, P. A. Thiel, K. A. R. Mitchell, Surf. Sci. 494 (2001) L799.

[38] M. Todorova, E. Lundgren, V. Blum, A. Mikkelsen, S. Gray, J. Gustafson, M. Borg, J. Rogal, K. Reuter, J. N. Andersen, M. Scheffler, Surf. Sci. 541 (2003) 101.

[39] P. Kostelník, N. Seriani, G. Kresse, A. Mikkelsen, E. Lundgren, V. Blum, T. Šikola, P. Varga, M. Schmid, Surf. Sci. 601 (6) (2007) 1574.

[40] E. Lundgren, J. Gustafson, A. Mikkelsen, J. N. Andersen, A. Stierle, H. Dosch, M. Todorova, J. Rogal, K. Reuter, M. Scheffler, Phys. Rev. Lett. 92 (2004) 046101.

[41] R. Westerström, M. E. Messing, S. Blomberg, A. Hellman, H. Grönbeck, J. Gustafson, N. M. Martin, O. Balmes, R. van Rijn, J. N. Andersen, K. Deppert, H. Bluhm, Z. Liu, M. E. Grass, M. Hävecker, E. Lundgren, Phys. Rev. B 83 (2011) 115440.

[42] M. Blanco-Rey, D. J. Wales, S. J. Jenkins, J. Phys. Chem. C 113 (38) (2009) 16757.

[43] C. Hakanoglu, J. M. Hawkins, A. Asthagiri, J. F. Weaver, J. Phys. Chem. C 114 (26) (2010) 11485.

[44] N. M. Martin, M. Van den Bossche, H. Grnbeck, C. Hakanoglu, J. Gustafson, S. Blomberg, M. A. Arman, A. Antony, R. Rai, A. Asthagiri, J. F. Weaver, E. Lundgren, J. Phys. Chem. C 117 (26) (2013) 13510.

[45] R. Nyholm, J. N. Andersen, U. Johansson, B. N. Jensen, I. Lindau, Nucl. Instr. and Meth. in Phys. Res. A 467-468, Part 1 (2001) 520.

[46] S. Doniach, M. Šunjić, J. Phys. C: Solid State Phys. 3 (2) (1970) 285.

[47] M. Brown, D. Dollimore, A. Galwey, Reactions in the Solid State, Vol. 22 of Comprehensive Chemical Kinetics, Elsevier Science, 1980.

[48] J. Málek, Thermochim. Acta 138 (2) (1989) 337.

[49] J. Málek, J. Therm. Anal. Calorim. 56 (2) (1999) 763.

[50] J. Šesták, G. Berggren, Thermochim. Acta 3 (1971) 1.

[51] V. M. Gorbachev, J. Therm. Anal. Calorim. 18 (1) (1980) 193.

[52] P. Šimon, Thermochim. Acta 520 (1-2) (2011) 156.

[53] J. Málek, J. M. Criado, J. Šesták, J. Militký, Thermochim. Acta 153 (1989) 429.

[54] J. Šesták, J. Málek, Solid State Ionics 63 (1993) 245.

[55] E. Lundgren, J. Gustafson, A. Resta, J. Weissenrieder, A. Mikkelsen, J. N. Andersen, L. Köhler, G. Kresse, J. Klikovits, A. Biederman, M. Schmid, P. Varga, J. Elect. Spectr. Rel. Phen. 144-147 (2005) 367.

[56] P. Dudin, A. Barinov, L. Gregoratti, M. Kiskinova, F. Esch, C. Dri, C. Africh, G. Comelli, J. Phys. Chem. B 109 (28) (2005) 13649.

[57] J. Klikovits, M. Schmid, J. Gustafson, A. Mikkelsen, A. Resta, E. Lundgren, J. N. Andersen, P. Varga, J. Phys. Chem. B 110 (20) (2006) 9966.

[58] C. T. Williams, E. K.-Y. Chen, C. G. Takoudis, M. J. Weaver, J. Phys. Chem. B 102 (24) (1998) 4785.

[59] V. R. Fernandes, J. Gustafson, I.-H. Svenum, M. H. Farstad, L. E. Walle, S. Blomberg, E. Lundgren, A. Borg, Surf. Sci. 621 (1) (2014) 31.

[60] T. Engel, H. Kuipers, Surf. Sci. 90 (1) (1979) 181.

[61] E. M. Stuve, S. W. Jorgensen, R. J. Madix, Surf. Sci. 146 (1) (1984) 179.

[62] C. Nyberg, C. G. Tengstal, J. Chem. Phys. 80 (7) (1984) 3463.

[63] C. Nyberg, P. Uvdal, J. Chem. Phys. 84 (8) (1986) 4631.

[64] M. Wolf, S. Nettesheim, J. M. White, E. Hasselbrink, G. Ertl, J. Chem. Phys. 92 (2) (1990) 1509.

[65] M. Wolf, S. Nettesheim, J. M. White, E. Hasselbrink, G. Ertl, J. Chem. Phys. 94 (6) (1991) 4609.

[66] M. Xu, P. Yang, W. Yang, S. Pang, Vacuum 43 (11) (1992) 1125.

[67] J. M. Heras, G. Estiú, L. Viscido, Appl. Surf. Sci. 108 (4) (1997) 455.

[68] T. Mitsui, M. K. Rose, E. Fomin, D. F. Ogletree, M. Salmeron, J. Chem. Phys. 117 (12) (2002) 5855.

[69] A. W. Aldag, L. D. Schmidt, J. Catal. 22 (2) (1971) 260.

[70] H. Conrad, G. Ertl, E. E. Latta, Surf. Sci. 41 (2) (1974) 435.

[71] R. J. Behm, K. Christmann, G. Ertl, M. A. Van Hove, J. Chem. Phys 73 (6) (1980) 2984.

[72] K. Schönhammer, O. Gunnarsson, Phys. Rev. B 24 (1981) 7084.

[73] M. P. Kiskinova, G. M. Bliznakov, Surf. Sci. 123 (1) (1982) 61.

[74] B. D. Kay, C. H. F. Peden, D. W. Goodman, Phys. Rev. B 34 (1986) 817.

[75] K. Christmann, Surf. Sci. Rep. 9 (13) (1988) 1.

[76] K. D. Rendulic, G. Anger, A. Winkler, Surf. Sci. 208 (3) (1989) 404.

[77] A. Winkler, K. D. Rendulic, Int. Rev. Phys. Chem. 11 (1) (1992) 101.

[78] M. Beutl, M. Riedler, K. D. Rendulic, Chem. Phys. Lett. 247 (3) (1995) 249.

[79] M. Johansson, O. Lytken, I. Chorkendorff, Top. Catal. 46 (1-2) (2007) 175–187.

[80] M. Johansson, O. Lytken, I. Chorkendorff, J. Chem. Phys. 128 (3) (2008) 034706.

[81] M. Johansson, E. Skúlason, G. Nielsen, S. Murphy, R. M. Nielsen, I. Chorkendorff, Surf. Sci. 604 (7-8) (2010) 718.

[82] R. J. Behm, K. Christmann, G. Ertl, Surf. Sci. 99 (2) (1980) 320.

[83] A. Noordermeer, G. A. Kok, B. E. Nieuwenhuys, Surf. Sci. 165 (2-3) (1986) 375.

[84] H. Okuyama, W. Siga, N. Takagi, M. Nishijima, T. Aruga, Surf. Sci. 401 (3) (1998) 344.

[85] L.-G. Petersson, H. M. Dannetun, I. Lundström, Phys. Rev. B 30 (1984) 3055.

[86] V. Sessa, M. Fanfoni, M. Tomellini, Phys. Rev. B 54 (1996) 836.

[87] M. C. Weinberg, D. P. Birnie III, V. A. Shneidman, J. Non-Cryst. Solids 219 (1997) 89.

[88] E. Pineda, T. Pradell, D. Crespo, Philos. Mag. A 82 (1) (2002) 107.

[89] L.-G. Petersson, H. Dannetun, I. Lundström, Surf. Sci. 161 (1) (1985) 77.

Paper IV

**In Situ X-Ray Photoelectron Spectroscopy of Model Catalysts:
At the Edge of the Gap**

S. Blomberg, M. J. Hoffmann, J. Gustafson, N. M. Martin, V. R. Fernandes, A. Borg, Z. Liu, R. Chang, S. Matera, K. Reuter, and E. Lundgren

P H Y S I C A L   R E V I E W   L E T T E R S

In Situ X-Ray Photoelectron Spectroscopy of Model Catalysts: At the Edge of the Gap

S. Blomberg,[1,][*] M. J. Hoffmann,[2] J. Gustafson,[1] N. M. Martin,[1] V. R. Fernandes,[3] A. Borg,[3] Z. Liu,[4] R. Chang,[4] S. Matera,[2] K. Reuter,[2] and E. Lundgren[1]

[1]*Division of Synchrotron Radiation Research, Lund University, Box 118, SE-221 00 Lund, Sweden*
[2]*Department Chemie, Technische Universität München, Lichtenbergstrasse 4, D-85747 Garching, Germany*
[3]*Department of Physics, Norwegian University of Science and Technology, NO-7491 Trondheim, Norway*
[4]*ALS, Lawrence Berkeley National Laboratory, Berkeley, California 94720, USA*
(Received 29 August 2012; published 12 March 2013)

We present high-pressure x-ray photoelectron spectroscopy (HP-XPS) and first-principles kinetic Monte Carlo study addressing the nature of the active surface in CO oxidation over Pd(100). Simultaneously measuring the chemical composition at the surface and in the near-surface gas phase, we reveal both O-covered pristine Pd(100) and a surface oxide as stable, highly active phases in the near-ambient regime accessible to HP-XPS. Surprisingly, no adsorbed CO can be detected during high CO_2 production rates, which can be explained by a combination of a remarkably short residence time of the CO molecule on the surface and mass-transfer limitations in the present setup.

Understanding the detailed structure and nature of the active site is a central paradigm in modern molecular-level catalysis. For transition metal (TM) based heterogeneous catalysts, this has motivated extensive studies of low-index single-crystal model catalysts, initially under controlled ultrahigh vacuum (UHV) conditions [1] and increasingly at higher pressures [2]. Notwithstanding, despite significant advances in *in situ* methods for surface characterization [3], even qualitative structural and compositional properties remain to date surprisingly unclear for the technological near-ambient regime.

There is little doubt that late TMs like Pd oxidize under ambient oxygen pressures and for low-index surfaces, the evolving O phases are well understood. At Pd(100), these are, for instance, two ordered O overlayers in UHV with $p(2 \times 2)$ and $c(2 \times 2)$ periodicity at 0.25 and 0.5 monolayer (ML, defined as number of O atoms per Pd surface atom) coverage, respectively [4,5]. If the pressure is increased above 1×10^{-6} Torr and the temperature is kept at 300 °C, oxidation proceeds to a well ordered $(\sqrt{5} \times \sqrt{5})R27°$ (henceforth, $\sqrt{5}$ for brevity) surface oxide structure, corresponding to a single PdO(101) plane on top of Pd(100) [5,6]. At pressures beyond 1 Torr and 300 °C, bulk PdO is formed [7,8].

What remains unclear, though, is whether or to what degree the presence of the other reactant, CO in the case of CO oxidation, inhibits oxide formation under steady-state operation. So far, well-controlled semirealistic CO oxidation studies over Pd(100) have been performed *in situ* using scanning tunneling microscopy (STM) [9], polarization-modulation infrared absorption spectroscopy (PM-IRAS) [10], and surface x-ray diffraction (SXRD) [11] as well as density-functional theory (DFT) calculations [12]. Despite the alleged simplicity of the reaction, the interpretation of this data with respect to the nature of the active phase under

technological ambient gas phase conditions is still controversial [13]. Part of the difficulties lies in the high reactivity of the unselective CO oxidation reaction, which gives rise to significant mass-transfer limitations (MTLs) and makes the results heavily sensitive to the different reactors used (see below). A significant part of the disagreement, however, also arises from differences between the experimental techniques. While PM-IRAS probes one of the reactants (CO) only, STM and SXRD are sensitive to the surface structure and morphology of the substrate. In contrast, x-ray photoelectron spectroscopy (XPS) enables detection of adsorbates (CO and oxygen) and the substrate simultaneously, and in the case of high-pressure XPS (HP-XPS), also the gas phase in the immediate vicinity of the model catalyst. This comprehensiveness of the information provided is a feature unique to this technique, with great potential for breakthrough discoveries in the surface catalytic context.

In an effort to further close the pressure gap between atomic-scale studies in UHV and real catalysis at ambient conditions, we illustrate this with a HP-XPS study of CO oxidation over Pd(100) covering the entire pressure range up to 1 Torr. Supported by detailed first-principles kinetic Monte Carlo (1p-kMC) modeling, the obtained data show exclusively that both O-covered pristine Pd(100) and the $\sqrt{5}$ surface oxide are highly active phases in the near-ambient regime. Which phase gets stabilized depends sensitively on temperature, total pressure, feed stoichiometry, i.e., the $CO:O_2$ partial pressure ratio, and due to MTLs also the macroscopic flow profile in the employed reactor. Our interpretation favors the presence of the surface oxide at technological conditions, but validation of this hypothesis will require extension of existing *in situ* techniques to ambient pressures and new reactor setups to control the severe MTLs clearly identified in this Letter.

The HP-XPS measurements were performed at the Molecular Science beam line 9.3.2 at the ALS in Berkeley [14,15]. XPS measurements *in situ* in gas pressures up to 1 Torr can be performed. The Pd $3d_{5/2}$, C $1s$, and O $1s$ core levels were recorded with photon energies of 435, 435, and 650 eV, respectively. Interpretation of the measurements was aided by 1p-kMC simulations focusing exclusively on the metal Pd(100) surface. With further details provided in the Supplemental Material [16], the model considers adsorption, desorption, diffusion, and reaction processes at a Pd(100) lattice, with O adatoms occupying the fourfold hollow and CO occupying bridge sites. Repulsive lateral interactions are described through nearest-neighbor site-blocking rules, and all kinetic parameters entering the simulations were determined by supercell geometry DFT calculations [17], using the semilocal PBE functional [18]. Steady-state catalytic activity was evaluated for given partial pressures and increasing temperatures. Observing a sharp increase in activity over a narrow temperature range, we define the ''activation temperature'' (see below) as the temperature corresponding to the inflection point of the activity increase.

We start illustrating the insights provided by the *in situ* XPS measurements with the continuous O $1s$ scans compiled in Fig. 1. The chamber was filled with 0.25 Torr CO and 0.25 Torr O_2 and the temperature was ramped from 265 °C up to 405 °C and then back down to 145 °C. Under these conditions, the O $1s$ region reveals the surface adsorbates, the phase of the substrate as well as the composition of the gas above the surface; i.e., we may follow the surface structure and reactivity, simultaneously. Starting at the bottom of the figure, the spectra show two major peaks corresponding to CO adsorbed on the surface, which unfortunately coincide with Pd $3p$, as well as CO and O_2 in the gas phase. The gas phase peaks are difficult to resolve from this figure, but consist of two O_2 related components at 537.5 and 538.6 eV [19] and one CO component at 536.4 eV. The absence of a CO_2 peak shows that the reactivity at this point is low. As the temperature is increased to 345 °C, the CO_2 peak (535.5 eV) suddenly dominates the gas phase region completely. There is still some oxygen, but the gas phase peak of the CO minority species is gone. This shows that the sample has suddenly become so active that almost all the CO near the surface is converted into CO_2; i.e., the measurements clearly suffer from MTLs (see below). Simultaneously, the peak corresponding to adsorbed CO is replaced by one corresponding to adsorbed O; i.e., the surface coverage changes from CO rich to O rich. We do not, however, see a split of the surface oxygen peak that would have been a fingerprint of (surface) oxide formation [5]. Further heating does not change the spectrum significantly. In the cooling process, the active phase is present until a temperature of 225 °C, when the CO reclaims the surface and the activity is turned off.
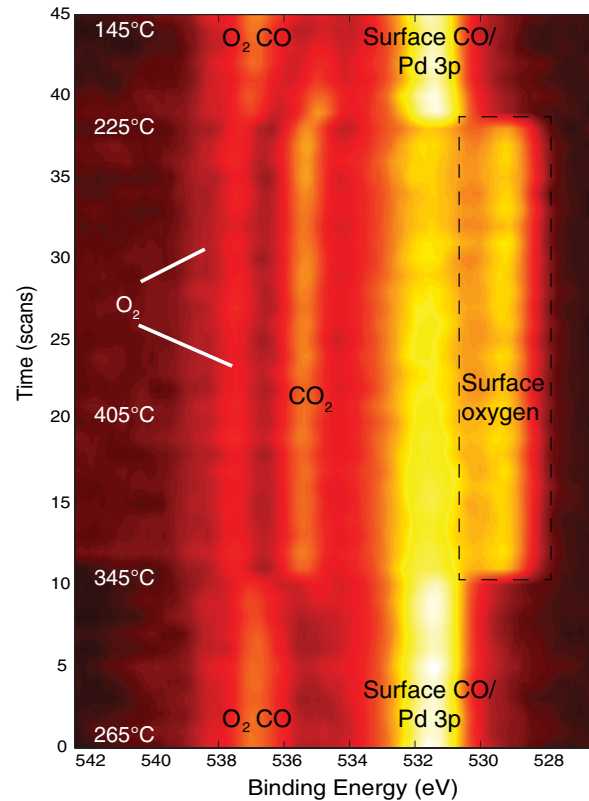

FIG. 1 (color online). O $1s$ region during CO oxidation in a gas mixture of 0.25 Torr CO and 0.25 Torr O_2. The temperature of the Pd(100) (shown to the left in the figure) was ramped up and down during the measurement.

The resulting picture of a low-temperature CO-poisoned and a high-temperature active metallic state with chemisorbed O coverage is fully consistent with the conclusions derived from vibrational spectroscopy by Gao *et al.* for the same gas phase ratios [10]. However, it was speculated that the latter active phase is of a transient nature due to the slow buildup of MTL-induced pressure gradients in the reactor [13]. To address this, we repeated the experiment with a finer stepwise temperature profile and extended the measurements to the Pd $3d$ and C $1s$ region. The behavior of the O $1s$ level [Fig. 2(a)] is similar to Fig. 1 with the first signs of CO_2 production appearing at around 310 °C and the activation temperature at 335 °C. While the different heating speed has thus a slight effect on the observed activation temperature, a transient nature of the active phase can be excluded from the measured C $1s$ level [Fig. 2(c)]. Below the activation temperature, we observe gas phase CO (289.9 eV) together with adsorbed CO in bridge sites (285.9 eV) [20]. At intermediate temperatures (310 °C), both CO and CO_2 can be detected in the gas phase and above the activation temperature, only a single peak corresponding to CO_2 remains. The minor amount of CO still present in the small gas phase volume to which we are sensitive is below the detection limit and can, therefore,
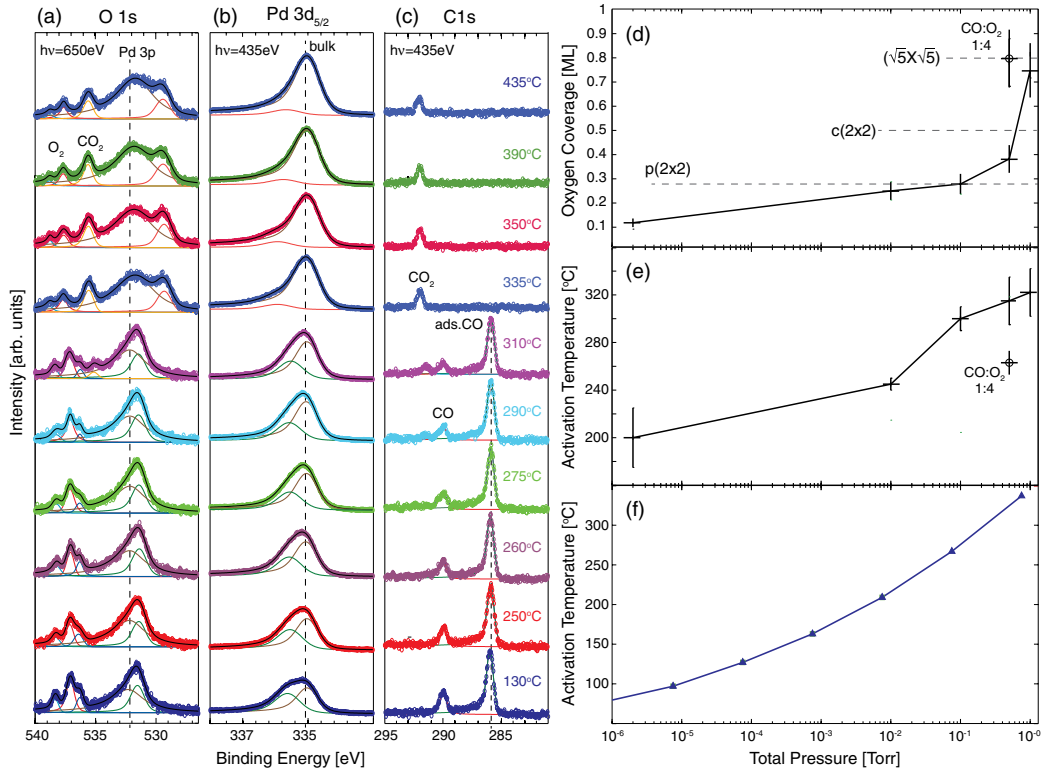
FIG. 2 (color online).   CO oxidation in a gas mixture of 0.25 Torr CO and 0.25 Torr O_2 showing the binding energy regions of (a) O $1s$, (b) Pd $3d$, and (c) C $1s$. (d) Derived oxygen coverage and (e) activation temperature for a CO:O_2 ratio of 1:1 and increasing total pressure. One measuring point from a CO:O_2 ratio of 1:4 is also included. (f) Calculated 1p-kMC activation temperature for 1:1 CO:O_2 ratio and increasing total pressure.

not be observed in the spectra. Simultaneously, the Pd $3d$ [Fig. 2(b)] shows a slight shift towards lower binding energy as would be expected for adsorbed CO being replaced by O [20]. Above the activation temperature, the mass transfer limited profile with very small amount of CO in the near-surface gas phase is thus fully established in our measurements, with the active phase being metallic Pd(100) with chemisorbed O.

In a next step, we continued the measurements at 1:1 CO:O_2 partial pressure ratio at different total pressures. The two-state behavior with defined activation temperature was always the same as the one just described, and we summarize in Fig. 2(e) the derived variation of the activation temperature with pressure. Even at the highest pressure attainable with the present *in situ* XPS setup, one Torr, we never observed a clear signature of surface oxide formation in the O $1s$ spectrum. This is consistent with the ±10% estimate of the O coverage above the activation temperature obtained from the ratios of the areas underneath the O $1s$ and Pd $3p$ levels against reference spectra of known oxygen structures prepared under UHV conditions [5]. As apparent from Fig. 2(d), apart from the measurement at one Torr, this coverage remains at the level anticipated for the formation of $p(2 \times 2)$ or $c(2 \times 2)$ O overlayers. The conclusion that the active phase above

activation temperature corresponds in the measured pressure range to O-covered metallic Pd(100) receives further support from our 1p-kMC simulations restricted to this metallic state. These simulations perfectly reproduce the two-state behavior with CO-poisoned low-temperature and O-covered active high-temperature state. The resulting activation temperature as a function of total pressure is shown in Fig. 2(f) and compares qualitatively well with the experimental data, considering the typical ±100 °C uncertainty due to the underlying semilocal DFT energetics [16,21].

Over the wide pressure range from UHV up to 0.1 Torr, our *in situ* XPS measurements thus reveal no qualitative change in the surface catalytic function. That the pressure gap is, nevertheless, not fully closed is indicated by the much higher O coverage obtained just at the highest attainable pressure of one Torr. This coverage of ~0.75 ML would rather be consistent with the (5×5) oxidic precursor structure characterized in UHV [5]. It could thus well be that the real gap phenomena just occur in the pressure range above one Torr which we can not yet access due to loss of photoelectron intensity. This tantalizing conjecture is indirectly corroborated by the 1p-kMC simulations that we can well run at ambient pressures. The activation temperature resulting from the metal Pd(100)-only model

for 1 atm is as high as 600 °C, with insignificant catalytic activity of the CO-poisoned state at around 300 °C. As this contradicts the known high activity of Pd(100) at these temperatures [22], there must be qualitative physics missing in the employed model, which we assign to the formation of oxidic overlayers at the surface. Support for this hypothesis comes from *in situ* XPS measurements at 0.5 Torr and more oxygen-rich feeds. Figure 3 summarizes the results from an experiment with a 4:1 mixture of O_2 and CO. The more oxidizing environment decreases the activation temperature to 270 °C.

More interestingly, the O coverage above the activation temperature now increases to 0.8 ML, as indicative of the formation of the $\sqrt{5}$ surface oxide. This suspicion is confirmed by the O 1s and Pd 3d spectra shown in detail in Fig. 3(d). The O 1s spectrum reveals two components at 528.7 and 529.5 eV, and the Pd 3d level has one component at 336.2 eV, shifted 1.3 eV from the bulk component. This leaves little doubt on the presence of the $\sqrt{5}$ oxide [5,6], cf. Fig. 3(e), and is again fully consistent with the interpretation of the CO vibrational data by Gao *et al.* at these O_2:CO ratios [10].

While at 1:1 CO:O_2 ratio, we thus cannot reach high enough total pressures to observe formation of oxidic overlayers, this is possible at more O-rich feeds. Extrapolating this view, we would thus conclude that the likely termination at technological (near-stoichiometric and ambient) gas phase conditions is the surface oxide. Validation of this hypothesis through dedicated *in situ* techniques is, however, not only a function of increasing their operation range beyond the presently attainable near-ambient regime. Equally important will be to battle the MTLs of which there are clear signatures already visible at the higher end

of pressures studied here. While in the present reactor chamber, no explicit measurement of the catalytic activity is possible, both the high-temperature metallic Pd(100) and the $\sqrt{5}$ surface oxide are highly active. In consequence, diffusion limitations in bringing the CO minority species to the active surface lead to a depletion of CO in the gas phase directly above the catalyst surface [23,24]. This is particularly consequential as the residence time of CO at both active phases is extremely short. Using the DFT-derived kinetic parameters, we estimate this residence time as the inverse of the sum of all rate constants of desorption and reaction processes and obtain about 9×10^{-10} s. In this situation, the catalytic function is highly sensitive to the impingement rate of CO molecules to the surface and thus to MTLs that modify the CO pressure profile directly above the active surface. A conclusive answer to the question whether the active phase in CO oxidation over Pd or other late TM catalysts is an O-covered pristine metal or an oxidic overlayer thus dictates new reactor setups that allow addressing technological ambient pressures without suffering from MTLs. We note though that the crucial question hereby is maybe not even which phase is the more active one (metal or oxide), but rather which phase is stabilized—and if the less reactive phase is stabilized, what can be done to stabilize the other and arrive at an improved catalytic function.

In conclusion, our presented *in situ* XPS and 1p-kMC data demonstrate that over the entire pressure range from UHV up to one Torr, the catalytic activity of Pd at near-stoichiometric pressure ratios can be understood in terms of a CO-poisoned inactive state at low temperatures and above the activation temperature by a highly active state composed of Pd(100) with a high coverage of chemisorbed O.
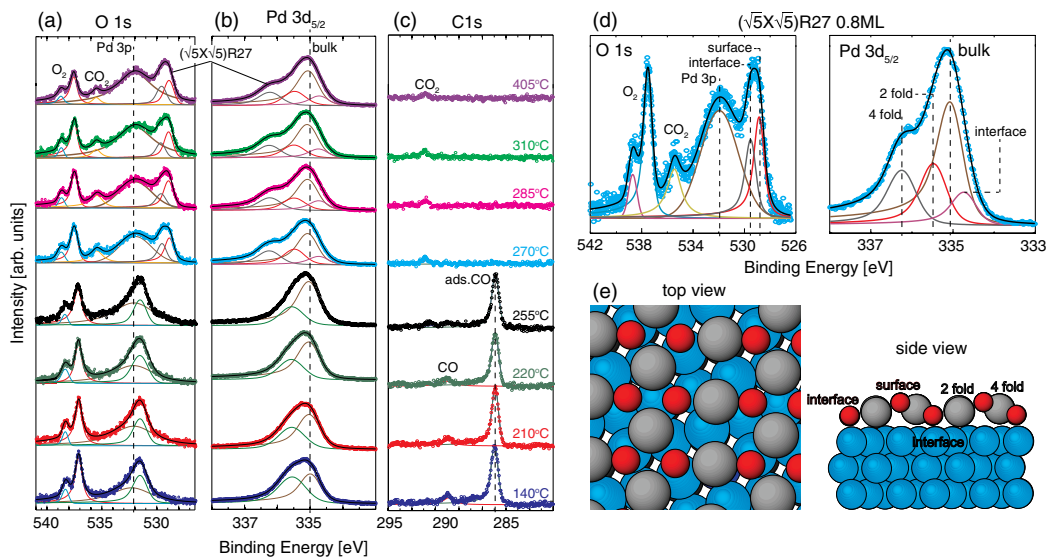

FIG. 3 (color online).   CO oxidation at 0.5 Torr and a 1:4 CO:O_2 partial pressure ratio. Shown are the binding energy regions of (a) O 1s, (b) Pd 3d, and (c) C 1s. (d) A more detailed view of the O 1s and Pd 3d spectra directly above activation temperature. (e) Structural model of the $(\sqrt{5} \times \sqrt{5})$ surface oxide on Pd(100) according to Refs. [5,6].

Unfortunately, this does not yet close the pressure gap, as formation of oxidic overlayers seems to emerge precisely at the upper edge of the presently accessible total pressure range. For more O-rich feeds, this formation starts at lower total pressures and we can unambiguously detect the formation of the $(\sqrt{5} \times \sqrt{5})$ surface oxide phase known from UHV studies. Both surface oxide and the high-temperature metallic Pd(100) phase are highly active under the probed gas phase conditions, making the measurements highly sensitive to mass-transfer limitations in the employed reactor. A true closing of the pressure gap will thus not only require efforts in extending atomic-scale electron spectroscopies to higher pressures but also reactor setups that overcome these limitations. However, already the present results demonstrate how the comprehensive insight provided by cutting-edge HP-XPS helps to qualify the relevant pressure range for the gap phenomenon and provide a better founded perspective on the long-standing controversy over the high pressure active phase.

Note added in proof.—While this Letter was in review, a similar study was performed on a Pd(111) surface [25].

---

*sara.blomberg@sljus.lu.se

[1] G. Ertl, H. Knözinger, and J. Weitkamp, *Handbook of Heterogeneous Catalysis* (Wiley, New York, 1997).

[2] E. Lundgren and H. Over, J. Phys. Condens. Matter **20**, 180302 (2008).

[3] A. Stierle and A. M. Molenbroek, MRS Bull. **32**, 1001 (2007).

[4] J. Wang, Y. Yun, and E. I. Altman, Surf. Sci. **601**, 3497 (2007).

[5] M. Todorova *et al.*, Surf. Sci. **541**, 101 (2003).

[6] P. Kostelník, N. Seriani, G. Kresse, A. Mikkelsen, E. Lundgren, V. Blum, T. Šikola, P. Varga, and M. Schmid, Surf. Sci. **601**, 1574 (2007).

[7] E. Lundgren, J. Gustafson, A. Mikkelsen, J. Andersen, A. Stierle, H. Dosch, M. Todorova, J. Rogal, K. Reuter, and M. Scheffler, Phys. Rev. Lett. **92**, 046101 (2004).

[8] R. Westerström *et al.*, Phys. Rev. B **83**, 115440 (2011).

[9] B. L. M. Hendriksen, S. C. Bobaru, and J. W. M. Frenken, Surf. Sci. **552**, 229 (2004).

[10] F. Gao, Y. Wang, Y. Cai, and D. W. Goodman, J. Phys. Chem. C **113**, 174 (2009).

[11] R. van Rijn, O. Balmes, A. Resta, D. Wermeille, R. Westerström, J. Gustafson, R. Felici, E. Lundgren, and J. W. M. Frenken, Phys. Chem. Chem. Phys. **13**, 13 167 (2011).

[12] J. Rogal, K. Reuter, and M. Scheffler, Phys. Rev. Lett. **98**, 046101 (2007); Phys. Rev. B **77**, 155410 (2008).

[13] R. van Rijn, O. Balmes, R. Felici, J. Gustafson, D. Wermeille, R. Westerstrom, E. Lundgren, and J. W. M. Frenken, J. Phys. Chem. C **114**, 6875 (2010); F. Gao, Y. Wang, and D. W. Goodman, *ibid.* **114**, 6874 (2010).

[14] M. E. Grass, P. G. Karlsson, F. Aksoy, M. Lundqvist, B. Wannberg, B. S. Mun, Zahid Hussain, and Z. Liu, Rev. Sci. Instrum. **81**, 053106 (2010).

[15] R. Chang, Y. Pyo Hong, S. Axnanda, B. Mao, N. Jabeen, S. Wang, R. Tai, and Z. Liu, Curr. Appl. Phys. **12**, 1292 (2012).

[16] See Supplemental Material at http://link.aps.org/supplemental/10.1103/PhysRevLett.110.117601 for corresponding HPXPS spectra.

[17] S. J. Clark, M. D. Segall, C. J. Pickard, P. J. Hasnip, M. I. J. Probert, K. Refson, and M. C. Payne, Z. Kristallogr. **220**, 567 (2005).

[18] J. P. Perdew, K. Burke, and M. Ernzerhof, Phys. Rev. Lett. **77**, 3865 (1996).

[19] K. Siegbahn *et al.*, *ESCA Applied to Free Molecules* (North-Holland, Amsterdam, 1969).

[20] J. N. Andersen, M. Qvarford, R. Nyholm, S. L. Sorensen, and C. Wigren, Phys. Rev. Lett. **67**, 2822 (1991).

[21] K. Reuter, D. Frenkel, and M. Scheffler, Phys. Rev. Lett. **93**, 116105 (2004).

[22] D. A. Logan and M. T. Paffett, J. Catal. **133**, 179 (1992).

[23] S. Matera and K. Reuter, Catal. Lett. **133**, 156 (2009).

[24] S. Matera and K. Reuter, Phys. Rev. B **82**, 085446 (2010).

[25] R. Toyoshima, M. Yoshida, Y. Monya, Y. Kousa, K. Suzuki, H. Abe, B. S. Mun, K. Mase, K. Amemiya, and H. Kondoh, J. Phys. Chem. C **116**, 18 691 (2012).

Paper V

Near-Ambient Pressure CO and H_2 Oxidation over Pd(100) and $Pd_{75}Ag_{25}$(100) Surfaces

V.R. Fernandes, M.H. Farstad, J. Knudsen, J. Gustafson, S. Blomberg, E. Lundgren, H.J. Venvik, A. Borg

In manuscript.

Near-Ambient Pressure XPS study of CO and H_2 Oxidation over Pd(100) and $Pd_{75}Ag_{25}$(100) Surfaces

V.R. Fernandes[a], M.H. Farstad[a], J. Knudsen[c], J. Gustafson[c], S. Blomberg[c], E. Lundgren[c], H.J. Venvik[b], A. Borg[a]

[a]*Dept. of Physics, Norwegian Univ. of Science and Technology, NO-7491 Trondheim, Norway*
[b]*Dept. of Chemical Engineering, Norwegian Univ. of Science and Technology, NO-7491 Trondheim, Norway*
[c]*Div. of Synchrotron Radiation Research, Lund Univ., Box 117, SE-221 00 Lund, Sweden*

Abstract

Oxidation of CO and H_2 over Pd(100) and $Pd_{75}Ag_{25}$(100) surfaces was studied under oxygen rich conditions at near-ambient pressure by means of high pressure X-ray photoelectron spectroscopy and quadrupole mass spectrometry. The activation for CO oxidation over Pd(100) was determined at 1.0 eV, while a value of 1.1 eV was obtained for $Pd_{75}Ag_{25}$(100). CO poisoning of the reaction is observed at low temperatures for both surfaces when CO only is oxidized as well as in the case of simultaneous oxidation of CO and H_2. In the latter case, the CO oxidation is determining the overall oxidation behavior. Above a critical temperature, the reactivity is high. While $(\sqrt{5} \times \sqrt{5})R27°$ surface oxide is the active surface in the reactions for Pd(100), chemisorbed oxygen plays this role for $Pd_{75}Ag_{25}$(100). Thus, presence of silver in the outermost surface layer significantly affects the surface chemistry during these reactions and thereby the reaction mechanism.

Keywords: CO oxidation, H_2 oxidation, Pd(100), $Pd_{75}Ag_{25}$(100), high pressure X-ray photoelectron spectroscopy, quadrupole mass spectrometry

1. Introduction

Palladium is a versatile oxidation catalyst, among others applied for CO removal from car exhaust [1, 2] or total oxidation of hydrocarbons [3–6]. Furthermore, palladium has high solubility, permeability and selectivity for hydrogen, thus being a suitable membrane material for hydrogen separation [7–10]. To tailor catalyst reactivity, selectivity, improve stability against poisoning, and reduce embrittlement when exposed to hydrogen (due to formation of hydride phases) Pd-based alloys are often used, with PdAg as a commonly selected alloy [11–13]. For such binary systems, surface segregation effects may influence the chemisorption and reaction behavior as well as the formation of surface oxides.

In PdAg alloys, silver segregation to the surface under UHV conditions has been observed experimentally [14, 15], as well as predicted from theoretical calculations [16–22]. This is due to the lower surface energy of Ag compared to Pd [18, 20, 23, 24], and geometric effects resulting from the slightly larger Ag atoms, which reduce the stress at the surface. In the presence of adsorbates, due to differences in chemisorption energies of the interacting molecules [25, 26], adsorbate-induced segre-

gation of Pd in PdAg alloys has been found experimentally as a result of adsorption of oxygen [27, 28] and hydrogen [29]. For instance, we have recently reported that the $Pd_{75}Ag_{25}$(100) surface forms a $(\sqrt{5} \times \sqrt{5})R27°$ surface oxide (henceforth denoted $\sqrt{5}$) similar to the one observed on Pd(100) [28]. In this case Pd segregates to the surface to form the oxide structure and an enrichment of Ag in the interface layer between the surface oxide and the $Pd_{75}Ag_{25}$ bulk is observed. Theoretical studies also find adsorbate-induced segregation as a result of oxygen [17, 30], hydrogen [22, 30–32], and CO [30] adsorption.

It has been reported that in several cases surface oxides formed on Pd surfaces at near ambient pressure conditions are more active in oxidation reactions than the metal surface covered with chemisorbed oxygen [33–44]. Theoretical kinetic Monte-Carlo simulations also indicate that surface oxide on Pd(100) could be responsible for increased reactivity [45, 46]. Palladium high oxidation activity under oxygen-rich conditions has been attributed to oxygen/oxide species on the surface [33, 36, 39, 42, 43, 47, 48]. In the case of the Pd(100) surface, it has been shown experimentally that the high activity of this surface towards CO oxidation studied at near-realistic conditions coincides with the presence oxide structures on the sur-

face, while the metallic surface appears to display lower reactivity. Although some studies indicate a chemisorbed oxygen phase as the active surface [36, 47], the emergent trend points to the surface oxide [37, 39, 42, 43] as the active phase under oxygen rich conditions. In the case of pure Pd, CO oxidation reaction under ultrahigh vacuum (UHV) conditions the can be described by a Langmuir-Hinshelwood mechanism [49–53]. Under more realistic conditions several studies indicate that the mechanism is of Mars van Krevelen type, where the catalyst surface is oxidized and gas phase CO interacts with the oxide to form CO_2 [33–37, 39, 41–44]. For hydrogen oxidation on Pd surfaces, surface oxygen structures have also been observed at high oxidation activity [54]. The influence of the alloying element Ag in the oxidation activity is not well known and is the target of the present work.

In the present work, using high pressure X-ray photoelectron spectroscopy (HP-XPS) and quadrupole mass spectrometry (QMS) we compare the CO and H_2 oxidation reaction, for CO and H_2 separately and in combination, under oxygen rich conditions over Pd(100) and $Pd_{75}Ag_{25}$(100) at pressures in the millibar range. In particular, the effect of Ag as an alloying element and presence of surface oxides in the catalytically active stage are addressed. Furthermore, poisoning effects during simultaneous oxidation of CO and H_2 are discussed.

2. Experimental

Pd(100) and $Pd_{75}Ag_{25}$(100) single crystals were cleaned by cycles of sputtering, oxygen treatment and annealing to 705°C for Pd(100) and 625°C for $Pd_{75}Ag_{25}$(100). Temperatures were measured with a type K thermocouple spotwelded to the edge of the crystal near the surface. The surface quality was evaluated by low energy electron diffraction (LEED), revealing well defines surfaces, and by XPS measurement of the C $1s$ and S $2p$ core level spectra, where no traces of these impurities were observed.

HP-XPS measurements were performed at the beam line I511 of the MAX IV Laboratory [55]. This beam line is equipped with a SPECS PHOIBOS 150 NAP analyzer for near ambient pressure measurements and a reaction cell, which is filled with gases during experiments. The HP-XPS data were recorded *in situ* at gas pressures about 1 mbar. Total gas flows of 2.0-3.0 cm^3/min were applied. Gas composition at the exhaust of the reaction cell was analyzed using a QMS connected to the gas exit lines via a leak valve. The QMS instrument is a Dycor LC-D Residual Gas Analyzer from AMTEK. The oxidation

experiments were carried out by introducing O_2/CO/H_2 gases at selected flow ratios and varying the sample temperature. XPS, QMS, and temperature data were collected continuously during the experiments.

O $1s$, Pd $3d_{5/2}$, and C $1s$ core level spectra were recorded at photon energies of 650 eV, 400 eV, and 380 eV, respectively. All spectra were measured at normal emission. The binding energy was calibrated by recording the Fermi edge immediately after the core level regions. For the analysis the spectra were normalized to the background at the low binding energy side of the core level peaks. Linear background subtraction was applied and Doniach-Sunjic line shapes used for fitting the spectra [56].

3. Results

3.1. Oxidation over Pd(100)

3.1.1. CO oxidation

In Figure 1(a) HP-XPS measurements of the O $1s$ core level region along with QMS data for CO oxidation over Pd(100) under oxygen rich conditions are presented. The experiment was performed using a ratio O_2:CO of 10:1 and ramping the temperature from about 110°C to 260°C. This flow results in a pressure close to 0.7 mbar in the reaction cell of the XPS system. The O $1s$ core level spectrum at this point, displayed in the lower panel (labeled 1) of Fig. 1(b), comprises contributions due to CO adsorbed in bridge sites on the metallic surface at a binding energy of 530.4 eV, the Pd $3p_{3/2}$ at approximately 531.7 eV, and two components at 537.0 eV and 538.1 eV both assigned to molecular oxygen in the gas phase. The contribution due to CO in the gas phase, partly overlapping with the gas phase molecular oxygen contributions can not be discerned in the spectrum. No CO_2 signal is observed by QMS at this point.

Increasing the temperature yields several changes. At about 135°C the CO_2 partial pressure recorded by QMS starts to increase. At this point the HP-XPS data does not indicate changes in the surface species, in line with previous observations [33, 41, 42]. Reaching a temperature of about 185°C, changes in the the HP-XPS spectra indicate altered Pd(100) surface chemistry. The O $1s$ core level spectrum at this stage, including curve fitting, is displayed in the upper panel (labeled 2) of Fig. 1(b). The component due to adsorbed CO is no longer present. Instead, two peaks located at binding energies 528.8 eV and 529.5 eV are observed, that are clear fingerprints of the $\sqrt{5}$ surface oxide on Pd(100) [57, 58], and represent interface and surface oxygen atoms in the $\sqrt{5}$ surface ox-
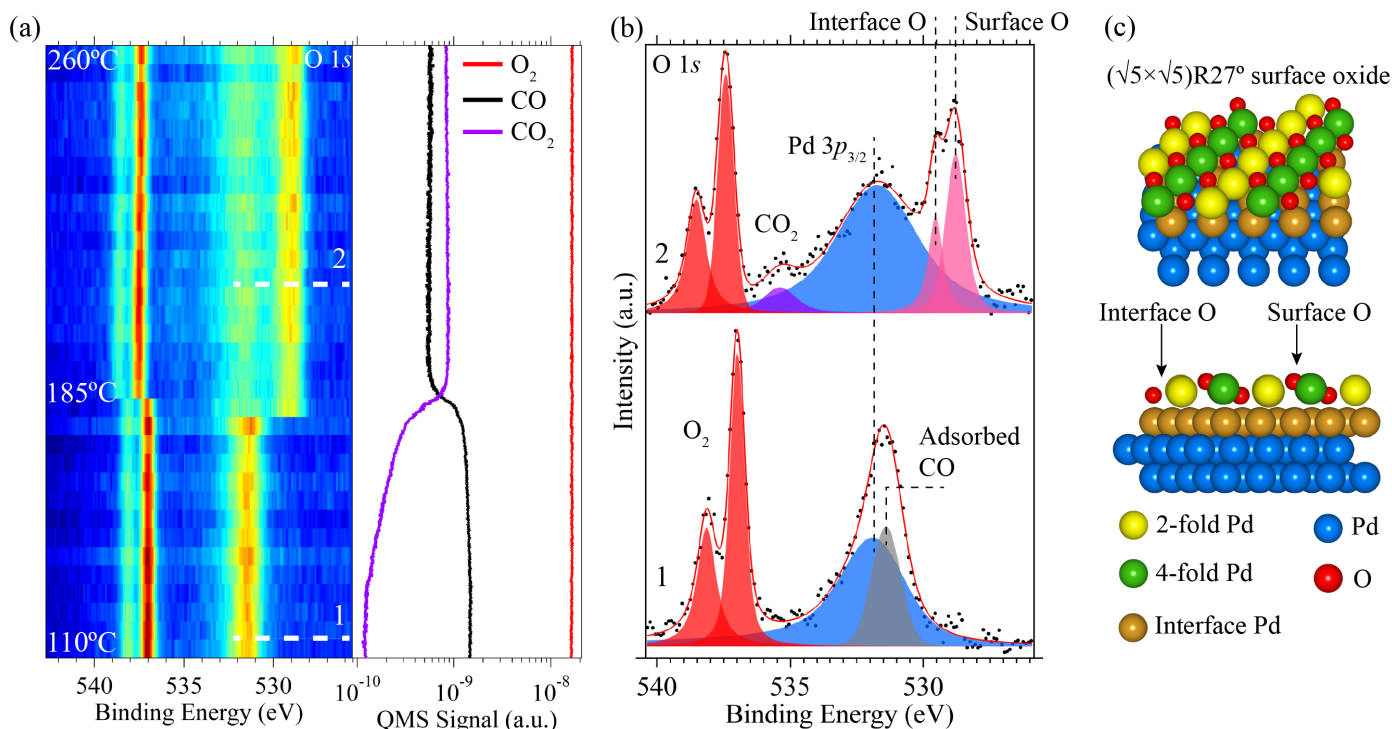
Figure 1: CO oxidation on the Pd(100) surface at 0.7 mbar and O_2:CO ratio 10:1. (a) O $1s$ core level region recorded as a function of sample temperature along with the corresponding recorded QMS data for O_2, CO and CO_2. (b) Decomposition of the O $1s$ core level spectra at two different stages during the CO oxidation experiment, (1) no activity and (2) high activity towards CO_2 production. (c) model of the $(\sqrt{5} \times \sqrt{5})R27°$ surface oxide.

ide [28]. An additional peak (535.4 eV) due to CO_2 in the gas phase is also observed. Moreover, the oxygen gas phase components are shifted to higher binding energies, as a consequence of changes in the work function of the sample, thus reflecting changes in the surface chemistry. Simultaneously, the QMS data shows a high, steady-state production of CO_2. These observations are in line with previous reports, which show higher reactivity when the Pd(100) surface is covered by a surface oxide [37, 39, 42, 43]. Further increase in temperature yields in no notable changes in the surface reactivity, indicating that the reaction is mass transfer limited once the temperature of the highly reactive stage is reached.

3.1.2. H_2 oxidation

Similar oxidation experiments as performed for CO were carried out for oxidation of H_2 over Pd(100), yielding a different behavior. The development of the HP-XPS measurements of the O $1s$ core level region along with QMS data, during exposure to an O_2:H_2 mixture of ratio 10:1, in the temperature range from about 265°C to about 560°C are illustrated in Fig. 2(a). Already at room temperature (RT), formation of water is observed and the O $1s$ and Pd $3d_{5/2}$ core level spectra (not shown) demonstrate presence of the $\sqrt{5}$ surface oxide on the Pd(100) sur-

face. This situation persists until the sample temperature reaches about 510°C. A change in the surface chemistry is observed at about 510°C, where the O $1s$ and Pd $3d_{5/2}$ core level spectra, displayed in Fig. 2(b), indicate that the $\sqrt{5}$ surface oxide is replaced by chemisorbed oxygen and an accompanying small increase in the H_2O production is seen.

3.1.3. Simultaneous CO and H_2 oxidation

HP-XPS and QMS results obtained for simultaneous oxidation of H_2 and CO over Pd(100), performed using a ratio O_2:CO:H_2 of 10:1:1, during ramping the sample temperature from about 130°C up to 290°C and then cooling down again to about 80°C are presented in Figure 3. Figure 3(a) displays the development of the O $1s$ core level region and corresponding QMS data for O_2, CO, CO_2, H_2, and H_2O. Initially, at the stage labeled 1, the QMS signals for CO_2 and H_2O are low and stem from residual gas in the system. Corresponding O $1s$ and Pd $3d_{5/2}$ core level spectra are presented in the lower panels of Figures 3(b) and (c), respectively. The decomposition of the O $1s$ spectrum shows the same contributions as found for the CO oxidation case. The Pd $3d_{5/2}$ core level spectra shows the bulk Pd component at 334.9 eV and a component attributed to CO adsorbed on the metal-
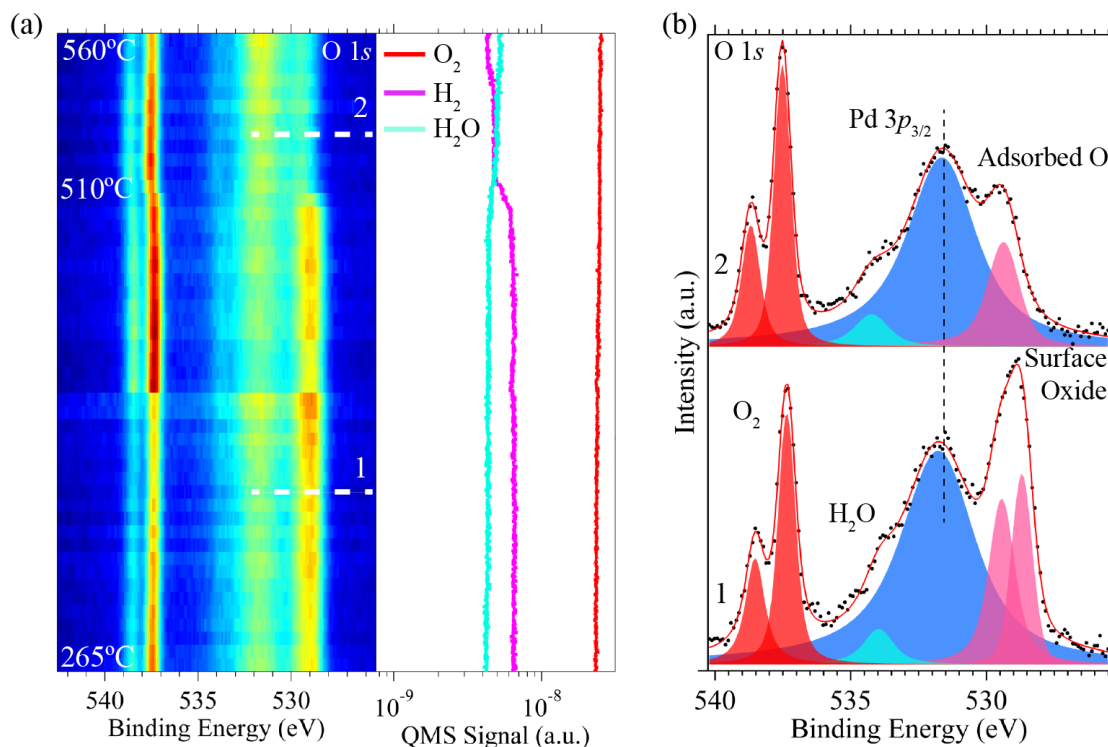
3

Figure 2: H_2 oxidation on the Pd(100) surface at 0.7 mbar and O_2:H_2 ratio 10:1. (a) O $1s$ core level region recorded as a function of sample temperature along with the corresponding recorded QMS data for O_2, H_2, and H_2O. (b) Decomposition of the O $1s$ core level spectra at two different stages during the H_2 oxidation experiment, (1) activity towards H_2O production in the presence of a $\sqrt{5}$ surface oxide and (2) activity towards H_2O production in the presence of chemisorbed oxygen.

lic surface at +0.6 eV relative to the bulk peak. The C $1s$ core level spectrum (see Figure S 1 in the supplemental information) for this temperature shows a peak of high spectral intensity located at 286.0 eV due to adsorbed CO on Pd(100) and a small gas phase CO peak at 289.85 eV. No CO_2 or H_2O production is observed at this stage. Increasing the sample temperature, yields a rise in the partial pressures of CO_2 and H_2O. Careful examination of the QMS data shows that the CO_2 partial pressure starts to increase at slightly lower temperature than the H_2O partial pressure.

Further increasing the sample temperature results in increased production of both CO_2 and H_2O, as seen in Figure 3(a). When a temperature of about 185°C is reached, the HP-XPS spectra provide signatures of an abrupt change in the surface chemistry, similar to that observed for the CO case. Moving to higher temperature does not significantly change this picture, except for a minor increase in water production, indicating that the reaction is mass transfer limited at this stage. The O $1s$ and Pd $3d_{5/2}$ core level spectra, at about 260°C, shown in the upper panels of Fig. 3(b) and (c), show clear evidence of a $\sqrt{5}$ surface oxide covered Pd(100) surface. At this point, the O $1s$ core level spectrum also displays contributions

due to H_2O and CO_2 in the gas phase, at 534.1 eV and 535.6 eV, respectively. No component due to adsorbed CO is present, indicating that the CO residence time is very short, i.e. all CO molecules that reach the surface immediately react to form carbon dioxide. As the sample temperature is decreased the behavior is reversed. At 155°C a major decrease in both CO_2 and H_2O production is observed, resulting from CO covering the surface preventing the oxidation reactions.
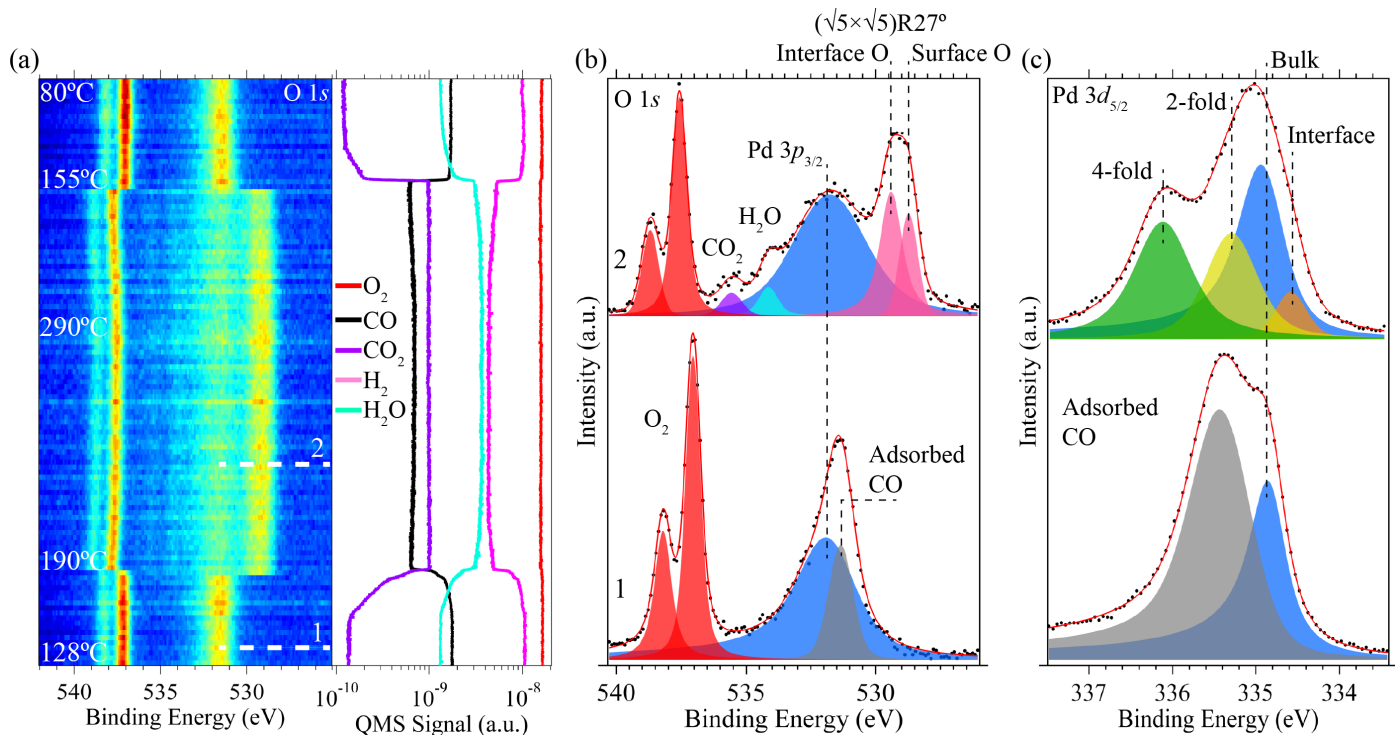
4

Figure 3: Simultaneous CO and H_2 oxidation over Pd(100) at 0.8 mbar and O_2:CO:H_2 ratio 10:1:1. (a) O $1s$ core level region recorded as a function of sample temperature along with the corresponding recorded QMS data for O_2, CO, H_2, CO_2 and H_2O. (b) and (c) Decomposition of the O $1s$ and Pd $3d_{5/2}$ core level spectra, respectively, at two stages in the reaction, (1) no activity and (2) high activity towards CO_2 and H_2O production.

3.2. Oxidation over $Pd_{75}Ag_{25}(100)$

3.2.1. CO Oxidation

The CO oxidation over $Pd_{75}Ag_{25}(100)$ was performed similarly to the CO oxidation over Pd(100). The results from experiments conducted at an O_2:CO ratio 10:1 during ramping the sample temperature from about 45°C up to 430°C and then cooling down again to about 60°C are presented in Figure 4(a). As in the case of Pd(100), at the initial stage, labeled 1 in Fig. 4(a), the QMS data shows no CO_2 formation. The corresponding HP-XPS O $1s$ core level spectrum shows three main contributions. The decomposition of the spectrum, displayed in the lower panel of Fig. 4(b), yields the same spectral components as for the CO oxidation over Pd(100) in the low reactivity stage. The intensity of the Pd $3p_{3/2}$ component, at 531.5 eV, for $Pd_{75}Ag_{25}(100)$ is lower compared to Pd(100), which is expected due to the presence of silver. Noteworthy is the corresponding lower amount of adsorbed CO.

At a sample temperature of about 140°C the CO_2 signal increases. Raising the temperature further results in growing CO_2 production, with a high CO oxidation activity reached at about 210°C. Interestingly, in contrast to the Pd(100) case, the HP-XPS spectra for $Pd_{75}Ag_{25}(100)$ do not display significant changes neither for the surface

related contributions nor for the gas phase components. Spectrum 2 in Fig. 4(b) displays a fitted O $1s$ core level spectrum measured at this temperature. At the low binding energy side of the Pd $3p_{3/2}$ contribution, a new peak at binding energy 530.1 eV is observed, while the component due to adsorbed CO is no longer present. The Pd $3p_{3/2}$ peak shows higher spectral intensity compare to spectrum 1. There is no indications of a $\sqrt{5}$ surface oxide formed. However, based on the fact that the new component is located at lower binding energy relative to the adsorbed CO peak in spectrum 1 and the Pd $3p_{3/2}$ peak intensity increases, we attribute the component at 530.1 eV to a chemisorbed oxygen phase, see below. Adsorption of oxygen induces segregation of Pd to the surface [17, 27, 28, 30], therefore the intensity of the Pd $3p_{3/2}$ peak is expected to increase. A component due to gas phase CO_2 is seen in addition to the peaks due to gas phase oxygen, which are shifted by approximately 0.1 eV relative to spectrum 1. This small variation indicates relatively minor changes in the sample work function compared to Pd(100), where the shift was about 0.4 eV.

Interestingly, as the temperature is increased to 430°C, the CO_2 partial pressure decreases, and consequently the CO partial pressure increases. Spectrum 3 in Figure 4(b),
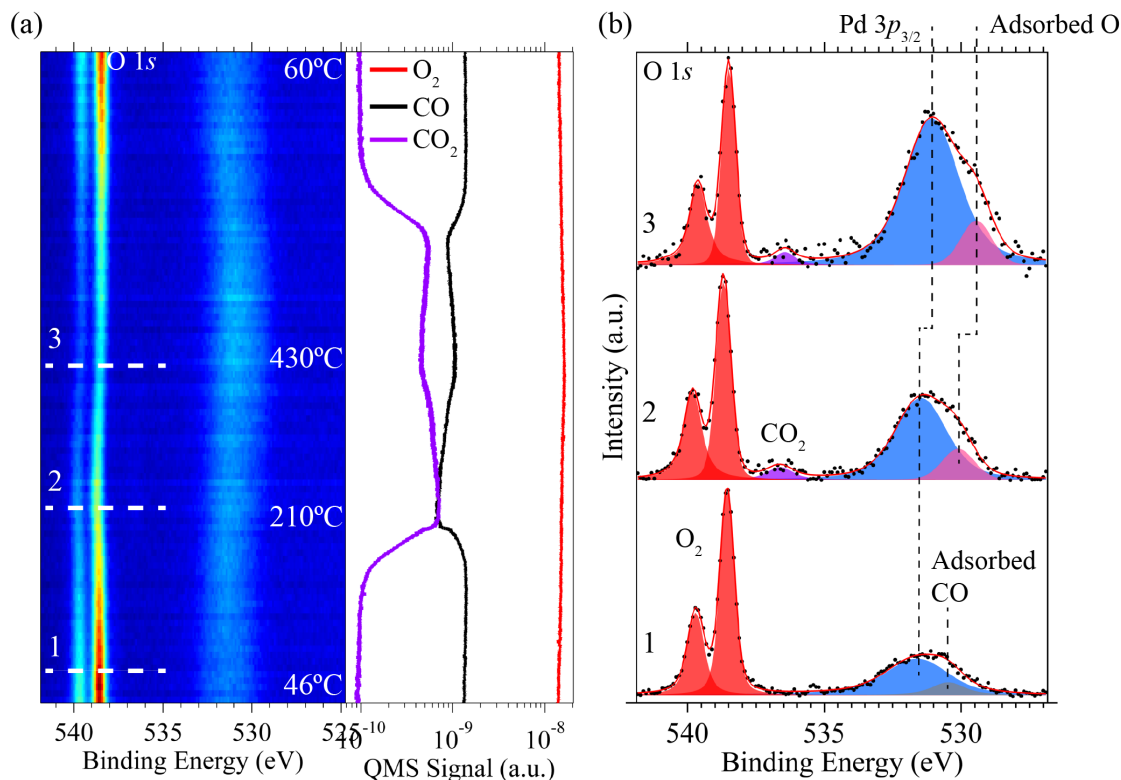
5

Figure 4: CO oxidation over the $Pd_{75}Ag_{25}(100)$ surface as a function of temperature, measured at about 0.7 mbar and a ratio of partial pressures of O_2:CO at 10:1. (a) O $1s$ core level region recorded by HP-XPS as a function of temperature along with corresponding QMS data for O_2, CO and CO_2. (b) Decomposition of the O $1s$ core level spectra at three stages during the reaction, (1) no oxidation activity, (2) high activity, and (3) highest temperature in the high activity regime.

measured at 430°C, shows that the chemisorbed O and Pd $3p_{3/2}$ peaks are now shifted towards lower binding energies, -0.6 eV and -0.4 eV, respectively, relative to the peak position in spectrum 2. Simultaneously, the O_2 gas phase peaks have shifted -0.2 eV to lower binding energies relative to spectrum 2.

Decreasing the temperature, but remaining in the high reactivity regime, leads to recovery of the CO_2 production, although to a less extent than the maximum CO_2 production initially obtained. Eventually, a temperature is reached (230°C) where CO covers the surface, inhibiting the oxidation reaction.

3.2.2. H_2 oxidation

The results from oxidation of H_2 over $Pd_{75}Ag_{25}(100)$ during exposure to an O_2:H_2 mixture of ratio 10:1 are presented in Fig. 5. The temperature was ramped from about 50°C up to about 490°C and then decreased to about 67°C. The development of the O $1s$ core level region along with QMS data are displayed in Fig. 5(a). The QMS data shows a more complex behavior compared to Pd(100). No water production is observed at the initial temperature of 50°C. At this stage, labeled 1 in Fig. 5(a), the decomposi-

tion of the spectrum, displayed in the lower panel of Fig. 5(b), reveals components attributed to adsorbed oxygen (at 530.3 eV), the Pd $3p_{3/2}$ component (at 531.5 eV), and oxygen gas phase components.

As the temperature is raised, H_2O production is initiated (at about 145°C). The highest activity for water production is observed at the maximum temperature of about 490°C. The decomposition of the O $1s$ core level spectrum at the maximum temperature, Fig. 5(b) spectrum labeled 2, shows an increase in the spectra intensity of the adsorbed oxygen O $1s$ and Pd $3p_{3/2}$ peaks, along with an additional peak due to gas phase H_2O. Cooling down the sample leads to a decrease in water production and eventual no water formation (at about 90°C).

3.2.3. Simultaneous CO and H_2 oxidation

The experiment of the simultaneous CO and H_2 oxidation over the $Pd_{75}Ag_{25}(100)$ surface was performed using the same reactant ratio as in the case of Pd(100), O_2:CO:H_2 ratio 10:1:1. The temperature was ramped from 70°C up to about 485°C and then cooling down to about 200°C. Overall, the oxidation behavior has strong resemblance to the Pd(100) case, but with some distinct
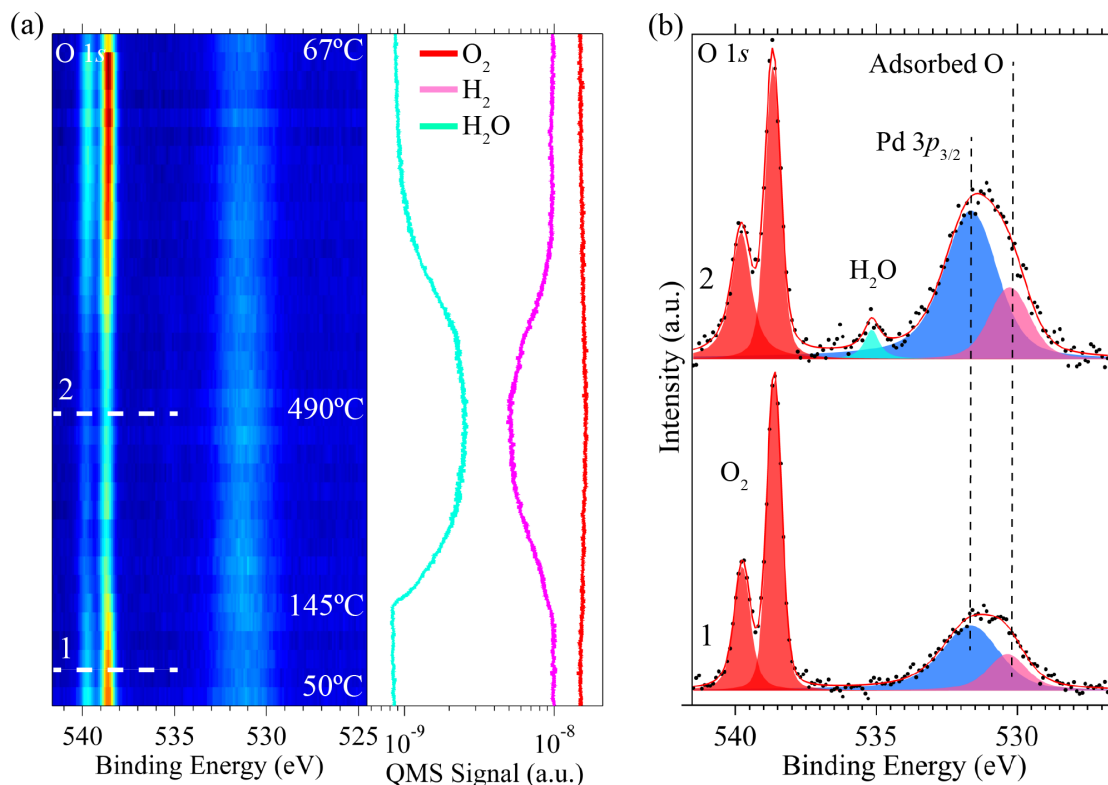
Figure 5: H_2 oxidation on the $Pd_{75}Ag_{25}(100)$ surface at 0.7 mbar and O_2:H_2 ratio 10:1. (a) O $1s$ core level region recorded as a function of sample temperature along with the corresponding recorded QMS data for O_2, H_2, and H_2O. (b) Decomposition of the O $1s$ core level spectra at two different stages during the H_2 oxidation experiment, (1) no activity and (2) high activity towards H_2O production.

differences with respect to surface chemistry. The results are presented in Figure 6. Initially, no H_2O or CO_2 formation is observed by QMS, as illustrated in Figure 6(a). Decomposition of the accompanying O $1s$ core level spectrum, labeled 1 in Figure 6(b) , displays components corresponding to adsorbed CO (at 530.6 eV), Pd $3p_{3/2}$, CO gas phase (at 537.8 eV), and two gas phase O_2 peaks (at 538.8 eV and 539.9 eV). At this point oxidation is inhibited by adsorbed CO covering the surface, confirmed by the CO induced peak present in the C $1s$ core level region, displayed in the supplementary material.

Slowly increasing CO_2 and H_2O production starts at about 130°C. Similarly to Pd(100), water formation is initiated at slightly higher temperature than the onset for CO_2 formation. At about 200°C a significant increase in CO_2 and H_2O partial pressures is visible. However, no significant changes are observed in the HP-XPS data. At 225°C maximum CO_2 production is obtained. Decomposition of the corresponding O $1s$ core level spectrum, Figure 6(b) spectrum 2, shows components due to chemisorbed oxygen (at 530.4 eV), Pd $3p_{3/2}$, gas phase H_2O, CO_2, and O_2. The spectral intensity of the Pd $3p_{3/2}$ peak is higher compared to spectrum 1 in Figure 6(b). As previously seen in the separate CO oxidation and H_2 oxidation experiments

over $Pd_{75}Ag_{25}(100)$, only chemisorbed oxygen is present on the surface when high oxidation reactivity is observed.

Upon increasing the temperature up to about 485°C the QMS data shows a decrease in the partial pressure of CO_2, analogous to the decrease observed during CO oxidation. No decrease in water formation is observed at this point. Figure 6(b), spectrum 3, shows the same spectral contributions as at 225°C. Reducing temperature results in partial recovery of CO_2 production, until CO_2 and H_2O formation again ceases below 240°C.

4. Discussion

On the Pd(100), recent studies have settled the question regarding the surface chemistry when CO oxidation is active [33, 36, 37, 39, 42, 43, 59]. The $\sqrt{5}$ Pd(100) surface oxide is clearly identified and in the inactive phase the surface is covered with CO, inhibiting the reaction. The CO oxidation experiments performed under highly oxygen rich conditions in the present work confirm this picture. Furthermore, our QMS data allows for determination of the activation energy of this reaction, which is found to be 1.0 eV.
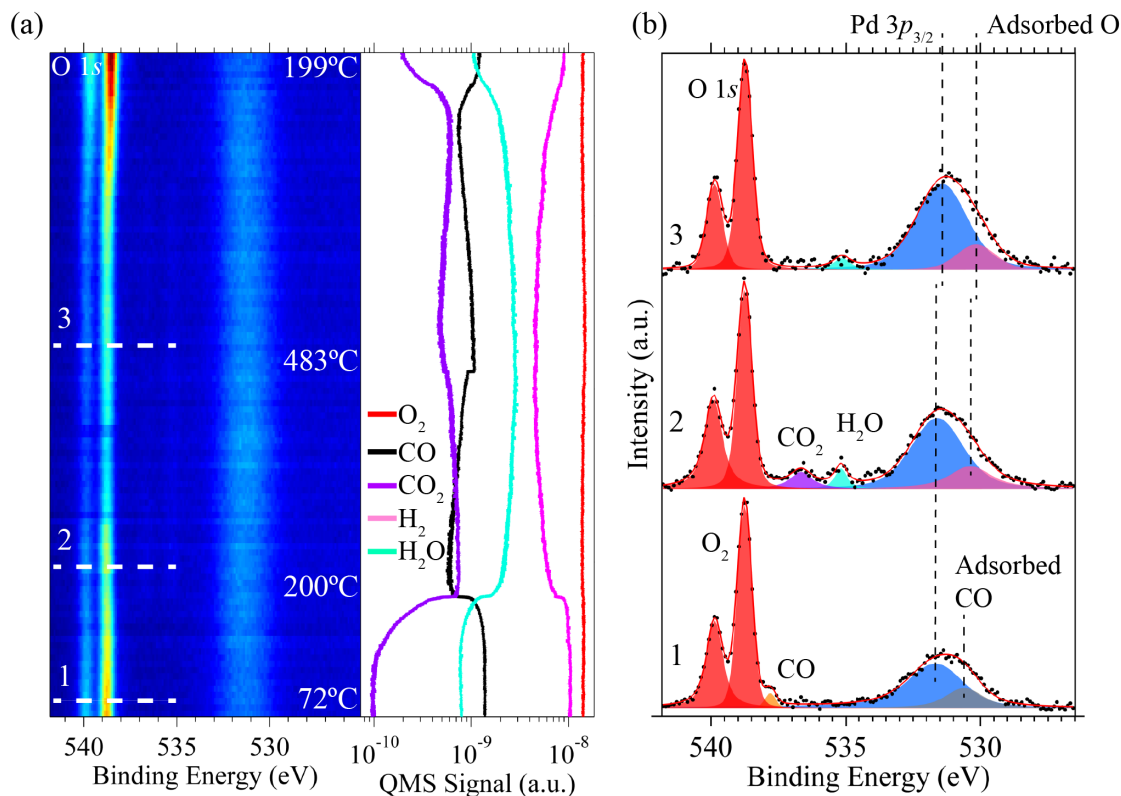
Figure 6: Simultaneous CO and H_2 oxidation over $Pd_{75}Ag_{25}(100)$ as a function temperature, recorded at pressure 0.8 mbar and O_2:CO:H_2 ratio 10:1:1. (a) O $1s$ core level region as a function of temperature along with the corresponding recorded QMS data for O_2, H_2 and H_2O. (b) Decomposition of the O $1s$ core level spectra at three stages during the reaction experiment, (1) no oxidation activity and (2) high activity. (At about 480°C the QMS data for the CO partial pressure shows a sudden change resulting from alterations in the CO flow. This has no significant impact in the main features of the data.)

Turning to H_2 oxidation over the same surface, some important differences are observed. Unlike CO oxidation, where the reaction is initiated at around 190°C, H_2 oxidation to H_2O is already running at RT. The amount of H_2O produced during the H_2 oxidation at O_2:H_2 ratio 10:1 does not change significantly with temperature up to about 510°C, indicating that the reaction may be mass transfer limit in this temperature range. Furthermore, the O $1s$ core level spectra show that the Pd(100) surface is covered by the $\sqrt{5}$ surface oxide, pointing to H_2 oxidation over the surface oxide being facile. The mechanism of this reaction is an interesting issue. Density functional theory (DFT) studies report that H_2 does not chemisorb on $\sqrt{5}$ surface oxide on Pd(100) [60]. Recently, we have analyzed the reduction of the $\sqrt{5}$ surface oxide on Pd(100) and $Pd_{75}Ag_{25}(100)$ under UHV conditions, observing a behavior consistent with the DFT prediction [61]. However, in the present study, we observe H_2O formation with the $\sqrt{5}$ surface oxide present on the surface, indicating that H_2 interacts with the oxide structure at higher pressures.

In the high activity regime for CO oxidation over Pd(100), when surface oxide is present, the reaction follow a Mars van Krevelen reaction mechanism [33, 36, 37, 39, 42, 43, 59]. The same mechanism is likely to be responsible for hydrogen oxidation. Several studied performed under UHV conditions on Pd surfaces have shown that water formation proceeds primarily through disproportionation of hydroxyl groups [62–66]. From our data we cannot confirm a reaction path involving OH, as we are unable to observe OH groups due to the Pd $3p_{3/2}$ peak in the O $1s$ core level spectra. When temperature exceeds about 510°C, the QMS data along with the corresponding O $1s$ core level spectrum in Fig. 2 show that there is a small increase in water production which is accompanied by a change in surface chemistry. At this temperature, which is well above the desorption temperature of the $\sqrt{5}$ surface oxide on Pd(100) under UHV conditions, at about 350°C, we have a Pd(100) surface with chemisorbed oxygen, which has similar reactivity with respect to H_2 oxidation as the $\sqrt{5}$ surface oxide. This change in surface chemistry is likely also to change the reaction mechanism. A Langmuir-Hinshelwood mechanism would be expected in this case.

When CO and H_2 are simultaneously oxidized over

8

Pd(100), the main features of the reactions are controlled by the CO oxidation reaction. Below 135°C the surface is covered with CO and neither CO_2 nor H_2O is formed. As the temperature is raised the surface enters a low activity state where CO_2 and H_2O formation is initiated. Noteworthy is that the CO_2 partial pressure starts to increase at slightly lower temperature than the H_2O partial pressure. This is expected since the surface is initially covered by CO. The presence of CO on the surface reduces the uptake of hydrogen [67–69] and increases the activation barrier for H_2 sticking [70], as well as for H_2 dissociation [70, 71]. It has been suggested that the interaction of hydrogen with CO on Pd surfaces is repulsive [67, 70]. Above a critical temperature of about 190°C the $\sqrt{5}$ Pd(100) surface oxide is clearly identified on the surface and the CO_2 and H_2O formation is mass transfer limited.

Introducing Ag as alloying element significantly affects the the oxidation reactions investigated. Starting with CO oxidation over $Pd_{75}Ag_{25}(100)$ the QMS data shows clear similarities, in particular at lower temperatures. The transition to the high activity phase appear at about 200°C, slightly higher than for Pd(100). Also the activation energy for the reaction is higher, 1.1 eV. As for Pd(100), gas conversion is observed at lower temperatures, about 130°C. The amount of adsorbed CO on the surface of $Pd_{75}Ag_{25}(100)$, below this temperature, is considerably less compared to Pd(100). In general CO favors adsorption in highly coordinated sites on ensembles of Pd atoms on PdAg alloy surfaces [30, 72–75], and does not adsorb on silver [68, 72–76]. Moreover, the presence of Ag in the surface leads to weaker Pd-CO bond strength [74, 75, 77]. This explains the observed lower amount of CO adsorbed on $Pd_{75}Ag_{25}(100)$. More importantly, the O $1s$ core level spectra show no sign of a $\sqrt{5}$ surface oxide being formed on $Pd_{75}Ag_{25}(100)$ under the highly oxygen rich conditions applied in our experiments. Instead, the signature of chemisorbed oxygen is observed at the stage when the surface displays high CO oxidation reactivity. This finding shows that Ag clearly affects the surface chemistry and a high oxidation reactivity can also be obtained for a Pd based alloy surface with chemisorbed oxygen.

Exposing the $Pd_{75}Ag_{25}(100)$ surface to pure O_2 at about 0.7 mbar and temperature 320°C yields a $\sqrt{5}$ surface oxide. However, if the O_2 flow is stopped *or the* temperature is lower than 320°C this structure is rapidly reduced by residual CO/H_2 in the system. In addition, at optimal O_2 and temperature conditions for observing the $\sqrt{5}$ structure, the introduction of either CO or H_2 (at ratio $O_2:CO/H_2$ 10:1) in the system leads to rapid reduction of the surface oxide. HPXPS measurements of the Pd $3d$ and Ag $3d$ core level regions in the same scan, shows an enrichment of silver at the surface, which may explain why surface oxide formation is not observed in the high activity regime. Still, when the activity for CO oxidation switches from low to high the reaction appears to be mass transfer limited also for the alloy surface. Interestingly, for $Pd_{75}Ag_{25}(100)$, increasing the temperature while in the high activity regime leads to a notable decrease in the CO_2 production. A possible explanation for this may be further segregation of silver to the outermost surface layer with increasing temperature due to thermodynamic effects. Since the surface displays a chemisorbed oxygen phase, one may speculate that the oxidation reaction proceeds via the Langmuir-Hinshelwood mechanism.

The oxidation behavior for H_2 oxidation over $Pd_{75}Ag_{25}(100)$ is quite complex. Also in this case, unlike for Pd(100), no $\sqrt{5}$ surface oxide is formed, but chemisorbed oxygen is present on the surface when water is formed. Furthermore, below 145°C no H_2O formation is seen, suggesting a higher activation energy also for this reaction on the alloy surface. The amount of water recorded by QMS has a quite different temperature dependence compare to Pd(100). The reason for this performance is yet to be understood.

Simultaneous oxidation of CO and H_2 over $Pd_{75}Ag_{25}(100)$ is also controlled by the CO oxidation reaction and the trend with onset of the CO oxidation reaction at slightly lower temperature compared to H_2 oxidation is seen.

Comparing the catalytic oxidation of CO and H_2 over Pd(100) and $Pd_{75}Ag_{25}(100)$ reveals that Ag as alloying element significantly affects the reaction behavior. Most importantly, the surface chemistry differs for the two surfaces when the oxidation reactions are running. Ag segregation effects influence available adsorption sites, activation energies and product yields in a complex manner, which have to be considered for catalysis applications.

5. Conclusions

Comparing the catalytic CO oxidation and simultaneous CO and H_2 oxidation on Pd(100) and $Pd_{75}Ag_{25}(100)$ surfaces under oxygen rich conditions at near-ambient pressures clearly shows that Ag as alloying element clearly affects the reaction behavior. The activation energy for CO oxidation over Pd(100) was determined at 1.0 eV, while a value of 1.1 eV for $Pd_{75}Ag_{25}(100)$ obtained. CO inhibition of the reaction is observed at low temperatures for both surfaces when CO only is oxidized

as well as in the case of simultaneous oxidation of CO and H_2. In the latter case the CO oxidation is determining the overall oxidation behavior. Above a critical temperature, the reactivity is high. While the $(\sqrt{5} \times \sqrt{5})R27°$ surface oxide is the active surface in the reactions for Pd(100), chemisorbed oxygen plays this role for $Pd_{75}Ag_{25}(100)$. The presence of silver in the outermost surface layer significantly thus affects the surface chemistry during these reactions and thereby the reaction mechanism.

References

[1] R. Heck, R. Farrauto, Catalytic Air Pollution Control: Commercial Technology, 3rd Edition, Van Nostrand Reinhold, 2009.

[2] G. Centi, J. Mol. Catal. A: Chem. 173 (1-2) (2001) 287.

[3] P. Henry, Palladium Catalyzed Oxidation of Hydrocarbons, Springer, 1980.

[4] B. K. Warren, S. T. Oyama, Heterogeneous hydrocarbon oxidation, American Chemical Society, 1996.

[5] D. Ciuparu, M. R. Lyubovsky, E. Altman, L. D. Pfefferle, A. Datye, Catal. Rev. 44 (4) (2002) 593.

[6] P. Gélin, M. Primet, Appl. Catal. B 39 (1) (2002) 1.

[7] N. Itoh, R. Govind, Ind. Eng. Chem. Res. 28 (10) (1989) 1554.

[8] J. Shu, B. P. A. Grandjean, A. V. Neste, S. Kaliaguine1, Can. J. Chem. Eng. 69 (5) (1991) 1036.

[9] S. Uemiya, Separ. Purif. Rev. 28 (1) (1999) 51.

[10] R. Dittmeyer, V. Höllein, K. Daub, J. Mol. Catal. A 173 (1-2) (2001) 135.

[11] A. K. M. Fazle Kibria, Y. Sakamoto, Int. J. Hydrogen Energy 25 (9) (2000) 853.

[12] R. Hughes, Membrane Technology 2001 (131) (2001) 9.

[13] O. Hatlevik, S. K. Gade, M. K. Keeling, P. M. Thoen, A. P. Davidson, J. D. Way, Separ. Purif. Method. 73 (1) (2010) 59.

[14] P. T. Wouda, M. Schmid, B. Nieuwenhuys, P. Varga, Surf. Sci. 417 (2-3) (1998) 292.

[15] T. Marten, O. Hellman, A. V. Ruban, W. Olovsson, C. Kramer, J. P. Godowski, L. Bech, Z. Li, J. Onsgaard, I. A. Abrikosov, Phys. Rev. B 77 (2008) 125406.

[16] J. R. Kitchin, K. Reuter, M. Scheffler, Phys. Rev. B 77 (2008) 075437.

[17] B. C. Khanra, M. Menon, Physica B 291 (3-4) (2000) 368.

[18] M. Ropo, K. Kokko, L. Vitos, J. Kollár, Phys. Rev. B 71 (2005) 045411.

[19] M. Ropo, Phys. Rev. B 74 (2006) 195401.

[20] O. M. Løvvik, Surf. Sci. 583 (1) (2005) 100.

[21] H. Y. Kim, H. G. Kim, J. H. Ryu, H. M. Lee, Phys. Rev. B 75 (2007) 212105.

[22] S. González, K. M. Neyman, S. Shaikhutdinov, H.-J. Freund, F. Illas, J. Phys. Chem. C 111 (18) (2007) 6852.

[23] L. Vitos, A. V. Ruban, H. L. Skriver, J. Kollár, Surf. Sci. 411 (1-2) (1998) 186.

[24] A. V. Ruban, S. I. Simak, P. A. Korzhavyi, B. Johansson, Phys. Rev. B 75 (2007) 054113.

[25] D. Tománek, S. Mukherjee, V. Kumar, K. H. Bennemann, Surf. Sci. 114 (1) (1982) 11.

[26] L. C. A. van den Oetelaar, O. W. Nooij, S. Oerlemans, A. W. Denier van der Gon, H. H. Brongersma, L. Lefferts, A. G. Roosenbrand, J. A. R. van Veen, J. Phys. Chem. B 102 (18) (1998) 3445.

[27] P. T. Wouda, M. Schmid, B. E. Nieuwenhuys, P. Varga, Surf. Sci. 423 (1) (1999) 229.

[28] L. E. Walle, H. Grönbeck, V. R. Fernandes, S. Blomberg, M. H. Farstad, K. Schulte, J. Gustafson, J. N. Andersen, E. Lundgren, A. Borg, Surf. Sci. 606 (23-24) (2012) 1777.

[29] J. Shu, B. E. W. Bongondo, B. P. A. Grandjean, A. Adnot, S. Kaliaguine, Surf. Sci. 291 (1-2) (1993) 129.

[30] I.-H. Svenum, J. A. Herron, M. Mavrikakis, H. J. Venvik, Catal. Today 193 (1) (2012) 111.

[31] O. M. Løvvik, R. A. Olsen, J. Chem. Phys 118 (7) (2003) 3268–3276.

[32] O. M. Løvvik, S. M. Opalka, Surf. Sci. 602 (17) (2008) 2840.

[33] B. L. M. Hendriksen, S. C. Bobaru, J. W. M. Frenken, Surf. Sci. 552 (1-3) (2004) 229.

[34] A. Piednoir, M. A. Languille, L. Piccolo, A. Valcarcel, F. J. C. S. Aires, J. C. Bertolini, Catal. Lett. 114 (1-2) (2007) 110.

[35] F. Gao, S. M. McClure, Y. Cai, K. K. Gath, Y. Wang, M. S. Chen, Q. L. Guo, D. W. Goodman, Surf. Sci. 603 (1) (2009) 65.

[36] M. Chen, X. V. Wang, L. Zhang, Z. Tang, H. Wan, Langmuir 26 (23) (2010) 18113.

[37] B. L. M. Hendriksen, M. D. Ackermann, R. van Rijn, D. Stoltz, I. Popa, O. Balmes, A. Resta, D. Wermeille, R. Felici, S. Ferrer, J. W. M. Frenken, Nat. Chem. 2 (9) (2010) 730.

[38] R. van Rijn, O. Balmes, R. Felici, J. Gustafson, D. Wermeille, R. Westerstroöm, E. Lundgren, J. W. M. Frenken, J. Phys. Chem. C 114 (14) (2010) 6875.

[39] R. van Rijn, O. Balmes, A. Resta, D. Wermeille, R. Westerström, J. Gustafson, R. Felici, E. Lundgren, J. W. M. Frenken, Phys. Chem. Chem. Phys. 13 (29) (2011) 13167.

[40] A. Hellman, A. Resta, N. M. Martin, J. Gustafson, A. Trinchero, P.-A. Carlsson, O. Balmes, R. Felici, R. van Rijn, J. W. M. Frenken, J. N. Andersen, E. Lundgren, H. Grönbeck, J. Phys. Chem. Lett. 3 (6) (2012) 678.

[41] R. Toyoshima, M. Yoshida, Y. Monya, Y. Kousa, K. Suzuki, H. Abe, B. S. Mun, K. Mase, K. Amemiya, H. Kondoh, J. Phys. Chem. C 116 (35) (2012) 18691.

[42] R. Toyoshima, M. Yoshida, Y. Monya, K. Suzuki, B. S. Mun, K. Amemiya, K. Mase, H. Kondoh, J. Phys. Chem. Lett. 3 (21) (2012) 3182.

[43] S. Blomberg, M. J. Hoffmann, J. Gustafson, N. M. Martin, V. R. Fernandes, A. Borg, Z. Liu, R. Chang, S. Matera, K. Reuter, E. Lundgren, Phys. Rev. Lett. 110 (2013) 117601.

[44] R. Toyoshima, M. Yoshida, Y. Monya, K. Suzuki, K. Amemiya, K. Mase, B. S. Mun, H. Kondoh, J. Phys. Chem. C 117 (40) (2013) 20617.

[45] J. Rogal, K. Reuter, M. Scheffler, Phys. Rev. Lett. 98 (2007) 046101.

[46] J. Rogal, K. Reuter, M. Scheffler, Phys. Rev. B 75 (20) (2007) 205433.

10

[47] F. Gao, Y. Wang, Y. Cai, D. W. Goodman, J. Phys. Chem. C 113 (1) (2009) 174.

[48] R. Westerström, M. E. Messing, S. Blomberg, A. Hellman, H. Grönbeck, J. Gustafson, N. M. Martin, O. Balmes, R. van Rijn, J. N. Andersen, K. Deppert, H. Bluhm, Z. Liu, M. E. Grass, M. Hävecker, E. Lundgren, Phys. Rev. B 83 (2011) 115440.

[49] G. Zheng, E. I. Altman, J. Phys. Chem. B 106 (5) (2002) 1048.

[50] J. Méndez, S. H. Kim, J. Cerdá, J. Wintterlin, G. Ertl, Phys. Rev. B 71 (2005) 085409.

[51] S. H. Kim, J. Méndez, J. Wintterlin, G. Ertl, Phys. Rev. B 72 (2005) 155414.

[52] I. Nakai, H. Kondoh, T. Shimada, A. Resta, J. N. Andersen, T. Ohta, J. Chem. Phys 124 (2006) 224712.

[53] S. Nagarajan, K. Thirunavukkarasu, C. S. Gopinath, J. Phys. Chem. C 113 (17) (2009) 7385.

[54] M. G. Jones, T. G. Nevell, R. J. Ewen, C. L. Honeybourne, Appl. catal. 70 (1) (1991) 277.

[55] J. Schnadt, J. Knudsen, J. N. Andersen, H. Siegbahn, A. Pietzsch, F. Hennies, N. Johansson, N. Mårtensson, G. Öhrwall, S. Bahr, S. Mähl, O. Schaff, J. Synchrotron Rad. 19 (5) (2012) 701.

[56] S. Doniach, M. Šunjić, J. Phys. C: Solid State Phys. 3 (2) (1970) 285.

[57] M. Todorova, E. Lundgren, V. Blum, A. Mikkelsen, S. Gray, J. Gustafson, M. Borg, J. Rogal, K. Reuter, J. N. Andersen, M. Scheffler, Surf. Sci. 541 (2003) 101.

[58] P. Kostelník, N. Seriani, G. Kresse, A. Mikkelsen, E. Lundgren, V. Blum, T. Šikola, P. Varga, M. Schmid, Surf. Sci. 601 (6) (2007) 1574.

[59] D. R. Butcher, M. E. Grass, Z. Zeng, F. Aksoy, H. Bluhm, W.-X. Li, B. S. Mun, G. A. Somorjai, Z. Liu, J. Am. Chem. Soc. 133 (50) (2011) 20319.

[60] M. Blanco-Rey, D. J. Wales, S. J. Jenkins, J. Phys. Chem. C 113 (38) (2009) 16757.

[61] V. R. Fernandes, J. Gustafson, L. E. Walle, M. H. Farstad, S. Blomberg, E. Lundgren, H. J. Venvik, A. Borg, In preparation.

[62] T. Engel, H. Kuipers, Surf. Sci. 90 (1) (1979) 181.

[63] E. M. Stuve, S. W. Jorgensen, R. J. Madix, Surf. Sci. 146 (1) (1984) 179.

[64] C. Nyberg, C. G. Tengstal, J. Chem. Phys. 80 (7) (1984) 3463.

[65] L.-G. Petersson, H. Dannetun, I. Lundström, Surf. Sci. 161 (1) (1985) 77.

[66] A. Johansson, A. Försth, M. Rosén, Int. J. Mol. Sci. 2 (5) (2001) 221.

[67] G. A. Kok, A. Noordermeer, B. E. Nieuwenhuys, Surf. Sci. 135 (1-3) (1983) 65.

[68] A. Noordermeer, G. A. Kok, B. E. Nieuwenhuys, Surf. Sci. 165 (2-3) (1986) 375.

[69] H. Amandusson, L.-G. Ekedahl, H. Dannetun, Appl. Surf. Sci. 153 (4) (2000) 259.

[70] M. Eriksson, L.-G. Ekedahl, Appl. Surf. Sci. 133 (1-2) (1998) 89.

[71] G. Barbieri, F. Scura, F. Lentini, G. De Luca, E. Drioli, Sep. Purif. Technol. 61 (2) (2008) 217.

[72] Y. Soma-Noto, W. M. H. Sachtler, J. Catal. 32 (2) (1974) 315.

[73] N. A. Khan, A. Uhl, S. Shaikhutdinov, H. J. Freund, Surf. Sci. 600 (9) (2006) 1849.

[74] Y. Ma, T. Diemant, J. Bansmann, R. J. Behm, Phys. Chem. Chem. Phys. 13 (2011) 10741.

[75] L. A. Mancera, R. J. Behm, A. Groß, Phys. Chem. Chem. Phys. 15 (2013) 1497.

[76] G. McElhiney, H. Papp, J. Pritchard, Surf. Sci. 54 (3) (1976) 617.

[77] V. R. Fernandes, J. Gustafson, I.-H. Svenum, M. H. Farstad, L. E. Walle, S. Blomberg, E. Lundgren, A. Borg, Surf. Sci. 621 (1) (2014) 31.

Supporting Information
Near-Ambient Pressure CO and H_2 Oxidation on Pd(100) and Pd$_{75}$Ag$_{25}$(100) Surfaces
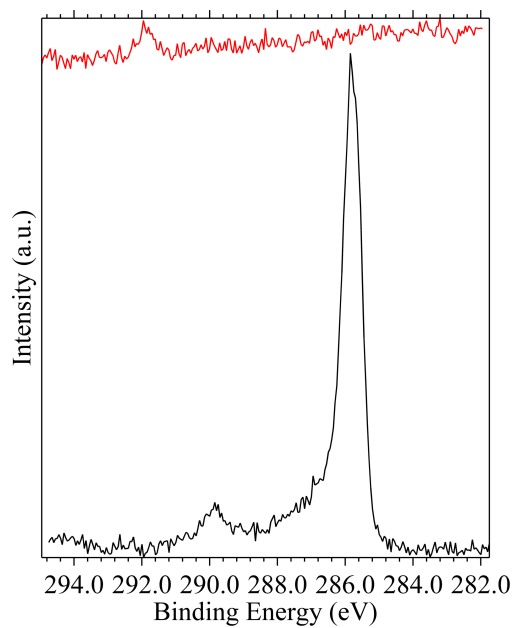
V.R. Fernandes[a], M.H. Farstad[a], J. Knudsen[c], J. Gustafson[c], S. Blomberg[c], E. Lundgren[c], H.J. Venvik[b], A. Borg[a]

[a]*Dept. of Physics, Norwegian Univ. of Science and Technology, NO-7491 Trondheim, Norway*
[b]*Dept. of Chemical Engineering, Norwegian Univ. of Science and Technology, NO-7491 Trondheim, Norway*
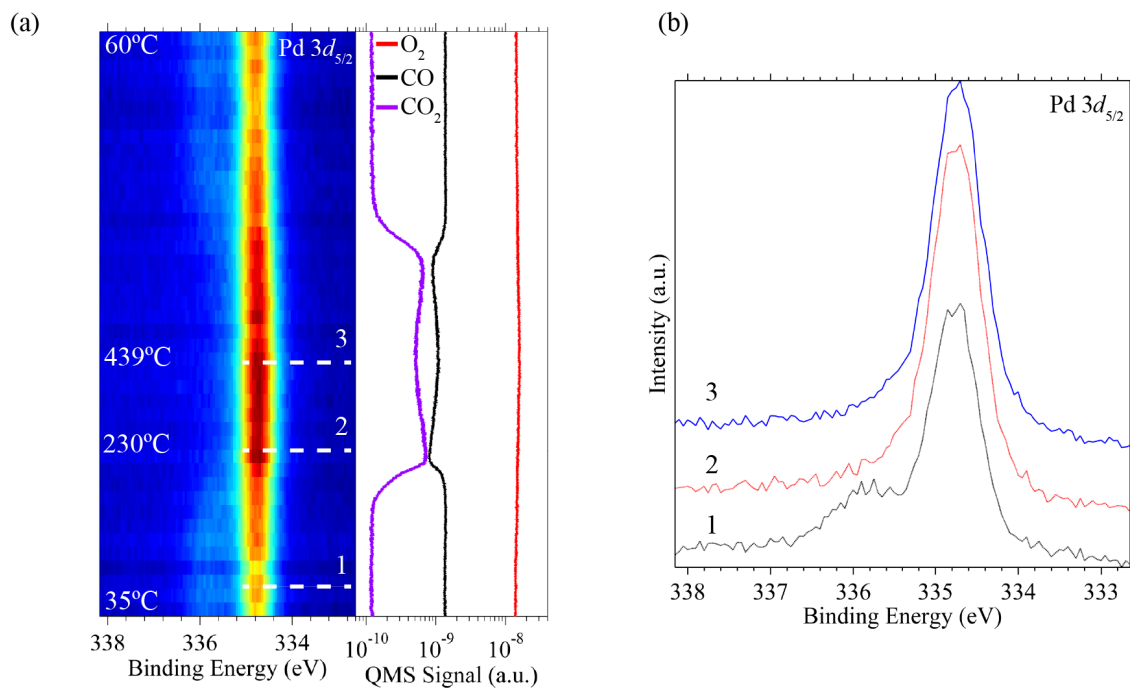[c]*Div. of Synchrotron Radiation Research, Lund Univ., Box 117, SE-221 00 Lund, Sweden*
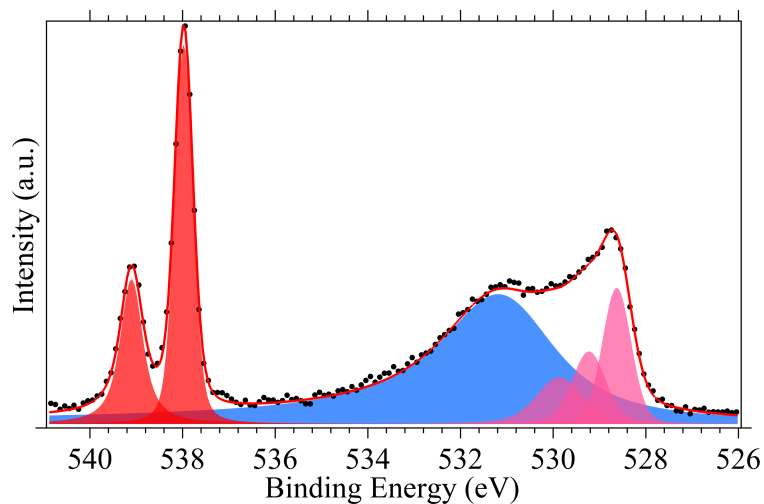
1. S1

S 1: Simultaneous CO and H_2 oxidation on the Pd(100) surface at 0.8 mbar and O_2:CO:H_2 ratio 10:1:1. C 1s core level region at 130°C and 260°C.

In manuscript

2. S2

S 2: CO oxidation on the $Pd_{75}Ag_{25}(100)$ surface at 0.7 mbar and O_2:CO ratio 10:1. (left) Pd $3d_{5/2}$ core level region and QMS data as a function of temperature and time. (right) Pd $3d_{5/2}$ core level at temperatures 40°C, 235°C, and 439°C.

3. S3

S 3: Oxidized $Pd_{75}Ag_{25}(100)$ surface.